



Durham E-Theses

Compact electrical generators for diesel driven generating sets

Brown, Neil Lovell

How to cite:

Brown, Neil Lovell (2002) *Compact electrical generators for diesel driven generating sets*, Durham theses, Durham University. Available at Durham E-Theses Online: <http://etheses.dur.ac.uk/3939/>

Use policy

The full-text may be used and/or reproduced, and given to third parties in any format or medium, without prior permission or charge, for personal research or study, educational, or not-for-profit purposes provided that:

- a full bibliographic reference is made to the original source
- a [link](#) is made to the metadata record in Durham E-Theses
- the full-text is not changed in any way

The full-text must not be sold in any format or medium without the formal permission of the copyright holders.

Please consult the [full Durham E-Theses policy](#) for further details.

Compact Electrical Generators for Diesel Driven Generating Sets

The copyright of this thesis rests with the author.
No quotation from it should be published without
his prior written consent and information derived
from it should be acknowledged.

Neil Lovell Brown

School of Engineering
University of Durham

A thesis submitted in partial fulfillment of the requirements of the Council of the
University of Durham for the Degree of Doctor of Philosophy (PhD)

2002



14 OCT 2002

Compact Electrical Generators for Diesel Driven Generating Sets

Neil Lovell Brown

2002

Abstract

This thesis explores two approaches for converting rotating mechanical power from diesel engines into electrical power of fixed frequency and voltage. Advances in high-energy permanent magnets and power electronics are enabling technologies that provide opportunities for electrical machines with increased efficiency and compact size. Two approaches are explored, Variable Speed and Fixed Speed power generation.

For variable speed, the concept of Variable Speed Integrated Generating Sets (VSIGs) are discussed and suitable electrical machine types reviewed. Axial and Radial permanent magnet machines are compared in detail. An axial flux machine often referred to as the TORUS is researched, and a 50 kW unit designed to integrate within the flywheel housing of a diesel engine. Manufacturing aspects are considered, and two prototype machines are built and tested, the second machine demonstrates a rating of 60kW at 3000rpm. A machine model based upon a combination of Finite Element Analysis and polynomial curve fitting is developed to provide an insight into the design of such machines.

During the course of this research a new form of axial electrical machine known as the Haydock Brown Machine was invented. The fundamental problem of regulating the output voltage for permanent machines has been overcome by the addition of an excitation coil. Saturation, significant leakage fields and three excitation sources make the electromagnetic design process for the Haydock Brown Machine complex. The intuitive application of an equivalent circuit model provides satisfactory results and a 10kW prototype machine operating at fixed speed is built and tested. Using the model new observations are made and a new improved version is proposed called the Haydock Brown Hybrid Machine.

Declaration

I hereby declare that this thesis is a record of work undertaken by myself, that it has not been the subject of any previous application for a degree, and that all the sources of information have been duly acknowledged.

© Copyright 2002, Neil Lovell Brown

The copyright of this thesis rests with the author. No quotation from it should be published without written consent, and information derived from it should be acknowledged.

Acknowledgements

I would like to thank:

My industrial supervisor and long term mentor, Prof. Lawrence Haydock, Technical Director of Newage AVK SEG, whose vision, advice, guidance and support has made this work possible.

Dr Jim Bumby and Prof. Ed Spooner, School of Engineering, University of Durham for excellent supervision and mentoring over the course of this research.

Colleagues at Newage AVK SEG namely Clive Bean, Cleveland Mills, Dr Nazar Al-Khayat and Jerry Dowdall for help in designing, drawing, procuring and building the initial TORUS prototypes. Dr Anca Novinschi and Dr Salem Mebarki for assistance with the Finite Element Analysis models for the Haydock Brown Machine. Simon Walton, Simon Ruffles and Shaun Coulson for the drawing, procurement of parts and general input into the building and test of the Haydock Brown and Haydock Brown Hybrid Machine.

Newage AVK SEG for financial and administrative support

My family for their support and endurance.

Contents

<i>Title Page</i>	i
<i>Abstract</i>	ii
<i>Declaration</i>	iii
<i>Acknowledgements</i>	iv
<i>Contents</i>	v
<i>List of Tables</i>	x
<i>List of Figures</i>	xii
<i>List of symbols and Abbreviations</i>	xvi
Chapter 1 Introduction	1
1.0 Introduction	1
1.1 Thesis Outline	5
1.2 Original Contributions to the Advancement of Knowledge	7
Chapter 2 Generators for Variable Speed Operation	9
2.1 Fixed Speed Power Generation	9
2.2 Variable Speed Benefits and Application	11
2.3 Review of Electrical Machines for Variable Speed Application	18
2.3.1 Traditional Machine Types	18
2.3.1.1 Induction Generator	18
2.3.1.2 Wound Field Machines	18
2.3.2 Permanent Magnet Machine Types	20
2.3.2.1 Radial Flux Permanent Magnet Machines	20
2.3.2.2 Axial Flux Permanent Magnet Machines	22
2.3.2.3 Reluctance Permanent Magnet Machines	23
2.4 Discussion	26

Chapter 3	Axial and Radial Flux Generators	27
3.1	The Axial Flux Generator	29
3.2	The Radial Flux Generator	33
3.3	An Idealised Approach to Electromagnetically Comparing Axial and Radial flux PM Machines	37
3.3.1	Electromagnetic Limit for Torque and Power	38
3.3.2	Geometric Approach	40
3.3.3	Calculation of the Volume Ratio between Axial and Radial Machines for a Given Mass of PM Material –Study 1	45
3.3.4	Calculation of the Volume Ratio between Axial and Radial Machines for a Given Outside Diameter – Study 2	47
3.4	Discussion	52
Chapter 4	Axial Flux Machine Design	53
4.1	Literature Review	53
4.2	Fundamental Equations for Axial Flux Machines	56
4.3	Design Process	57
4.3.1	No Load Magnetic Circuit	58
4.3.2	Calculation of EMF	59
4.3.3	Synchronous Inductance	61
4.3.4	Loss Mechanisms	63
4.3.5	Thermal Equivalent Circuit	65
4.3.6	Prototype Dimensions	68
4.4	FEA Model	70
4.4.1	The No Load Waveform	72
4.4.2	Inductance Calculations	74
4.4.2.1	Self Inductance	76
4.4.2.2	Mutual Inductance	76
4.4.2.3	Synchronous Inductance	76
4.4.2.4	Armature Leakage Inductance	77

4.4.2.5 Generator Model	78
4.4.3 Summary of FEA Results	79
4.5 Refined Thermal Model	80
4.6 Predicted Machine Performance	81
4.7 Discussion	82
Chapter 5 Axial Flux Machine Prototype and Test	84
5.1 Generator Construction	84
5.1.1 Rotor Assembly	87
5.1.2 Stator Assembly	89
5.1.3 Machine Assembly	93
5.2 Test Results	95
5.3 Discussion	103
5.4 Further Work	104
Chapter 6 Axial Flux Machine Optimisation	107
6.1 Setting Up The Model	108
6.2 Model Boundaries	110
6.3 The FEA Model	111
6.4 The EMF Polynomial	112
6.5 The Synchronous Reactance Polynomial	114
6.6 The Stator Resistance Model	117
6.7 Maximum Output Current Model	118
6.8 Results	120
6.9 Discussion	127
Chapter 7 The Haydock Brown Machine Design	130
7.1 Literature Review	130
7.2 Introduction	131
7.3 The HB Configuration	132
7.4 Operation	135

7.5 Modelling	138
7.5.1 Magnetic Equivalent Circuits	138
7.5.2 Equivalent Circuit Parameters	141
7.5.2.1 Iron Poles	141
7.5.2.2 Permanent Magnet Poles	141
7.5.2.3 Stator D-Axis MMF	142
7.5.2.4 Stator Q-Axis MMF	144
7.5.2.5 Leakage Paths	144
7.5.3 Non-Linear Shaft Model	148
7.5.4 D-Axis Magnetic Circuit Analysis	149
7.5.5 Allowance For Varying Power Factor Loads	152
7.5.6 Thermal Model	153
7.5.7 Stator Leakage	155
7.5.7.1 Slot Leakage	156
7.5.7.2 End Winding Leakage	156
7.5.7.3 Air-gap Armature Leakage	158
7.5.7.4 D and Q Axis Leakage over Ferrous Pole	159
7.5.7.4.1 Q Axis Leakage	160
7.5.7.4.2 D Axis Leakage	162
7.5.7.4.3 Variation in D and Q Axis Leakage Inductance	163
7.5.8 Finite Element Analysis	165
7.5.9 Pole Face Losses	166
7.10 Prototype Dimensions	167
7.11 Discussion	169
Chapter 8	The Haydock Brown Machine Construction and Test
8.1 Stator Assembly	170
8.2 Rotor Assembly	175
8.3 End Brackets	177
8.4 Assembly	178
8.5 Test and Validation	179

8.5.1 Static Inductance Test	179
8.5.2 No Load Voltage Waveform	180
8.5.3 Full Load Waveforms	182
8.5.4 No Load Magnetisation Curve without Magnets	183
8.5.5 Short Circuit Curve without Magnets	184
8.5.6 Open Circuit Voltage with Magnets	185
8.5.7 Zero Power Factor Loading	187
8.5.6 0.8 Power Factor Loading	189
8.5.7 Unity Power Factor Loading	190
8.5.8 Thermal Tests	191
8.6 Design Variations	194
8.7 The Haydock Brown Hybrid Machine	196
8.8 Discussion	198
Chapter 9	Conclusion and Further Work
	199
9.1 Conclusion	199
9.1.1 Fixed Speed Power Generation	200
9.1.2 Variable Speed Power Generation	202
9.2 Further Work	204
9.2.1 Fixed Speed	204
9.2.2 Variable Speed	205
Appendix A	206
Optimisation Support Data	
Appendix B	211
Calculation of leakage fields by applying Vector Potential Analysis	
References	221

List of Tables

Table 4.1 Machine dimensions	69
Table 4.2 Machine mass	69
Table 4.3 Electrical parameters	70
Table 4.4 Losses breakdown and efficiency	70
Table 4.5 Calculation of Fourier components	73
Table 4.6 Compares lumped parameter and FEA models	79
Table 4.7 Self and mutual inductance FEA results	79
Table 5.1 Compared measured and calculated values for prototype 1	95
Table 5.2 Measured magnet characteristic	96
Table 5.3 Measured no load voltage, prototype 1	97
Table 5.4 Heat run data	98
Table 5.5 Comparison between calculated and measured harmonic and RMS voltage	100
Table 5.6 Comparison between measured and calculated mutual and self inductance	101
Table 5.7 Heat run data for prototype 2	102
Table 6.1 Highlights which variables describe the four functions in the equivalent circuit	110
Table 6.2 List of model design boundaries	110
Table 6.3 Model details	111
Table 6.4 Per unit variation of resistance	117
Table 6.5 Per unit current allowance for insulation build up on the windings	120
Table 6.6 Different combinations of design parameters for different magnet weights	124

Table 7.1 12kVA machine dimensions	168
Table 7.2 Electrical parameters	168
Table 8.1 Measured slot leakage and end winding leakage inductance	179
Table 8.2 Compares no load, line to line and line to neutral voltages	181
Table 8.3 Harmonic analysis for 0.8 power factor load	182
Table 8.4 Harmonic analysis for 1 power factor load	182
Table 8.5 6kVA 0.8 power factor heat run	192
Table 8.6 9kVA, unity power factor heat run	193
Table 9.1 Comparison between a conventional synchronous machine and the Haydock Brown Hybrid machine	200
Table A.1 Coefficients for the 4th order polynomial used to describe E_{model} compared to pre-computed FEA solutions	207
Table A.2 Normalised E_{rms} for values of K	208
Table A.3 Compares E_{model} with random pre-computed FEA solutions	209
Table A.4 Compares the polynomial model with pre-computed FEA solutions	210

List of Figures

Figure 2.1 Example of a 300 kVA diesel driven synchronous generators	10
Figure 2.2 Block diagram of a variable speed integrated Generating set (VSIG).	11
Figure 2.3 Variation in engine output power with respect to speed	12
Figure 2.4 Engine fuel map for an internal combustion engine	14
Figure 3.1 Axial flux machine evolution	28
Figure 3.2 Typical axial flux generator arrangement	29
Figure 3.3 Plan view showing the direction of flux paths within an axial flux generator	30
Figure 3.4 General arrangement for a radial flux machine	34
Figure 3.5 Flux lines within radial flux machine	35
Figure 3.6 Simple geometry of axial and radial air-gap	40
Figure 3.7 Axial and radial machine dimensions	42
Figure 3.8 Axial/radial volume for a given volume of PM material with respect to K and P	46
Figure 3.9 Compares axial/radial volume for a given machine outer diameter with respect to K and P	50
Figure 4.1 Equivalent circuit to calculate air-gap flux density	58
Figure 4.2 Calculation of RMS phase voltage	60
Figure 4.3 Armature reaction flux paths	62
Figure 4.4 Lumped parameter equivalent circuit	62
Figure 4.5 Half cross section of stator for single layered winding	67
Figure 4.6 Thermal equivalent circuit for single layered winding	67
Figure 4.7 Shows 1/32th model	71
Figure 4.8 Flux linkage with respect to electrical angle	72
Figure 4.9 Shows the calculated voltage waveform.	74
Figure 4.10 FEA model with conductors	75

Figure 4.11 Equivalent circuit	78
Figure 4.12 Equivalent circuit including loss mechanisms	80
Figure 4.13 Predicted performance	82
Figure 5.1 The 4 cylinder diesel engine	85
Figure 5.2 Exploded view of axial flux generator	86
Figure 5.3 Provides an external view of the rotor.	87
Figure 5.4 Magnets, separators and retaining ring assembled onto rotor	89
Figure 5.5 Stator retaining rings	90
Figure 5.6 Shows winding moulding around core with stator winding	91
Figure 5.7 Complete stator	92
Figure 5.8 Indicates the magnetic forces when the stator is offered to the rotor	93
Figure 5.9 Shows the internal rotor and stator bolted onto the engine	93
Figure 5.10 Shows how a displacement between the stator and the rotors results in an axial force	94
Figure 5.11 Second prototype with radial air intake and radial outlet	99
Figure 5.12 Measured phase voltage	100
Figure 5.13 Prototype 2, efficiency curves	103
Figure 6.1 A simple equivalent circuit	109
Figure 6.2 Two dimensional discretisation of mesh	111
Figure 6.3 Synchronous inductance compared with gross air-gap	114
Figure 6.4 Variation in inductance for various K values for a given air-gap	115
Figure 6.5 Variation in inductance for various air-gaps for a given K value	116
Figure 6.6 Variation in power with magnet weight for a 400mm outer diameter machine	123
Figure 6.7 Relationship between τ for different K values	126
Figure 6.8 Compares power increase with weight for different K values when $\tau = 0.8$	127

Figure 7.1 Machine structure	133
Figure 7.2 Developed 2 dimensional diagram	137
Figure 7.3 Magnetic equivalent circuit of HB machine with armature current in the D – axis.	140
Figure 7.4 Illustration showing the calculation of D and Q axis flux	143
Figure 7.5 Leakage flux within machine	147
Figure 7.6 Compares the real and the modelled data	149
Figure 7.7 Reduced D axis equivalent circuit	150
Figure 7.8 Current sourced equivalent circuit	150
Figure 7.9 Reduced Thevenin equivalent circuit	151
Figure 7.10 Shows shaft flux and MMF for no load and full load operation	151
Figure 7.11 Reduced Q axis equivalent circuit	153
Figure 7.12 Slot profile and thermal equivalent circuit	155
Figure 7.13 Q axis leakage flux	161
Figure 7.14 D axis leakage flux	163
Figure 7.15 Three dimensional FEA plots of HB machine	166
Figure 7.16 Pole face losses	167
Figure 8.1 Finished stator core	171
Figure 8.2 Stator during winding process	172
Figure 8.3 Finished excitation coil	173
Figure 8.4 Complete Stator	174
Figure 8.5 Non drive end view of shaft	175
Figure 8.6 View of rotor plate	176
Figure 8.7 Aluminum end bracket	177
Figure 8.8 Complete generating set	179
Figure 8.9 No load voltage waveform line to neutral	181
Figure 8.10 No load magnetisation graph without magnets	184
Figure 8.11 Short circuit curve without magnets	185
Figure 8.12 No load voltage with magnets	187
Figure 8.13 Zero power factor loading with fixed excitation	188

Figure 8.14 0.8 power factor loading for fixed excitation	189
Figure 8.15 Unity power factor loading for fixed excitation	191
Figure 8.16 Design variations	195
Figure 8.17 Rotor design of Haydock Brown Hybrid rotor plate	197
Figure 9.1 A slide showing General Motors vision of the future car industry	203
Figure A.1 Thermal equivalent circuit for three layered winding	211
Figure B.1 Simplified model	212
Figure B.2 Equivalent uniform air-gap	218

List of symbols and Abbreviations

A	Area (m^2)
A	Electric Loading (A/m)
A_m	Magnet Area (m^2)
A_p	Pole Area (m^2)
A_{rms}	RMS Electric Loading (A/m)
B	Flux Density (T)
B_{gap}	Air-gap Flux Density (T)
B_{rem}	Magnet Remanence Flux Density (T)
CB	Core Back depth (m)
D	Radial Air-gap Diameter (m)
D_1	Stator Inner Diameter (m)
D_2	Stator Outer Diameter (m)
D_R	Rotor Outer Diameter (m)
D_{SH}	Shaft Outer Diameter (m)
D_{mean}	Mean Diameter of Stator (m)
E	Energy (J)
E_{ld}	Energy in D axis stator leakage field over ferrous pole (J)
E_{lq}	Energy in Q axis stator leakage field over ferrous pole (J)
F	MMF (A)
F	Force (N)
F_1	Thevenin Equivalent MMF (A/Wb)
F_a	Armature Reaction MMF (A)
F_D	Direct Axis Armature MMF (A)
F_e	Excitation Coil MMF (A)
F_m	Magnet MMF (A)
F_Q	Quadrature Axis Armature MMF (A)
H_m	Magnet coercive Force (A/m)

I	Current (A)
ID	Inner Diameter (m)
I_{DC}	DC current (A)
K	ID/OD
K_d	Winding Distribution Factor
K_w	Winding factor including pitch and distribution
L	Length (m)
L	Inductance (H)
L_C	Stator Core length (m)
L_D	Rotor Disk length (m)
L_{DS}	Rotor disk to stator length (m)
L_{SH}	Shaft Length (m)
L_m	Magnet Length (m)
L_w	Winding Thickness (m)
L_{eq}	Equivalent Length of Uniform Field (m)
L_{air}	Stator Air-gap Leakage Inductance (H)
L_{gap}	Air-gap Length (m)
$L_{gross\ gap}$	Gap length between magnet face and stator (m)
L_{al}	Armature Leakage Inductance (H)
L_{aao}	Space Fundamental Air-gap Inductance (H)
L_{ld}	D Axis Stator Leakage Inductance (H)
L_{lq}	Q Axis Stator Leakage Inductance (H)
L_{lqd}	Variation of stator leakage inductance with pf (H)
L_{mut}	Mutual Inductance (H)
L_{self}	Self Inductance (H)
L_{slot}	Slot Leakage Inductance (H)
L_{synch}	Synchronous Inductance (H)
L_{ENDI}	Inner Stator End Leakage Inductance (H)

L_{ENDO}	Outer Stator End Leakage Inductance (H)
M	Mass (kg)
N_{ph}	Phase Turns
N_{coil}	Turns Per Coil
N_{slot}	Number of Turns in a Slot
N_{group}	Number of Turns in a Group
OD	Outer Diameter (m)
P	Power (W)
P	Number of Poles
PP	Pole Pitch
P_c	Copper Losses (W/m^2)
P_e	Conductor Eddy Current Loss (W/m^2)
P_E	Engine Power (W)
P_i	Iron Losses (W/m^2)
P_{DC}	DC Power (W)
P_{eddy}	Conductor Eddy Current Loss (W/m^3)
R	Torque Radius (m)
R_1	Stator/Magnet/Pole Inner Radius (m)
R_2	Stator/Magnet/Pole Outer Radius (m)
R_c	Thermal Resistance of Core Insulation (K/Wm^2)
R_o	Resistance at Zero Degrees $^{\circ}C$ (Ω)
R_s	Stator Resistance (Ω)
R_w	Thermal Resistance of Conductor Insulation (K/Wm^2)
R_L	Load Resistance (Ω)
R_{ph}	Phase Resistance (Ω)
R_{air}	$1/h_{tc}$ (K/Wm^2)
R_{HOT}	Hot Resistance (Ω)
R_{slot}	Thermal Resistance of Slot Liner ($^{\circ}C/W$)

R_{stator}	Thermal Resistance from Stator Core to Air ($^{\circ}\text{C}/\text{W}$)
S	Reluctance (A/Wb)
SA	Surface Area (m^2)
S_1	Air-gap Reluctance over Half a Pole Pitch (A/Wb)
S_2	Air-gap Reluctance over Half a Pole Pitch (A/Wb)
S_m	Magnet Reluctance including Air-gap (A/Wb)
S_p	Ferrous Pole Reluctance including Air-gap (A/Wb)
S_s	Shaft Reluctance (A/Wb)
S_t	$S_1//S_2$
S_{t1}	Back of Rotor Disk Leakage Reluctance (A/Wb)
S_{t2}	Rotor Disk to Disk Edge Leakage Reluctance (A/Wb)
S_{t3}	Rotor Disk Edge to Stator Edge Leakage Reluctance (A/Wb)
S_{t4}	Shaft Leakage Reluctance (A/Wb)
S_{t5}	Rotor Disk to Stator Leakage Reluctance (A/Wb)
S_{air}	Stator Air-gap Leakage Reluctance (A/Wb)
S_{gap}	Gap Reluctance (A/Wb)
S_{mag}	Magnet Reluctance (A/Wb)
S_{leak}	Leakage Reluctance (A/Wb)
S_{slot}	Slot leakage reluctance (A/Wb)
S_{ENDI}	Inner Stator End Winding Leakage Reluctance (A/Wb)
S_{ENDO}	Outer Stator End Winding Leakage Reluctance (A/Wb)
S_{tooth}	Tooth Reluctance (A/Wb)
T	Torque (Nm)
T_E	Engine Torque (Nm)
T_{ca}	Temperature drop between Copper and Air (K)
T_{ic}	Temperature drop between Core and Copper (K)
T_{WID}	Tooth Width (m)
V_{DC}	DC Voltage (V)

Y_{DEP}	Slot Depth (m)
Y_{LEN}	Slot Length (m)
Y_{WID}	Slot Width (m)
d	Conductor Diameter (m)
e	Electromotive Force (V)
f	Frequency (Hz)
f_e	Specific Force (N/m ²)
h	Harmonic Order
htc	Thermal heat transfer coefficient for air (K/m ² W)
n	Mechanical Speed (revs/sec)
n	Number of Slots on One Stator Side
pf	Power Factor
r	Radius (m)
t	Temperature (°C)
t	Time (s)
t_{ins}	Slot Liner Thickness (m)
w_e	Electrical Speed (rads/sec)
w_m	Mechanical Speed (rads/sec)
z	Slots/Pole/Phase
α	Temperature Coefficient
χ	Electrical displacement angle between turns in degrees
μ_r	Relative Permeability
μ_0	Permeability of Free Space (H/m)
ρ	Resistivity (Ωm)
τ	Pole Arc to Pitch Ratio
ϕ	Flux Linkage (Wb)
ϕ_{ld}	D axis stator leakage flux over ferrous pole (Wb)

ϕ_{lq}	Q axis stator leakage flux over ferrous pole (Wb)
ϕ_{gap}	Airgap Flux (Wb)
ϕ_{rem}	Magnet Remanence Flux (Wb)
Ω	Thermal Conductivity Coefficient (K/mW)
Ω_{ins}	Insulation Thermal Conductivity Coefficient (K/mW)

Chapter

1.

Introduction

The global market for standalone diesel driven generating sets below 2MVA is estimated to have annual sales valued at over \$5.7 Billion, with \$2.2 Billion of sales being in Asia, \$1.9 Billion in the Americas and \$1.6 Billion, in Europe and Africa. From a manufacturers point of view, the Cummins Power Generation Group alone offers diesel powered generating sets up to 4MVA, and has annual sales in excess of \$1.6 Billion per year.

Generally any improvement in size, weight or efficiency for such generating sets and associated infrastructure has a significant impact on costs. In addition there are military and marine applications where such features as compact size, light weight, low emissions and high efficiency are paramount.

Currently, generating sets mainly use 4 pole wound field brushless synchronous generators[1], driven by diesel engines at a fixed speed of 1500/1800rpm for 50/60Hz operation. The wound-field brushless synchronous machine combines two individual electrical machines in a common housing. The main stator and wound rotor provide the nameplate VA rating. The exciter has a rotating armature that feeds excitation current to the main rotor winding via diodes mounted on the shaft. A small permanent magnet

generator may also be included to provide power to the control electronics that supply the stator field winding of the exciter. While the system gives the desired control capability, the resulting package is physically quite large with efficiency compromised by field winding loss and the presence of the second machine. Nevertheless, the absence of brushes and the ability to control excitation from low power electronics makes this the preferred option for the vast majority of applications, ranging from a few kVA to hundreds of MVA rating.

Three new rival technologies for small standalone power generation are Micro Turbines[2], Variable Speed Integrated Generating Sets(VSIGs)[3] and Fuel Cells[4].

Micro Turbines have been developed by companies such as Capstone, Bowman, Elliot (same generator and turbine as Bowman) and Turbo Genset Company. These systems offer a relatively small prime mover and generator, by exploiting high speeds in the region of 60-130 000 rpm. Additional auxiliary equipment is needed including heat exchangers, oil cooling pumps, power electronics, etc, making the overall generating unit large compared with the conventional. The efficiency of small turbines is low, resulting in relatively poor overall system efficiency, and for this reason units are marketed as Combined Heat and Power units. The concept of micro turbines is not new, Petbow was marketing such systems in 1955[5].

VSIG's use conventional reciprocating engines but allow the engine to run at variable speed. This presents many advantages compared to the conventional synchronous

generating set such as reduced size, weight, emissions and fuel consumption. The subject of VSIG's are covered in more detail later.

Most large industrial companies such as General Motors, Ballard Power, Daimler-Benz, General Electric and Honeywell are developing Fuel Cells[4]. Such units offer the ideal of no moving parts and zero emissions. It should be remembered, zero emissions only apply where the fuel is used, not necessarily where the fuel is processed. Invented over a 100 years ago, Fuel Cells have received renewed interest and significant funding over the last decade. While advances have been made, weight, size and cost still preclude the mass exploitation of such technology. Hydrogen is the favoured fuel for fuel cells, however, hydrogen is not a primary fuel and reforming or electrolysis must produce it. Reforming is the process of obtaining hydrogen by the in situ steam forming, and/or partial oxidation of fuels such as methane or diesel. The reformer has cost, weight and size issues. If the hydrogen is provided by electrolysis, it only makes sense to use nuclear or renewable energy sources. The difficulty of safely storing and transporting highly combustible fuel such as hydrogen then becomes an issue.

Diesel engine technology is also advancing driven by economics, the electronics revolution and more recently stringent emissions legislation. The short and medium term solution for the established small diesel engine driven generating set is still very good. Ironically if a solution to safely storing hydrogen were resolved, a reciprocating engine would equally benefit thus prolonging its use.

The purpose of this thesis is to examine what improvements could be made to the diesel driven generating set, by primarily focusing on the electrical generator. For example, any improvement in the efficiency of the electrical machine not only reduces fuel consumption, but the generating set will benefit from a smaller engine and overall size. One way of increasing generator efficiency is to replace the field winding with permanent magnets, thereby eliminating the field winding Joule loss.

Over the last few decades, the energy density of permanent magnet material has increased significantly. In particular Neodymium Iron Boron (NdFeB) has been commercialised[6] and energy densities in excess of 50 MGOe achieved. With the cost of such materials reducing, ferrite magnets are no longer the first choice when designing electrical machines. Such materials have been successfully applied to all sizes of electrical machines from small brushless dc motors to multi-Mega Watt generators and these trends are likely to continue. The use of such material in electrical machines offers reduced size, weight and increased efficiency.

Permanent magnet materials have not been wholly applied to electrical generators because their excitation is fixed, hence output voltage tends to reduce as lagging load current is drawn. A common solution to this problem is to place a power electronics converter in series with the main power flow, so that a conditioned output voltage is applied to the load. This series approach offers design freedom in terms of the electrical machine, as the quality of the electrical output is not important, only the electromagnetic conversion of mechanical power into electrical power. The prime mover is also freed

from having to run at synchronous speed so that variable speed engines can be used with advantage. Strictly, any electrical machine could be used with a series converter but certain machines offer high power density and simple construction.

During the course of this research, a new form of electrical machine known as the ‘Haydock Brown Machine’ (HB Machine) has been invented that combines permanent magnets with wound field excitation[7]. Here a regulated output voltage can be achieved without the need for a power electronics converter in series with the electrical machine.

1.1 Thesis Outline

This thesis explores two approaches with respect to permanent magnet generators, **variable speed power generation** and **fixed speed power generation**.

Variable speed power generation, discussed in chapter 2, offers many advantages such as reduced engine/generator size, high efficiency and low emissions. The variable speed idea exploits the low load factor associated with small standalone generators and should not be considered a viable alternative for constant full power applications. This concept suffers from the additional cost and sophistication of a power electronics converter rated for full line current. However power electronic modules of this type are now increasingly used. Long term the cost and reliability of such devices is likely to improve. In addition chapter 2 will discuss which machine types are most suited to variable speed applications.

Chapter 3 compares the advantages and disadvantages of axial and radial machines, followed by a detailed electromagnetic comparison between the two.

Chapter 4 includes a literature review for a type of axial flux machine referred to as a TORUS. Design equations are first derived from lumped parameter electromagnetic and thermal equivalent circuits. The design equations are used to design a 50kW unit and the geometry of the machine is modelled using Finite Element Analysis (FEA) to check some of the electromagnetic assumptions. Finally, the FEA results are placed into a more refined thermal model to establish the predicted performance of the machine.

Chapter 5 describes the design, construction and test of a 50kW prototype running at 3000rpm. Design calculations are checked and the associated manufacture and constructional issues discussed. A 50kW prototype is proven to work.

In chapter 6 a novel method of using a hybrid of polynomial curve fitting and three dimensional FEA is explored, to understand how the magnetic material content affects the output power for an axial flux generator of given diameter.

Fixed speed power generation benefits from not having the complexity and cost of a full line current power electronics converter. The market already accepts fixed speed power generation and improvements could be readily made. One such advance is the new invention the 'Haydock Brown Machine'. The 'Haydock Brown machine' is truly

integrated, with active material occupying most of the available volume providing good material utilisation and a very compact structure.

Chapter 7 describes the machines complex operation, complicated by three excitation sources, saturation and significant leakage effects within a 3 dimensional structure. A design procedure based upon a lumped parameter equivalent circuit is developed and designs evaluated with the aid of 3 dimensional FEA.

Chapter 8 describes the design, construction and test of a 10kW prototype running at 1500rpm. Design calculations are checked and the associated manufacture and constructional issues discussed.

Finally, in chapter 9 the thesis is brought to a conclusion, when the different technologies are compared and their market potential evaluated.

1.2 Original Contributions to the Advancement of Knowledge

It is claimed by the author that the following points can be considered as independent contributions to the advancement of knowledge.

- A geometric approach to comparing axial and radial flux machines is presented in Chapter 3.
- A practical 50kW, 3000rpm axial machine with novel features [8,9,10,11] has been designed and tested, Chapters 4 and 5.

- A novel approach to the optimisation of electrical machines using a hybrid of FEA solutions and polynomial curve fitting is applied to an axial flux machine, Chapter 6.
- The author is co-inventor of the novel ‘Haydock Brown machine’
 - Design equations are developed, Chapter 7
 - Machines are tested, evaluated and new observations made, Chapter 8
- The author is co-inventor of the novel ‘Haydock Brown Hybrid machine’ [12] which is an improvement to the original concept and is discussed briefly in Chapter 8
- Other new concepts either invented or co-invented by the author and related to this work, but not directly discussed in this thesis, are
 - An electromagnetic gearbox based upon the TORUS concept [13], inventor
 - A power electronics control strategy for the VSIG application [14], co-inventor
 - Novel methods for regulating permanent magnet machines [15], co-inventor
 - Modular stator construction [16], co-inventor

Chapter

2.

Generators for Variable Speed Operation

Over the past hundred years synchronous generators have provided nearly all the worlds electrical power needs. At present, the most common solution for providing electrical power is to use a fixed speed diesel engine, in conjunction with a synchronous generator and associated controls to form a generating set. A paradigm shift is to operate the generating set at variable speed. This chapter explains variable speed power generation. Unfortunately a power converter is necessary to condition the variable frequency output voltage. The expense of this additional sophistication can be offset by simplifications to the system as a whole. Furthermore many additional features present themselves, particularly if the system is fully integrated as will be explained in section 2.2.

2.1 Fixed Speed Power Generation

In synchronous generators the frequency of generation is linked directly with mechanical rotational speed by equation (2.1).

$$f = n \frac{p}{2} \quad (2.1)$$

f = frequency(Hz), p = number of poles, n = mechanical speed (revs/sec)

When load is applied to a diesel generating set, a transient voltage dip occurs, while the generator excitation system establishes the correct excitation level. The engine speed and hence frequency will also drop as the engine governor cannot supply fuel quickly enough to maintain fixed speed. For turbo assisted engines only a percentage of full load can be applied at any given time. When load is rejected, the converse happens and voltage rises and the engine speed increases. If a short circuit is applied large transient currents occur that mechanically stress the integrity of the set. The engine when part loaded will burn fuel inefficiently, resulting in poor fuel consumption and potential engine damage [17].

Figure 2.1 shows a typical diesel engine driven generating set. An important point to note is that the size of the generator is typically about 40% of the engine size.

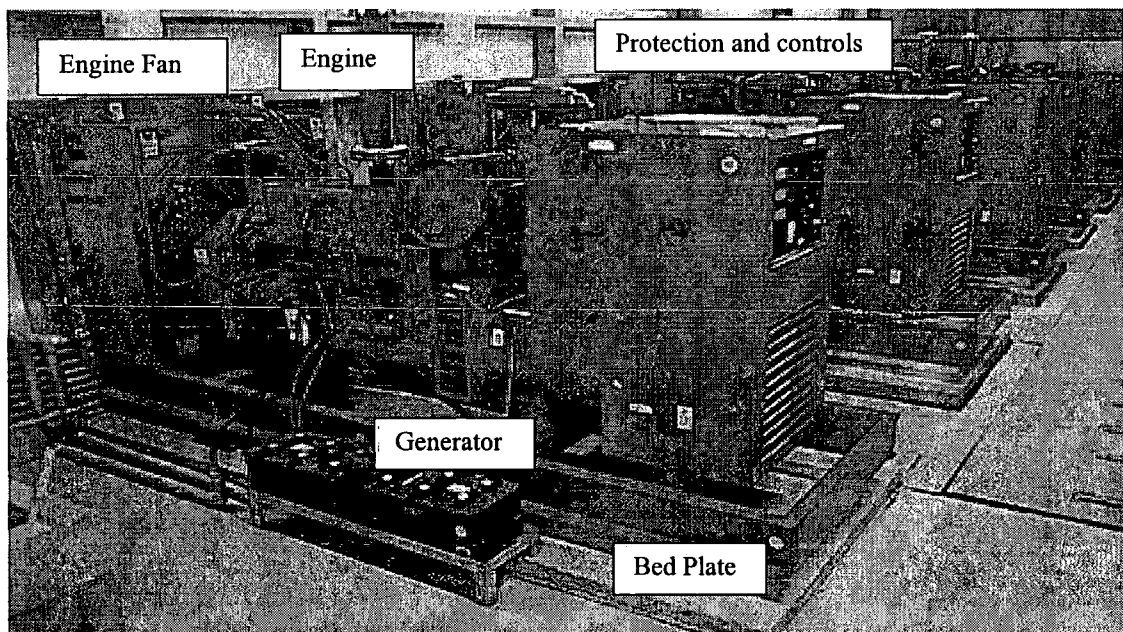


Figure 2.1 Example of a 300 kVA diesel driven synchronous generators

2.2 Variable Speed Benefits and Application

Figure 2.2 shows a block diagram for a Variable Speed Integrated Generating Set (VSIG). Rotational power is provided by the diesel engine and converted into electrical power by a permanent magnet generator. With varying speed the frequency and amplitude of the voltage provided by the generator will also vary. To overcome this problem the output from the generator is rectified and boosted to a reference dc level, so that a constant dc link voltage is maintained. The dc voltage can then be inverted to the desired frequency and voltage using Pulse Width Modulation (PWM) techniques. Additionally a battery system or alternative energy storage system allows power to be supplied to the dc link, even when the engine is switched off.

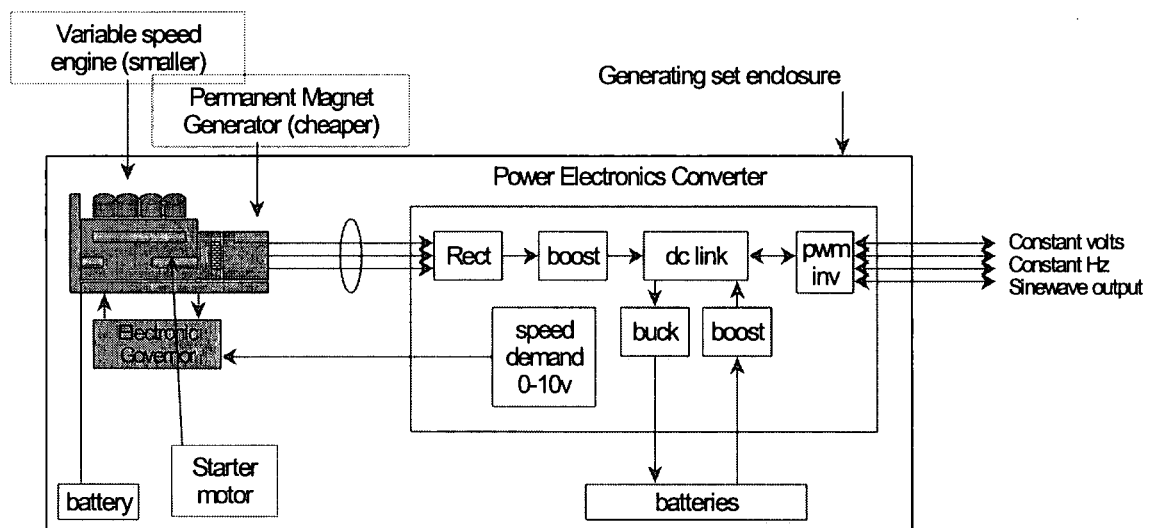


Figure 2.2 Block diagram of a variable speed integrated generating set (VSIG).

With a variable speed engine more power can be made available above synchronous speed. Figure 2.3 shows how the output for a given industrial engine varies with speed. In this example an 18kW engine at 1500rpm could deliver 32kW at 2800rpm. This

allows the advantage of a smaller engine and therefore lower cost for a given power output.

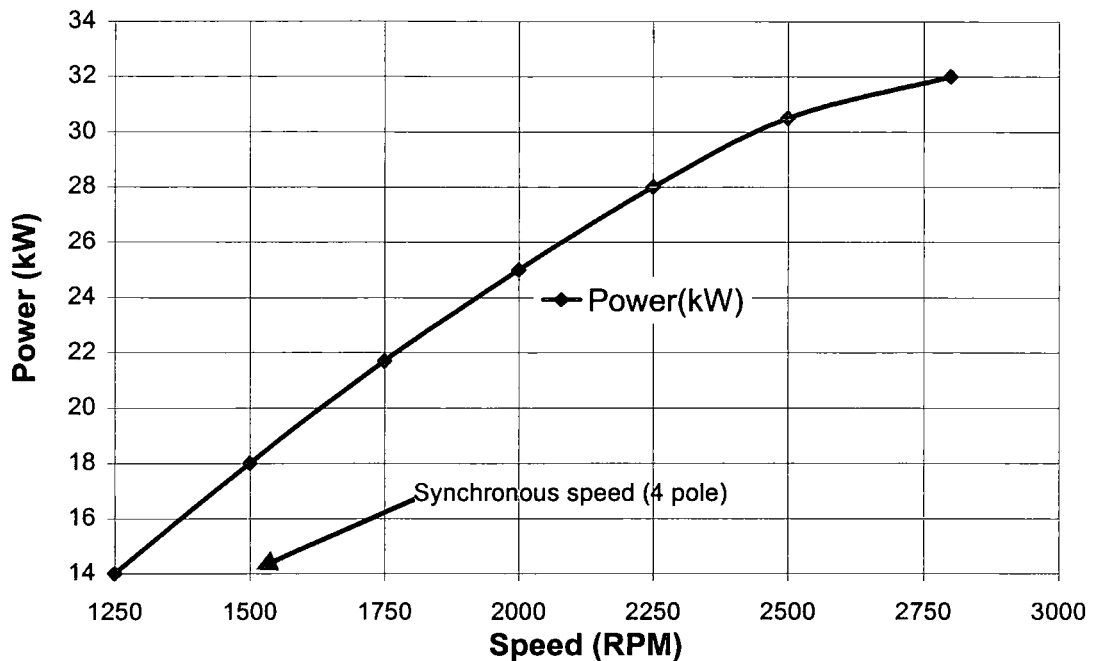


Figure 2.3 Variation in engine output power with respect to speed

Traditionally, industrial diesel engines have been used in the power generation market. The speed of industrial diesels is normally limited to around 3800rpm below 50kW, and the maximum speed tends to reduce as power ratings increase. At 200kW, the maximum speed for an industrial diesel engine is likely to be around 2200rpm, and therefore the increase in power with speed is not as significant as for smaller power ratings. For automotive engines below 200kW high-speed diesels can operate up to 5000rpm, and petrol engines around 7000rpm. This is important because the use of automotive engines will offer the most advantages for variable speed operation. An increase in speed permits

the use of a smaller generator. Unfortunately to date, automotive engines above 200kW are rare. For this reason, the concept of variable speed operation using reciprocating engines is likely to be limited to around 200kW and below, on account of engine performance. Additionally, generating sets below 200kW are likely to be standalone. This is important as the typical load profile seen by standalone sets, is of a low load factor with short duration power peaks and so most suited to variable speed.

Constant full power applications are unlikely to benefit as much from variable speed operation, unless a VSIG is employed to sit on top of blocks of fixed speed generation, to smooth out local variations in the 'Peak-Lopping' or 'Peak-Shaving' mode. VSIG's could also be used to enhance system stability and reduce power surges and fluctuations when used in conjunction with wind power schemes. In such applications VSIG's of higher ratings may be useful.

With no need to run at constant speed the engine can be run at speeds that return minimum fuel consumption for a given power output. Figure 2.4 highlights a typical fuel map for a diesel engine and indicates the operating characteristic for minimum fuel consumption. System efficiency could be improved further, particularly for light load as the engine could be switched off, and the load supported from the battery or other energy storage medium, such as a flywheel connected directly to the dc link. This will lead to lower running costs over the life cycle of the set.

Maximum power will be delivered at the engine's maximum speed, while conversely for light loads the engine speed can be reduced, reducing engine noise.

Engine Torque (Nm)

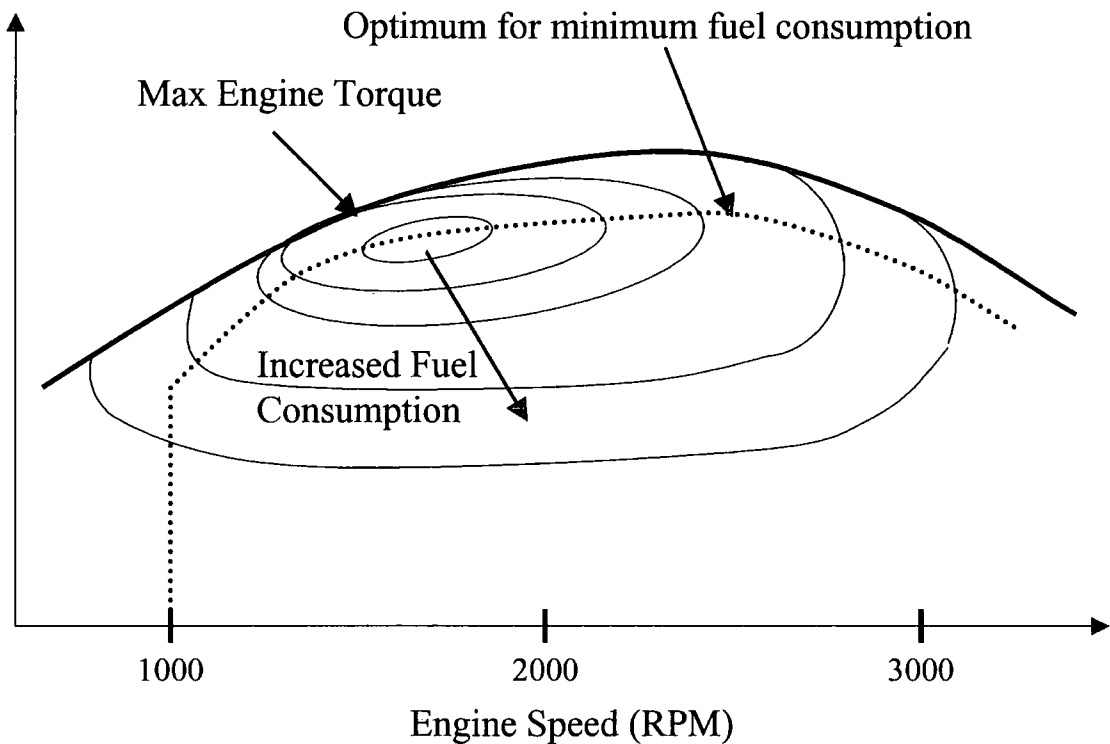


Figure 2.4 Engine fuel map for an internal combustion engine

With variable speed the engine can be run at an optimum Break Mean Effective Pressure (BMEP), reducing cylinder glazing and fuel/oil contamination which in turn reduces emissions, maintenance and increases engine life. With engine speed control, vibration levels can be reduced and mechanical system resonance conditions avoided, reducing maintenance and increasing engine life further. This is a great advantage over fixed speed synchronous generating sets, where the choice between any load other than full load is accepting drastically reduced engine life, and increased maintenance costs due to

the ‘wet stacking’ effects described above, or to connect resistive ‘dummy loads’ to keep the engine at its full rating at synchronous speed, resulting in wastage of fuel, pollution and unwanted heating of the atmosphere. It is also worthy of note that the emission performance of a diesel engine working at fixed synchronous speed is only valid at full load, whereas a VSIG engine can be made to give acceptable emissions at any load.

With the addition of a battery or flywheel or any other energy source, transient overloads larger than the rating of the engine can be supported. Here energy is supplied from the engine and alternative energy source simultaneously.

With the rotating energy being isolated from the load, the dynamic performance of the system can be improved compared to a conventional generating set. For example, loads that require a surge in power, such as induction motors, can be accommodated by energy stored within the system. This not only relieves the engine of intermittent overloads but also removes the adverse effects of transient overloads on sensitive electronic equipment, ensuring the frequency or voltage does not dip.

To illustrate how power can be drawn from the alternative energy source and/or the rotating energy, consider equation (2.2) and (2.3).

$$\text{Engine power,} \quad P_E = T_E \cdot \omega_m \quad (2.2)$$

$$\text{DC link power,} \quad P_{DC} = I_{DC} V_{DC} \quad (2.3)$$

Where, T_E = Fuel Stop Engine Torque, ω_m = Mechanical speed (rads/sec),

I_{DC} = DC Current, V_{DC} = DC Voltage

If more power is demanded on the dc link, then more power is demanded from the engine. As the engine cannot respond immediately speed drops causing the dc link voltage and therefore power to reduce. If the power demand is to be supported, the dc power needs to be supported by an increase in dc current. Power can be drawn from the alternative energy source and/or the rotating inertia within the system until the engine starts to burn more fuel. Meanwhile the inverter is providing a fixed voltage and frequency on the output.

The voltage regulation for unbalanced single-phase loads can be improved as the inverter is controlled using PWM techniques. With PWM techniques the output waveform is sampled on each phase at high frequency (5-20kHz), and adjusted to provide a good sine wave regardless of the load. For this reason, technical loads such as Soft-Starters and Switch Mode Power Supplies will have little effect on the quality of the output voltage.

With the load being isolated from the engine and generator, cyclic engine variations have no detrimental impact on the output voltage and frequency. Any transients from the power system can be 'snuffed out' at the power electronic terminals (or before), so that the set sees no electromagnetic or mechanical shocks. The system can eventually be made very robust and self-protective. It can also be made very intelligent, self-diagnostics and prognostics are possible along with communication for service and operation via satellite and internet links, etc. When this stage is reached, the set becomes a Variable Speed Integrated Intelligent Generating set (VSIIG).

Modifying the converter for 4-quadrant operation could allow power from re-generating loads, such as lifts or cranes to be fed back into the battery system or flywheel, or any other storage medium improving system efficiency further.

Conceptually, the output stage of the variable speed generating set with battery support is very similar to a Static Un-interruptible Power Supply(UPS), and would obviously be a natural selection for this type of application, operating as a combined genset/UPS.

However the engine, generator and battery size would be greatly reduced compared to a conventional Genset/UPS, as the engine/generator can be operated above synchronous speed resulting in a smaller engine/generator, and the battery only needs to be rated to allow the engine to ramp up speed.

The variable speed system can be adapted to a hybrid of renewable energy sources and engine power with both sources feeding the dc link. Here Mother Nature provides a limited amount of energy that can be supplied to the load immediately, or used to top up battery supplies or flywheel, etc at off peak times. The engine will cut in to meet higher load requirements and provide back up if insufficient renewable energy is available.

The variable speed generating set has similarities with an auxiliary power unit required in a hybrid electric vehicle [18, 19]. Here power is drawn from an engine and generator, before being fed into electric motors at the drive shaft to the wheels via a power electronics converter.

2.3 Review of Electrical Machines for Variable Speed Application

The following section provides a broad discussion of the different machine types that could be used for the variable speed application.

2.3.1 Traditional Machine Types

2.3.1.1 Induction Generator

The induction motor is the workhorse of the electrical machines industry, but when operated as a generator requires magnetisation from an external source. For stand-alone units, this could be provided by capacitors in parallel with the generator output, but the required reactive demand varies with load and speed. The capacitance of capacitors cannot be readily varied and may only be applied in discrete steps. These step changes in capacitance may create stability and protection issues. A solution might be to place an inverter in parallel with the induction generator output, to maintain the terminal voltage and provide excitation from a reservoir capacitor on the dc link of the inverter [20,21]. Developing a control system to provide external excitation for variable speed in the opinion of the author is unjustified on the grounds of complexity and cost. The induction motor also suffers from poor power density and low efficiency.

2.3.1.2 Wound Field Machines

The wound field synchronous generator [22] has certain limitations when variable speed is considered. A field winding is bulky and usually has to be accommodated on a rotating structure and restrained from centrifugal forces. The synchronous generator is an

electrically 'soft' machine, so harmonic currents fed back into the generator from a bridge rectifier load or any other non linear load, flow into a relatively large impedance. This can result in significant voltage distortion, unless the generator is grossly oversized to reduce the impedance.

Wound field generators produce additional field losses and heat that requires cooling. As speed reduces, the axial flow of air compromises the heat transfer capability of the cooling circuit and armature current must reduce. Reduced speed reduces the level of induced voltage for a given flux level. The combination of reduced armature current and voltage significantly reduces the level of power that may be drawn at lower speeds.

With a wound field machine, additional excitation and control is required on the field to maintain a given voltage. With two control variables, speed and excitation, both of which have different time constants, the overall control strategy would be complex. An additional difficulty is that most synchronous machines are brushless, that is excitation is provided from an additional wound field machine known as an exciter. This complicates the control strategy further as additional time constants are introduced and the exciter has less power at lower speeds.

Wound field topologies that have been used for variable speed operation are the brushless doubly wound induction machine [23] and the slip ring doubly fed machine [24]. Here the rotor winding is arranged to allow the field to rotate independently of mechanical rotation. This topology has the advantage over other traditional machine types of not

requiring a fully rated power converter to condition the output voltage to 50Hz. It does however require a power converter to be rated dependent upon the slip speed between the electrical synchronous speed and speed of mechanical rotation. These systems have been used successfully for wind turbines and flywheel 'no-break' uninterruptable power supplies. Due to their limited speed range and the problem of importing energy from another source, this type of machine is unsuitable for the VSIG application.

In summary, the disadvantages of wound field solutions for the variable speed application are additional loss resulting in poor efficiency, cooling issues at lower speeds, tedious manufacture, mechanical retention of wound components, insulation of wound components and providing external excitation which needs control.

2.3.2 Permanent Magnet Machine Types

With recent developments in Neodymium Iron Boron (NdFeB), both in terms of energy density and commercialisation, many novel machine topologies have been researched.

2.3.2.1 Radial Flux Permanent Magnet Machines

Radial flux machines [25] have a conventional type stator construction with various rotor constructions such as surface mounted magnets, loaf shaped surface mounted magnets, buried magnets or multi-layer interior permanent magnets [26].

Rotors using surface mounted magnets have the advantage of simple construction but high air-gap flux densities are difficult to achieve. This is compensated to some degree

by the low armature reaction flux, due to the increased air-gap on account of the NdFeB having a relative permeability similar to air. Loaf shaped surface magnets offers a more sinusoidal waveform. If ferrous material is left between magnet poles, an inverse saliency [27] condition results where the direct-axis inductance is lower than the quadrature-axis inductance. While this does not increase power density, it does result in an interesting regulation characteristic, where the output voltage may in fact rise with increased lagging load current.

Buried magnets are ideally suited to ferrite materials as flux focusing helps to increase air-gap flux densities. Using NdFeB for buried magnet arrangements can result in air-gap flux densities being too high to sensibly utilise the stator, due to the teeth tending to saturate. Flux focusing ferrous segments are required that present a good magnetic path to the armature reaction and so the armature inductance may increase. Leakage flux between poles is likely to be high compromising power density. Assembly issues due to having to embed the magnets into the rotor structure often with non-ferrous supports should not be underestimated.

Multi-layer interior permanent magnet machines reduce pole leakage, offer some flux focussing and exhibit inverse saliency but do suffer serious assembly issues.

In terms of power density, there is little to choose from the above rotor arrangements as generally a given volume of PM material provides the same output.

Due to the large effective air-gap with permanent magnet machines, air-gap windings may not unduly compromise the magnetic circuit. Air-gap windings may offer manufacturing advantages, good cooling and high peak torque but eddy current loss in the armature conductors require consideration. Air-gap windings have to be restrained carefully, as they need to transmit the machine output torque. This force on the conductors alternates with the machine frequency, and may be a potential failure mode for machines with high output torque. The low internal impedance of such machines may also make them intolerant to any short circuit fault condition.

A family of machines has been developed that axially focuses flux set up by a coil or permanent magnet to increase radial air-gap flux densities. Examples of this are the Imbricated [28] or Lundell rotor. These rotors have two claw like iron pieces that are sandwiched together and the axial flux is focussed into radial protrusions, which direct flux radially into the air-gap. These arrangements do suffer significant flux leakage, but due to their robust construction are used extensively in the automotive industry.

2.3.2.2 Axial Flux Permanent Magnet Machines

Axial flux machines are electromagnetically similar to radial types and can be built with similar magnet configurations to the radial, except flux travels axially through the air-gap. A point worth noting is that these machines do not make good utilisation of the magnetic circuit on account of the number of conductors being limited by the inner radius on the stator, see chapter 3. Small axial machines can be single sided as the axial forces are low, but as powers increase they become double sided. With flux cutting on both

sides of the stator high power density is possible, the topology could be described as two machines that share a common stator. The axial flux machine can have an iron stator with or without slots or be iron less. The axial flux machine with an iron core and no slots, and the ironless versions are likely to be electrically 'stiff' on account of the low armature reaction flux. This does require more permanent magnet material but the peak torque is high.

Axial flux machines are axially short offering mechanical integration benefits for engine driven applications, as the machine can replace the engine flywheel and be fully integrated into the flywheel housing.

2.3.2.3 Reluctance Permanent Magnet Machines

Switched reluctance machines [29] have received interest in recent years, and due to their simple construction, may eventually become a competitor to the universal machine used extensively in hand tools. The fault tolerant nature of such machines has also gained interest in the aerospace industry, as reliability is essential.

The rotors are a simple structure with saliency providing a reluctance variation in the air-gap. With no excitation on the rotor, excitation needs to be provided via the stator either in the form of coils or permanent magnets. With the excitation system and main working flux sharing the same air-gap, a larger machine is inevitable. The performance of such machines is heavily influenced by the air-gap, with a very small air-gap being desirable.

One solution that improves the power density in a switched reluctance machine is to have permanent magnet excitation all the way round the stator bore producing the Flux Reversal Machine FRM[30]. In this machine the flux from the permanent magnets links with the stator coils, but is arranged in such a manner that the flux will reverse as the reluctance of the rotor varies. This doubles the rate of change of flux and therefore doubles the induced EMF. This rapid change in flux is offset by only half the air-gap flux being used. The power density of such machines is likely to be lower than a more conventional radial machine, because of increased leakage between poles and only half the air-gap being used. This arrangement also suffers from high iron losses, cogging, acoustic noise and eddy currents being induced in the magnets.

The Flux Reversal Machine has been combined with the concept of Lorenz and Guy slottings to produce a Vernier Reluctance Magnet Machine, VRMM[31].

Electromagnetic gearing is applied to improve the power density from a FRM. Here as the pole number and teeth are increased, the induced voltage increases with frequency. The synchronous inductance on the other hand remains nearly constant. If a short circuit is applied to the machine, a given level of current will be sustained irrespective of how much gearing is applied, as the frequency increases the synchronous reactance proportionally. Theoretically, the percentage increase in pole number corresponds to a similar increase in power for a resistive load. Unfortunately as the pole number increases the pole leakage increases, as does the iron losses within the machine. To achieve flux reversal the air gap flux density is halved. The magnets also compound this reduction in air-gap flux density as they are surface mounted and can only produce a percentage of the

magnets remnant flux density. The power increase as a result of electromagnetic gearing is greatly diluted.

The magnets in a Vernier Reluctance Magnet Machine are exposed to a relatively high frequency flux, and induced eddy losses in the magnets will increase magnet temperature. A high frequency torque pulsation as a result of the flux reversal is likely to create noise and vibration issues. Iron losses need careful consideration on account of the high frequency. Managing such a high frequency output at high power ratings is likely to be an issue.

All arrangements that rely on reluctance variation suffer torque pulsation, vibration, noise, high synchronous reactance and relatively high iron loss.

The Transverse flux machine [32], is similar to the Flux Reversal Machine in that the magnetic circuit is arranged in such a manner so as to offer a high rate of change of flux. This rapid change in flux offers very high torque densities when viewed as a motor, as reactive power from the supply maintains air-gap flux densities. Unfortunately as a generator, this high level of induced EMF is offset by an increase in synchronous reactance. With increased pole number the leakage flux between poles is very significant, so in reality, the potential for increased power density is compromised. The transverse flux machine is inherently single phase with three phases possible by cascading. Torque pulsations cause noise and vibration problems. The assembly of such machines is very complex, with a requirement for exotic electrical steel on account of the

high frequency. Some arrangements that use surface magnets will also suffer eddy current loss in the magnets. This type of generator is also electrically soft, creating power flow and control problems for the power electronics.

In summary, all reluctance machines have a large internal power factor that needs to be corrected if they are to be used as a standalone generator. The reactive demand and rating of the reactive compensation is often many times larger than the required generator rating, making these topologies expensive.

2.4 Discussion

The benefits of variable speed power generation have been highlighted. Having considered the above machine types and their associated characteristics, a balanced judgement was made to evaluate the use of axial and radial permanent magnet generators. The next chapter distinguishes between the merits of the axial and radial permanent magnet arrangements.

Chapter

3.

Axial and Radial Flux Generators

This chapter explores the fundamental differences between axial and radial flux machines. The choice of machine type for a given application is complex and often depends upon the designer's experience and preconceptions. Radial permanent magnet (PM) machines, for good reasons, have traditionally made up the majority of commercial PM machines for they offer good magnetic and electric loading and so provide very compact electromagnetic devices with high efficiency. The use of Axial PM machines has increased in recent years, applications such as Motor/generators for Hybrid Electric Vehicles [18], Micro Turbines [33] and Wind Turbines [34] are all examples of where axial flux machines are employed.

The evolution of the axial flux machine from a radial flux machine is shown in Figure 3.1. If the radial flux machine, Figure 3.1a is "cut" and unrolled as in Figure 3.1b, a linear machine is produced. It has a single air-gap so that the magnetic force of attraction is no longer balanced as it is in the original machine. If now a second "rotor" is introduced immediately opposite the first, on the other side of the stator, Figure 3.1c, the axial force between the rotor and stator is neutralised. However, because the direction of the magnetic field has now changed from being vertically upwards (from the first "rotor") to vertically downwards (from the second "rotor"), the direction of the induced EMF in the upper armature coil is in the opposite direction. This means that an armature coil can now

be “wrapped” round the stator rather than being pitched along the stator, Figure 3.1d. If now the two ends are wrapped round in the plane of the paper the disc arrangement of Figures 3.1e (stator) and 3.1f (rotor) is obtained. In this arrangement each armature coil is simply wound toroidally round the stator.

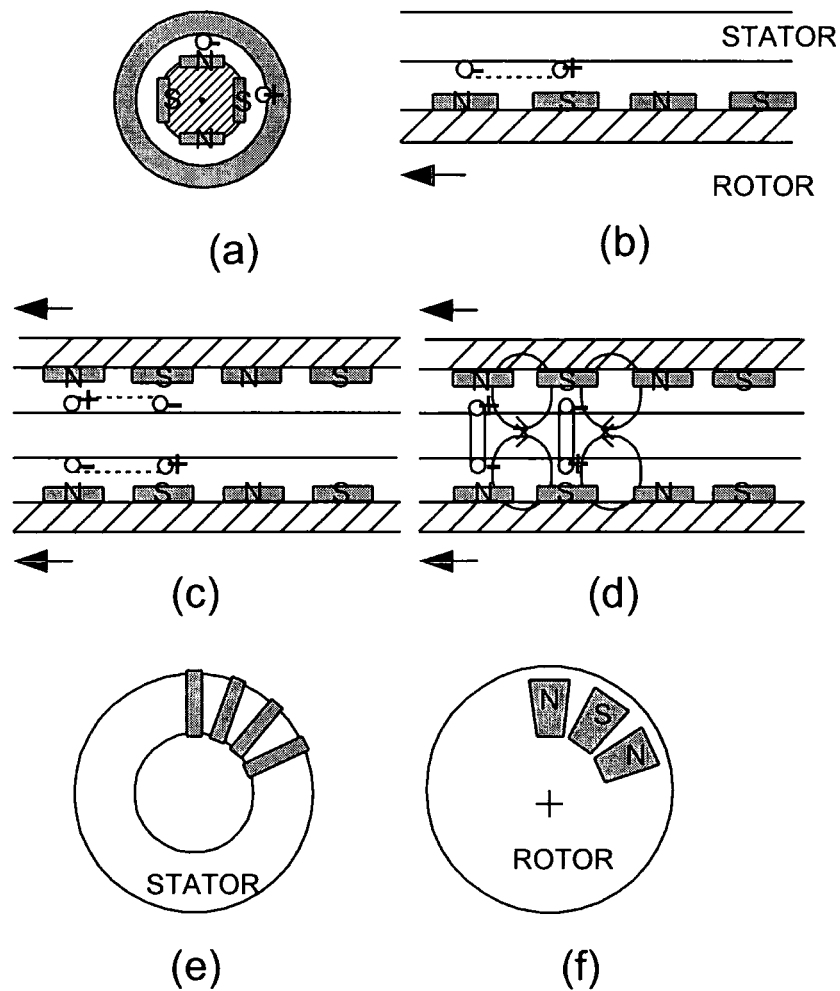


Figure 3.1 Axial flux machine evolution

3.1 The Axial Flux Generator

The axial flux generator has been chosen as an interesting topology that has a number of advantages over a conventional generator [18,19,35,36,37,38]. The following discusses the machines operation and presents these advantages.

The general arrangement for a typical axial flux machine is shown in Figure 3.2.

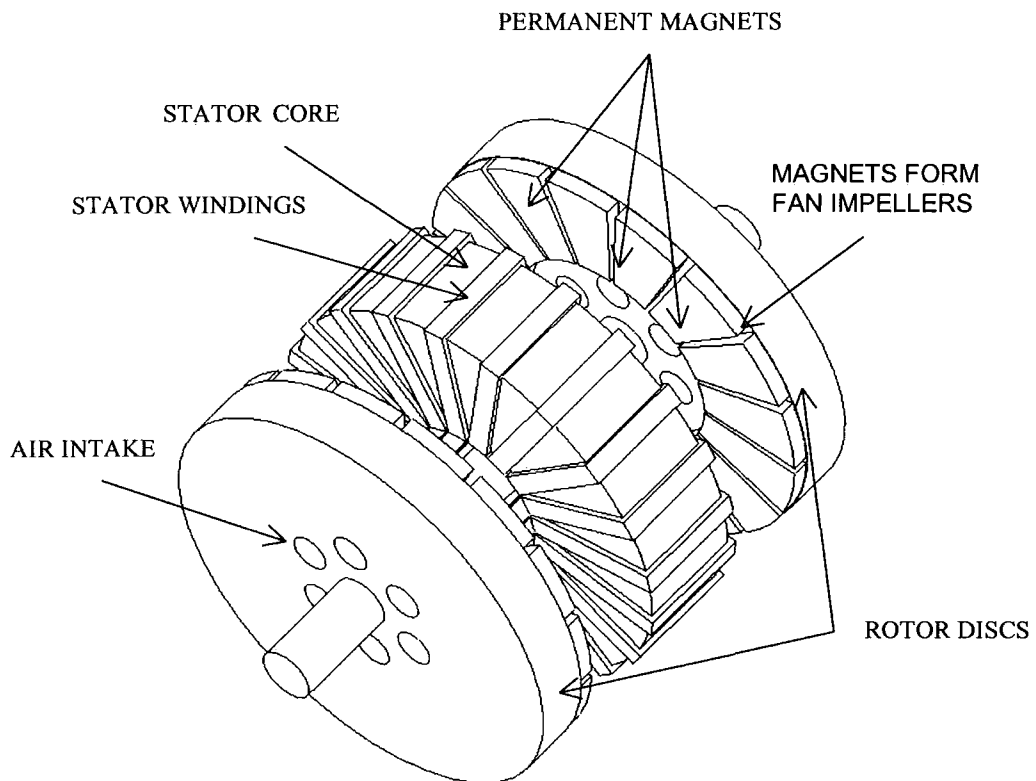


Figure 3.2 Typical axial flux generator arrangement

The machine produces axial flux from permanent magnets mounted on ferrous plates. These plates act as the rotor and mount directly onto the prime mover drive shaft, forming the rotating member. The stator is a strip-wound slotless toroidal magnetic core,

which carries the output winding. The stator is positioned between the two plates and flux passes axially from the magnets.

Figure 3.3 is a view from above Figure 3.2 and is partly developed to show the direction of simplified flux paths within the machine, where flux passes from the magnet on the rotor through the air-gap and into the stator. Flux then travels circumferentially through the stator core and back across the air-gap into the adjacent magnet, closing the flux path through the rotor. This effect is mirrored on the opposite side of the stator.

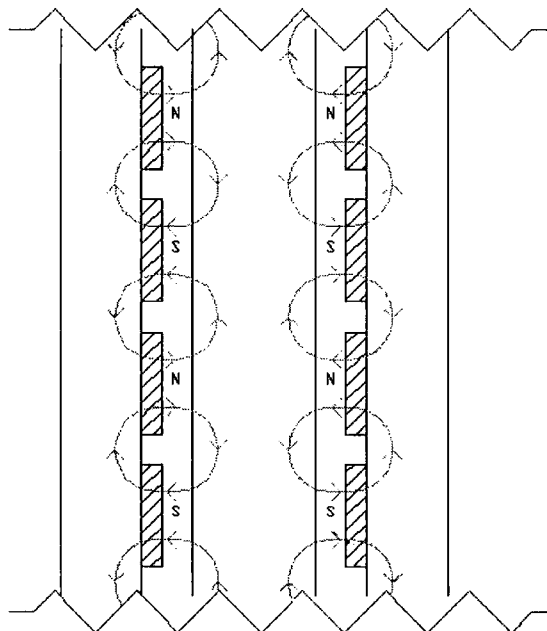


Figure 3.3 Plan view showing the direction of flux paths within an axial flux generator

Since the stator winding is wound in a toroidal fashion and has two working surfaces, a higher percentage of the stator winding is cut by the flux compared with a conventional

machine, allowing more torque to be developed. With no stator teeth and double-sided excitation, the stator is very compact, saving steel and improving power density. An air-gap winding is used which provides lower values of self and mutual inductance on account of the large air-gap. These inductance's are reduced further by the absence of slot leakage and reduced end winding leakage.

When feeding a rectifier load, the reduced inductance reduces commutation overlap and fully utilises the power available from the generator. The generator output voltage can be tailored to reduce the dc link ripple voltage and increase the RMS harmonic content of the voltage waveform, increasing power densities further.

With holes positioned near the mechanical shaft, the rotating discs will act naturally as fans, allowing high electrical loading. Because of the permanent magnets, high pole number and high electrical loading, the axial flux generator is likely to have a high efficiency compared with conventional generators.

Mechanically, the axial flux machine is compact with a short axial length. For engine driven applications, the axial flux generator can be mounted directly onto the engine crankshaft, eliminating the need for bearings and coupling, inherently reducing weight.

The axial flux machine has a larger diameter than an equivalent radial flux machine. The resulting high moment of inertia allows the rotor to take the place of the engine flywheel

providing further integration into the engine. This high moment of inertia allows energy to be stored in the rotating parts to help transient overloads.

A bed plate for the generator is unnecessary, with support provided from the flywheel housing and crankshaft bearing. In the future, the axial flux machine could replace the engine starter motor and alternator.

For manufacture, the axial flux generator has no iron wastage and no stamping requirements. The slot-less winding is easy to wind automatically and impregnate. No skewing is required. The design is simple with reduced component count thus reduced inventories and assembly time. The perceived capital investment to automate the manufacture of the axial flux machine is low compared with a conventional synchronous generator.

This type of axial flux machine does have some disadvantages. With the windings situated in the air-gap, additional magnet excitation is required, so this topology is likely to have a large magnet content. With an air-gap winding, eddy currents will be induced in the conductors creating additional losses and heat that needs to be considered.

Winding in the air-gap can limit the design when different voltages and ratings are required as the number of turns that can be wound is linked to the coil width.

Furthermore, the coil width and number of turns limit the cross sectional area of the conductor, which affects the air-gap length adjusting the level of flux within a machine as

well as the thermal performance. This does make targeting specific voltages and ratings more difficult compared with conventional topologies, particularly if standardisation of components and good utilisation of materials is desirable.

Utilisation of magnets and iron core will also be less compared with a conventional radial flux machine on account of the inner radius limiting the number of conductors on the stator. Consequently, the diameter of an axial flux machine cannot be reduced as much as a radial flux machine. In addition, losses created in the stator iron are difficult to cool.

With high magnetic loading in the air-gap, large axial forces exist which create assembly issues. Fortunately, when the second rotor is in place these axial forces balance, however the system is inherently unstable, as the possibility of the stator being exact centre of the two rotors is small. Any increase in air-gap on one side reduces the axial force on that stator side, while a decrease in gap on the other side increases the force.

3.2 The Radial Flux Generator

The general arrangement for a radial flux machine is shown in Figure 3.4.

This machine produces flux radially from permanent magnets mounted on a ferrous rotor. The rotor is supported between two bearings and is mechanically coupled to the primemover. The stator is a slotted laminated structure that links the flux around the conductors in the slots. A mechanical structure is required to support the bearings and stator so that the rotor runs concentric with the stator bore.

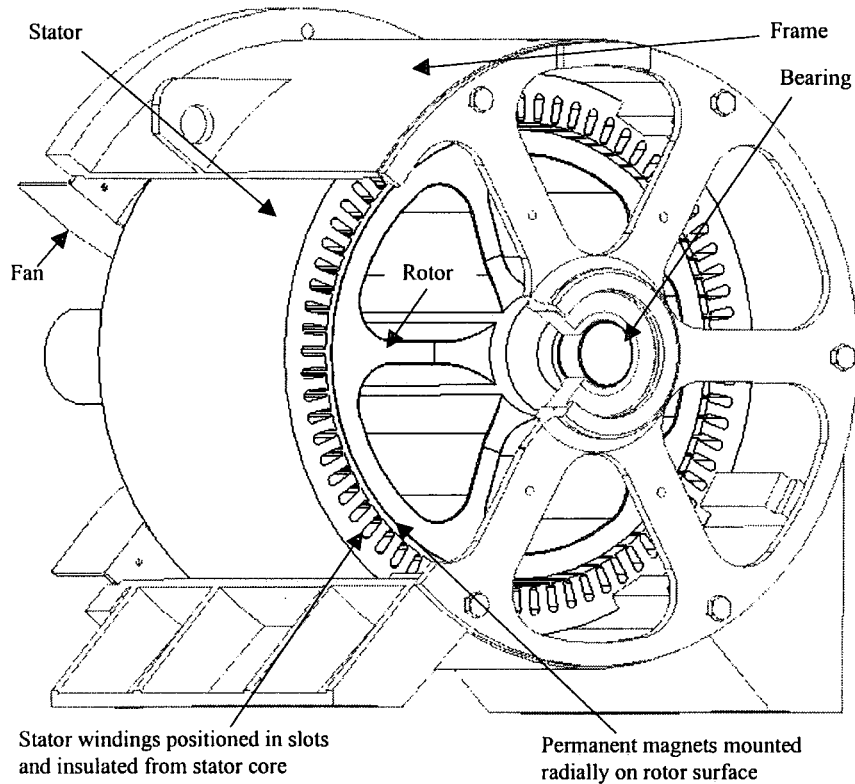


Figure 3.4 General arrangement for a radial flux machine

Radial flux machines have a degree of mechanical strength in the radial plane, making it easier to work with smaller air-gaps and the high forces associated with them. Small air-gaps provide better material utilisation but thermal expansion must be accommodated.

Figure 3.5 shows the flux lines within the machine where flux passes from the permanent magnets, through the air-gap then into the teeth, travels circumferentially through the back iron and around the conductors, returning back through the teeth and air-gap and into the adjacent magnet closing the magnetic circuit.

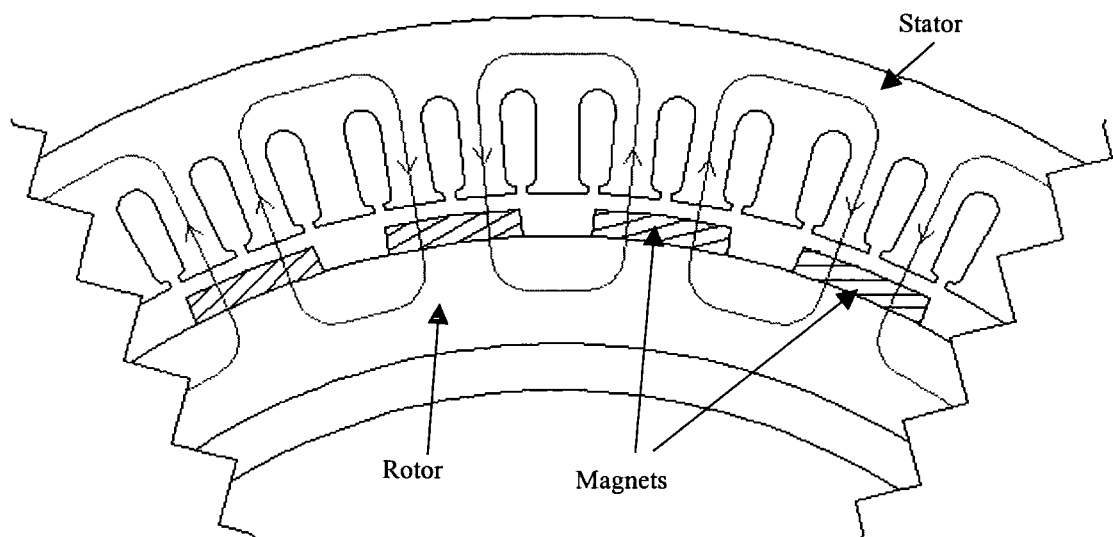


Figure 3.5 Flux lines within radial flux machine

The magnetic field on the rotor is a stationary field and therefore electrical steel is not a requirement on the rotor. The stator is subjected to an alternating field and laminated electrical steel is required to reduce eddy loss. If a solid rotor is used, the stator could be punched from a laminated blank, but this would result in a high percentage of wastage. Alternatively, modular stator assembly ensures electrical steel is placed where it is most needed reducing usage and wastage. Modular stator assembly is the term applied to manufacturing the stator from a number of piece parts. The number of juxtapositions for using modular stator design are great, but one example is to consider a traditional stator angularly segmented into a number of equal parts. Interlock features such as dovetails allow these parts to be interconnected and welded. This has the advantage of a low cost stamping tool and the material wastage is greatly reduced.

Electromagnetically, the flux paths are well defined and good utilisation of iron and permanent magnet material is possible. The conductors are placed in slots preventing the conductors being subjected directly to eddy current loss. The slots provide good mechanical support and location.

With permanent magnet machines, there are no copper losses on the rotor so the generator will have high efficiency compared with conventional synchronous generators. Furthermore, less loss has to be removed by the cooling circuit. With losses mainly created on the outer periphery, the stator can be ventilated effectively on its outer and inner surfaces. Combined with heat convection on the outer surface, good cooling is possible.

The topology is similar to conventional electrical machines, and therefore the assembly techniques are well understood. This type of machine is scalable in power, however the author envisages some significant assembly issues as the machine goes into Mega-Watts. For there are significant forces associated with inserting the rotor into the stator.

The topology has some disadvantages. With permanent magnets radially facing the air-gap, it is hard to achieve high air-gap flux densities. The design suffers slot and end winding leakage, however this is offset to some degree by the good utilisation of permanent magnet material. A fine line exists between power density and having short circuit protection of the magnets. Significant forces exist when the rotor is brought into contact with the stator. Care not to damage the magnets during assembly is necessary

and centralisation of the rotor can be a problem. Eccentricity results in a radial force due to a lengthening of the air-gap on one side and shortening on the other, leading to unbalanced magnetic pull and ovalisation distortion. Force variations cause noise and vibration, which can damage insulation. Inserting coils into slots can also damage insulation. The retention of magnets is required due to centrifugal forces. Gluing magnets is unreliable with the preparation of surfaces being important. These machines often have external banding which appears in the air-gap, increasing the reluctance of the magnetic circuit.

3.3 An Idealised Approach to Electromagnetically Comparing Axial and Radial flux PM Machines

If the specific force for both the axial and radial arrangements is assumed constant, that is the magnetic and electric loading for the two arrangements are taken as equal, the analysis becomes one of geometry. The Author has completed two studies and fundamental equations have been derived that compare the two topologies, reference [39]. Because of the cost of PM material, the first study compares the two machine types on a volumetric basis for a given volume of PM material. Here the pole number is varied and the volume ratio of the axial flux to radial flux machine calculated for different torque requirements. In some applications, the available space for the machine imposes a physical limit on the outside diameter, and this becomes the main design driver. Consequently, in the second study, the outer diameter of both the axial and radial flux machines is fixed at the same value, and the volume ratio of the two machine types

calculated for different values of torque and pole number. In contrast to the first study, the second approach does not limit surface area, and therefore the content of PM material.

Both studies apply equally well to machines of equivalent structure. For example, if both radial and axial machines have a slotted stator or if both machines have an air-gap winding. The radial machine is compared only to a single sided axial flux machine, however, the analysis could be applied equally well to other axial arrangements. End windings are ignored in the analysis for they would take up a similar volume in both machines. Reference [40] details some of the different types of axial machines available. It is fair to say that for practical axial flux machines other than machines of a few hundred Watts, a double-sided configuration is now common.

3.3.1 Electromagnetic limit for Torque and Power

The power developed by an electrical machine is proportional to the tangential force in the air-gap between rotor and stator at any speed. It is common when comparing electrical machines to assess the magnetic loading and the electric loading of the machine to obtain the specific force, f_e (N/m^2), which is also sometimes referred to as shear stress.

$$\text{Lorentz Force, } F = B.I.L \quad (3.1)$$

F =Force(N), B =Flux Density(T), I =Current(A), L =Length(m)

$$f_e = \frac{F}{\text{Area}} = \frac{B.I.L}{\text{Area}} = B.A \quad (3.2)$$

A =Electric Loading (A/m)

Typically the magnetic and electric quantities are spatially distributed in a roughly sinusoidal pattern and their product has an average value of up to half the product of the peak values. It is more normal to represent quantities in terms of the peak flux density, \hat{B} and RMS electric loading A_{rms} , equation (3.3).

$$f_e = \frac{\hat{B} \cdot A_{rms}}{\sqrt{2}} \quad (3.3)$$

The specific force may be applied to the geometry of an electrical machine to obtain the torque and therefore power for a given topology:

$$T = f_e \cdot SA \cdot R \quad (3.4)$$

Where T is the torque (Nm), SA is the surface area between rotor and stator (m^2) and R is the torque radius (m).

Four parameters therefore determine the maximum torque from an electrical machine, two electromagnetic parameters of flux density and electric loading, and two mechanical parameters of radius and surface area.

The magnetic loading cannot exceed the saturation value of the magnetic materials used and surface magnet air-gap densities rarely exceed a peak value of 0.7 T on load.

The electric loading is directly linked to the effectiveness of the cooling circuit within an electrical machine. Radial flux machines do not naturally ventilate themselves and some form of external ventilation is required to force air over the surfaces. Due to rotational

effects of the rotor confined by a fixed stator, a helical air flow path forms, making the machine more difficult to cool so there is often a limit on length. Conversely, the axial arrangement self ventilates and therefore no external cooling circuit may be needed.

While the axial arrangement is inherently self-ventilating, if additional cooling is required there is some difficulty in getting an external cooling circuit to function.

For these studies the electric loading is assumed constant, however the electric loading for axial flux machines is fundamentally limited when compared to a radial machine as the inner diameter restricts the number of conductors. The electric loading for an axial flux machine will always be compromised, dependent upon the ratio of inner to outer diameter, K , this limiting feature is taken into account in the analysis.

3.3.2 Geometric Approach

Taking the outer diameter of the axial machine as the reference and considering only the torque interaction in the air-gap, consider the two simple axial and radial air-gap geometry's in Figure 3.6.

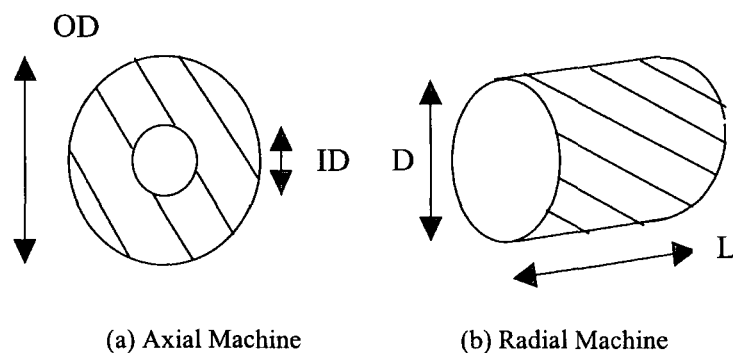


Figure 3.6 Simple geometry of axial and radial air-gap

For the axial arrangement of Figure (3.6a), the effective cross sectional area of the air-gap is shown shaded. Dimension OD is the outer diameter taken as 1 per unit. The ID is the inner diameter taken as K where $K=ID/OD$.

To calculate the torque for the axial machine the mean radius is taken as

$$R = \frac{(1+K)}{4} \quad (3.5)$$

The surface area for the axial arrangement is

$$SA = \frac{\pi \cdot (1-K^2)}{4} \quad (3.6)$$

To maintain the equivalent torque in the radial machine for the same surface area shown shaded in Figure 3.6, then

$$R = \frac{D}{2} = \frac{(1+K)}{4} \quad (3.7)$$

$$SA = \pi \cdot D \cdot L = \frac{\pi \cdot (1-K^2)}{4} \quad (3.8)$$

Where D = radial air-gap diameter (m), L = length (m)

Rearranging, the radial equivalent becomes

$$D = \frac{(1+K)}{2} \quad (3.9)$$

$$L = \frac{(1-K)}{2} \quad (3.10)$$

Figure 3.7 includes a schematic of a single sided axial and radial arrangement. Clearly both topologies require magnetic material either side of the air-gap to provide a low reluctance path to direct the flux. For the single sided axial flux arrangement both rotor and stator core backs, CB , directly contribute to the volume of the machine. While for the radial arrangement, the rotor core back does not contribute directly to the machine volume, but the rotor core back does enclose additional volume that cannot always be utilised. The stator and rotor core backs for both arrangements are a function of pole number but calculated differently.

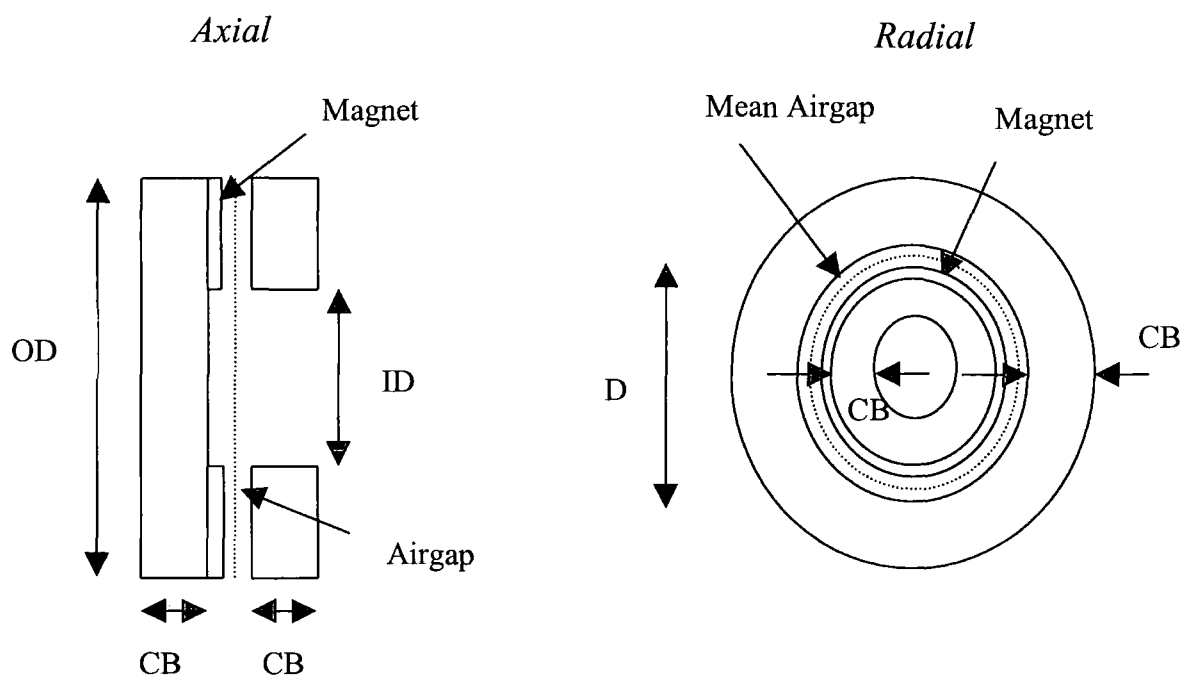


Figure 3.7 Axial and radial machine dimensions

A reasonable assumption for calculating the core-back depth CB , is to assume twice the flux density can be carried in the core-back compared with the air-gap. That is the core-

back area is equal to one quarter of the pole area, as the pole flux splits into two paths when it enters the core-back. In the axial flux arrangement this means that

$$\frac{CB \cdot OD(1-K)}{2} = \frac{\frac{\pi}{4} \cdot OD^2(1-K^2)}{4P} \quad (3.11)$$

Where CB =core-back depth (m) and P =number of poles.

Rearranging with $OD=1 pu$, provides a general expression for the core-back depth as

$$CB = \frac{\pi \cdot (1-K^2)}{8 \cdot P \cdot (1-K)} = \frac{\pi(1+K)}{8 \cdot P} \quad (3.12)$$

Likewise for the radial flux arrangement

$$CB = \frac{\pi \cdot D}{4 \cdot P} = \frac{\pi \cdot (1+K)}{8 \cdot P} \quad (3.13)$$

Where D =Air-gap diameter of radial machine (m)

Equation (3.12) and (3.13) confirm the core-back thickness CB , is identical for both arrangements.

To estimate comparative volumes some assumptions need to be made. Based upon experience, reference [18] and [41], the air-gap L_{gap} between the magnet and stator surface for an axial flux machine is determined by (3.14).

$$L_{gap} = 0.006 \times OD \quad (3.14)$$

Practically, axial flux machines require larger running clearances compared with radial types due to manufacturing tolerances being amplified by the aspect ratio of the length compared to diameter. Conversely, radial flux machines can run with relatively small running clearances but suffer in that magnet retention is required in the air-gap. While magnet retention for the radial machine depends upon speed, experience has demonstrated the net air-gaps are similar for both arrangements with respect to the magnetic circuit. The inclusion of the air-gap dimension in the calculation of volume is a second order effect.

The maximum power output, from either a radial or axial PM arrangement will depend on the maximum energy available from the magnets. For the fully loaded condition, the machine should be designed so that the magnets will be operating at their maximum energy product. Therefore to counter the effect of armature reaction, it is normal to design PM machines with a flux density above the load line for maximum energy. The magnet length L_m for the magnet is therefore likely to be larger than the air-gap L_{gap} and is assumed to follow equation (3.15) for both cases.

$$L_m = L_{gap} \times \frac{4}{3} \quad (3.15)$$

3.3.3 Calculation of the Volume Ratio between Axial and Radial Machines for a Given Mass of PM Material –Study 1

An earlier constraint was to ensure both the axial and radial machines had the same surface area SA , and torque radius R . It follows if the air-gap L_{gap} is also the same, both machine types will have the same mass of PM material for a given torque defined by K .

The volume for an axial flux machine can be calculated using (3.16)

$$\begin{aligned} \text{Axial Volume} &= \frac{\pi \cdot OD^2}{4} \times (2 \times CB + L_{gap} + L_m) \\ &= \frac{\pi}{16} \times \left(\frac{\pi(1+K)}{P} + 0.056 \right) \end{aligned} \quad (3.16)$$

The volume for a radial flux machine can be calculated using equation (3.17)

$$\begin{aligned} \text{Radial Volume} &= \frac{\pi}{4} \times (D + L_{gap} + 2 \times CB)^2 \times L \\ &= \frac{\pi}{4} \times \left(\frac{(1+K)}{2} + 0.006 + \frac{\pi \cdot (1+K)}{4 \cdot P} \right)^2 \times \frac{(1-K)}{2} \end{aligned} \quad (3.17)$$

The electric loading for the axial machine is restricted by the inner diameter so the radial volume should be further reduced by equation (3.18).

$$\frac{OD.K}{D} = \frac{2.K}{(1+K)} \quad (3.18)$$

For a given torque determined by K the ratio of axial volume to radial volume may be calculated as a function of pole number P by equation (3.19)

$$\frac{Axial}{Radial} = \frac{\left(\frac{\pi(1+K)}{P} + 0.056\right)}{4 \times \left(\frac{(1+K)}{2} + 0.006 + \frac{\pi(1+K)}{4.P}\right)^2 \times \frac{(1-K).K}{(1+K)}} \quad (3.19)$$

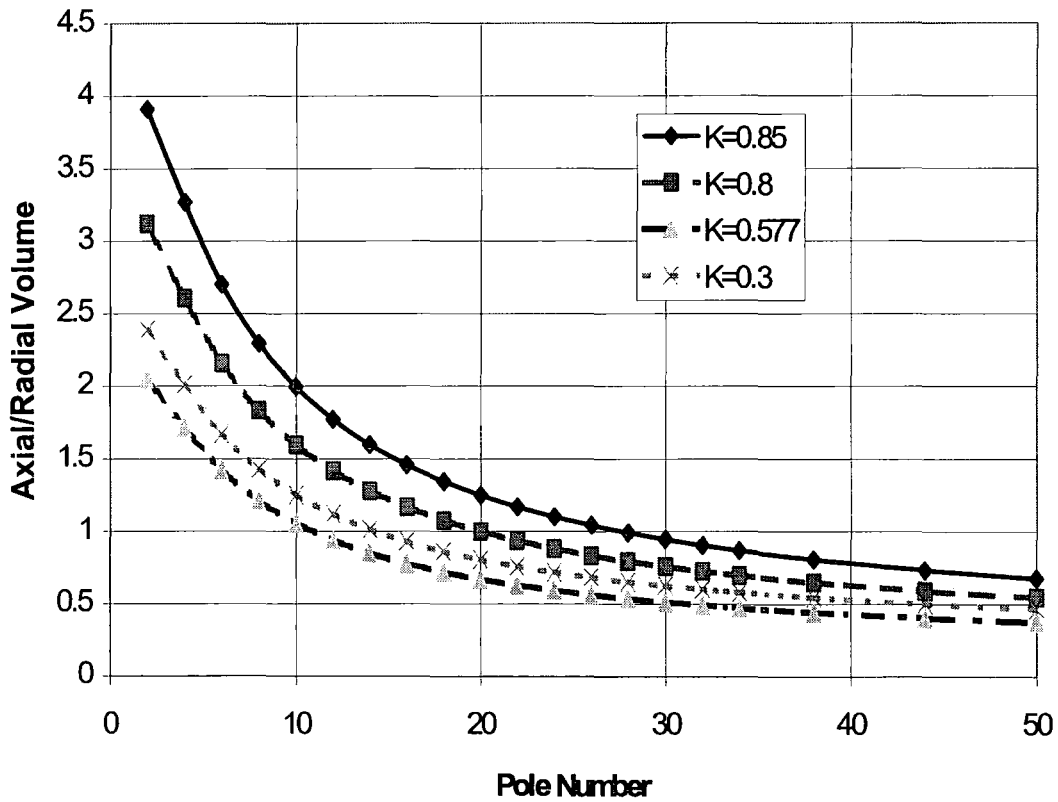


Figure 3.8 Axial/radial volume for a given volume of PM material with respect to K and P

Inspection of Figure 3.8 shows that as pole number increases the volume required by an axial arrangement tends to reduce. The case where $K=0.85$ is unlikely to be an attractive machine in reality as end effects will start to become significant. Axial flux machines tend to have a peak torque when $K = 1/\sqrt{3} = 0.557$, and for machines with pole numbers above 10, the axial machine is smaller than the corresponding radial machine. Only for a very low pole number arrangement does the radial arrangement show significant improvement.

For low pole number, the axial arrangement needs increased volume to carry flux on both sides of the air-gap compared with the radial machine. As pole number increases the core-back reduces, but the volume enclosed by the air-gap of the radial flux machine is not utilised and so giving the axial arrangement a volume advantage.

Figure 3.8 also indicates that as K reduces, the relative volume of the axial machine also reduces. However if taken to extremes, for example, $K=0.3$, the significantly reduced electric loading due to the small inner diameter forces the volume to increase.

3.3.4 Calculation of the Volume Ratio between Axial and Radial Machines for a Given Outside Diameter – Study 2

Often a given application has an outside diameter restriction in which the machine must fit. It is also beneficial for electrical machines to have a large diameter so as to increase

sweep speed. This analysis compares the volume of an axial and radial flux machine whilst keeping the outer diameter constant for both cases.

For the axial arrangement, given the outer diameter is fixed and specific force is constant, the torque T will be related to the surface area SA and torque radius R , which are both dependent upon K , equation (3.20).

$$T \propto SA.R \text{ and } SA.R = \frac{\pi.(1-K^2)}{4} \times \frac{(1+K)}{4} \quad (3.20)$$

The air-gap diameter of the radial machine D can be obtained from

$$D = OD - 2.CB - L_{gap}$$

Previously a value for CB was calculated in equation (3.13) so with $OD=1pu$, and L_{gap} from equation (3.14) gives

$$D = \left(1 - \frac{\pi.(1+K)}{4.P} - 0.006\right) \quad (3.21)$$

For the radial flux arrangement the torque T is given by equation (3.22)

$$T \propto SAR \text{ and } SAR = \frac{\pi.D^2.L}{2} = \frac{\pi\left(1 - \frac{\pi.(1+K)}{4.P} - 0.006\right)^2 .L}{2} \quad (3.22)$$

For a given torque equation (3.20) can be equated to equation (3.22) to obtain the radial machines length for a given K and P value, equation (3.23).

$$\frac{\pi.(1-K^2)}{4} \times \frac{(1+K)}{4} = \frac{\pi(1 - \frac{\pi.(1+K)}{4.P} - 0.006)^2}{2} .L$$

$$L = \frac{(1-K^2).(1+K)}{8.(1 - \frac{\pi.(1+K)}{4.P} - 0.006)^2} \quad (3.23)$$

The radial machine's length should be reduced to allow for the increased electric loading in the radial machine, equation (3.24).

$$\frac{OD.K}{D} = \frac{K}{(1 - \frac{\pi.(1+K)}{4.P} - 0.006)} \quad (3.24)$$

The length in equation (3.23) is then modified using equation (3.24) to equation (3.25)

$$L = \frac{(1-K^2).(1+K).K}{8.(1 - \frac{\pi.(1+K)}{4.P} - 0.006)^3} \quad (3.25)$$

The volume of the radial machine can be calculated using equation (3.26)

$$Radial\ Volume = \frac{\pi.OD^2}{4} .L = \frac{\pi.(1-K^2).(1+K).K}{32.(1 - \frac{\pi.(1+K)}{4.P} - 0.006)^3} \quad (3.26)$$

The volume of the axial machine is given by equation (3.16), and the ratio of axial over radial volume can be calculated dependent upon K and P , equation (3.27).

$$\frac{\text{Axial}}{\text{Radial}} = \frac{\left[\frac{\pi(1+K)}{P} + 0.056 \right]}{\left[\frac{(1-K^2).(1+K).K}{2.(1 - \frac{\pi.(1+K)}{4.P} - 0.006)^3} \right]} \quad (3.27)$$

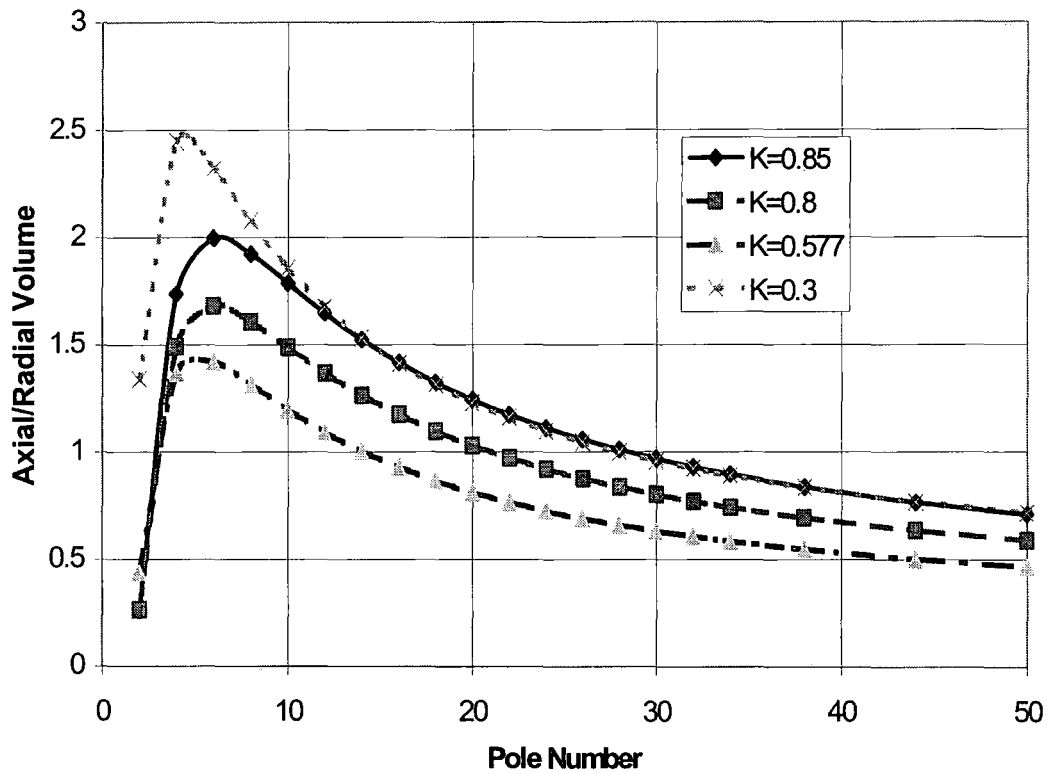


Figure 3.9 Compares axial/radial volume for a given machine outer diameter with respect to K and P

Considering Figure 3.9, the 2-pole case is unusual in that the core-back required is so large for both cases that the volume of both machines is exaggerated. The axial machine has two large core-backs but the air-gap surface area is still large. The radial machine has such a small air-gap diameter the length of the machine has to be significantly increased, making the axial case more attractive for the 2 pole arrangement, unless K is so low that the electric loading is compromised.

The 6-pole case is the worst for the axial machine but as pole number increases the axial machine volume decreases compared to the radial arrangement.

Examining the case when $K=0.577$, the axial machine is volumetrically beneficial for the two pole case and when the pole number increases above 14. When the pole number is greater than 50, the axial machine clearly only takes up half the volume, and therefore for a fixed outer diameter has only half the length which is a significant observation.

Comparing Figures 3.8 and 3.9 suggests there is a much smaller difference between axial and radial volumes as a result of the fixed outer diameter and varied PM mass.

Looking at the case when $K=0.3$, the axial arrangement suffers again on account of the reduced electric loading.

3.4 Discussion

For pole numbers greater than 14 poles the axial flux machine is superior in terms of reduced overall volume. With respect to diesel engines, replacing the flywheel, removing coupling, bearings and utilising the existing flywheel housing has obvious integration and economic benefits. For these reasons, the axial machine is the preferred choice for the VSIG application. Chapter 4 discusses the design equations, Chapter 5 discusses the prototype build and compares test with predictions. Finally Chapter 6 establishes an approach for machine optimisation.

Experience has shown as ratings increases above say, 75kW at 3000rpm, the axial machine suffers certain mechanical limitations. For example the relatively large diameter tended to hang below the sump of the engine, resulting in a larger generating set envelope. The rotor weight for machines of higher rating prohibited the use of the engine bearing, so replacing the flywheel became impractical resulting in additional coupling, bearings and housing. Tolerances are amplified by the aspect ratio of diameter to length and so mechanical clearances need to be carefully controlled. Otherwise larger airgap clearances would have to be accepted increasing the reluctance of the magnetic circuit, resulting in more magnet mass. The axial forces during assembly of this type of machine will increase for higher ratings creating assembly issues.

For the above reasons a radial permanent magnet machine was researched for the higher ratings. A radial flux permanent magnet generator operating at 200kW, 3600rpm has been designed, built and tested by the author[41].

Chapter

4.

Axial Flux Machine Design

The following sections provide a literature review and design equations for a particular type of axial flux machine, sometimes referred to as a TORUS. This machine uses a toroidal core, air-gap armature winding and utilises NdFeB magnets for excitation. Design equations are derived from lumped parameter electromagnetic and thermal equivalent circuits. The design equations are used to design a 50kW unit and the geometry of the machine is modelled in Finite Element Analysis(FEA) to check some of the electromagnetic assumptions. Finally the FEA results are placed into a more refined thermal model to establish the predicted performance of the machine.

4.1 Literature Review

Campbell [42] should take credit for many of the optimisation equations developed by subsequent authors. Strictly Campbell's topology was different but he explored the ratio of pole arc to pole pitch ratio for arc shaped magnets on a disc with constant distance between poles. He identified a pole arc to pole pitch ratio of 0.8 as a reasoned choice. Furthermore the extensively publicised optimum ratio of $1/\sqrt{3}$ between the inner and outer diameter was found. An assumption of constant flux density between the inner and outer radius is made to obtain the equation for maximum power as discussed in the next section.

The first paper to explore the axial flux arrangement with a toroidal core and airgap winding was Rash [43] in 1985 who suggested such machines could be used as an electrodynamic railway brake. The paper examines the magnet field distribution of an 8 pole unit using finite elements and a prototype is built.

A small 400W, 3000rpm axial flux permanent magnet motor was published by Evans [44] who identified an optimum depth of winding compared to the magnet depth. Evans also argued increasing pole number reduced the efficiency of the magnets, but ignored the gains of a reduced coreback. Spooner and Chalmers [45, 46, 47, 48] published a more rigorous analysis between 1988-91. Reference [46] looks at the thermal aspect of this machine and provides a heat transfer coefficient of $150\text{W/m}^2/\text{K}$ for the cooling air passing through the air-gap. A 2.5kW machine was constructed [48] and demonstrated to operate as a brushless dc motor. Spooner and Chalmers [49] summarised their research in 1992 and compared 3 different generator designs with a nominal rating of 28 Vdc, 2.5kW at 3000rpm and a machine is prototyped. The dc voltage was obtained by placing diodes on individual coils but commutation difficulties observed due to mutual coupling on the stator.

In 1991, Caricchi, Napoli, Crescimbeni, Noia [50, 51], at the University of Rome, designed and built a 1.3kW motor and provided electronic control. Caricchi [52] designed and built a 16-pole unit for wind applications and identified a significant improvement in power density compared with a conventional generator, the advantage of increased pole

number and double excitation was ignored in this comparison. Stiebler [53] repeated most of the work documented in [50].

Jensen and Lipo [54] at the University of Wisconsin in 1992, experimented with amorphous iron, as the manufacture of such material was suited to the TORUS topology.

Wei[55] revisited a 3 dimensional Finite Element Analysis to document the effect of no load leakage flux. Dostal [56] designed an electronic controller at UMIST to drive the 2.5kW 9-phase machine discussed in reference [49] as a motor and a field-weakening concept was developed by Pan [57].

Chalmers[58] published the 8kW Torus developed at Dornier in 1995. This was a commercialised TORUS driven by Wankel engines offering a 28V dc output. To date UMIST hardware activity on the TORUS has diminished with only the publication of modelling techniques [59, 60] in 1997.

With Spooner moving to Durham University, Wu [61] developed a self regulating PM generator by saturating the iron core.

Since 1994, the University of Rome has been very active with regards to the TORUS. An interesting concept of having counter rotating rotor plates [62] has been investigated. A 2.4kW motor was placed in the “Di-Elettrica” scooter [63]. Recently the TORUS topology has been modified and the iron stator removed. An air-gap winding has been used with liquid cooling of the conductors to form a totally enclosed unit [64, 65, 66].

All the above are low power machines below 8kW. Information contained in these papers was used by the author as a basis for higher power designs in the order of 50kW.

4.2 Fundamental Equations for Axial Flux Machines

Referring to equation (3.3) in the previous Chapter, the specific force f_e , can be calculated with respect to the electric loading A_{rms} at the inner diameter.

$$f_e = \frac{\hat{B} \cdot A_{rms}}{\sqrt{2}} \cdot \frac{2 \cdot K}{(1 + K)} \quad (4.1)$$

\hat{B} = Peak flux density(T), A_{rms} = RMS electric loading(A), ID = Inner Diameter(m), OD = Outer Diameter(m), $K = ID/OD$

The surface area SA , for double-sided excitation is

$$SA = 2 \cdot \frac{\pi}{4} \cdot OD^2 \cdot (1 - K^2) \quad (4.2)$$

The torque radius R , is

$$R = \frac{OD \cdot (1 + K)}{4} \quad (4.3)$$

From equation (3.4) in the previous Chapter the torque and power P , can be calculated as

$$P = \frac{\hat{B} \cdot A_{rms}}{2 \cdot \sqrt{2}} \cdot \pi^2 \cdot n \cdot K \cdot (1 - K^2) \cdot OD^3 \quad (4.4)$$

Where n = speed (revs/sec)

The power is a maximum when $K=1/\sqrt{3}$ and the power increases with the cube of the outer diameter.

Some authors have included non sinusoidal waveforms in their analysis and their results differ marginally from equation (4.4). While this is applicable to motor applications when a controlled bridge is used, this approach is really not suitable for this application. As explained in chapter 2, the permanent magnet generator feeds an uncontrolled 3 phase bridge rectifier. Therefore triplen harmonics are immediately tuned out of the three phase supply. Waveforms having a more trapezoidal shape may also introduce commutation issues with the rectifier. For these reasons a more sinusoidal waveform is sought.

4.3 Design Process

The design procedure is a four-stage process. First, a simplified model is created based on lumped parameters to obtain an estimate of the dimensions required and includes electrical, thermal, electromagnetic and economic aspects. Here the engineer judges the prime design criteria by balancing efficiency, material cost and power output for a given application. The design can then be assessed using 3 dimensional FEA to optimise the magnetic design and provide waveform data and inductance parameters. The FEA results are then combined with a thermal model to predict the machine's performance in more detail by iterative manipulation. These parameters are then used to predict the performance of the complete VSIG system using power electronics simulation software.

The following section provides the theory and design equations for the axial flux generator.

4.3.1 No Load Magnetic Circuit

With this type of axial flux machine the air-gap reluctance is significant on account of the stator winding being in the air-gap. The permanent magnet material NdFeB has a similar relative permeability to air of between 1.05-1.1. It is therefore a valid assumption to ignore the reluctance of the stator and rotor, and only consider the reluctance of the magnet and air-gap through which the flux passes. Figure 4.1, provides an equivalent circuit for this condition.

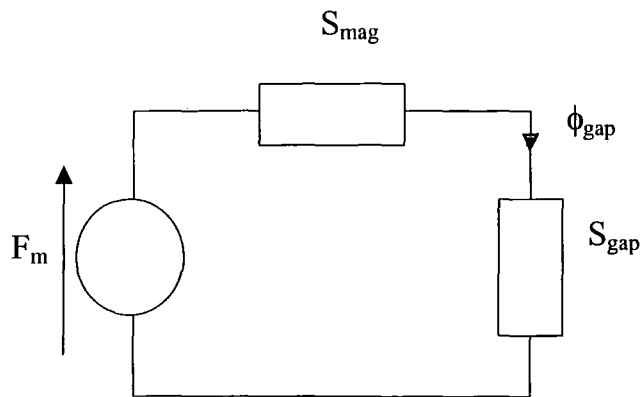


Figure 4.1 Equivalent circuit to calculate air-gap flux density

From the equivalent circuit the gap flux ϕ_{gap} , can be calculated from the remanent magnet MMF F_m , the magnet reluctance S_{mag} and the air-gap reluctance S_{gap} .

$$\phi_{gap} = \frac{F_m}{S_{mag} + S_{gap}} = \frac{\phi_{rem} \cdot S_{mag}}{S_{mag} + S_{gap}} \quad (4.5)$$

Assuming the magnet and air-gap area is the same

$$B_{gap} = \frac{B_{rem} \cdot L_m}{L_m + \mu_r \cdot L_{gap}} \quad (4.6)$$

Where B_{gap} = airgap flux density (T), B_{rem} = magnet remnant flux density (T), L_m = magnet length (m), L_{gap} = airgap length (m), μ_r = relative permeability

Leakage at the inner and outer edge will cause the flux density to be a little less than indicated by equation (4.6). However the magnets are designed to overhang the stator a little so the magnet and gap area is larger than the stator area. Consequently, the leakage at the ends of the plates is compensated by a contribution of useful flux from fringe fields.

4.3.2 Calculation of EMF

The peak induced voltage with a knowledge of $e = B \cdot L \cdot V$, may be readily calculated using equation (4.7).

$$e_{pk} = B_{gap} \cdot OD^2 \cdot (1 - K^2) \cdot N_{ph} \cdot \pi \cdot \frac{n}{2} \quad (4.7)$$

Where N_{ph} = number of phase turns, n = speed (revs/sec)

Waveshape is important as equation (4.7) only provides a peak value. The pole arc to pole pitch ratio of the magnet and air-gap directly influences the shape of the induced voltage. An approximate method for calculating waveshape is to plot the air-gap flux density based upon the pitch of the magnet, Figure 4.2a. Relating all dimensions to the

mean circumference, a section of reduced flux density proportional with the air-gap length L_{gap} , may be plotted to create an approximate trapezoidal waveshape, Figure 4.2b. The flux density is directly proportional to the induced EMF, so the RMS of the waveform can be calculated.

The target was to develop a machine with a near sinusoidal voltage waveform. Ignoring leakage this would be represented by a two thirds pole arc. To allow for leakage the pole arc for the magnet is increased by an amount equivalent to the gross air-gap within the machine and taken to be a constant 0.76 for this exercise. Due to the approximate nature of these calculations winding factors are ignored.

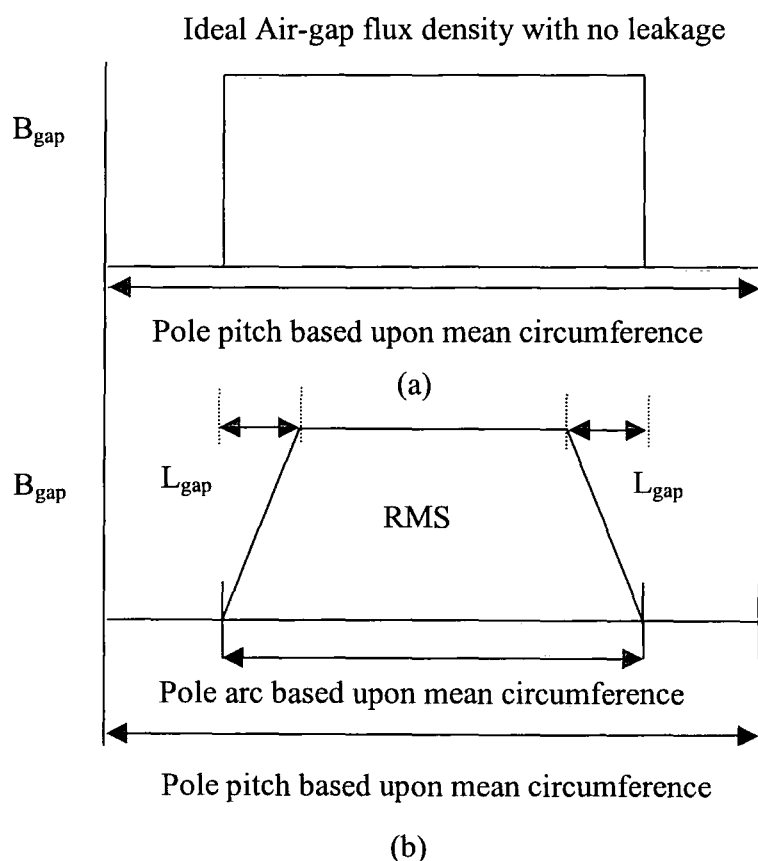


Figure 4.2 Calculation of Root Mean Square phase voltage

4.3.3 Synchronous Inductance

Figure 4.3 shows the flux paths within the axial flux machine when a three-phase balanced current is drawn from the stator. At a given instant, one phase conducts full line current and the other two phases half line current. Due to pole reversal the flux is forced into the air-gap, through the rotor and returns to the stator through the air-gap. If leakage flux in the air-gap and on the end turns is ignored, an approximate calculation may be made to estimate the synchronous inductance using a lumped parameter equivalent circuit, Figure 4.4. Three coils are represented by 3 series MMF sources in parallel with two reluctance paths formed by the air-gap on the stator sides. Flux resulting from the 3 coils is assumed to pass through an area on the stator side covered by half a pole pitch and return through an area covered by half a pole pitch. The reluctance length $L_{gross\ gap}$ is the path length between the stator and rotor.

The stator side area over half a pole pitch is

$$Stator\ side\ Area = \frac{OD^2 \cdot (1 - K^2) \cdot \pi}{8 \cdot P} \quad (4.8)$$

So that the airgap reluctance for a single stator side is

$$S1 = S2 = Airgap\ Reluctance\ on\ stator\ side = \frac{16 \cdot L_{gross\ gap} \cdot P}{\mu_0 \cdot OD^2 \cdot (1 - K^2) \pi} \quad (4.9)$$

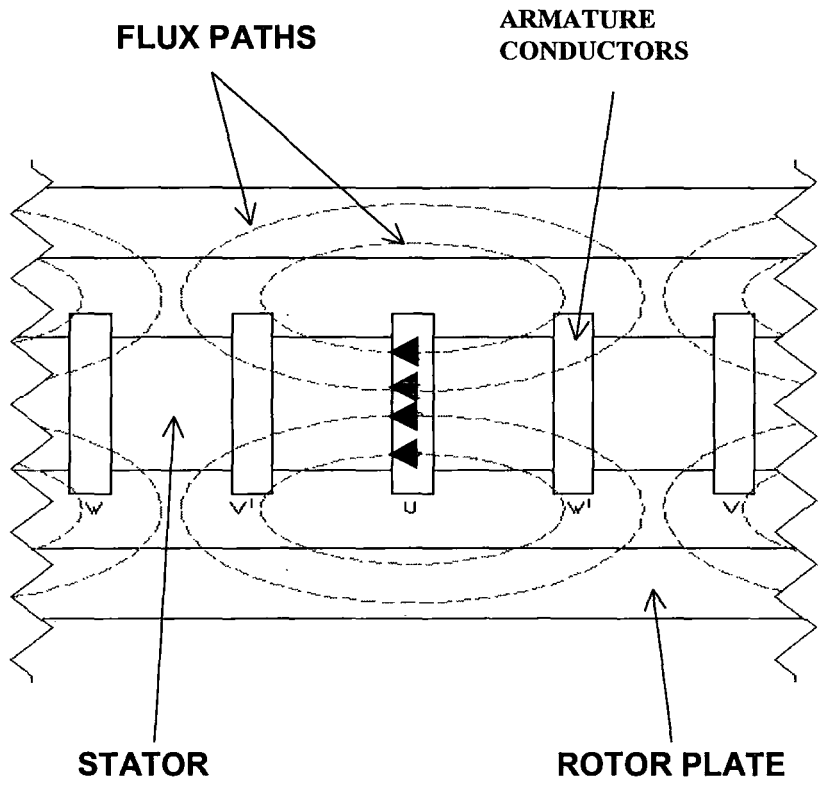


Figure 4.3 Armature reaction flux paths

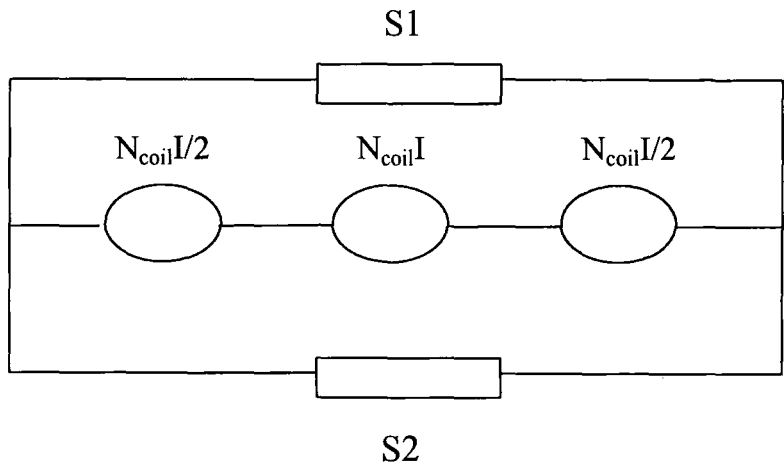


Figure 4.4 Lumped parameter equivalent circuit

The three series coil MMF's are in parallel with the two stator sides so

$$St = S1 // S2 = \frac{8.L_{gross\ gap}.P}{\mu_0.OD^2.(1-K^2).\pi} \quad (4.10)$$

Effectively the coils provide $2.N_{coil}.I$ of MMF to create the armature flux, ϕ

$$\phi = \frac{2.N_{coil}.I}{St} \quad (4.11)$$

Therefore, the synchronous inductance for P poles can be calculated

$$L_{synch} = \frac{N_{coil}.\phi.P}{I} = \frac{2.N_{coil}^2.P}{St} = \frac{N_{coil}^2.\mu_0.OD^2.(1-K^2).\pi}{4.L_{gross\ gap}} \quad (4.12)$$

4.3.4 Loss Mechanisms

There are four primary sources of loss within this type of axial flux machine:

- Windage loss
- Iron loss
- Joule loss
- Eddy current loss

The windage loss is a function of the geometry and is basically a product of head pressure and air flow rate through the machine. The relationship between head pressure and flow rate is interdependent where maximum pressure occurs at zero flow rate and visa versa.

The resistance to air flow is non linear and dependent upon flow rate as well as geometry.

The windage loss may be estimated by applying known relationships to previous prototypes. Examples of rough rules of thumb are head pressure increases with the square of diameter, and flow rate increases with the cube of diameter, so the power needed to drive the fan varies with diameter to the power of five. Flow rate varies proportionally with speed. The friction and windage in reference [49], of 10W for a 0.167m diameter was used as a basis for estimating this loss.

The iron losses can be calculated from the geometry and related to a general curve fitting formula that is referenced to manufacturers data sheets at 1T, 400Hz, equation (4.13).

Using manufacturers data sheets ensures both hysteresis and eddy loss is included.

$$\text{Iron loss based on manufacturers data} = K_n \cdot \left(\frac{f}{400}\right)^x \cdot B^y \quad \text{W/kg} \quad (4.13)$$

For 0.3mm thick grade M4 steel used in the prototype, $K_n=10$, $x=1.5$, $y=2$.

Joule loss is simply the $I^2 \cdot R$ loss within the copper. The uncertainty comes from estimating the temperature within the machine and consequent stator phase resistance.

$$R_{HOT} = R_0 \cdot (1 + \alpha t) \quad (4.14)$$

Where R_{HOT} =Resistance at t temperature Ω , α =temperature coefficient =0.004265, R_0 =Resistance at zero degrees Ω , t = Operating temperature $^{\circ}C$

With conductors in the air-gap circulating currents can be induced in the conductor, a loss known as eddy current loss. Carter [67] provides a formula for the calculation of eddy loss, P_{eddy} for round conductors with respect to per unit conductor volume, equation (4.15).

$$P_{eddy} = \frac{B_{gap}^2 \cdot w_e^2 \cdot d^2}{32\rho} \quad \text{W/m}^3 \quad (4.15)$$

Where $w_e = 2 \cdot \pi \cdot f$, f = electrical frequency (Hz), d = conductor diameter (m), ρ = conductor resistivity = $1.782 \times 10^{-8} \Omega\text{m}$

The conductors will have a small diameter to reduce eddy current loss, so ac resistance as a result of skin effects can be ignored - copper wire at 400Hz has a skin depth of 3.3mm.

4.3.5 Thermal Equivalent Circuit

The thermal model for this machine was simplified by only considering the cooling circuit over the two stator sides directly under the magnets, the reason is that most of the losses will be generated over this surface. It is worth noting that the cooling circuit will not be so effective over either the bottom or particularly the top of the stator. No conductor eddy losses will however be present in these regions and the losses directly under the magnets should be more significant.

The heat generated by the iron losses will radiate through the top and bottom of the stator as well as through the stator mounting structure. It is believed that the actual iron losses

will be larger than calculated due to machining stresses on the core sides. On balance, it was assumed all the iron loss radiated through the stator sides.

Looking at just half the machine in Figure 4.5, heat is generated by the iron loss then passes through the core insulation and the conductor insulation. At this point additional Joule and eddy loss will be generated in the conductor, the heat then needs to pass through conductor insulation into the surrounding air. Figure 4.6 provides an equivalent thermal model for the stator.

The thermal conductivity coefficient of insulation, Ω_{ins} , was taken as 0.2W/m/K, while the thermal heat transfer coefficient for the ventilated air, h_{tc} , was assumed to be 150 W/m²/K as suggested by Spooner and Chalmers [49].

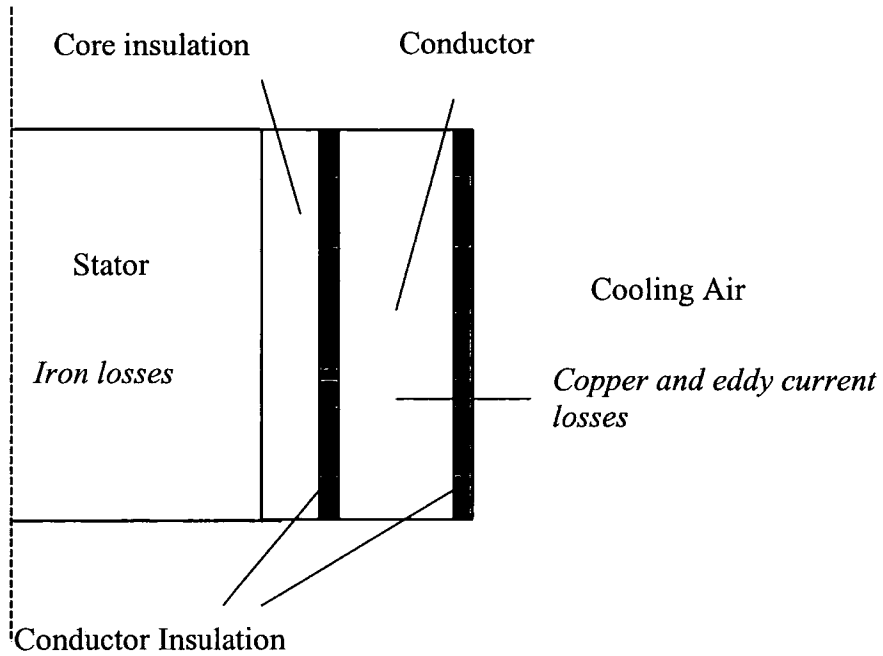


Figure 4.5 Half cross section of stator for single layered winding

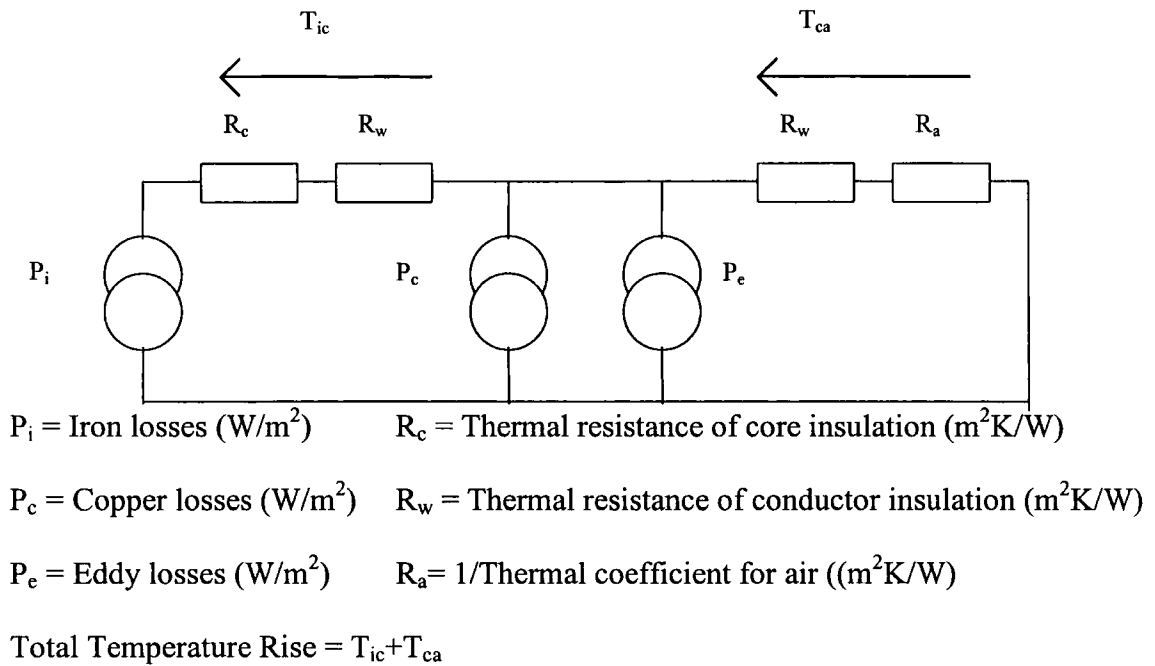


Figure 4.6 Thermal equivalent circuit for single layered winding

As all the heat is assumed to conduct through the same surface area, the power loss and thermal resistances may be calculated with respect to surface area, so the thermal resistance may be simplified to equation (4.16).

$$\text{Thermal Resistance (m}^2\text{K/W)} = \frac{\text{Length}}{\Omega} \quad (4.16)$$

Where Ω = thermal conductivity (W/m/K)

The above thermal equivalent circuit makes a number of assumptions such as, no convection of heat through the machine body or no input of heat from the engine crankshaft. In reality these have an impact, however, the true geometry of the ventilation system including air in and out let will also play their part. Thermal analysis of electrical machines is complex and these models only provide guidance.

4.3.6 Prototype Dimensions

From the lumped parameter analysis a design was proposed with the dimensions, mass, electrical parameters and losses given in Tables 4.1 to 4.4. The generator was targeted to have a rating of 50kW at 3000rpm. The output line to line voltage was selected to be 425V to allow for voltage drops within the power converter, which is required to supply 400V. Permanent magnet material has a significant effect on the rating of the machine. In this sizing exercise the NdFeB had a high temperature grade of 150 C, a maximum energy density of 33MGOe, a relative permeability of 1.05, and a remanence flux density of 1.17T

Number of Poles	16
Core OD mm	400
Core ID mm	253
Core Thickness mm	25
Magnet OD mm	405
Magnet ID mm	240
Magnet Thickness mm	9
Rotor OD mm	420
Rotor Thickness mm	12
Net Airgap Thickness mm	7
Winding Thickness mm	3.5
Running Clearance mm	3.5
Overall Machine Diameter mm	480
Overall Machine Width mm	185

Table 4.1 Machine dimensions

Weight	kg
Copper	2.4
Stator Iron	13.8
Magnet	8.4
Rotor per plate	14.0
Total Rotor Assembly	50.0
Total Stator Assembly	25.0
Flywheel Housing	19.0

Table 4.2 Machine mass

Turns per coil	4
Parallel Conductors	12
Conductor Diameter mm	0.75
No of coils per phase	16
No of phases	3
Phase Resistance (20 C)	0.0552
No load voltage(RMS) at 3000rpm	245.5
Rated Current at 3000rpm (A)	70.5
Current Density A/mm ²	13.3
Synchronous Inductance(uH)	94.5
Frequency (Hz)	400
Rating at 3000rpm (kW)	50
Temperature Rise (C)	125
Ambient (C)	40

Table 4.3 Electrical parameters

Friction and Windage Loss (W)	1262
Iron Loss (W)	227
Copper Loss (W)	1275
Eddy Loss (W)	401
Efficiency (%)	94.1

Table 4.4 Losses breakdown and efficiency

4.4 FEA Model

The axial flux generator was modelled using OPERA-3D a finite element analysis package offered by Vector Fields [68]. Modelling in three dimensions was required due to the non-uniform flux distribution in the air-gap. The non-uniformity is seen as fringe fields at the edges of the magnets and at the inner and outer edges of the stator core. In practice, the magnets may overhang the stator to concentrate the flux a little and utilise the small end turn conductor of the stator winding, but this does make the fields more non-uniform.

Modelling using FEA also provides valuable information allowing the RMS phase voltage and synchronous inductance to be calculated. Table 4.1, provides dimensional data for the FEA model.

To reduce processing time only 1/32th of a 16 pole machine has been modelled, due to symmetry through the stator core and reflective symmetry between poles. Figure 4.7 shows the 1/32th model. Boundary conditions had to be placed around the model.

Reflective symmetry boundaries are placed in the plane that cuts through both the stator and rotor at the edge of the model. Only half the stator width is modelled since a tangential magnetic boundary exists at the centre of the stator. The problem is then enclosed by a tangential magnetic boundary at some distance from the machine.

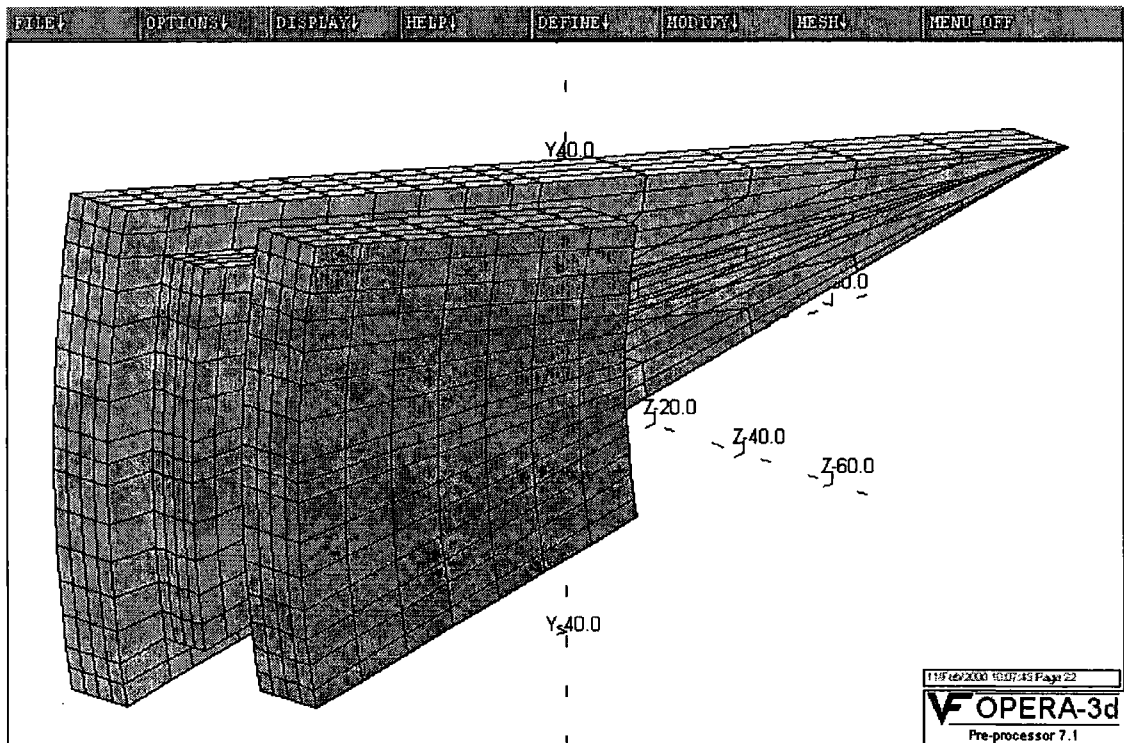


Figure 4.7 Shows 1/32th model

4.4.1 The No Load Waveform

Flux linkage in the stator core was observed rather than flux cutting in the air-gap. This was due to the difficulty in accurately assessing the flux density distribution in the air-gap and flux fringing at the top and bottom of the stator core.

Cutting regular slices into the stator and calculating the normal component of flux over the slice allowed the flux linkage to be obtained. The flux linkage with respect to mechanical angular displacement was taken over a full cycle. The mechanical angular displacement was then converted into an electrical angle, Figure 4.8.

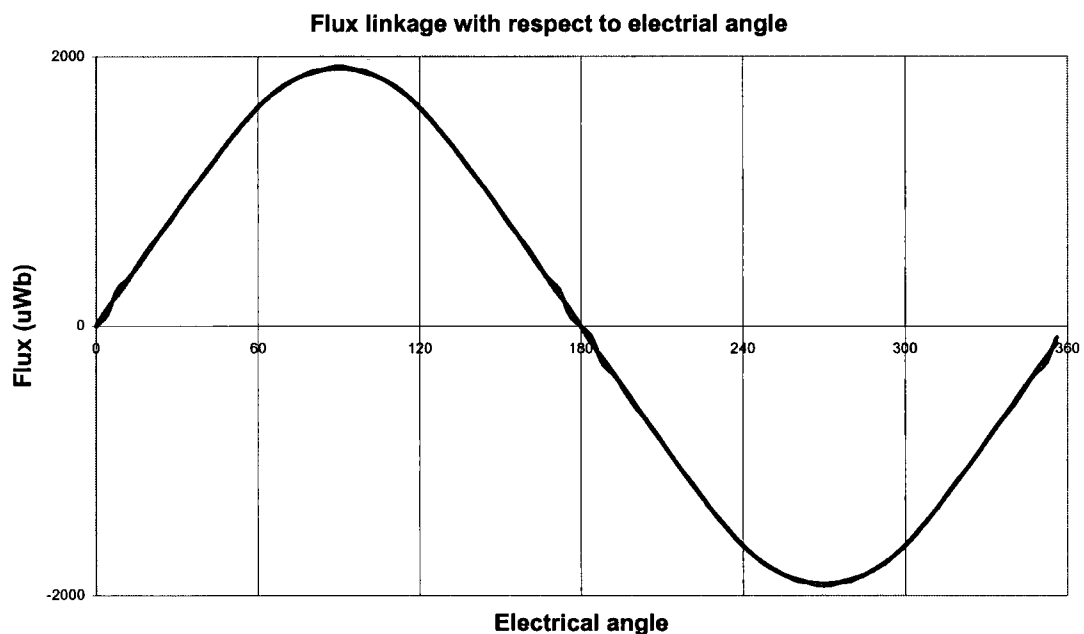


Figure 4.8 Flux linkage with respect to electrical angle

The flux waveform was then transposed into a Fourier series, a method for doing this can be found in Lander [69].

At each 4° interval, the value of $\sin hx$ and $\cos hx$ can be tabulated for each harmonic order, Table 4.5. The product of the current value at that angle with $\sin hx$ (or $\cos hx$) is tabulated. Having tabulated $\phi \sin hx$, it can then be summed. Over a full cycle, the number of 4° intervals is 90. The summation is divided by 90 and multiplied by 2 to give a_n .

x	0	4	8	12	etc	sum .2/90
ϕ	0	102	333	434		
$\phi \sin x$	0	7	46	90		a1= 2290
$\phi \cos x$	0	102	330	424		b1= 0
$\phi \sin 3x$	0	21	135	255		a3=-81
$\phi \cos 3x$	0	100	304	351		b3= 0
$\phi \sin 5x$	0	35	214	376		a5=-10
$\phi \cos 5x$	0	96	255	217		b5= 0
etc						

Table 4.5 Calculation of Fourier components

The voltage waveform in Figure 4.9 can be obtained using equation (4.17).

$$e = K_d \cdot N_{ph} \cdot \frac{d\phi}{dt} \quad (4.17)$$

Where N_{ph} = no of phase turns, ϕ = Fourier distribution for the flux waveform

= $\phi_1 \cdot \sin(\omega_e t) + \phi_3 \cdot \sin(3\omega_e t) + \phi_5 \cdot \sin(5\omega_e t)$up to the 15th harmonic.

$$K_d = \text{winding distribution factor for a single layer winding} = \frac{\sin\left(\frac{h \cdot N_{coil} \cdot \chi}{2}\right)}{N_{coil} \cdot \sin\left(\frac{h \cdot \chi}{2}\right)}$$

N_{coil} = turns per coil , χ = electrical angle displacement between turns , h = harmonic order

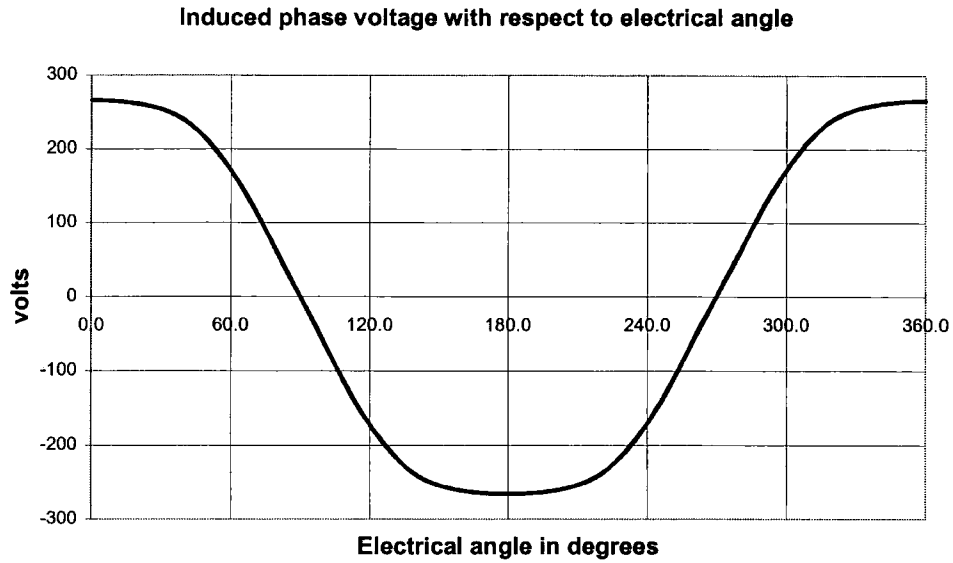


Figure 4.9 shows the calculated voltage waveform.

4.4.2 Inductance Calculations

Before inductance calculations could be performed, 48 coils, see Table 4.3, were placed in the FEA model, Figure 4.10. Only 16 coils are necessary to calculate the synchronous inductance, however 48 coils allowed alternative calculation methods to be tried.

Two methods were adopted to calculate the inductance of the stator windings. The first uses the energy E , from the FEA solution to give the inductance L , via equation (4.18). The second uses the flux linkage ϕ , from the FE solution to determine inductance L , equation (4.19).

$$E = \frac{L.I^2}{2} \quad (4.18)$$

$$L = \frac{N\phi}{I} \quad (4.19)$$

Calculating the inductance using the energy in equation(4.18) is considered the more accurate method, and should result in a slightly higher value than that given by equation (4.19). Two calculation methods ensure proper allowances have been made as only 1/32th of the entire machine is modelled.

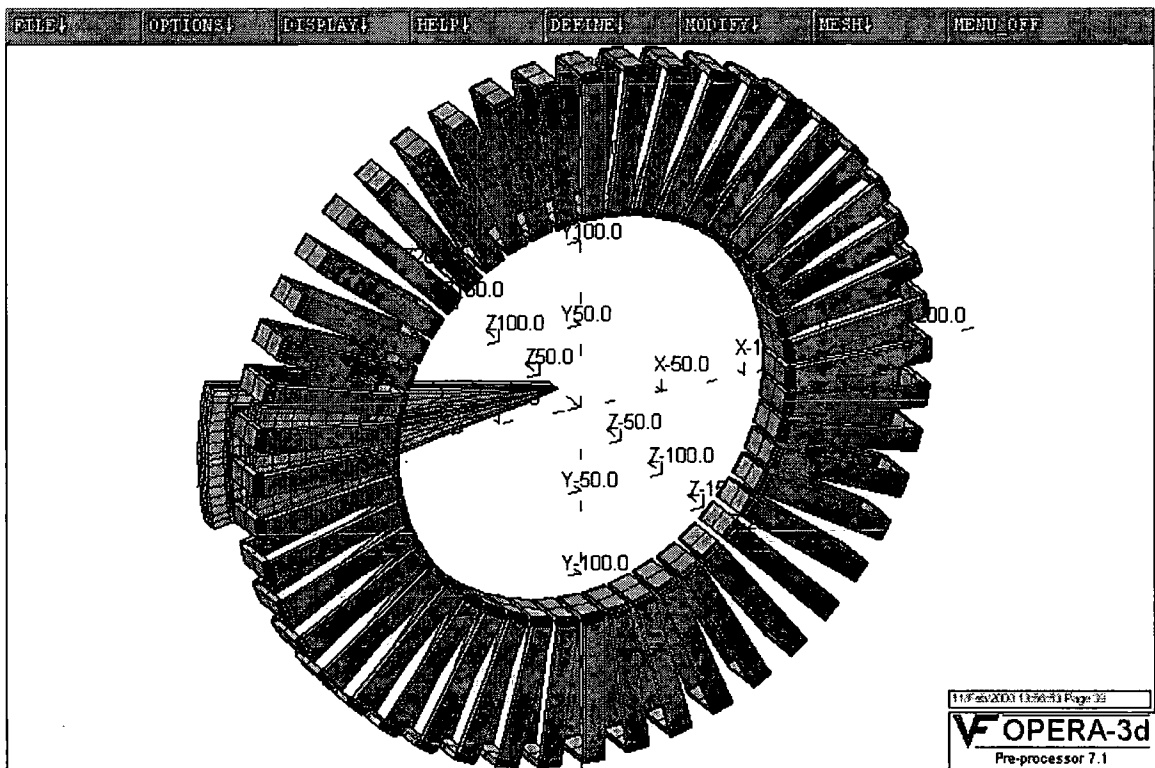


Figure 4.10 FEA model with conductors

4.4.2.1 Self Inductance

Figure 4.3 shows the flux paths when one phase is conducting current. It can be seen, due to pole reversal, the flux is forced into the air-gap through the rotor and returns to the stator through the air-gap. Therefore, the self-inductance is predominately determined by the MMF across the air-gap.

All 16 coils of one phase are energised with each adjacent coil carrying flux in the opposite direction. OPERA-3D can return a value for the total energy in the model and therefore the self-inductance calculated using equation (4.18) remembering only half the machine is modelled. Alternatively, the normal component of flux within one of the excited coils can be integrated over the area to provide the flux linkage and the self-inductance calculated using equation (4.19). This provides the self-inductance, L_{self} , for half of one coil in the machine.

4.4.2.2 Mutual Inductance

This may be calculated by energising one phase in the machine as indicated above but this time the normal component of flux within a coil of another phase is integrated over the area to provide the mutual flux. The mutual inductance L_{mut} , for one half coil can be obtained using equation (4.19).

4.4.2.3 Synchronous Inductance

A direct method for obtaining the synchronous inductance L_{synch} , can be obtained by energising one phase with full load current and the two adjacent phases with half current.

The direction of all the currents will be in the same direction as this is a 3-phase system. The total energy in the model will be half that of the total machine and the synchronous inductance can be obtained using equation (4.18).

Alternatively, using flux linkage the synchronous inductance is calculated using equation (4.20).

$$L_{synch} = L_{self} + L_{mut} \quad (4.20)$$

4.4.2.4 Armature Leakage Inductance

The self-inductance of one phase could be broken down into two components, the self-inductance due to the space fundamental air-gap flux, L_{aa0} and armature leakage, L_{al} , equation (4.21).

$$L_{self} = L_{aa0} + L_{al} \quad (4.21)$$

The leakage component includes the end winding leakage on the inner and outer diameter of the stator as well as air-gap leakage.

For a 3 phase winding the mutual inductance L_{mut} between phases can be calculated using Equation (4.22). This assumes the mutual air-gap leakage in the gap and around the end winding between the windings is negligible.

$$L_{mut} = \frac{L_{aa0}}{2} \quad (4.22)$$

From the self and mutual inductance calculated in the previous sections the synchronous inductance can be written, and re-arranging equation (4.23) gives the armature leakage inductance.

$$L_{synch} = L_{al} + \frac{3}{2}L_{aa0} \quad (4.23)$$

4.4.2.5 Generator Model

The generator performance can be evaluated using the equivalent circuit in Figure 4.11.

Where e is the no load EMF, R_s is the stator resistance and R_L the load resistance.

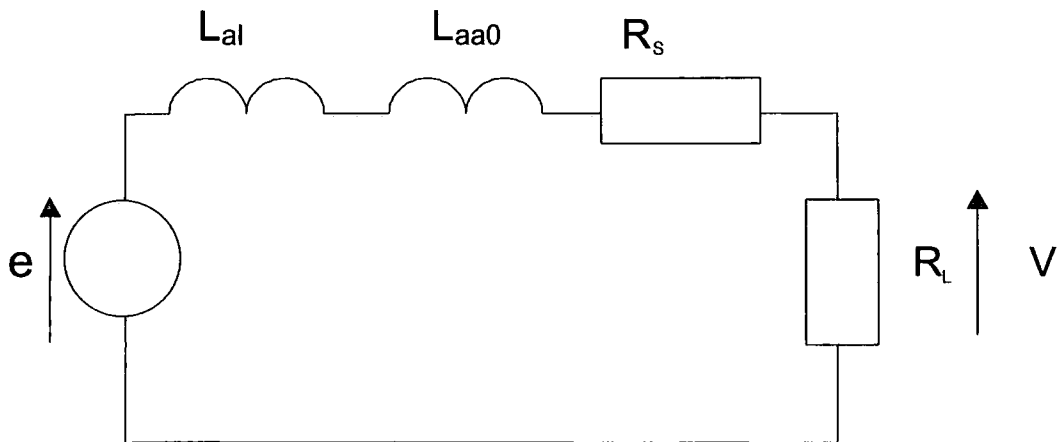


Figure 4.11 Equivalent circuit

It is sometimes necessary to keep the air-gap armature reaction inductance and leakage inductance separate when considering a rectifier load as harmonic currents set up a higher frequency field on the rotor. The induced eddy currents resist the flux so making the

airgap inductance low with respect to the harmonic currents. Therefore strictly any model should make this distinction. In reality however for this type of machine L_{aa0} is so low, it is reasonable to use the synchronous inductance.

4.4.3 Summary of FEA Results

Table 4.6, highlights the differences between the lumped parameter model and FEA. Clearly the lumped parameter compares favourably even though the overhang of the magnet and the reluctance of the stator and rotor is ignored. It should be borne in mind that while FEA provides a very sophisticated method of calculation, the tolerances of materials and the processes involved with machining and assembling prototypes tends to alter their characteristics. The lumped parameter model provides a convenient calculation method that can include more details other than electromagnetic.

	Vrms	Lsynch (uH)
Lumped Parameter	245.5	94.7
FEA	242	94.5

Table 4.6 Compares lumped parameter and FEA models

Table 4.7 provides more detail for the self and mutual inductance detailing the FEA result using the energy and flux linkage method. Notice that as expected the self inductance is higher using the energy method compared to flux linkage. However for the calculation of mutual inductance the flux linkage method provides a higher result. This discrepancy is a direct result of the flux linkage being observed mid point of the coil and does not allow for the spread of flux linkage across the coil, as is the case with the energy method.

	Lself (uH)	Lmutual (uH)
Energy Method	75.7	18.8
Flux Linkage	73.6	24.3

Table 4.7 Self and mutual inductance FEA results

4.5 Refined Thermal Model

The difficulty in modelling the thermal performance of an electrical machine is made complex not just by the difficulty in obtaining the thermal coefficient of the cooling circuit, but the cooling and losses are intimately dependent on each other. For example, the Joule loss depends on the temperature within the machine, but the temperature of the machine depends on the Joule loss. Furthermore the iron losses as well as the conductor eddy loss within the machine will reduce as load current is drawn, on account of the reduction in air-gap flux density.

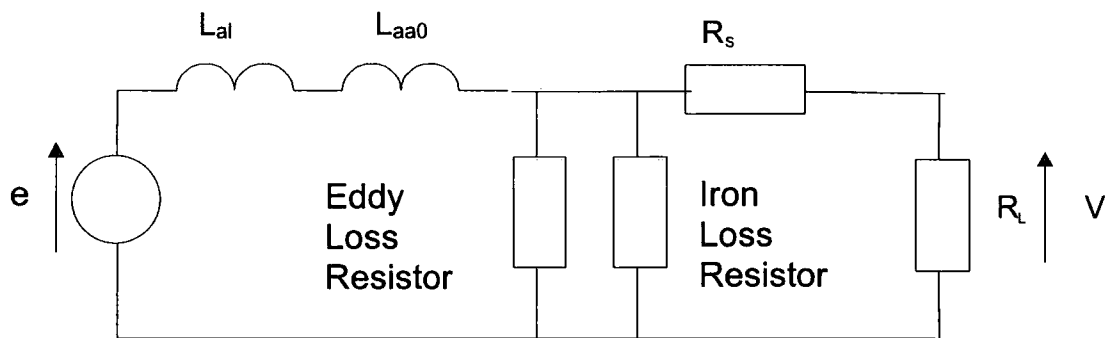


Figure 4.12 Equivalent circuit including loss mechanisms

To overcome this problem additional resistors are placed into the equivalent circuit to represent these losses and compensate for any reduction in air-gap flux density, Figure

4.12. Target temperatures can be specified so that the joule loss is correctly represented in the equivalent circuit. With the resistance referenced to the target temperature and fixed, the load resistor can be iteratively reduced until the total temperature rise for the machine converges with the target. The performance of permanent magnets are dependent upon operating temperature, and can be represented in the equivalent circuit by adjusting the induced EMF as the target temperature is known. This method ensures a better representation of voltage regulation, efficiency, winding temperature and power output.

4.6 Predicted Machine Performance

The graphs in Figure 13 provide the predicted performance for the proposed machine described in Table 4.1. The improved thermal model indicates a higher rating than previously calculated, due to the conductor eddy current losses and iron losses reducing as load current is drawn. At a 125 K rise in a 40 C ambient the output rating is estimated to be 59kW at 3000rpm with an efficiency of 94 %. The voltage regulation is calculated to be 6.9% for this loading.

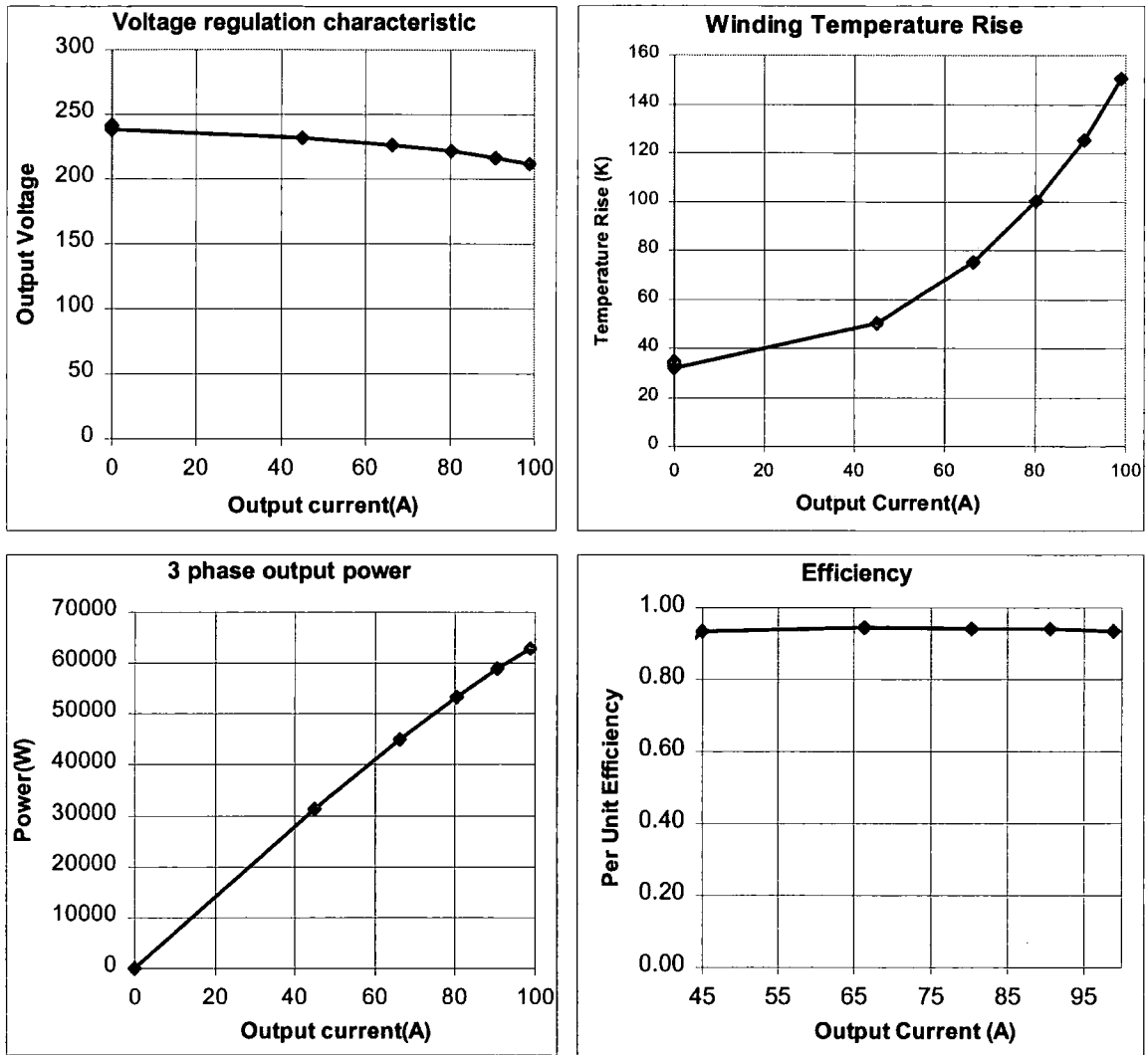


Figure 4.13 Predicted performance

4.7 Discussion

A literature review provides historical developments of the iron cored axial flux topology commonly referred to as the TORUS. Simplified lumped parameter models have been used to represent the magnetic, electrical and thermal performance of the machine. These simplified representations allow the designer to balance a large number of variables when sizing. Such models will have limits but experienced designers should understand these

limits. A procedure for checking the electromagnetic aspects in more detail using Finite Element Analysis is also presented just to ensure the models are realistic. These refined parameters are then included in a more detailed thermal model. Chapter 5 will discuss the construction and test of the machine designed in this Chapter.

Chapter

5.

Axial Flux Machine Prototype and Test

This chapter describes the design, construction and test of a 50kW prototype running at 3000rpm. The purpose of the prototype was to prove the concept, check design calculations, and understand the associated manufacture and constructional issues. The exercise fundamentally had to prove a 50kW unit was feasible. To the author's knowledge this was the first axial flux machine of this rating and speed to be prototyped anywhere in the world.

Previously an 8-pole, 8kW prototype using ferrite magnets was constructed at Durham University and used to benchmark calculations, Reference [35]. Furthermore Durham had a parallel development programme to construct a 50kW unit. It should be understood at the time of design only limited work had started at Durham and the Newage 50kW prototype was based upon what was learnt from the 8kW unit.

5.1 Generator Construction

The axial flux generator was designed to be integrated into a 4-cylinder diesel engine. This four cylinder engine was only capable of delivering a gross mechanical power of 41.4 kW at 3000rpm. The engine manufacturers intention was to develop the engine with a turbo charger to achieve in excess of 50kW. While this particular engine was not capable of producing the required power for a 50kW generator important information

could still be obtained and the concept proven. A picture of the engine is presented in Figure 5.1.

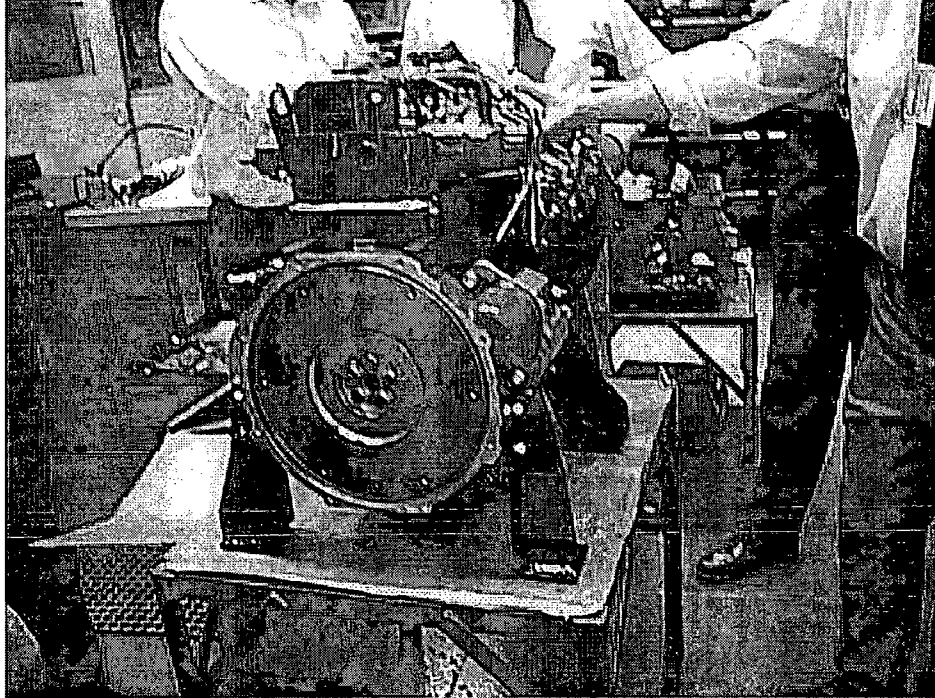


Figure 5.1 The 4 cylinder diesel engine

To realise the full potential of the axial flux generator, full integration into the engine was required. The engine flywheel housing was redesigned to enclose the generator, with the generator rotors forming the engine flywheel. With no requirement for an engine flywheel and coupling disc, nor a housing or bearing for the generator, the number of components was significantly reduced. By forming the generator within the flywheel housing the overall length of the generating set was reduced particularly as no bed-plate was required to support the generator.

Figure 5.2 conceptually illustrates the generator design. Viewing from the right hand side is the redesigned flywheel housing and the crankshaft to which the rotor of the generator is directly bolted. On the back of the first rotor plate the engine ring gear is attached so that the engine can be started using the starter motor in the normal way. It is envisaged long term that the engine will start by generator acting as a motor rather than the existing starter motor, providing further system integration.

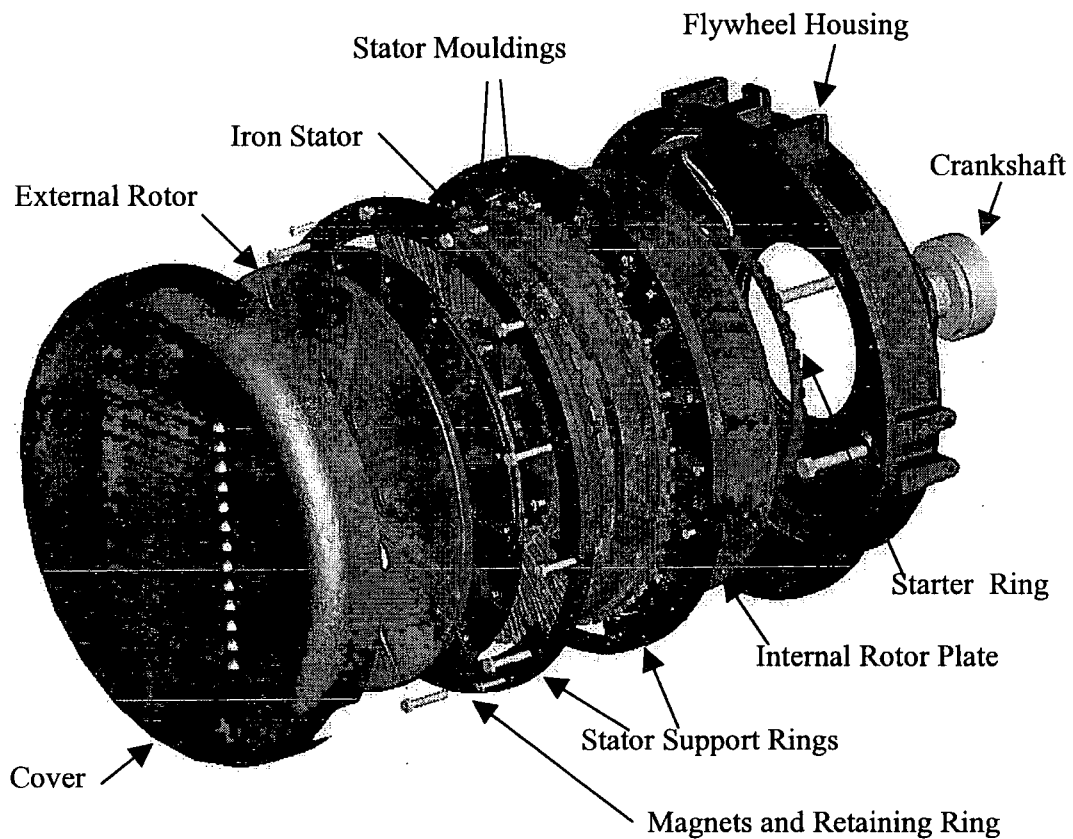


Figure 5.2 Exploded view of axial flux generator

The stator is sandwiched between two rotor plates and held stationary by two stator support rings mounted directly onto the flywheel housing. The two rotor plates form the rotating member and support the magnets. Finally, a cover is mounted onto the stator support rings for environmental protection.

5.1.1 Rotor Assembly

The rotor plates are cast from Spheroidal Graphite (SG) iron with the surface on which the magnets are to be attached machined clean. A boss feature separates the internal and external rotor plates. One nice feature of this boss is that it allows access to the engine crankshaft bolts which bolt the internal rotor into position. The external rotor plate is then bolted onto the internal plate with 6 bolts. With access to the crankshaft bolts, the machine can be removed from the engine without disassembling the machine. However, an additional transit bracket will be required to make sure the stator windings do not foul on the magnets. Other mechanical features of the rotor plate are the strengthening ribs and the axial air intake holes.

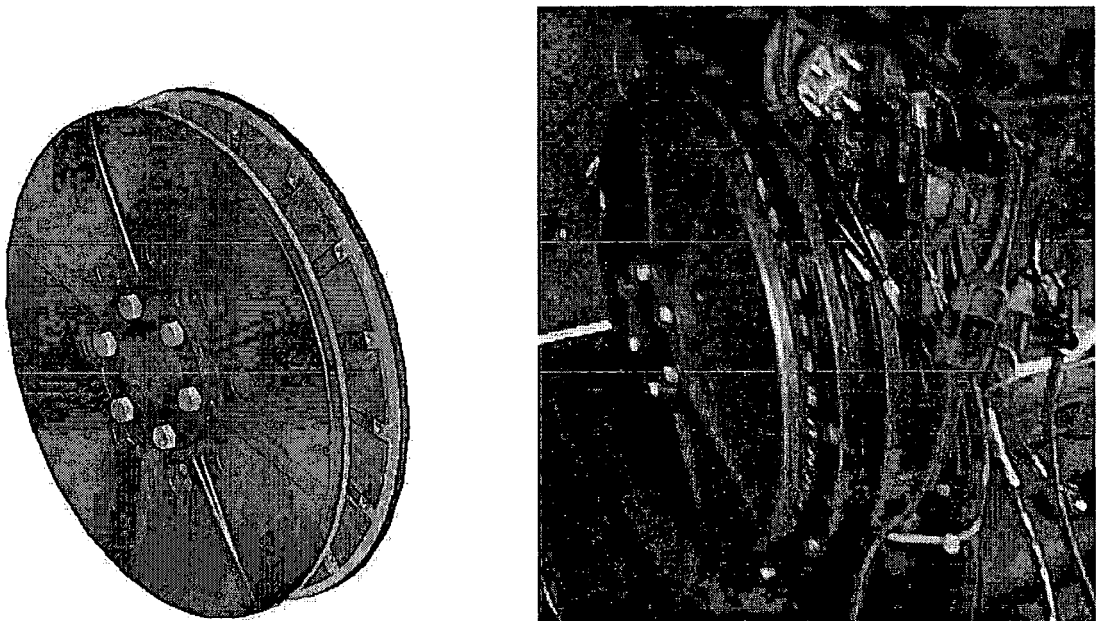


Figure 5.3 Provides an external view of the rotor.

Sixteen magnets were placed on each rotor plate to form a 16-pole machine. These magnets are separated with nylon spacers to prevent the magnets sliding together.

Axially the pull of the magnets will retain them on the plate however in shear the magnet

pull is minimal, and dependent upon the coefficient of friction between the plate and magnet. As the rotors spin there will be high centrifugal forces acting on the magnets equation (5.1), at 3000rpm this force is 4kN.

$$\text{Centrifugal force} = \omega_m^2 \cdot M \cdot r \quad (5.1)$$

Where ω_m = speed in radians = 314.2 rad/sec, M = mass of a magnet (kg) = 0.26 kg,

r = equivalent radius of magnet (m) = 0.155 m

Magnets were retained in position by a laser cut stainless steel ring and placed around the outer radius of the magnets. Applying load tests checked the strength of the ring with forces up to 10kN not producing any obvious deformation. A destructive test up to 26kN was applied to the ring, which resulted in serious deformation, but the ring did not break. This type of analysis is appropriate for a prototype machine but for a production machine, fatigue issues need to be considered. A rotor with magnets, separators and magnet retaining ring is shown in Figure 5.4.

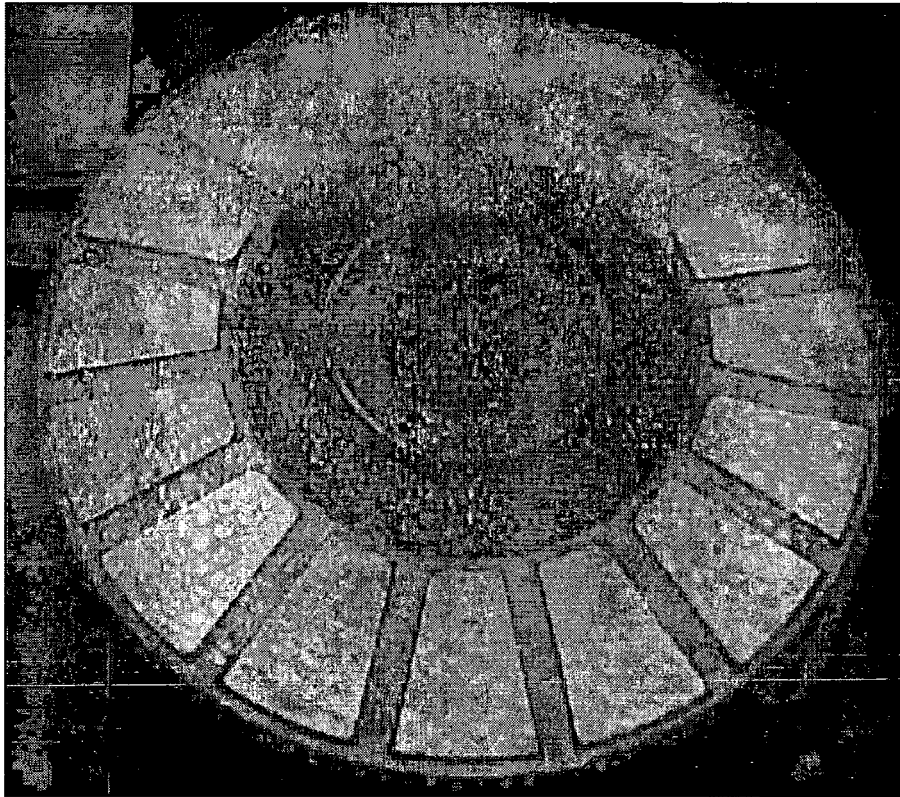


Figure 5.4 Magnets, separators and retaining ring assembled onto rotor

5.1.2 Stator Assembly

Two stator support rings that mount directly onto the iron core provide support for the stator, Figure 5.5. Twelve pins support the iron core that is sandwiched between the two support rings. A concern was that the pins are placed at the fringe of the magnetic circuit so eddy currents may be induced creating additional loss and heat. To try and minimise this problem 12 pins were selected. The advantage of this support system is that the stator can be processed independently and assembled simply.

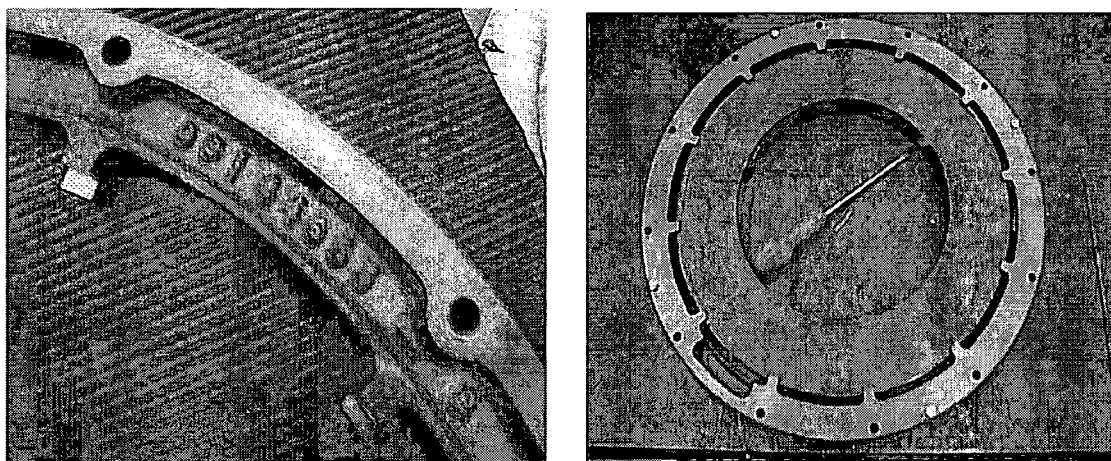


Figure 5.5 Stator retaining rings

The iron core was constructed from insulated 0.3mm thick electrical steel which is rolled into a core. This type of construction has the advantage of reducing the path of eddy currents in the core as well as having no material wastage.

A two piece nylon moulding was placed around the iron core to provide electrical insulation and winding guides, Figure 5.6. The moulding was tailored to ease the automatic winding processes allowing a toroidal winder normally associated with winding toroidal chokes to be used.

The winding consists of 48 coils or 3 coils per pole, each coil has 4 turns. The stator is wound automatically by winding every 6th coil, 8 times, finishing of the lead and then repeating the process, indexed around by one slot pitch. The winder can only wind in one direction so by winding every 6th coil each phase has 16 coils made up of 2 groups, 1 group for all north facing coils and 1 group for all south facing coils. With 12 leads out,

3 leads are connected to form the star point, 3 connections are made to join the two groups in each phase leaving 3 leads out of the machine. The machine was designed to provide approximately $250V_{RMS}$ line to neutral with all turns in series. Parallel coils were avoided due to the possibility of circulating currents on account of the low winding impedance.

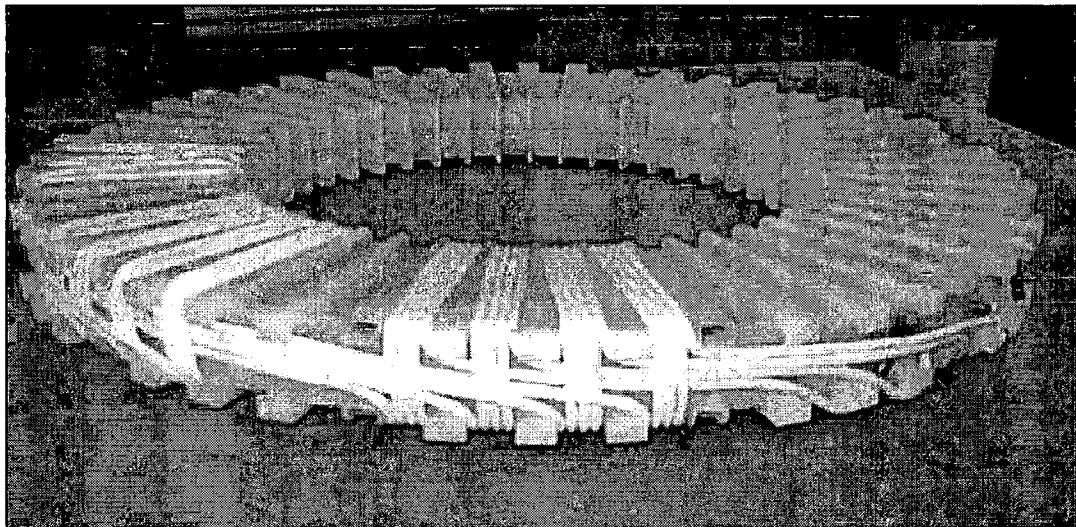


Figure 5.6 Shows winding moulding around core with stator winding

The stator conductors are multi-stranded and twisted to reduce the effect of eddy currents in the winding. This was a significant advance, for previously only solid conductors had been considered. With stranded wire the net cross sectional area of the copper may be increased without necessarily increasing the eddy loss. The wire is additionally coated with an epoxy so that when it is cured the conductors form a solid. Primary enamel still insulates the individual conductors. Using a solderable wire also helps assembly preventing the need to clean individual wires.

The conductors are additionally taped with Nomex filled with an impregnate. Taping the conductors ensures good insulation between conductors particularly on the end winding where different phases cross. Insulation is also required between the conductors and frame. The impregnate in the tape and epoxy coating of the wire allows the stator to be cured using a pulse of current. This removes the need for an epoxy bath or trickle rig to impregnate the stator. Additionally the conductors on the stator surface can be pinned back during curing to make sure air gap clearances are maintained.

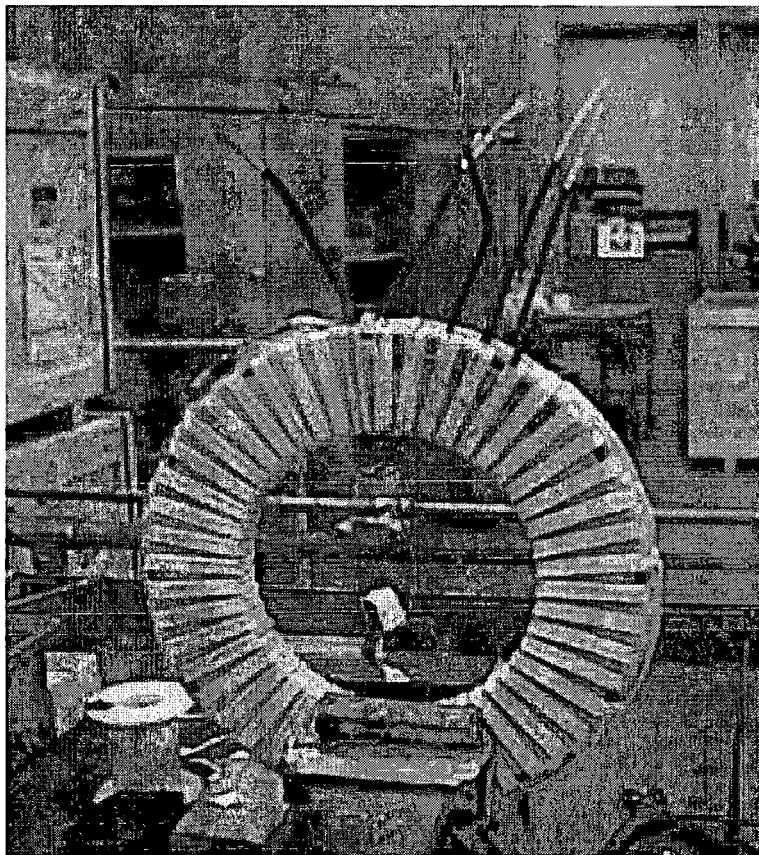


Figure 5.7 Complete stator

After winding, the stator is clamped between the stator support rings.

5.1.3 Machine Assembly

Care needs to be taken when offering the stator to the first rotor as substantial magnetic forces will exist between the core and the magnets, Figure 5.8.

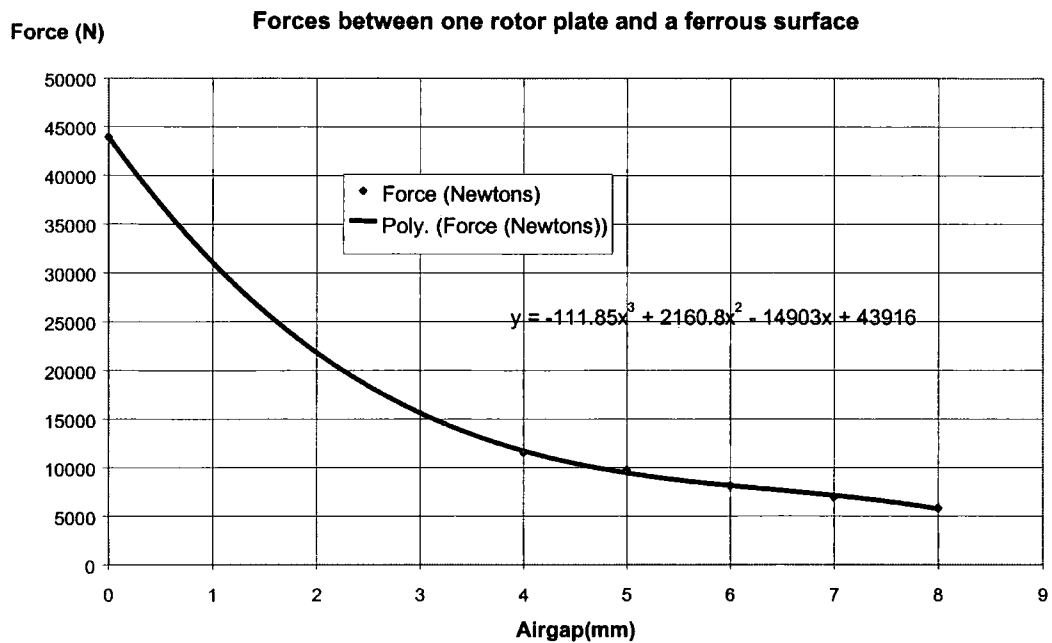


Figure 5.8 Indicates the magnetic forces when the stator is offered to the rotor

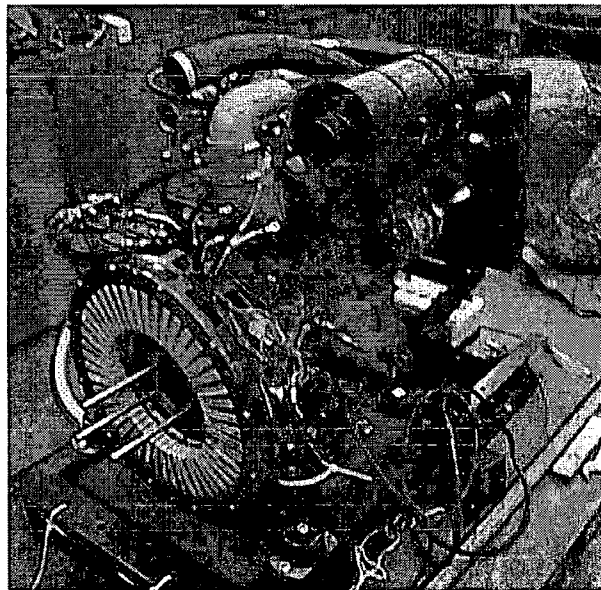


Figure 5.9 Shows the internal rotor and stator bolted onto the engine

To allow ease of assembly a special tool was constructed. The stator is bolted to the tool and a threaded bolt allows the stator to be offered to the rotor gradually. The same tool was then used to put the external rotor in position with the aid of some guiding pins, Figure 5.9 show the internal rotor and stator assembled onto the machine.

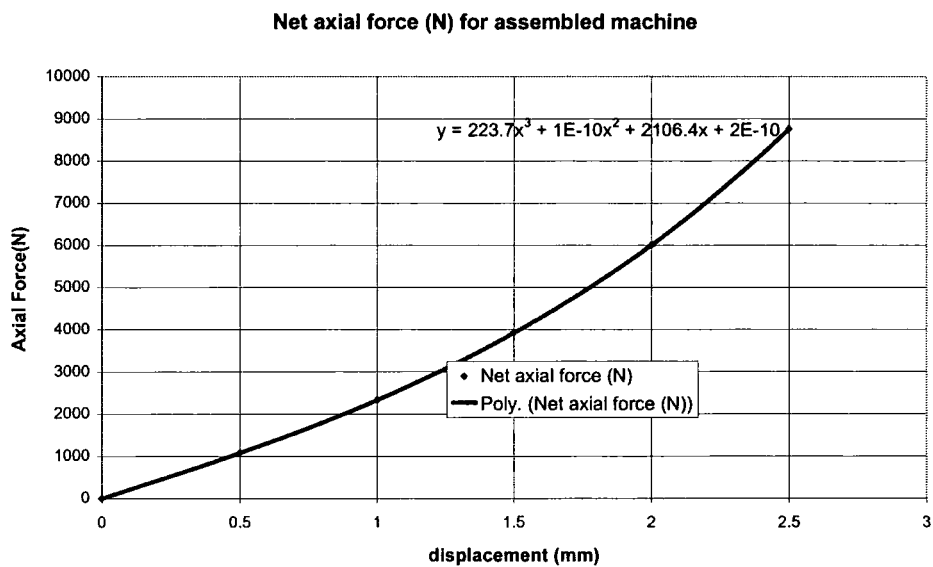


Figure 5.10 Shows how a displacement between the stator and the rotors results in an axial force

Fortunately, once the external rotor is in place a balanced condition will exist if the stator is central. Figure 5.10 indicates the axial forces if the stator is slightly off centre and is important when considering the engine bearing.

5.2 Test Results

The following section discusses the test results taken from two prototypes. For prototype 1 compromises were made during assembly. The armature windings tended to lift away from the moulding during the winding process. In addition, the lead out from each coil did not sit in the slot correctly reducing the available running clearance. Additional spacing was required between the rotor plates to ensure the rotor did not foul on the windings. The distance between the magnet faces was increased from 39mm to 46.3mm. This increased the distance from the stator iron to the magnet from 7mm to 10.65mm. Prototype 2 was constructed to the dimensions in Table 4.1, but in addition the axial ventilation holes were replaced by radial holes.

Table 5.1 documents the measured voltage for prototype 1 and compares these with FEA and lumped parameter calculations. The FEA and lumped parameter calculations are adjusted for the increased air-gap.

Prototype 1	Measured	FEA	Lumped
Voltage	206	179	185
Synchronous Inductance (uH)	-	60.1	77.1

Table 5.1 Compared measured and calculated values for prototype 1

The measured voltage is clearly much higher than calculated. It is known the air-gap reluctance and permanent magnet material heavily influences the level of flux within the machine, and the material characteristics of the stator and rotor are of secondary importance. With this in mind samples of the permanent magnet material have been characterised, Table 5.2. Comparing published data with the test samples the measured

characteristic is significantly higher than published with a degree of variability. This accounts for the discrepancy to some degree. It also highlights the reliance of any model on good material data.

	Br	Hc
Published	1.17	875
Measured sample 1	1.31	914
Measured sample 2	1.30	909
Measured sample 3	1.20	919
Average of 1,2,3	1.27	919

Table 5.2 Measured magnet characteristic

Allowing for the unexpected increase in magnet performance the results in Table 5.1 are remarkably close considering the variability of the prototypes. Slight magnet misalignments on the rotor, concentricity and parallelism of the adjacent rotor plate as well as variations in location of the stator coils, are likely to exist in the prototype but not represented in either models. The FEA results are a similar percentage less than the measured which is encouraging considering the permanent magnet variability discussed above. The lumped parameter model is a much cruder estimate with no allowance for the magnet overhang, or the reluctance of the stator and rotor.

Voltage regulation was measured to be 9%, for a load current of 68.8A compared with a calculated value of 6.9%.

Figure 5.3 compares the voltage reduction due to temperature demagnetisation of the magnets after a heat run the reduction of 1.7% is much lower than expected. Based upon this degradation of magnet performance, the magnets only seem to be exposed to a 16 K

rise for a stator temperature rise of 96K. Therefore only 17% of the winding temperature is transferred to the magnet.

3000rpm	Vrms
V l-n (Cold)	206.4
V l-n (Hot)	202.8

Table 5.3 Measured no load voltage, prototype 1

Table 5.4 provides details of the heat run to establish the operating temperature of the machine. The loaded results are at 353Hz on account of the engine not maintaining speed. N-V1 phase gave a high resistance reading and is probably due to a bad connection. The power output was 33.8kW at unity power factor. The rise by resistance was 96.1 and predictions indicate for a loading of 68.8Amps the temperature rise should be 65 °K at 3000rpm, so thermally the machine tended to perform hotter than expected but the prediction was made at a higher speed. The Resistor Temperature Devices (RTD) measurements indicate temperature rise and show localised higher temperatures particularly around the bottom of the stator in the end winding, contributing to the higher average temperature. Immediately after shut down a laser thermometer was used to measure the absolute temperature of the rotor, stator winding, and stator support ring.

Initial Amb	3.6	°C
Final Amb	49.5	°C
Initial stator resistance (cold)		
N-U1 Ohm	0.0578	Ω
N-V1 Ohm	0.0880	Ω
N-W1 Ohm	0.0548	Ω
Machine Loaded at 353Hz		
Iu rms	69.3	A
Iv rms	68.2	A
Iw rms	68.8	A
Vu rms	165	V
Vv rms	162.4	V
Vw rms	166	V
Power kW	33.8	kW
Hot machine left to stabilise for 1.5 hours		
Temperature Rise by Resistance (C)	96.1	°K
RTD temperature Rises		
End winding at bottom of stator	126.2	°K
End winding in leads at 9 o'clock position	103.8	°K
End winding at top under coil	96.5	°K
End winding at top in leads	92.2	°K
Machine temp immediately after shut down		
Back of rotor	60	°C
Stator winding	100	°C
Stator support ring	100	°C

Table 5.4 Heat run data

With the generator mounted directly onto the engine crankshaft it was difficult to measure efficiency. As an approximation the engine was driven to its fuel stop loading, the output power from the generator recorded and compared to the maximum power shown within engine manufacturers data sheets. The author accepts the subjective nature of such tests but this still provides some insight in the generator losses.

From the test the efficiency was estimated to be 91.9% compared with a predicted of 94%.

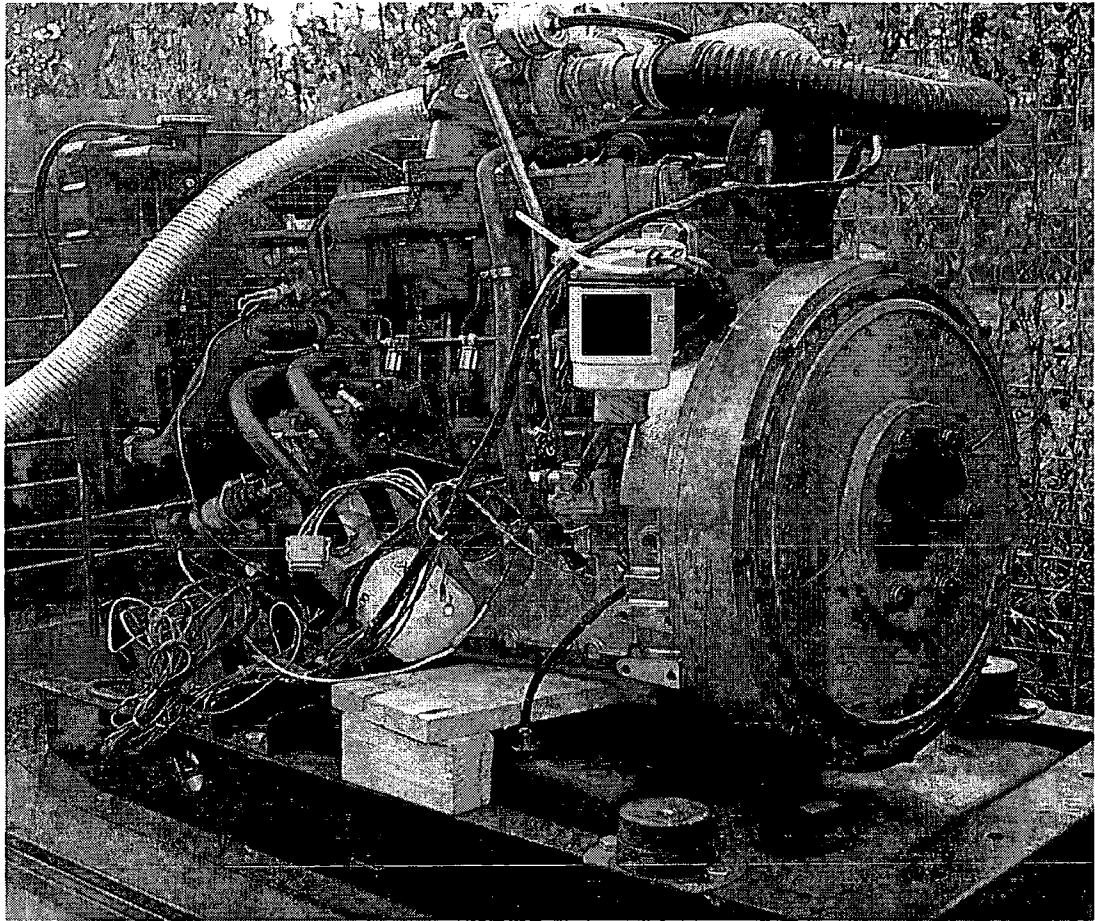


Figure 5.11 Second prototype with radial air intake and radial outlet

Using FEA the thermal performance of the axial flux machine was investigated within the company and the following observations made. Drawing the air into the machine axially or radially makes little difference to the velocity of air pulled through the machine. However axial holes mechanically weaken the rotor plates and radial holes are preferred. The feature which has most impact on the air flow is the air outlet. Ensuring the air is not radially obstructed can have considerable gains. For this reason prototype 2

was constructed, Figure 5.11. With this prototype the correct air-gap clearances were achieved.

Figure 5.12 shows the measured phase voltage for the prototype 2 machine, and Table 5.5 provides a comparison of measured and calculated harmonics and RMS voltage. The calculated voltage was based upon published data sheets for the permanent magnet material, as the magnets in the second machine were of different supply and their characteristics not measured.

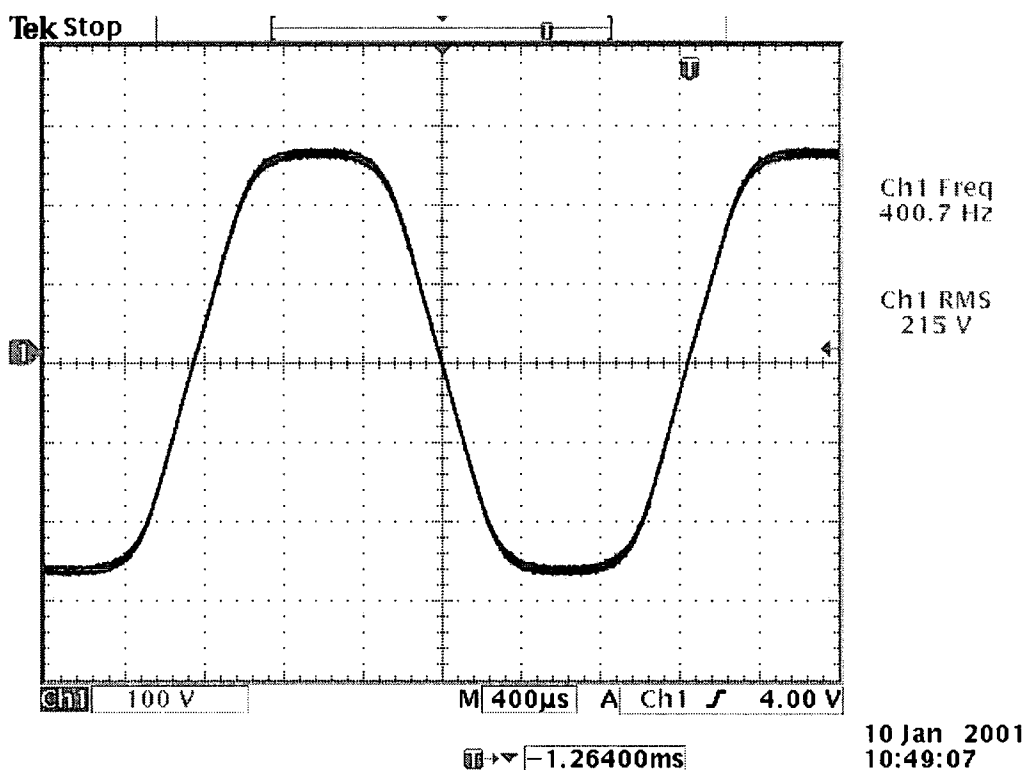


Figure 5.12 Measured phase voltage

Harmonic	Calculated	Measured
1	100%	100.00%
3	8.20%	7.70%
5	0.30%	0.10%
7	0.90%	1.20%
Volt RMS	242	236

Table 5.5 Comparison between calculated and measured harmonic and RMS voltage

The self-inductance was measured by energising one phase with 10 Arms. The voltage across the energised coil was measured and impedance calculated. Making allowance for the stator resistance the self-inductance is obtained. With such low values of inductance accuracy was a problem as the measured impedance and resistance is similar, and the inductance calculated from the difference between two large numbers.

With knowledge of equation (5.2), the mutual inductance L_{mut} can be calculated by measuring the induced voltage e on the other two phases, and recording the phase current, i .

$$e = L_{mut} \cdot \frac{di}{dt} \quad (5.2)$$

	Measured	Calculated (energy)	Calculated (Flux)
Self Inductance (uH)	108.5-103.7	75.7	73.6
Mutual Inductance (uH)	33.4-28.6	18.8	24.3

Table 5.6 Comparison between measured and calculated mutual and self inductance

Comparing the mean measured inductance in Table 5.6 with the FEA results using the energy method, the measured self inductance is 28.6% higher than calculated and the measured mutual inductance is 40% higher than calculated. While this may not appear particularly close, considering the issues associated with measuring such low values of inductance in electrical machines should be considered reasonable. However, the static tests do apply an ac field to the rotor plate which is a solid inducing eddy current. These eddy currents are not represented in the magnetostatic solution but should increase the reluctance and therefore reduce the inductance. The measurement of inductance in



electrical machines is far from simple, hence the measurement can only be taken as a rough indication. It may well be that the FEA value is closer to the actual.

In electrical machine terms these results are practically so low the magnet temperature coefficient and stator resistance will dominate the voltage regulation of the generator.

Table 5.7 provides results of the prototype 2 heat run. A test bed was constructed for the second prototype so the full rating could be tested. With the improved cooling circuit the rating of the machine could be increased to run at 60kW. This relates to a thermal heat transfer coefficient of 200 W/m²/K. Additionally the RTD measurements indicate a more thermally balanced machine than prototype 1.

Initial Ambient	27.4 °C
Final Ambient	28.8 °C
Average Phase Voltage	214.3 V
Average Phase Current	93.9 A
Power Output (kW)	60.4 kW
Rise by Resistance (C)	99.2 °K
Max RTD measurement (Rise)	128 °K
Rotor Plate	54 °C
Retaining Ring	88 °C

Table 5.7 Heat run data for prototype 2

A torque transducer was included in the test bed so that the input torque and therefore mechanical input power could be measured. Simultaneously measuring the electrical output power and mechanical input power allowed the efficiency to be calculated. Figure 5.13 plots the efficiency with respect to speed and power. While every effort was made to capture the efficiency of the generator accurately, there was some variability of results even for the same operating point. The measured efficiency appears much less than

calculated. Subsequent to these tests the retaining ring holding the stator in place was getting hot, suggesting an additional source of stray loss had not been accounted for.

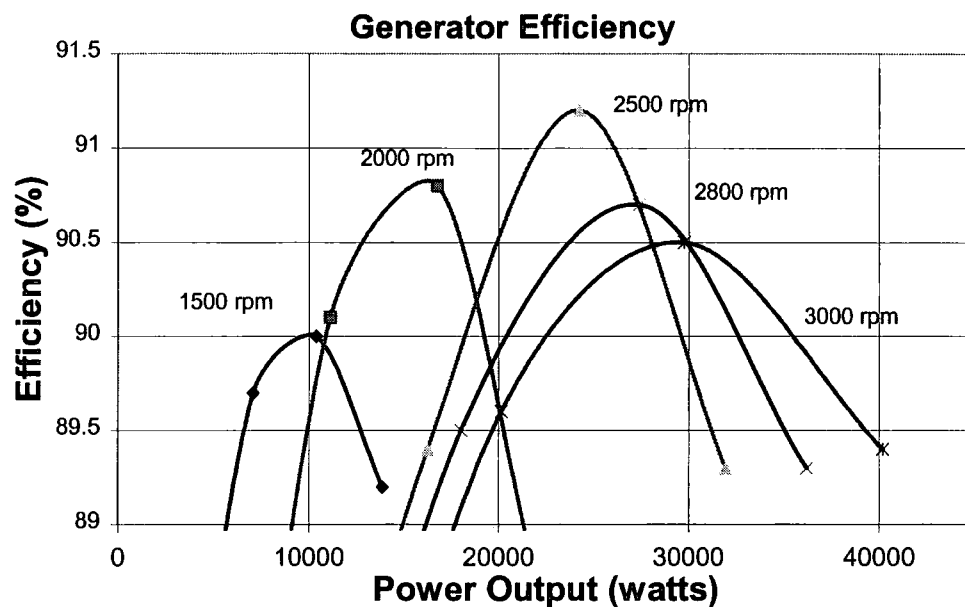


Figure 5.13 Prototype 2, efficiency curves

5.3 Discussion

The details of how a first prototype was constructed have been discussed with particular reference to improving the manufacture of a practical machine. Unfortunately the desired clearances could not be achieved on the first prototype but test results compared well to predictions when the models reflected these differences. A second prototype with the correct clearances and improved cooling, have demonstrated both the lumped parameter and the electromagnetic FEA model compares well with measurements, when the correct material characteristics are used. The improved cooling provides the bonus of increased electric loading and therefore ratings have increased beyond initial predictions.

Based upon prototype 2, a new production facility has been established and at the time of writing market seeding had begun.

5.4 Further Work

In the author's opinion a machine with higher internal impedance would be necessary to avoid warranty issues. The issue of high force on the windings during short circuit conditions is not to be underestimated and the generator has to be mechanically robust enough to withstand these forces. Thermally the machine will also be exposed to excessive temperatures. Air-gap windings increase the amount of permanent magnet material required due to the windings occupying part of the magnetic circuit. These problems may exclude the use of an air-gap winding on the grounds of reliability and cost. This suggests that future work should concentrate on increasing the internal impedance of the original TORUS concept. In summary the advantages of an airgap winding are

- Good thermal contact with cooling air and therefore high electric loading
- Ease of assembly
- High torque which is important for engine starting
- Good overload current capability, particularly important when pulling rotating energy out the system
- Output voltage virtually proportional to speed and therefore simple control
- Low inductance reduces commutation overlap
- Voltage distortion as a result of harmonic currents reduced

However an air-gap winding has the disadvantages of

- Very high short circuit currents that result in high torque – a dead short circuit on the machine is likely to result in failure unless special provisions are made.
- Low inductance increases the high rate of change of current, which may create EMF spikes. This may also result in Electromagnetic Compatibility(EMC) issues.
- The generator has no self-protection and if not carefully managed more likely to thermally burn out.
- Due to the windings occupying the magnet circuit, this increased reluctance significantly increases the mass of permanent magnet material.

An alternative arrangement might be to place the conductors into slots. Slotting the stator structure has the advantages of

- Good utilisation of permanent magnet material
- Can be self protecting by limiting short circuit current
- Under fault or overload conditions the thermal stress levels are likely to be lower
- Conductors are fully supported and located
- Winding in slots can protect the winding from damage

But the disadvantages of a slotted winding are:

- On load rejection voltage will rise and may effect the inverter output. A crowbar may be needed to ensue over voltages cannot occur.
- Voltage varies with both load current and speed making the control more sophisticated.

- Commutation overlap increases, reducing power density
- Closer magnetic coupling between stator and rotor may increase eddy current losses in the rotor.
- The effects of armature reaction will increase high frequency losses in the stator teeth.
- Increased inductance will slow down the rate of change of current and therefore impede the ability to respond to transient load changes.
- The machine may not naturally have a high overload capability, and the output is likely to be limited by the synchronous inductance rather than thermal considerations.
- Cooling of the conductors will be compromised as they are in slots
- Voltage distortion as a result of distorted current may complicate control issues
- Tooth ripple harmonics will increase losses
- More difficult to manufacture

Another solution to increasing the machines internal impedance while reducing the mass of permanent magnet material in the rotor might be to replace every other magnet with a ferrous pole. In doing so the effective air-gap of the magnetic circuit is reduced. While this reduces the peak torque from the machine, if the continuous rating is a thermal limit as it is with previously discussed design, the mass of permanent magnet can be reduced making a more economic design.

The design of an electrical machine for variable speed operation is a complex interaction between the machine and power electronics. Further work should examine what machine characteristics are desirable when feeding a power converter.

Chapter

6.

Axial Flux Machine Optimisation

The aim of this chapter is to demonstrate a method for understanding how the magnetic material content affects the output power for an axial flux generator of given diameter. The analysis addresses thermal aspects whilst also providing an accurate electromagnetic model of the problem.

Finite element analysis (FEA) provides very good accuracy in terms of the electromagnetic design of an axial flux machine. Unfortunately FEA is expensive in terms of processing time and rarely used as a first cut design tool. Optimisation routines can be written using FEA but processing time may be measured in weeks dependent upon the complexity of the problem. Furthermore, the volume and format of results may not be readily useable in an optimisation routine focusing on different criteria.

The object of this exercise was to optimise the design of an axial flux generator with certain parameters already fixed. The outer diameter was fixed to 400mm to ensure the generator fitted within a given housing. Sixteen poles are chosen to provide 400Hz at 3000rpm. Increasing the pole number further would increase magnet leakage as well as increase iron and conductor eddy loss. Decreasing the number of poles increases the size of the ferrous parts that carry the flux, resulting in a larger machine.

With respect to increasing the output power to magnet mass ratio, forming a magnet overhang has little benefit compared with increasing the magnet thickness. The justification for this is more magnet mass is required in the overhang, and the flux path length from the overhang is longer compared to the normal path length between the magnet face and stator iron face. Simply increasing the magnet thickness to increase flux and reduce armature reaction is likely to return more power for a given mass of material. This general statement is to be balanced with not increasing magnet thickness too much, as increasing the thickness to increase the magnetic loading above say, two thirds of the remanence flux will waste magnet material. For these reasons the magnet overhang was ignored in the analysis.

6.1 Setting Up the Model

The output power of an axial flux machine may be theoretically obtained using the simple equivalent circuit in Figure 6.1, comprising of an induced EMF e , synchronous inductance L_{synch} , stator resistance R_s , and the maximum output current thermally acceptable, I . With the diameter and pole number fixed all the parameters within the equivalent circuit depend predominately upon a maximum of four variables, namely stator inner/outer diameter ratio K , winding thickness L_w , magnet thickness L_m , and magnet pole arc to pitch ratio τ .

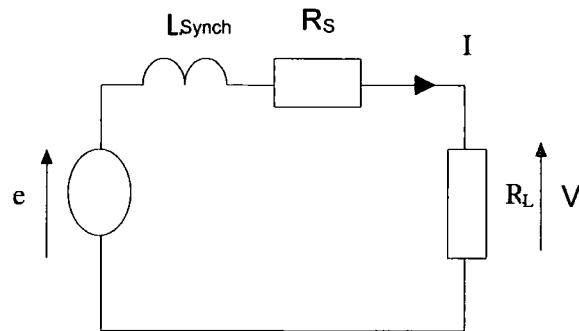


Figure 6.1 A simple equivalent circuit

With suitable assumptions, the stator resistance and output current are readily available from the geometry of the problem. However the calculation of induced EMF and synchronous reactance is complex and requires 3 dimensional modelling.

To investigate all the combinations of machine dimensions would take thousands of simulations dependent upon the resolution of results. An alternative approach is to fit a coarse grid to the problem by taking at least 3 points for a given variable and fitting a polynomial function. The number of points taken and the order of the polynomial will depend upon the problem but experiments can be performed to balance computed errors with computational complexity. This method reduces simulation time, dictates a rigorous calculation procedure, maintains good accuracy and the model becomes continuous.

Table 1 Variable's describing the four main functions in equivalent circuit

Function	Variables			
	Inner/Outer Diameter	Winding Thickness	Magnet Thickness	Pole Arc/ Pole Pitch
Induced EMF	X	X	X	X
Synchronous reactance	X	X	X	
Stator Resistance	X	X		
Maximum Output current	X	X		

Table 6.1 Highlights which variables describe the four functions in the equivalent circuit

Table 6.1 illustrates how the calculated induced EMF, synchronous reactance, stator resistance and maximum output current all vary with respect to geometric conditions.

The equivalent circuit was further normalised with 1 turn per pole per phase. This simplified the analysis by removing the complexity of multiple stator turns. The power available from the equivalent circuit is transparent to such detail.

6.2 Model Boundaries

Table 6.2 shows the design boundaries of the model where the outer diameter was fixed at 400 mm and pole number at 16.

Inner/Outer Diameter, K	0.5-0.85
Pole arc/ Pole pitch, τ	0.5-1.0
Winding Thickness, L_w , mm	1-7.5
Magnet Thickness, L_m , mm	2-10

Table 6.2 List of model design boundaries

6.3 The FEA Model

Chapter 4 explained in detail how to calculate the EMF and synchronous reactance for an axial flux machine using 3 dimensional Finite Element techniques. Figure 6.2 illustrates in 2 dimensions the discretisation of the model. Table 6.3 provides more model details.

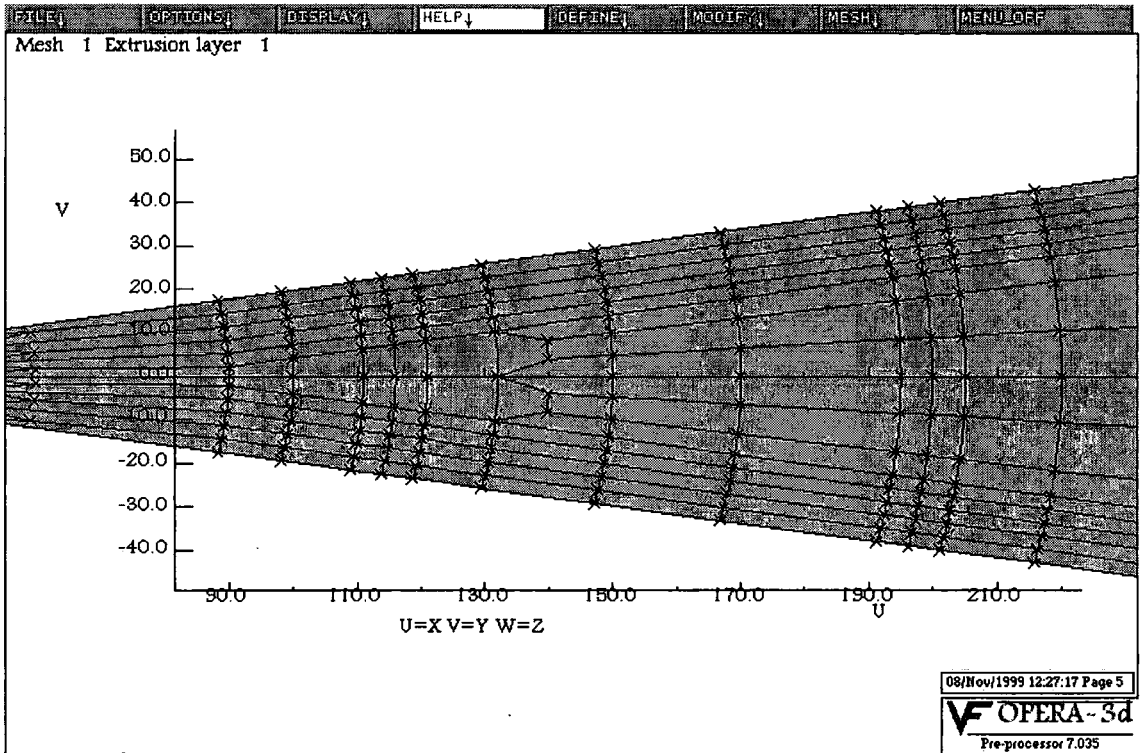


Figure 6.2 Two dimensional discretisation of mesh

Stator Outer Diameter	400	mm
Stator Inner Diameter	200,232,264,300,340	mm
Stator Thickness	30	mm
Rotor Thickness	15	mm
Insulation Thickness between iron and conductor	1	mm
Running Clearance	2.5	mm

Table 6.3 Model details

The permanent magnetic material used was NdFeB with a Remanence Flux Density B_r of 1.12 and a coercivity of 781 kA/m. A thicker stator core and rotor was chosen to ensure there was no saturation. The ferrous material on the stator and rotor could then be described with a relative permeability of 30 000. This was justified, as the flux paths in the iron are well defined, as there are no stator slots and the air-gap dominates the magnetic circuit.

6.4 The EMF Polynomial

Tests were performed to determine which type of polynomial would provide the best-fit solution. Taking just three variables, pole arc to pitch ratio τ , winding thickness L_w , and magnet thickness L_m , a 4th order polynomial was required. For this reason a polynomial of the form shown in equation (6.1) was used.

$$\begin{aligned}
 E_{\text{model}} = & a_1 + a_2 \cdot \tau + a_3 \cdot \tau^2 + a_4 \cdot L_w + a_5 \cdot \tau \cdot L_w + a_6 \cdot \tau^2 \cdot L_w + a_7 \cdot L_w^2 + a_8 \cdot \tau \cdot L_w^2 + a_9 \cdot \tau^2 \cdot L_w^2 + a_{10} \cdot L_m \\
 & + a_{11} \cdot \tau \cdot L_m + a_{12} \cdot \tau^2 \cdot L_m + a_{13} \cdot L_w \cdot L_m + a_{14} \cdot \tau \cdot L_w \cdot L_m + a_{15} \cdot \tau^2 \cdot L_w \cdot L_m + a_{16} \cdot L_w^2 \cdot L_m + a_{17} \cdot \tau \cdot L_w^2 \cdot L_m \\
 & + a_{18} \cdot \tau^2 \cdot L_w^2 \cdot L_m + a_{19} \cdot L_m^2 + a_{20} \cdot \tau \cdot L_m^2 + a_{21} \cdot \tau^2 \cdot L_m^2 + a_{22} \cdot L_w \cdot L_m^2 + a_{23} \cdot \tau \cdot L_w \cdot L_m^2 + a_{24} \cdot \tau^2 \cdot L_w \cdot L_m^2 \\
 & + a_{25} \cdot L_w^2 \cdot L_m^2 + a_{26} \cdot \tau \cdot L_w^2 \cdot L_m^2 + a_{27} \cdot \tau^2 \cdot L_w^2 \cdot L_m^2
 \end{aligned} \tag{6.1}$$

Where a_n = polynomial coefficients

The solution of 27 coefficients was necessary to complete the polynomial. This ordinarily requires the solution and inversion of a 27x27 matrix using the least squares method. Within Microsoft Excel a solver exists, this provides solutions in minutes. The

solver uses iterative techniques and experimentation is required to obtain the closest result. Table A.1 in Appendix A, compares the FEA data used to describe the polynomial expression and the fit is shown to be within 0.08% to -0.12%.

Expanding the polynomial to cover 4 variables would have required a polynomial to contain 81 coefficients, and 81 data points would be needed to describe the function. This would add a high degree of complexity to the problem but experiments showed a normalised polynomial could adequately describe the effect of the variable K , see Table A.2 in Appendix A. By normalised it is meant all the data is referenced to the condition when K is 0.66, then keeping L_m, L_{gap}, τ , constant and varying K the per unit values for different K values are obtained. Equation (6.2), describes the K polynomial which when multiplied by Equation(6.1), provides a model of the induced EMF E_{model} .

$$K_{polynomial} = -1.8423.K^2 + 0.2946.K + 1.6081 \quad (6.2)$$

This allowed the 4 variable function to be described by a total of only 45 data points.

Table A.3 in Appendix A compares the E_{model} polynomial with a number of random pre-computed FEA solutions. The accuracy of the model is within 2.96, -1.29%. By adopting this approach it cannot be guaranteed that the polynomial fits between the data reference points and will be subject to the polynomial order. It is recommended that trends be observed by manually varying parameters rather than expanding the number of FEA solutions.

6.5 The synchronous reactance polynomial

The synchronous reactance was calculated for five different values of K , 0.5, 0.58, 0.66, 0.75, 0.85 and plotted against the gross air-gap $L_{gross\ gap}$. The gross air-gap thickness is basically the distance from stator iron face to rotor iron face and includes magnet thickness, winding thickness, insulation thickness and running clearance. Figure 6.3 shows the relationship between inductance, K and various gross air-gaps.

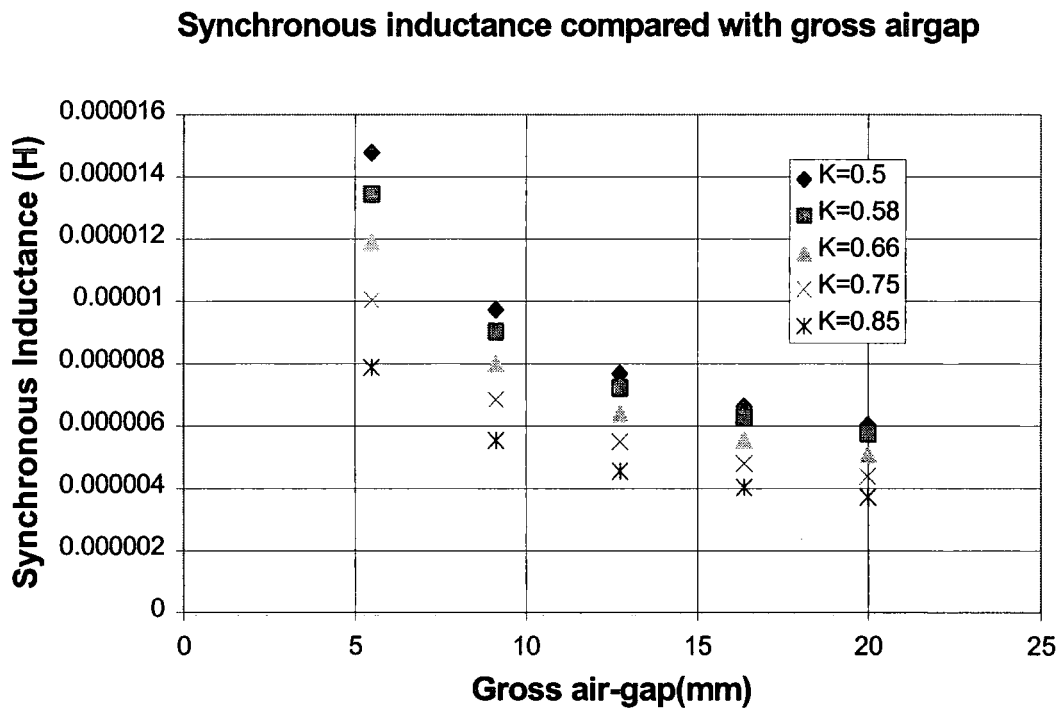


Figure 6.3 synchronous inductance compared with gross air-gap

The variation in synchronous inductance is dependent on two variables, K and $L_{gross\ gap}$. By fixing one of the parameters and varying the other, polynomial expressions could be derived. Consider Figure 6.4, all values for different gross air-gaps and K values are

referenced to a gross gap of 12.75mm. A curve is fitted to represent the mean of the data points and a polynomial calculated equation (6.3). This exercise was repeated in Figure 6.5 but a K value of 0.66 is taken as the reference and air-gap varied to obtain the polynomial, equation (6.4).

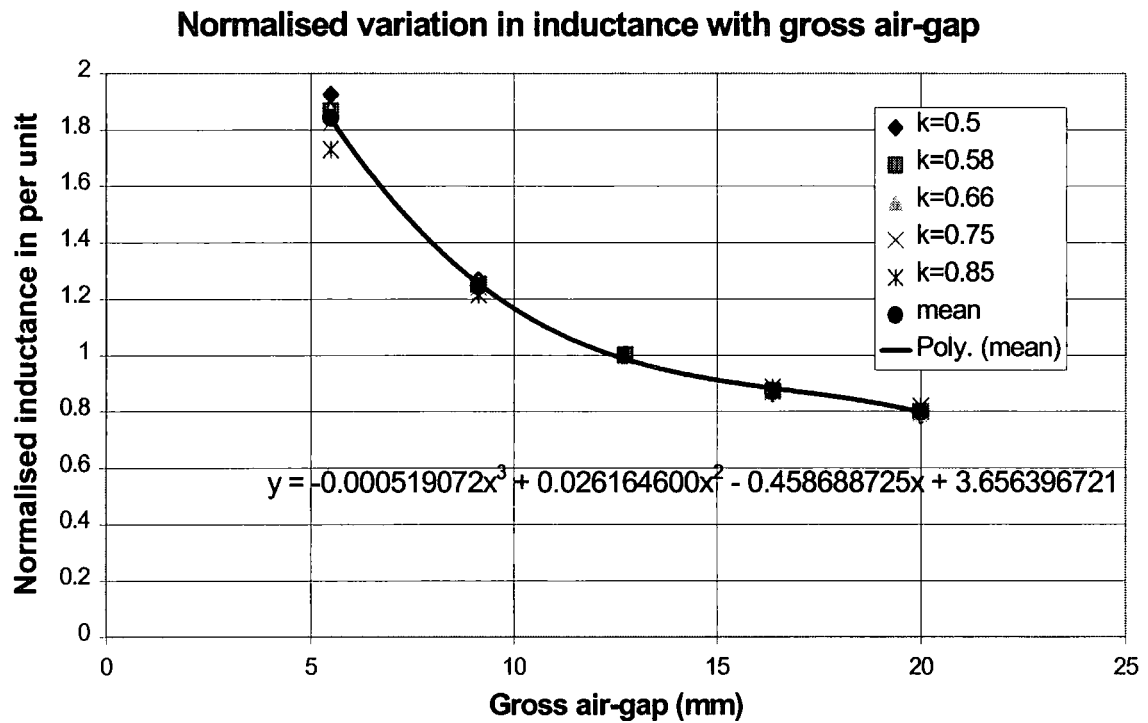


Figure 6.4 Variation in inductance for various K values for a given air-gap

$$L_{normalised, L_{gross\ gap} = 12.75mm}$$

$$= -0.000519072L_{gross\ gap}^3 + 0.0261646L_{gross\ gap}^2 - 0.458688725L_{gross\ gap} + 3.656396721 \quad (6.3)$$

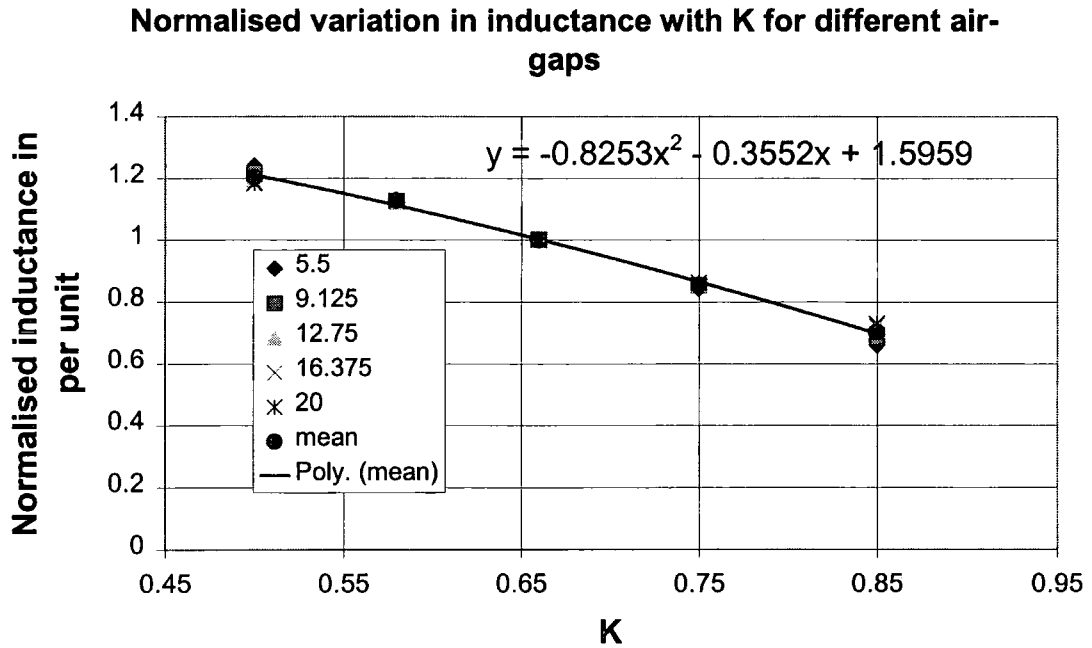


Figure 6.5 Variation in inductance for various air-gaps for a given K value

$$L_{normalisedK=0.66} = -0.8253K^2 - 0.3552K + 1.5959 \quad (6.4)$$

Both polynomials are referenced to an inductance when the gross air-gap is 12.75mm and K is 0.66, which relates to an inductance of $6.41E-6$ H. The synchronous inductance can be calculated using the product of Equation (6.3), (6.4) and $6.41E-6$ H.

Table A.4 in appendix A, compares the polynomial model with the pre-computed FEA source data and indicates an error between -4.6% and 4.2% exists with the model.

Considering for this type of machine thermal aspects tend to limit the available output power rather than the synchronous inductance this error was accepted.

6.6 The Stator Resistance Model

The resistance for the various K values is referenced to a known design described in Table 4.1 to allow for fill factors. Ignoring the winding thickness L_w in the axial plane, there are two mechanisms that dictate the resistance for various values of K . The first is length which assuming the end winding length is constant can be obtained by estimating the length of mean turn. Including a constant end turn length from the reference machine of 0.264 per unit, the length along the stator face will be proportional to the outer diameter minus the inner diameter or $(1-K)$. The second mechanism that varies winding width depends on the stator inner diameter and is directly proportional to K . Table 6.4 indicates how these parameters vary with K to calculate the per unit variation in resistance.

k	Per unit length	Per unit Width	Per unit Resistance
0.850	0.654	1.349	0.485
0.750	0.811	1.190	0.682
0.660	0.953	1.047	0.909
0.630	1.000	1.000	1.000
0.580	1.079	0.920	1.173
0.500	1.205	0.788	1.529

Table 6.4 Per unit variation of resistance

The phase resistance for the reference machine was $5.07e-3 \Omega$. Expression (6.5) provides a polynomial that describes the phase resistance R_{ph} .

$$R_{ph} = -0.02380875364K^2 - 0.0470683164K + 0.025295576 \quad (6.5)$$

Expression (6.5) is applicable to the reference machine that has a winding thickness of 2.5 mm, and should be multiplied by $2.5/L_w$ to make it dependent on winding thickness.

6.7 Maximum Output Current Model

This is referenced to a previous machine with a K value of 0.63 where the power which can be dissipated over the air-gap area is assumed constant. With respect to the stator winding, the winding width on the inner diameter is the same as the outer diameter.

Assuming the power dissipated per unit area is constant, the acceptable losses that can be generated without exceeding the temperature rise of the reference machine are as follows.

$$\text{Surface Area} \propto \text{Acceptable Loss} \propto \frac{K(1-K)}{0.63(1-0.63)} \quad (6.6)$$

Assuming the acceptable loss within the reference machine depends on the Joule loss.

$$I^2.R \propto \frac{K(1-K)}{0.63(1-0.63)} \quad (6.7)$$

The phase resistance varies with K and assuming the heat transfer only occurs in the gap the end winding can be ignored. The resistance becomes proportional to the following.

$$\text{Resistance} \propto \text{length} \propto \frac{(1-K)}{(1-0.63)} \quad (6.8)$$

Due to the variation in inner diameter and therefore circumference, the stator width will also vary directly with K .

$$\text{Resistance} \propto \frac{1}{\text{area}} \propto \frac{0.63}{K} \quad (6.9)$$

Referring back to equation(6.7) and considering equation(6.8) and (6.9), the maximum current that may be drawn from the machine for the reference temperature rise is given by

$$I^2 \propto \frac{K(1-K)}{0.63(1-0.63)} \frac{(1-0.63)}{(1-K)} \frac{K}{0.63} \propto \frac{K^2}{0.63^2} \quad (6.10)$$

The total current loading is 302.6AT for the reference design, so the maximum current that may be drawn from the machine can be calculated using equation (6.11). This equation is consistent with a larger K increasing the electric loading.

$$I = 302.6 \frac{K}{0.63} \quad (6.11)$$

Equation (6.11) is true for a winding thickness of 2.5 mm but must be modified to equation (6.12) to account for winding thickness.

$$I = 302.6 \frac{K}{0.63} \sqrt{\frac{L_w}{2.5}} \quad (6.12)$$

A further correction was applied to equation(6.12) as some degradation of thermal performance with respect to increased winding thickness will occur. This parameter will depend upon the detail of the design making the parameter subjective. An approximate

allowance can be made by examining the simple thermal network used to calculate the thermal performance of the reference design, shown in Figure A.1, Appendix A. The reference machine included 3 wire layers of 0.75 mm, providing a total winding thickness of 2.5 mm. The estimated temperature rise for different layers and winding thickness can be calculated, Table 6.5, and referred to the reference machine to create a polynomial correction factor, equation(6.13). Equation(6.12) was then multiplied by equation(6.13) to obtain the maximum current that can be drawn from the machine.

L_w	Layers	Temp Rise	Per Unit Power loss	Per Unit Correction Factor
0.83	1	100.6	1.147	1.071
2.5	3	115.4	1.000	1.000
5	6	137.5	0.839	0.916
7.5	9	159.7	0.722	0.850

Table 6.5 Per unit current allowance for insulation build up on the windings

$$\text{Correction Factor} = 0.0017014564L_w^2 - 0.0471863502L_w + 1.1084775896 \quad (6.13)$$

6.8 Results

A visual Basic program was written to examine the equivalent circuit and return the maximum power per weight of magnet, by iteratively stepping through all the different machine parameters. This optimum occurred when the pole arc to pitch ratio τ was 0.5, magnet thickness L_m was 3.5 mm, winding thickness L_w was 2.25 mm, and K was 0.85. Logically there are very good arguments for this to be the case and these are discussed

later. Surprisingly the level of power at which this occurs is only 12.4kW for a 400mm outer diameter. Another way of looking at this is the bigger the diameter at which the magnet is placed the larger the velocity the magnet travels and therefore the higher the power density. This is important because the larger outer diameter has a definite electromagnetic advantage. Nevertheless, this parameter taken to extremes soon becomes a problem. For example, due to the height of the crankshaft on an engine there are clearance issues, stored energy within the machine becomes difficult to control, acceleration of such a machine becomes difficult particularly as limited engine torque is available, and retaining accurate clearances at large diameters becomes unrealistic. If the magnet weight is to be minimised the largest practical diameter should be chosen.

The τ value of 0.5 is the lower boundary limit set in the equivalent circuit but logically higher values of τ will result in more leakage between magnet poles. In addition, the gross air-gap between the stator and rotor will be relatively large for a given magnet mass and the synchronous reactance will be reduced. There is a limit to how far the parameter τ can be reduced because if more power is required it needs to increase. Increasing the magnet thickness indefinitely becomes counter productive, with increased magnet mass not returning an associated increase in flux.

The combination of L_m equal to 3.5 mm and L_w equal to 2.25 mm is of interest considering the clearance and insulation thickness amounts to 3.5mm the magnet thickness is only 37.8% of the gross air-gap. This compares to the traditional idea that the magnet thickness should be around 50% with a relatively high τ ratio. Therefore,

for some designs it is not a simple case of operating the magnets at their maximum energy density.

The K value of 0.85 is on the upper boundary limit for the equivalent circuit, which suggests increasing the K value will further improve the maximum power per magnet weight ratio. This may be the case however increasing the K value further will result in a very low output power compared to the outer diameter and therefore would not represent a practical machine. Furthermore as the K value approaches 1, the end region of the stator will start to reduce the available output and this effect is not well represented in the model.

To appreciate why increasing the K value for such a machine improves the power to magnet weight ratio a number of parameters need to be considered. In terms of the stator resistance, increasing K reduces the length of mean turn and the conductor area increases, which reduces resistance. This lower resistance allows more current to be drawn from the machine. With a high K value less magnet material sits adjacent to a magnet of opposite polarity resulting in less leakage. With a reduction in surface area the synchronous inductance reduces. These parameters tend to outweigh the influence a high K value has on reducing surface area over which the losses can be dissipated, and the end winding regions become more significant. A high K value also reduces the length of active conductor and induced EMF, but on balance the magnet weight is still reduced.

A further program was written to plot how the output power varies with increased magnetic material. Here the magnet weight was increased from 1kg to 14kg in steps of 0.5kg and the maximum power for the given weight computed. Figure 6.6 highlights how increasing the power for a given outer diameter compromises the utilisation of magnet material, and if increased too far the power tends to reduce as a result of limits set in the model. Table 6.6 shows the parameter combinations necessary to achieve maximum power for the given magnet weight. Clearly this type of optimisation is complex as all the 4 variables change. There are however some trends to be observed in this data. The K value continually decreases and τ increases for increased power. The magnet thickness to gross air-gap tends to stabilise at around 58% as power increases. As power in Table 6.6 increases the τ ratio tends to increase rather than the K value reduce. This suggests leakage between poles for a higher τ is a more effective use of permanent magnet material than reducing K .

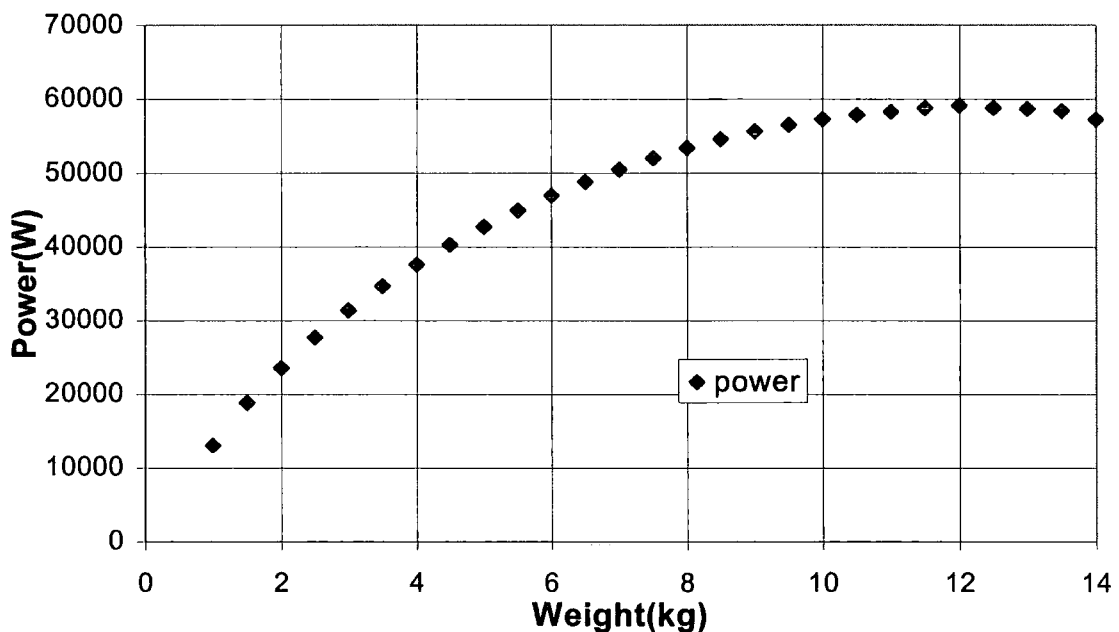


Figure 6.6 Variation in power with magnet weight for a 400mm outer diameter machine

Reassuringly looking through Table 6.6 the maximum power condition occurs between a K value of 0.58 and 0.63 as expected. It should be remembered the K value of $1/\sqrt{3}$ assumes a constant flux density over the stator surface which is not the case in reality.

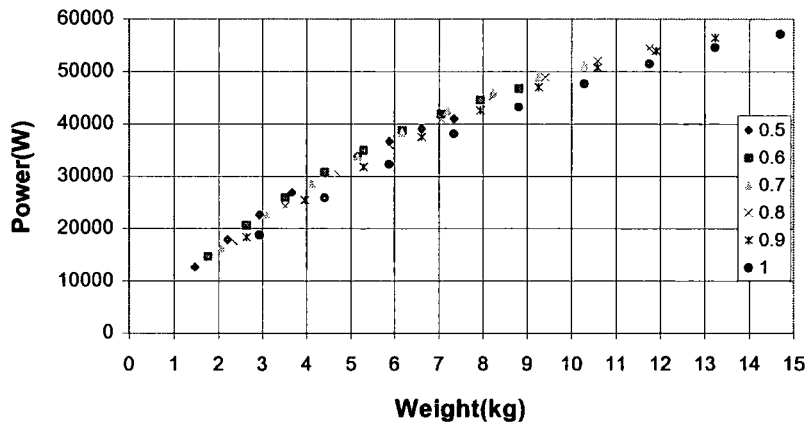
weight	power	τ	L_m	L_w	K	% of magnet in gross airgap
1	13049.31	0.5	3.676006	2.25	0.85	39
1.5	18824.46	0.55	5.012736	2.75	0.85	45
2	23575.94	0.575	5.70258	3	0.83	47
2.5	27707.11	0.6	6.487152	3.25	0.82	49
3	31387.75	0.625	6.800612	3.25	0.8	50
3.5	34662.78	0.65	7.013281	3.25	0.78	51
4	37618.35	0.65	7.710007	3.5	0.77	52
4.5	40308.27	0.675	8.049966	3.5	0.76	53
5	42744.13	0.7	8.327279	3.5	0.75	54
5.5	44951.25	0.725	8.552859	3.5	0.74	55
6	46967.64	0.725	9.036757	3.75	0.73	55
6.5	48814.25	0.75	9.178566	3.75	0.72	56
7	50485.45	0.75	9.599573	3.75	0.71	57
7.5	52019.64	0.775	9.67829	3.75	0.7	57
8	53386.02	0.8	9.735558	3.75	0.69	57
8.5	54587.83	0.825	9.774959	3.75	0.68	57
9	55627.67	0.85	9.799466	3.75	0.67	57
9.5	56524.47	0.85	9.871017	3.75	0.65	58
10	57272.14	0.875	9.873129	3.75	0.64	58
10.5	57865.26	0.9	9.866581	3.75	0.63	58
11	58306.05	0.925	9.852843	3.75	0.62	58
11.5	58779.06	0.975	9.975005	3.75	0.63	58
12	59120.05	0.975	9.997591	3.75	0.61	58
12.5	58813.47	0.975	9.853902	3.75	0.58	58
13	58698.74	0.975	9.907651	3.75	0.56	58
13.5	58400.31	0.975	9.969189	3.75	0.54	58
14	57227.91	0.975	9.898277	3.75	0.51	58

Table 6.6 Different combinations of design parameters for different magnet weights

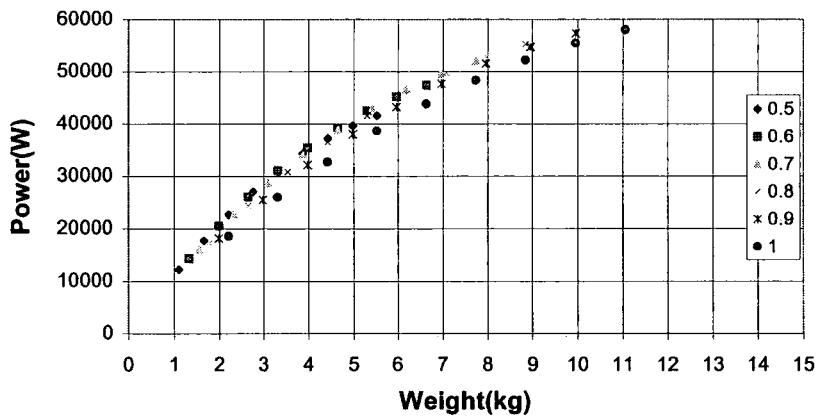
A final program plotted power against magnet weight for different K and τ values.

Consider the case in Figure 6.7 when the K value is 0.66. For low levels of magnet mass the smaller pole arcs are beneficial, but as ratings increase they return less power for a given magnet mass. Above 50kW the 0.8 pole arc seems a reasonable value as respectable power density is achieved but flux is not wasted in excessive interpolar leakage. Inspecting the case when K is 0.82 the power density is relatively poor with a maximum power of just over 40kW possible. For example when the magnet mass is 5kg a K value of 0.66 and 0.82 returns over 40kW but only about 33kW for the 0.5 case, so for a K value of 0.5 compromises are made.

Comparison of pole arc to magnet weight and maximum power for K=0.5



Comparison of pole arc to magnet weight and maximum power for K=0.66



Comparison of pole arc to magnet weight and maximum power for K=0.82

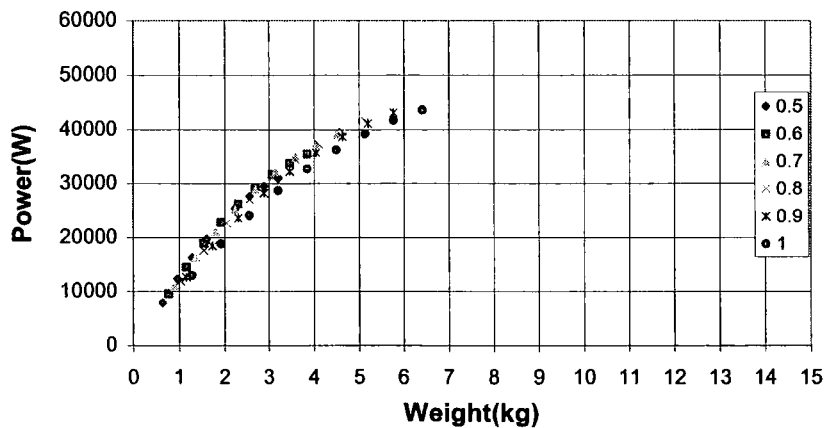


Figure 6.7 Relationship between τ for different K values

With reference to Figure 6.8 where τ is fixed at 0.8, if the K value is low the return in power for a given magnet mass is reduced. This suggests K should be kept as high as possible. Comparing $K=0.5$ and $K=0.66$ a large reduction in power for a given mass of magnet is present and low values of K should be avoided.

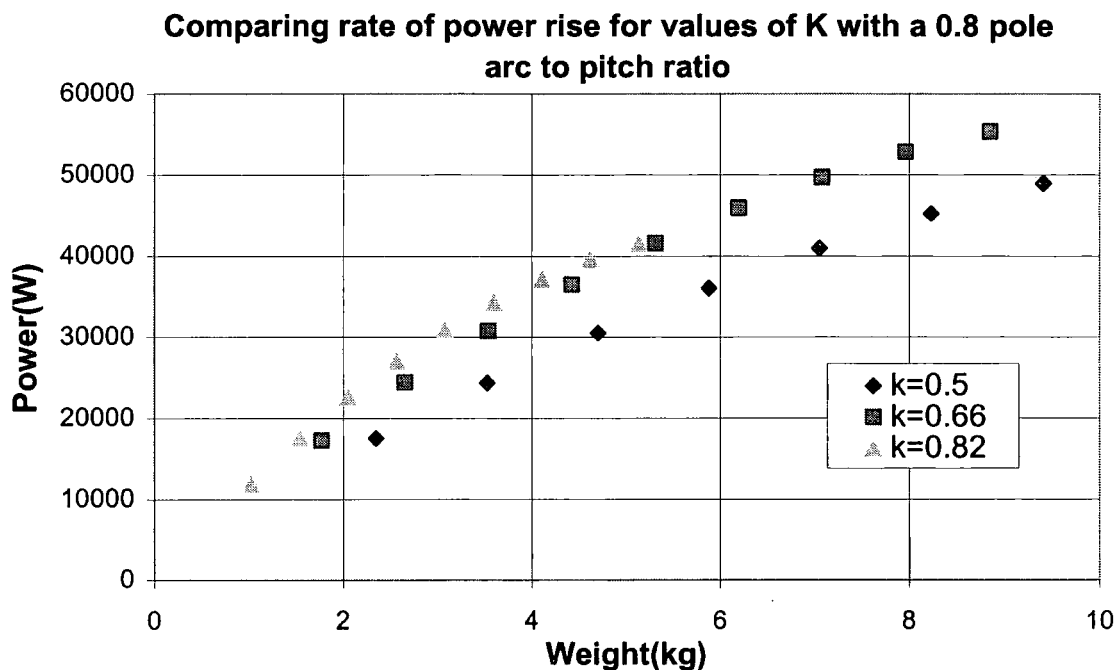


Figure 6.8 Compares power with magnet weight for different K values when $\tau=0.8$

6.9 Discussion

A convenient method for machine optimisation has been demonstrated which retains accuracy while reducing processing time. Using widely available tools such as the solver and curve fitting functions in Excel has allowed a non-linear system to be modelled as a continuous function. Even greater gains may be made if the data is looked at objectively and where possible normalised to a simple polynomial expression.

The axial flux machine has been examined and proved very complex. Simple rules of thumb are not readily available and analysis has shown many interesting features that would have otherwise not been realised. From a designer's point of view other limiting factors such as designing for a given voltage, power or having an outer diameter restriction will at least help to reduce the number of design variables for such a complex problem.

From this analysis when the axial flux machine is viewed with respect to minimising magnet mass the following design rules should be applied.

- The largest practical diameter should be sought
- A pole arc to pole pitch ratio of $\tau = 0.8$ is a reasoned compromise between power density and inter-polar leakage
- The K value should be as high as possible accepting the power density will be compromised.

The justification for this is

- Largest diameter provides increased velocity
- Increasing τ above 0.8 increases leakage, but a low τ reduces power density
- A high K value
 - Reduces inter-pole leakage

- Increases the number of conductors possible on the inner diameter, increasing the electric loading
- Presents lower resistance to the passage of air, improving thermal conductivity
- Presents a lower surface area to the armature reaction, reducing synchronous inductance

It is important to understand that to minimise the magnet mass, the material and overall power density of the generator is compromised.

The Haydock Brown Machine Design

The 'Haydock Brown machine' combines permanent magnet and wound coil excitation to provide a single-stage brushless alternator. It provides an efficient and compact solution for small and medium scale engine driven generator requirements. The simple construction conceals a rather unusual magnetic circuit that displays complex interactions between excitation sources in the presence of saturation and leakage fields. The following section describes the machines operation. A design procedure based on a lumped-parameter magnetic equivalent circuit is developed and designs have been evaluated with the aid of 3 dimensional finite element studies.

7.1 Literature Review

The 'Haydock Brown machine' (HB Machine) is a new invention and therefore not previously researched. However the concept has some similarity with the 'Double-disc alternator with AC-side excitation' researched by Evans and Eastham[70,71,72,73]. The stator topology is similar to the TORUS but excited by a wound coil fixed to the stator which forces flux through the shaft. Two paddles form the rotor either side of the stator but juxtaposed by one pole pitch. This concept has been extended to include permanent magnet excitation on the rotor paddles [74,75].

The HB machine also has similarities with some of the concepts discussed in US patent 'Direct control of air gap flux in permanent magnet machines' [76], here methods of effecting the field within permanent magnet machines are explored.

7.2 Introduction

The HB machine [7] is named after the author and co-inventor Professor L. Haydock. The name is also appropriate considering the significant impact the material B-H characteristic has on the operation of the machine.

For most ac generator applications, the electrical machine is required to be brushless, compact, efficient and able to regulate its output voltage under a wide range of load conditions. Although the introduction of new permanent magnet materials has inspired the development of efficient, compact, brushless synchronous machines, the absence of any means of excitation control, bars their use in mainstream generator applications. Power electronic systems can be designed to give the required control but these are at present too costly for most applications

The HB machine attempts to exploit permanent magnets in combination with a field winding fixed to the stator to provide the desired features in a single machine. It is truly integrated with active material occupying most of available volume providing good material utilisation and a very dense structure. The structural simplicity hides an intricate magnetic circuit for which the analysis is complicated by the presence of three excitation

sources within a three-dimensional structure prone to saturation and to significant leakage effects.

Excitation control allows the HB machine to be operated as a stand alone synchronous generator with a regulated output voltage, or to be connected in parallel with the mains. Other potential applications where the features of the HB machine offer useful benefits include Uninterruptible Power Supplies, Hybrid Electric Vehicles, wind turbines and Variable Speed Integrated Generator Sets. In such applications the output frequency does not need to be fixed and the machine design is free to use more compact multi-pole arrangements. With the output voltage regulated the output can be fed into an uncontrolled rectifier and the dc voltage level maintained for inversion. Thus a controlled rectifier or dc regulator may be omitted from the power electronics. Motoring operation has not so far been investigated, the machine having been conceived and developed primarily with generator applications in mind. It is not clear at present whether any means of starting could be incorporated into the machine and its use as a motor may therefore be restricted to inverter-fed systems. However with field control simple torque control may be achievable.

7.3 The HB Configuration

Figure 7.1 shows a schematic diagram of the machine in a 4-pole arrangement. The rotor consists of two discs mounted on a common shaft and is entirely ferromagnetic. Each disc carries a set of alternate north and south poles directed axially toward the stator. On one disc the two north poles are permanent magnets and the two south poles are steel.

The north poles are located opposite the north poles of the second disc, however, the north poles of the second disc are steel and the south poles are permanent magnets. Excitation for the steel south poles of the first disc and north poles of the second is provided by a single coil surrounding the shaft and fixed to the stator. The rotor does not carry alternating flux and it can be constructed conveniently from cast iron provided that the material specification includes suitable magnetic properties. The permanent magnets are sintered Neodymium-Iron-Boron, providing a high magnetic loading, leading to a compact machine design. Underneath each magnet is a ferrous shim in an attempt to reduce inter-polar leakage.

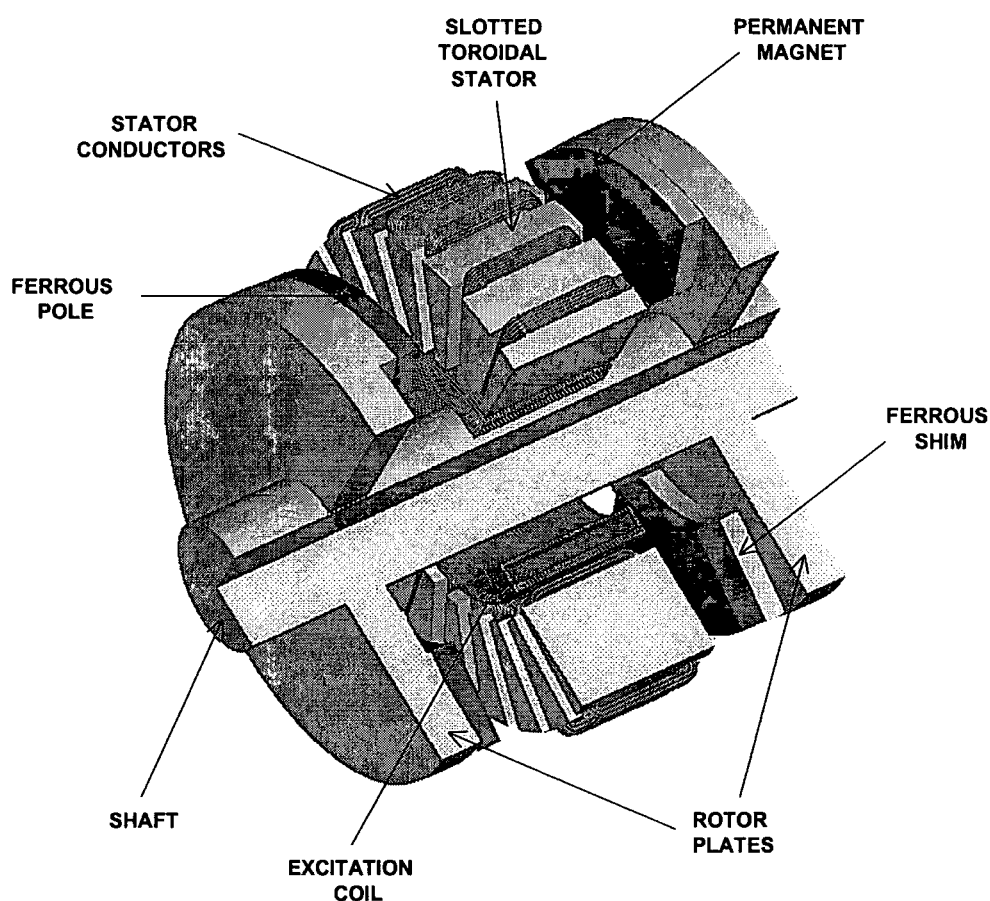


Figure 7.1 Machine structure

The stator is a laminated toroid placed between the two rotor discs and carries flux tangentially between the rotor north and south poles. The stator is laminated in the required direction by rolling a single strip of magnetic steel sheet. Slots are formed in the two annular faces by an indexed punching machine as the rolling process takes place. The manufacture of the core pack is straightforward and material wastage is significantly lower than with a more conventional radial-flux synchronous machine.

The stator winding is toroidal, comprising a set of coils each occupying one slot on each of the two faces. The stator resembles that of the TORUS machine considered in previous sections, but unlike the TORUS machine it uses a winding in slots. The use of a winding in slots rather than in the airgap influences the design in several ways:

- The air-gap MMF requirement is lower
- The windings are not subject to eddy current losses due to the main field
- While cooling of the conductors is not as good compared to an air-gap winding the electric loading can be increased without compromising the magnetic circuit significantly.
- The number of turns and wire size can be freely chosen to provide the required output voltage
- The winding depth does not directly influence the air-gap and an increased electric loading does not result in a corresponding increase in MMF
- The winding mechanical support is more positive
- Windings are protected in the slots
- The leakage inductance is higher

- The axial length of the stator is greater
- Tooth ripple may result in additional pole face losses
- The flux waveform will have tooth ripple superimposed
- The teeth are likely to have a high magnetic loading and iron losses will increase

7.4 Operation

Consider the developed 2 dimensional diagram of Figure 7.2. The physical layout has been simplified to clarify the flux paths. Figure 7.2a shows the flux component due to the permanent magnets for a low reluctance shaft. The MMF is unidirectional and drives flux from one rotor disc across the air-gap to the stator where it passes circumferentially and crosses the second air-gap to magnets on the second disc. The path is completed through the shaft. A second set of flux paths from the permanent magnets shown in Figure 7.2b exists if the shaft is of high reluctance. Here flux passes from a magnet across the air-gap into the stator and returns to the same disc across the air-gap at the adjacent iron poles.

If the shaft has low reluctance, the paths in Figure 7.2b carry very little flux but if the shaft reluctance is high, for example due to saturation, then a large fraction of the flux passes this way.

Figure 7.2c shows the paths taken by the flux due to the excitation coil MMF. Like the magnet flux, it crosses two air-gaps and completes its circuit through the shaft. It passes mostly across the air-gaps at the iron poles because these have much lower reluctance

than paths through the magnets. A little flux does pass through the magnets and through various leakage paths as indicated. The excitation flux passes along the shaft in the opposite direction to the magnet flux and so it reduces the total shaft flux. However, in the stator core the two flux components combine additively. Thus field control is achieved without brushes in a single machine that derives its principal excitation from permanent magnets.

Figure 7.2d shows the flux due to armature reaction MMF with zero power factor loading neglecting stator leakage reactance and resistance. Figure 7.2d may also be considered to be showing the direct(D) axis flux. When the power factor is zero (with inductive load) the armature MMF directly opposes the excitation MMF, and because of the lower reluctance of the iron poles the armature reaction flux in the shaft is in the same direction as the magnet flux.

Figure 7.2e shows the flux due to armature reaction MMF with unity power factor loading neglecting stator leakage reactance and resistance. This Figure shows the quadrature(Q) axis flux. Here flux is forced into the inter-polar regions on each disc and theoretically zero flux passes into the shaft. This is an important observation as only flux in the D axis interacts with shaft excitation.

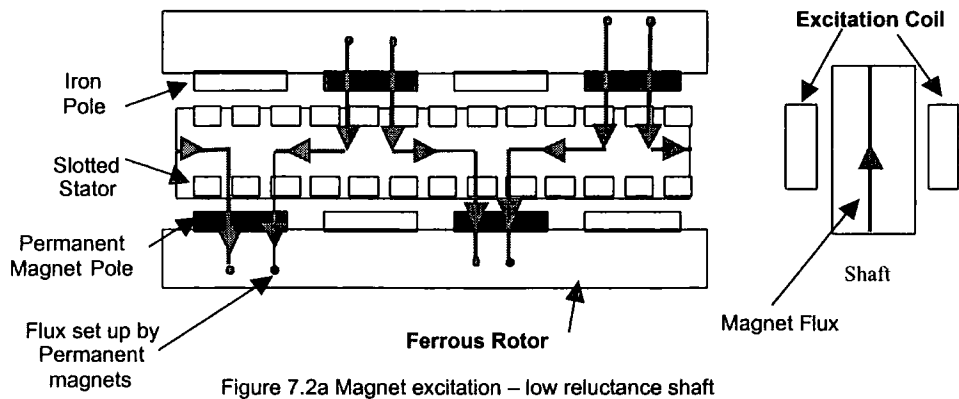


Figure 7.2a Magnet excitation – low reluctance shaft

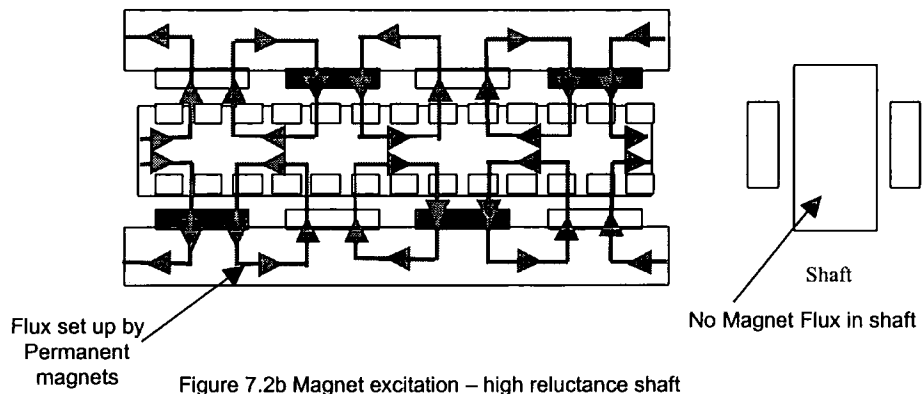


Figure 7.2b Magnet excitation – high reluctance shaft

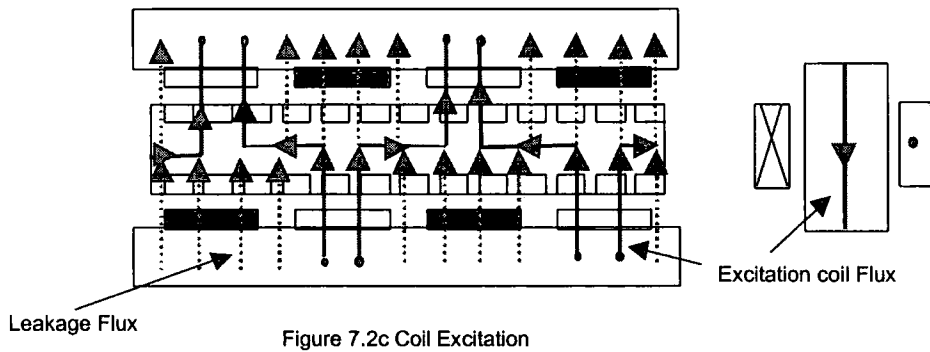


Figure 7.2c Coil Excitation

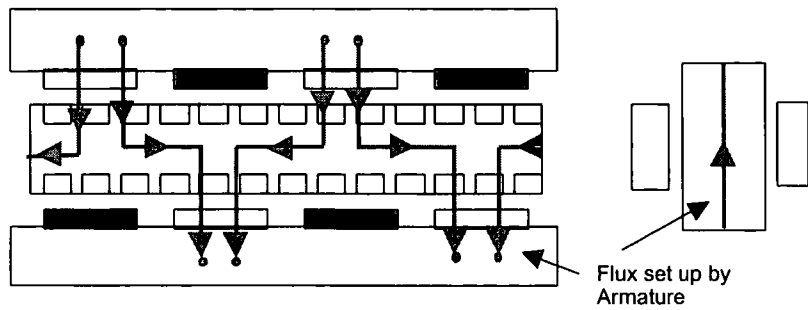


Figure 7.2d Armature Excitation – D axis

Figure 7.2 Developed 2 dimensional diagram

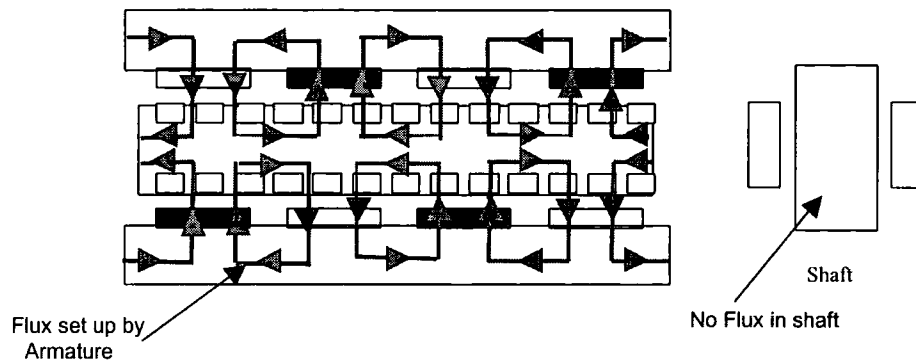


Figure 7.2e Armature Excitation Q-axis

Figure 7.2 Developed 2 dimensional diagram

One design concern with the HB machine was that the magnet excitation and coil excitation set up a homopolar MMF across the rotor plates. So effectively one rotor formed a north pole while the other a south pole. This MMF causes a significant amount of leakage flux between the rotor plates and is an important part of the following analysis.

7.5 Modelling

7.5.1 Magnetic Equivalent Circuits

Magnetic equivalent circuits with parameter values calculated from the machine dimensions are used as the principal design tool. Magnetic equivalent circuits are employed to:

1. Calculate the armature flux linkage due to the combined PM and coil excitation
2. Calculate shaft flux and determine the shaft diameter required
3. Subsequently obtain the full load field requirements

A lumped-parameter magnetic equivalent circuit for the machine with armature reaction in the D axis is given in Figure 7.3. The magnet is represented by an MMF source F_m in series with a reluctance that includes the air-gap and magnet, S_m . The ferrous poles are represented by the reluctance of the air over the pole arc, S_p . The machine has 4 poles, hence with two rotors the equivalent circuit includes 4 magnet poles and 4 ferrous poles. The stator is assumed to be infinitely permeable and represented by armature reaction MMF's, F_a . Both the shaft reluctance S_s and leakage reluctance S_{leak} are in parallel with the poles and stator. S_{leak} is an equivalent reluctance which accounts for leakage flux between rotor plates as a result of the unipolar MMF across the machine. F_e is the excitation MMF created by the coil around the shaft.

All magnetic paths other than in the shaft have been assumed linear to simplify the modelling process. These circuits do not include the stator leakage paths but they do include the leakage paths that carry flux driven by the excitation coil. The latter is essential for calculating the total shaft flux, and since saturation is a prominent concern the main and leakage fluxes must be computed together. The stator leakage flux can be calculated separately because it does not pass through any regions liable to saturation.

Note that certain parameters in the equivalent circuit of Figure 7.3, such as S_{leak} , F_a , S_s and F_e are split in half and a common potential identified. Three further potentials are labelled 'core potential A', 'core potential B' and 'core potential -B'. Identifying these potentials allows further simplifications to be made to the equivalent circuit later.

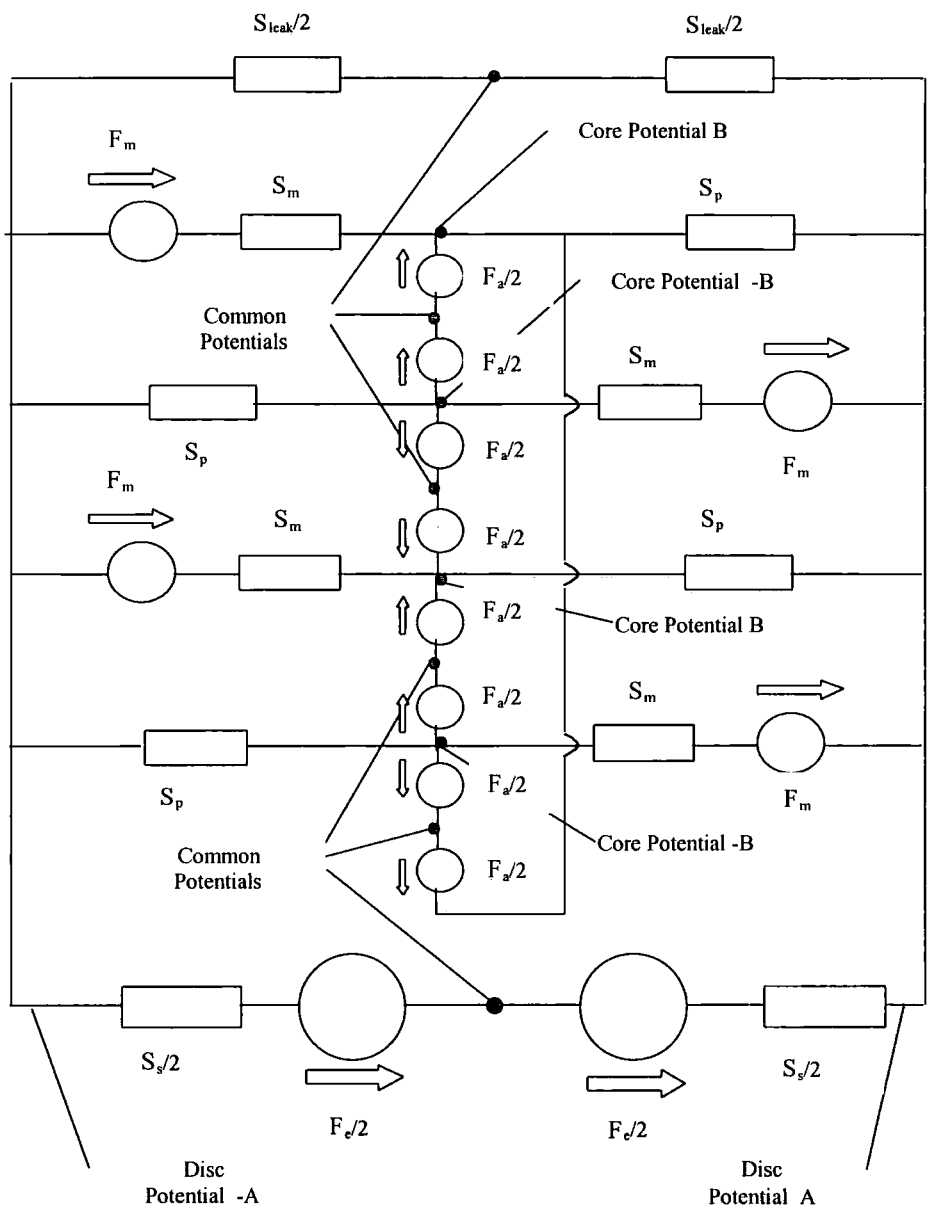


Figure 7.3 Magnetic Equivalent circuit of HB Machine with armature current in the D – axis.

7.5.2 Equivalent Circuit Parameters

7.5.2.1 Iron Poles

Flux driven by the permanent magnets and the excitation coil passes across the air-gap with a uniform distribution apart from fringe effects near the edges of the pole and the edges of teeth. The usual simple expression for reluctance applies equation (7.1).

$$S_p = L_{gap} / (\mu_0 A_p). \quad (7.1)$$

Where L_{gap} = air-gap length (m), A_p = pole area (m²)

An adjustment is applied to the area to make allowance for the fringe effects. For this study the pole area was increased by the air-gap length all the way around the perimeter of the pole. The path length was also increased using the Carter coefficients to account for slotting.

7.5.2.2 Permanent Magnet Poles

Sintered Neodymium-Iron-Boron magnets are used. The material has a linear second quadrant demagnetisation characteristic with slope typically $1.05 \times \mu_0$. Each magnet is therefore represented in the usual way by reluctance, equation (7.2) in series with a MMF source, equation (7.3).

$$S_{mag} = L_m / (\mu_0 \mu_{rec} A_m) \quad (7.2)$$

$$F_m = H_m L_m \quad (7.3)$$

Where
$$A_m = \tau \pi (R_2^2 - R_1^2) / P \quad (7.4)$$

τ = pole arc to pitch ratio, P = poles, R_2 = outer radius of magnet (m), R_1 = inner radius of magnet (m), L_m = magnet length (m), A_m = magnet area (m²), H_m = magnet coercive force (A/m)

Note the equivalent circuit of Figure 7.3 uses a magnet reluctance S_m , which includes S_{mag} of equation(7.2) and the reluctance of the air-gap under the magnet pole.

7.5.2.3 Stator D-Axis MMF

The effective armature MMF values for use in the magnetic equivalent circuit are related to the winding current, and assume the stator MMF and the resulting air-gap flux are distributed approximately sinusoidally.

$$\text{Flux Density, } B = \frac{\hat{F}}{L_{gap}} \cdot \mu_0 \cdot \cos \frac{P}{2} \theta \quad (7.5)$$

Where
$$\hat{F} = \sqrt{2} \cdot I \cdot N_{ph} \cdot \frac{3}{2} \cdot \frac{K_w}{p} \cdot \frac{4}{\pi} \quad (7.6)$$

L_{gap} = airgap length (m), P = number of poles, θ = mechanical displacement angle (degrees). I = stator current (A), N_{ph} = phase turns, K_w = winding factor

The elemental area, A over a pole is given by

$$A = (R_2 - R_1) \cdot \frac{(R_1 + R_2)}{2} \cdot d\theta \quad (7.7)$$

where R_2 = outer radius (m), R_1 = inner radius (m)

The total D-axis flux, ϕ_D per pole is found by integrating over the pole arc, assuming the flux density is at a peak in the centre of pole, Figure 7.4a.

$$\begin{aligned}\phi_D &= B.A = \mu_0 \frac{\hat{F}}{L_{gap}} \cdot \frac{(R_2^2 - R_1^2)}{2} \cdot 2 \cdot \int_0^{\tau \cdot \pi / p} \cos \frac{p}{2} \theta d\theta \\ &= \frac{\hat{F}}{L_{gap}} \cdot \mu_0 \cdot (R_2^2 - R_1^2) \cdot \frac{1}{p/2} \cdot \sin\left(\frac{\pi \cdot \tau}{2}\right)\end{aligned}\quad (7.8)$$

since $F_D = \phi_D \cdot S$, and $F_D =$ Direct axis MMF(A), $S =$ Pole reluctance (A/Wb)

then

$$S = \frac{1}{\mu_0} \cdot \frac{L_{gap}}{\frac{\pi \cdot (R_2^2 - R_1^2) \cdot \tau}{p}} \quad (7.9)$$

and

$$F_D = \hat{F} \frac{\sin(\tau \cdot \pi / 2)}{\tau \cdot \pi / 2} \quad (7.10)$$

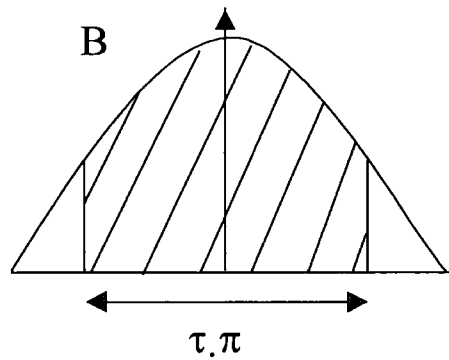


Figure 7.4a Direct axis flux

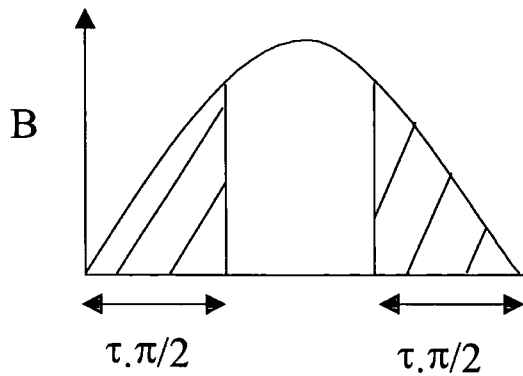


Figure 7.4b Quadrature axis flux

Figure 7.4 Illustration showing the calculation of D and Q axis flux

7.5.2.4 Stator Q-Axis MMF

MMF in the Q axis creates a flux in the iron pole that is greatest at its ends and is zero at the centre, Figure 7.4b. The flux per pole is found from:

$$\phi = \mu_0 \frac{\hat{F}}{L_{gap}} \cdot \frac{(R_2^2 - R_1^2)}{2} \cdot 2 \cdot \int_0^{\tau \cdot \pi / p} \sin \frac{p}{2} \theta d\theta \quad (7.11)$$

giving:

$$F_Q = \hat{F} \frac{\{1 - \cos(\tau \cdot \pi / 2)\}}{\tau \cdot \pi / 2} \quad (7.12)$$

where, \hat{F} is the peak value of the sinusoidal distribution but does not occur within the span of the pole. F_Q was not needed in the analysis for it was identified earlier it had no effect on the excitation coil but included here for completeness.

7.5.2.5 Leakage Paths

The complex 3 dimensional geometry and homopolar MMF make flux leakage a major design concern. Several distinct paths have been combined in parallel to form the single reluctance, S_{leak} shown in the magnetic equivalent circuit of Figure 7.3. Figure 7.5, identifies the principal leakage paths and their separate reluctance values have been estimated as follows:

S_{e1} -- refers to leakage from the outer faces of the rotor discs and was derived by scaling from a 3D finite-element study for a simple steel cylinder of 1m diameter, 0.2m length excited by a solenoid coil.

$$S_{I1} = \frac{3 \cdot 10^6}{D_R} \quad (7.13)$$

D_R = Rotor outer diameter (m)

S_{I2} -- refers to the leakage between the edges of the two rotor discs. This was estimated by means of a simple analytical formula based on the fact that an open magnetic circuit carries a total flux similar to that carried by a uniform field in an air-gap equal to (pole-pitch)/ π - see case 1, Appendix B.

$$S_{I2} = \frac{L_{SH} + L_D}{\pi \cdot (D_R \cdot \pi \cdot L_D) \cdot \mu_0} \quad (7.14)$$

L_{SH} =Shaft length (m), L_D =Rotor disk length (m)

S_{I3} -- refers to leakage between the edge of each rotor disc and the edge of the stator core. It is estimated in the same manner as S_{I2} .

$$S_{I3} = \frac{L_{DS} + L_D}{\pi \cdot (D_R \cdot \pi \cdot L_D) \cdot \mu_0} \quad (7.15)$$

L_{DS} =Rotor disk to stator length (m)

S_{I4} -- refers to leakage flux passing between the shaft and the inside surface of the stator. This component was estimated in a very approximate way by assuming the flux to follow purely radial paths and neglecting curvature and the fringe flux around the ends of the coil. This calculation resembles the calculation of leakage flux due to current in an armature slot – see slot leakage, section 7.5.7.1.

$$S_{I4} = \frac{\frac{D_1 - D_{SH}}{2}}{\mu_0 \cdot \pi \cdot \left(\frac{D_1 + D_{SH}}{2}\right) \cdot \left(L_{DS} + \frac{L_C}{2 \cdot 3}\right)} \quad (7.16)$$

D_1 =Stator inner diameter (m), D_{SH} =Shaft outer diameter (m), L_C =Stator Core length (m)

S_{I5} -- refers to the flux passing axially from rotor disk to stator in the regions between poles. In a P -pole machine there are $P/2$ magnet and $P/2$ iron poles on each disc thus:

$$S_{I5} = \frac{L_{DS}}{\left(\frac{\pi \cdot (D_R^2 - D_{SH}^2)}{4} - \frac{P}{2} \cdot A_m - \frac{P}{2} \cdot A_p\right) \cdot \mu_0} \quad (7.17)$$

A_m =Magnet area (m^2), A_p =Pole area (m^2)

The various leakage paths are combined in parallel to form the single leakage path shown in the equivalent circuit. The regions corresponding to S_{I2} and S_{I3} overlap and so the parallel combination overestimates the total leakage somewhat.

$$S_{leak} = \frac{1}{\left(\frac{1}{S_{I1}} + \frac{1}{S_{I2}} + \frac{1}{2 \cdot S_{I3}} + \frac{1}{2 \cdot S_{I4}} + \frac{1}{2 \cdot S_{I5}}\right)} \quad (7.18)$$

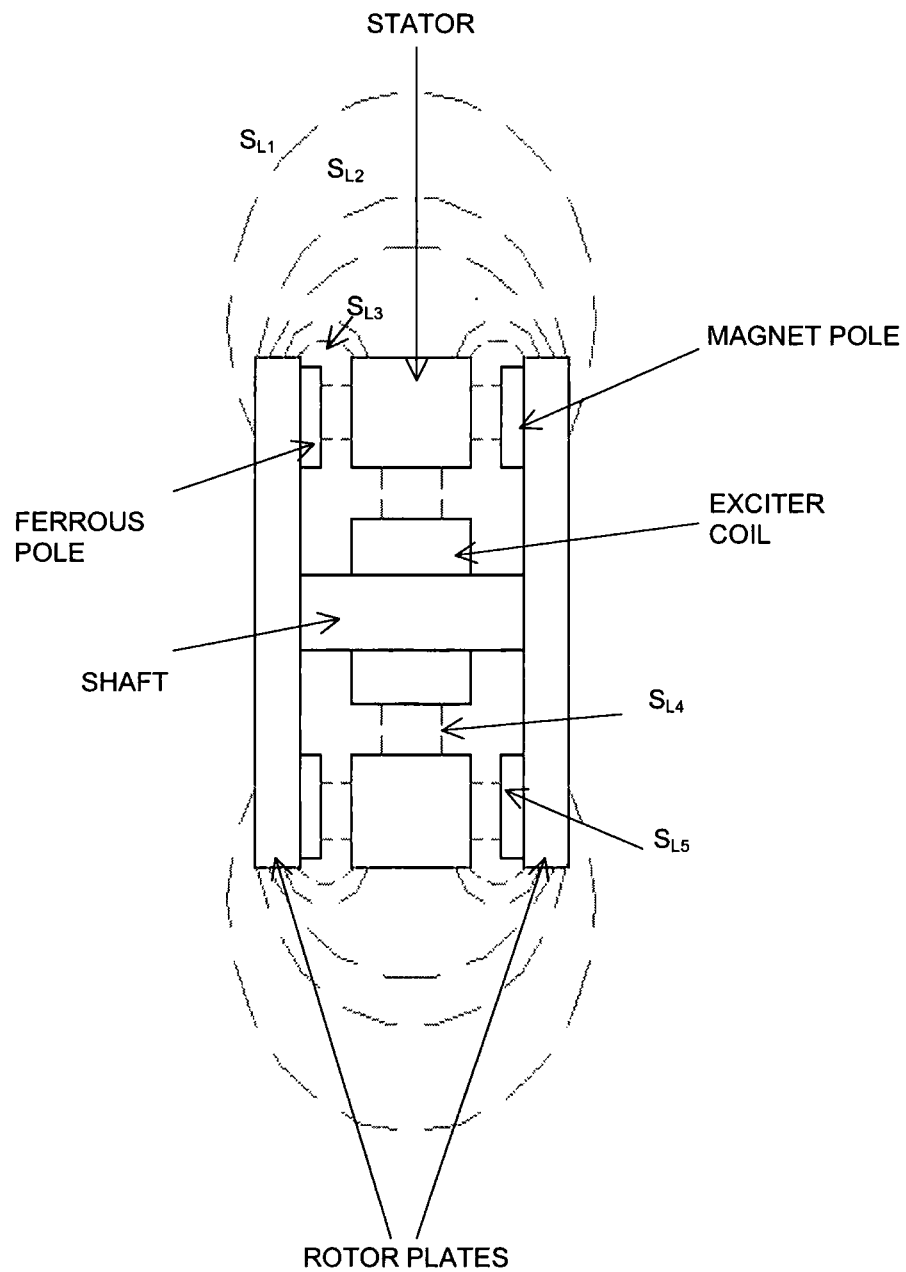


Figure 7.5 Leakage flux within machine

7.5.3 Non-Linear Shaft Model

The shaft is the principal bottleneck in the magnetic circuit. The transition from no-load to full-load operation reverses the shaft flux and saturation can occur in either case unless adequate cross section is provided.

Consider the case with magnet excitation alone, Figure 7.2a and Figure 7.2b. The principal flux path is through the shaft, Figure 7.2a. If a significant MMF is developed across the reluctance of the shaft then this same MMF, applied to the air-gap reluctance at the steel poles causes a proportion of the flux to return to the magnets by this route, Figure 7.2b. The overall air-gap flux is thereby enhanced somewhat and saturation of the shaft has the counter-intuitive effect of increasing the armature flux linkage.

Feeding current to the excitation coil, still with no current in the stator, first takes the shaft out of saturation with little effect on the total armature flux and EMF. Increasing excitation current reduces then reverses the shaft flux and eventually causes saturation in the opposite sense. Clearly a non-linear model of the shaft is required. This should take account of any ventilation holes in the shaft and flux concentrations at the junction between the shaft and the disc. Models were developed with guidance from 3D finite-element studies in which the shaft is represented as a number of sections with defined length and cross section. The material characteristic of EN1A low carbon steel used in the shaft was measured and represented by an analytical approximation, Equation (7.19).

$$H = 500 B + 3.3 (B - 0.19)^{27} \quad (7.19)$$

A comparison between this analytical approximation and measured is provided in Figure 7.6.

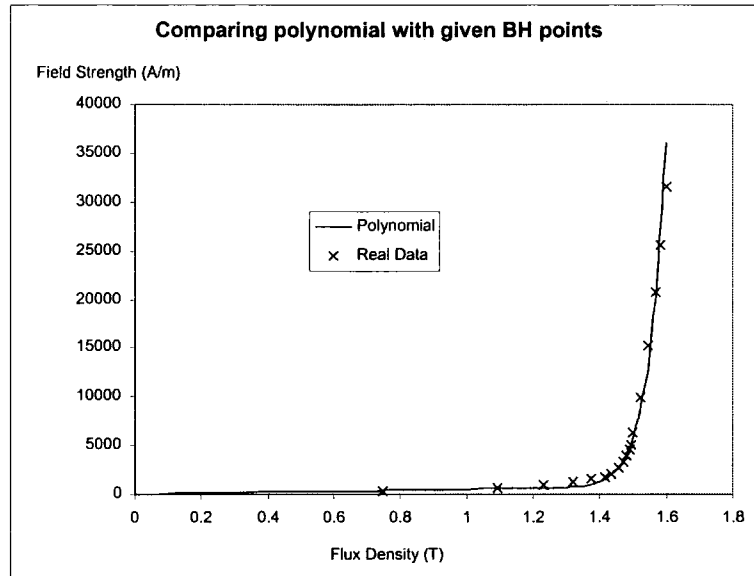


Figure 7.6 Compares the real and the modelled data

4.5.4 D-Axis Magnetic Circuit Analysis

Recognising that the centre point of each armature branch is at the same potential as the centre point of the shaft in Figure 7.3 reveals a symmetrical pattern, allowing analysis to proceed using the reduced circuit of Figure 7.7. The reduced circuit is further transformed into a current sourced equivalent circuit using Norton equivalents shown in Figure 7.8. Finally the circuit is further reduced to the shaft with a non-linear reluctance driven by a Thevenin source, Figure 7.9, where

$$S1 = \frac{1}{\frac{1}{2.S_m/P} + \frac{1}{S_{leak}/2} + \frac{1}{2.S_p/P}} \quad (7.20)$$

and

$$F1 = S1 \times \left\{ \frac{(F_m - \frac{F_a}{2})}{2.S_m / P} + \frac{\frac{F_a}{2}}{2.S_p / P} \right\} \quad (7.21)$$

$F1$ = Thevenin equivalent MMF (A), $S1$ = Thevenin equivalent reluctance (A/Wb), S_m = Magnet reluctance including air-gap (A/Wb), S_{leak} = leakage reluctance (A/Wb), S_p = Pole reluctance (A/Wb), F_m = Magnet MMF (A), F_a = Armature reaction MMF (A)

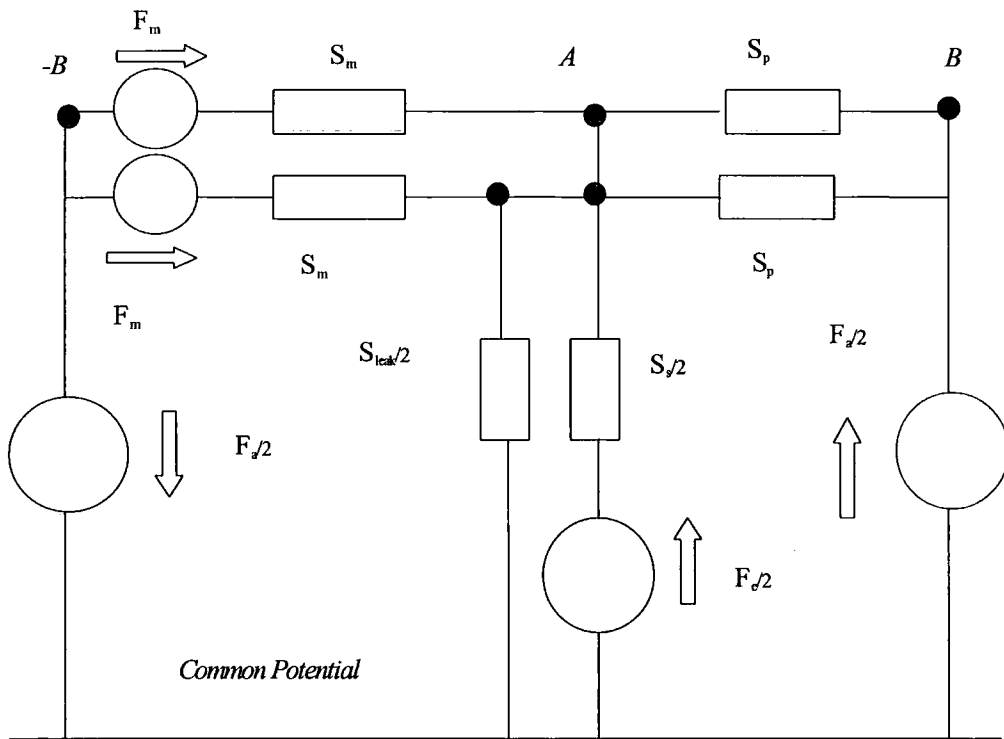


Figure 7.7 Reduced D axis equivalent circuit

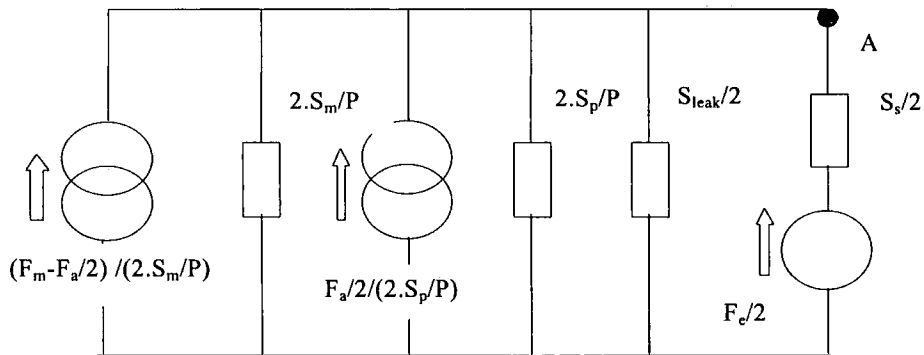


Figure 7.8 Current sourced equivalent circuit

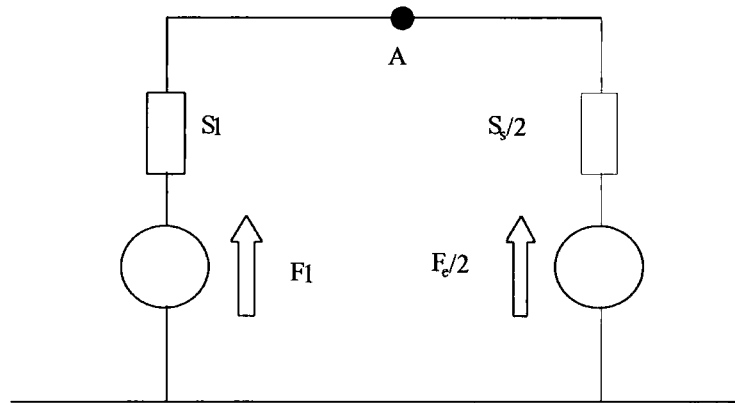


Figure 7.9 Reduced Thevenin equivalent circuit

The flux / MMF characteristic of the shaft is plotted together with the linear characteristic of the Thevenin source and the intersection gives the shaft flux and MMF in Figure 7.10. With reference to Figure 7.9, the potential (A) of the rotor disc allows all the fluxes in the original circuit of Figure 7.3 to be calculated.

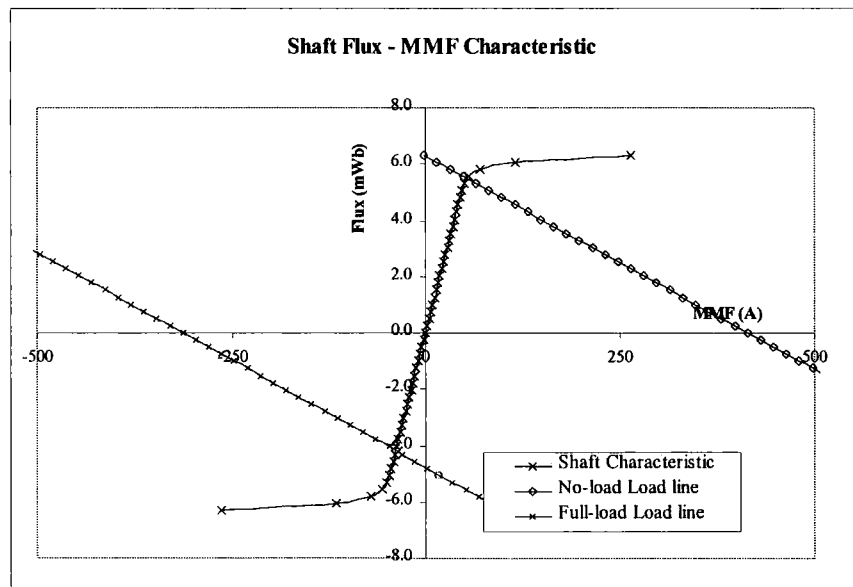


Figure 7.10 Shows shaft flux and MMF for no load and full load operation

The no load voltage may be calculated by setting F_a to zero and computing $F1$ and $S1$, then using the Thevenin equivalent circuit in Figure 7.9 to calculate potential A and the subsequent flux within the original circuit of Figure 7.3. The case of full-load D-axis current gives the maximum operational shaft flux from which the requisite shaft diameter can be derived. The same case also gives the armature full load flux linkage. Adjusting the field current to restore the flux linkage to the no-load value leads to the required coil excitation.

7.5.5 Allowance For Varying Power Factor Loads

So far the analysis has only considered the machine operation for zero power factor loads when the armature flux is in the D axis. It has been recognised earlier that when the armature supports flux in the Q axis no flux links with the shaft, Figure 7.2e. Therefore unity power factor loads do not contribute to any shaft flux. The MMF source F_a in Figure 7.7 therefore does not make a contribution. The equivalent circuit for the Q axis may be redrawn as shown in Figure 7.11.

Here $F1$ reduces to equation (7.22)

$$F1 = S1 \times \frac{F_m}{2.S_m / p} \quad (7.22)$$

The calculation for $F1$ may be generalised to equation (7.23), for operation between zero and unity power factor where a sinusoidal variation between D axis and Q axis armature reaction is assumed.

$$F_1 = S_1 \times \left\{ \frac{(F_m - \frac{F_x}{2})}{2.S_m / p} + \frac{\frac{F_x}{2}}{2.S_p / p} \right\} \quad (7.23)$$

Where $F_x = F_D \cdot \sin \theta$, $\theta = \text{Internal power factor}$, F_D is calculated using Equation(7.10)

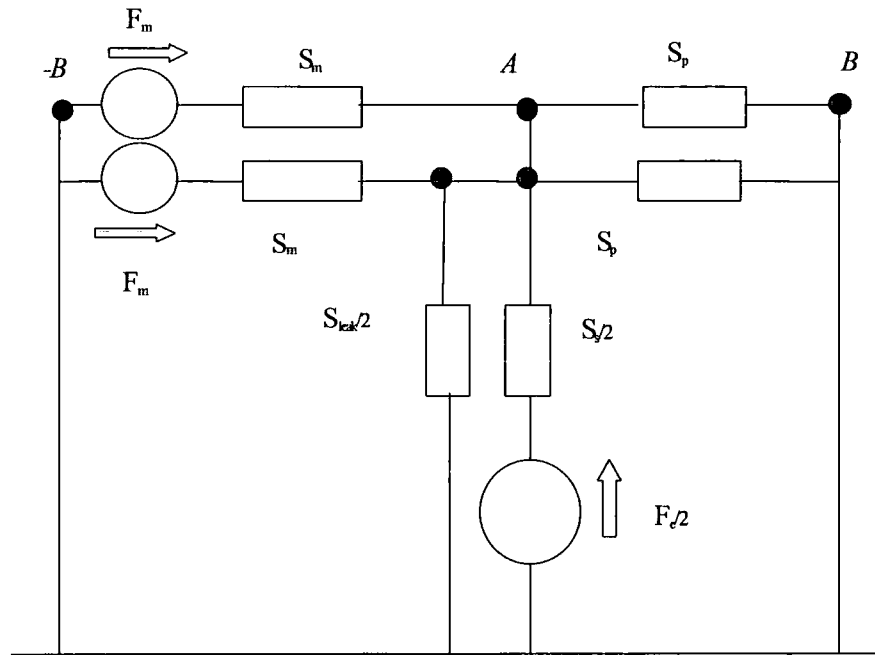


Figure 7.11 Reduced Q axis equivalent circuit

7.5.6 Thermal Model

A simple thermal model of the stator slot is used to predict the maximum allowed continuous stator current within a slot. The model assumes all the heat generated by the stator conductor radiates through the slot insulation into the stator and then radiates over the stator surface area, see Figure 7.12a. The additional contribution from the iron losses has been ignored. The thermal resistance for the insulation and stator surface area can be calculated, equations (7.24, 7.25).

$$\text{Slot liner thermal resistance, } R_{slot} = \frac{1}{\Omega_{ins}} \cdot \frac{t_{ins}}{(R_2 - R_1) \cdot (2 \times Y_{DEP} + Y_{WID})} \quad (7.24)$$

$$\text{Stator side thermal resistance, } R_{stator} = \frac{1}{htc} \cdot \frac{1}{\frac{\pi \cdot (R_2^2 - R_1^2)}{n} - (Y_{WID} \times (R_2 - R_1))} \quad (7.25)$$

Y_{DEP} =Slot depth (m), Y_{WID} =Slot width (m), t_{ins} =Slot liner thickness (m), Ω_{ins} =insulation conductivity (W/m/k), htc =heat transfer coefficient of air (60 W/m²/k), n = number of slots on one stator side, R_2 =Stator outer radius (m), R_1 =Stator inner radius (m).

Using the simple equivalent circuit in Figure 7.12b, the allowable copper loss is calculated using Equation (7.26), based upon an acceptable temperature rise, t .

$$\text{Acceptable Slot loss / Slot} = \frac{t}{(R_{slot} + R_{stator})} \quad (7.26)$$

With knowledge of the stator geometry and assuming a slot fill factor, the slot resistivity can be calculated and the maximum slot current obtained.

The excitation coil temperature rise was simply calculated by relating the calculated coil loss to the coil surface area and heat transfer coefficient for air assumed to be 60W/m²/K.

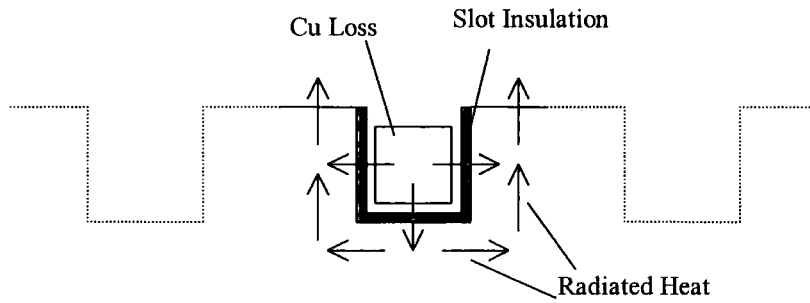


Figure 7.12a Slot profile

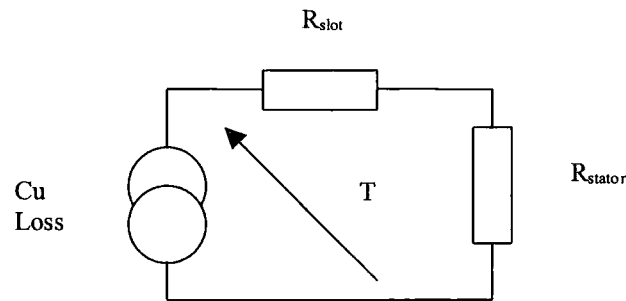


Figure 7.12b Slot thermal equivalent circuit

Figure 7.21 Slot profile and thermal equivalent circuit

7.5.7 Stator Leakage

The definition of stator leakage in the context of this machine is armature borne flux paths that do not link directly with the equivalent circuits of Figure 7.3. A common approach is applied where energy for these fields is related back to the leakage inductance. For example for a 3 phase system referenced to 1A per phase the energy can be calculated by

$$\text{Energy} = \frac{1}{2} . L i_1^2 + \frac{1}{2} . L i_2^2 + \frac{1}{2} . L i_3^2 = \frac{3}{4} . L = \frac{3}{4} \frac{F^2}{S} = \frac{3}{4} \frac{N^2}{S} \quad (7.27)$$

$$i_1 = \sin w_e t, i_2 = \sin(w_e t + \frac{2}{3} \pi), i_3 = \sin(w_e t + \frac{4}{3} \pi), \quad L = \text{inductance(H)}, \quad S = \text{Reluctance(A/Wb)}$$

and F is the MMF which for 1A is related directly to the number of turns, N .

7.5.7.1 Slot Leakage

The calculation of slot leakage in a square bottomed slot is well known[25] and based upon the assumption of infinitely permeable steel and the flux crossing parallel from slot side to side. Where no slot iron bridge exists the slot is occupied by just air at the top of the slot and the reluctance is readily calculated from the geometry of the slot. Due to the conductors being distributed, the MMF contribution to the slot leakage flux will increase from zero at the bottom of the slot proportional with the conductor depth, reaching a maximum at the top of the conductor. Reference [25] shows the net area used to calculate the slot leakage reluctance is reduced by a third for the region occupied by the conductor.

On the assumption of copper filling two thirds of the slot, the slot leakage reluctance S_{slot} is calculated, using equation (7.25).

$$S_{slot} = \frac{1}{\mu_0} \cdot \frac{Y_{WID}}{Y_{LEN} \cdot \left(\frac{Y_{DEP}}{3} + Y_{DEP} \cdot \frac{2}{3} \cdot \frac{1}{3} \right)} \quad (7.28)$$

Y_{LEN} = Slot Length (m), Y_{WID} = Slot width (m), Y_{DEP} = Slot depth (m)

Having calculated the slot reluctance S_{slot} , the slot leakage inductance L_{slot} was calculated using equation (7.27) which includes a slot from each phase, and the number of slot turns N_{slot} provides the required MMF F for 1A.

$$L_{slot} = \frac{N_{slot}^2}{S_{slot}} \cdot \frac{n}{3} \cdot 2 \quad (7.29)$$

where n = number of slots on one stator side.

7.5.7.2 End Winding Leakage

This section explains a method for calculating the end winding inductance of the stator armature winding at the outer and inner surface of the stator. Appendix B demonstrates

an open magnetic circuit carries a total flux similar to that of a uniform field in an air-gap equal to the pole-pitch/ π .

Consider the stator outer end winding

$$\text{Pole - Pitch} = \frac{\pi \cdot D_2}{P} \quad (7.30)$$

$$\text{Equivalent Length of uniform field, } L_{eq} = \frac{D_2}{P} \quad (7.31)$$

D_2 = Stator outer diameter (m), P = Number of poles

Considering only one coil the area over which the flux passes is given by

$$A = \frac{\pi \cdot D_2 \cdot L_C}{2 \cdot p} \quad (7.32)$$

L_C = Stator Core length (m), A = Area (m^2)

Therefore the end winding reluctance S_{ENDO} per coil group for a three phase balanced current is

$$S_{ENDO} = \frac{2 \cdot L_{eq}}{\mu_0 \cdot A} = \frac{4}{\mu_0 \cdot \pi \cdot L_c} \quad (7.33)$$

End winding reluctance on the stator inner diameter S_{ENDI} , is calculated in a similar way to S_{ENDO} , however the equivalent airgap L_{eq} in Equation(7.31) is reduced by an amount explained in case 2 of Appendix B. The reason for this is that the shaft provides a low reluctance path for the inner end winding leakage flux and the equivalent air-gap and therefore reluctance reduces by

$$\frac{(D_I/D_{SH})^P - 1}{(D_I/D_{SH})^P + 1} \quad (7.34)$$

D_I = Stator inner diameter (m), D_{SH} = Shaft outer diameter (m), P = Number of poles

Having calculated S_{ENDO} and S_{ENDI} , the end winding leakage inductance can be calculated using equation 7.27. Remembering that this equivalent reluctance relates to a concentrated coil and therefore the number of turns per pole per phase, or number of turns in a group N_{group} . Equation(7.35) provides the leakage inductance for the stator outer end winding L_{ENDO} , with the maximum RMS stator current assumed to be 1 A .

$$L_{ENDO} = \frac{N_{group}^2}{S_{ENDO}} . P \quad (7.35)$$

The stator inner end winding inductance L_{ENDI} , is calculated by dividing equation(7.35) by equation (7.34)

7.5.7.3 Airgap Armature Leakage

Considering only the gap between stator and rotor disc and ignoring the ferrous poles (these will be dealt with separately in sections 7.5.7.4 and 7.5.7.5) the air-gap leakage may be calculated in a similar manner to equation (7.33) and (7.34). This assumes that the leakage paths in the radial plane over a cylindrical surface analysed in Appendix B are similar to that over a linear surface. First determining the mean diameter of the stator face D_{mean} , and extruding the machine into the radial plane, that is the diameter of the outer ferrous boundary in case 2, Appendix B becomes D_{mean} plus twice the distance

between rotor disc and stator, L_{DS} . Then the total air-gap leakage reluctance S_{air} on one stator side is given by

$$S_{air} = \frac{\frac{D_{mean}}{P}}{\mu_0 \cdot \pi \cdot \frac{(D_2^2 - D_1^2)}{4} \cdot \frac{1}{2 \cdot P}} \cdot \frac{\left\{ \frac{(D_{mean} + 2 \cdot L_{DS})}{D_{mean}} \right\}^P - 1}{\left\{ \frac{(D_{mean} + 2 \cdot L_{DS})}{D_{mean}} \right\}^P + 1} \quad (7.36)$$

L_{DS} = Distance between stator and rotor, D_{mean} = Mean diameter of stator (m)

The air-gap leakage inductance L_{air} for both stator sides was calculated using equation (7.37).

$$L_{air} = \frac{N_{group}^2}{S_{air}} \cdot 2 \cdot P \quad (7.37)$$

The air-gap leakage inductance, equation (7.37) was reduced further by $\frac{(2-\tau)}{2}$ to exclude the effect of the ferrous poles which are dealt with separately in sections 4.5.7.4.1 and 4.5.7.4.2. Where τ is the pole arc to pitch ratio for the ferrous pole. This is an approximation as the airgap leakage even with the ferrous poles excluded will vary with power factor.

7.5.7.4 D and Q Axis Leakage over Ferrous Pole

The author identified that the ferrous poles presented an effective magnetic short circuit for the flux created in the armature. Furthermore the amount of leakage flux depends upon the power factor. By simplifying the problem to 3 slots per pole for a 3 phase system, an equivalent circuit was used to calculate D and Q axis leakage flux. Note that within the design process the number of slots per pole can be greater than 3 but all machine designs are converted to 3 slots for this part of the analysis.

7.5.7.4.1 Q Axis Leakage

Figure 7.13a shows a cross section of ferrous pole and stator slots with the armature conductors energised to set up flux in the Q axis. Figure 7.13a may be reduced to the equivalent circuit in Figure 7.13b. The equivalent circuit relates solely to the two teeth S_{tooth} under the pole, and an MMF driven by the centre coil of 1 per unit to calculate the flux. Note 1A is again assumed to be 1 per unit current to simplify the analysis.

To calculate the tooth reluctance S_{tooth}

$$S_{tooth} = \frac{L_{gap}}{\mu_0 \cdot Y_{LEN} \cdot T_{WID}} \quad (7.38)$$

Where L_{gap} = Air-gap length (m), Y_{LEN} = Slot length (m), T_{WID} is an equivalent tooth width based on the mean diameter of the stator.

The Q axis leakage flux, ϕ_{lq} may be calculated by

$$\phi_{lq} = \frac{N_{group}}{2 \cdot S_{tooth}} \quad (7.39)$$

N_{group} = Number of turns per pole per phase.

The energy E_{lq} under the ferrous poles due to the Q axis leakage flux for P poles is given by

$$E_{lq} = \frac{1}{2} \cdot \phi_{lq}^2 \cdot S_{tooth} \cdot 2 \cdot P \quad (7.40)$$

Relating the energy in these fields under the ferrous poles to a 3 phase system using equation (7.27) provides the Q axis leakage inductance L_{lq} , equation (7.41)

$$L_{lq} = \frac{4}{3} \cdot E_{lq} \quad (7.41)$$

Note equation(7.41) overestimates the Q axis leakage flux a little as in reality flux will enter the pole sides as a result of the other two conductors and oppose the calculated flux,

ϕ_{lq} .

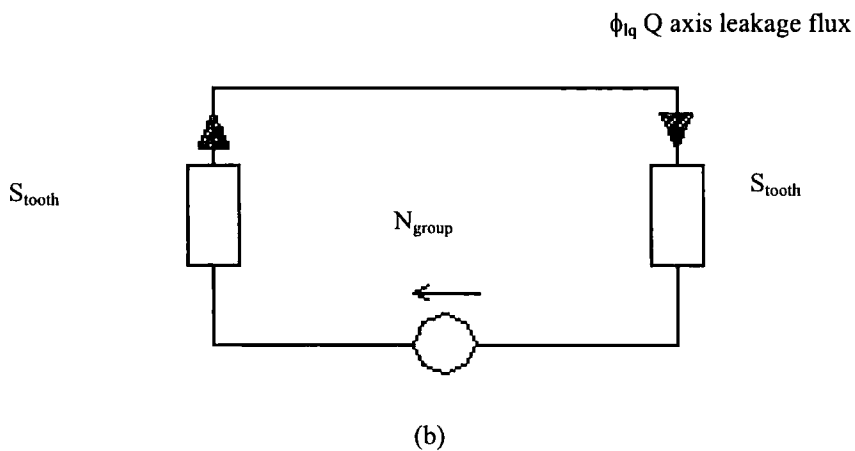
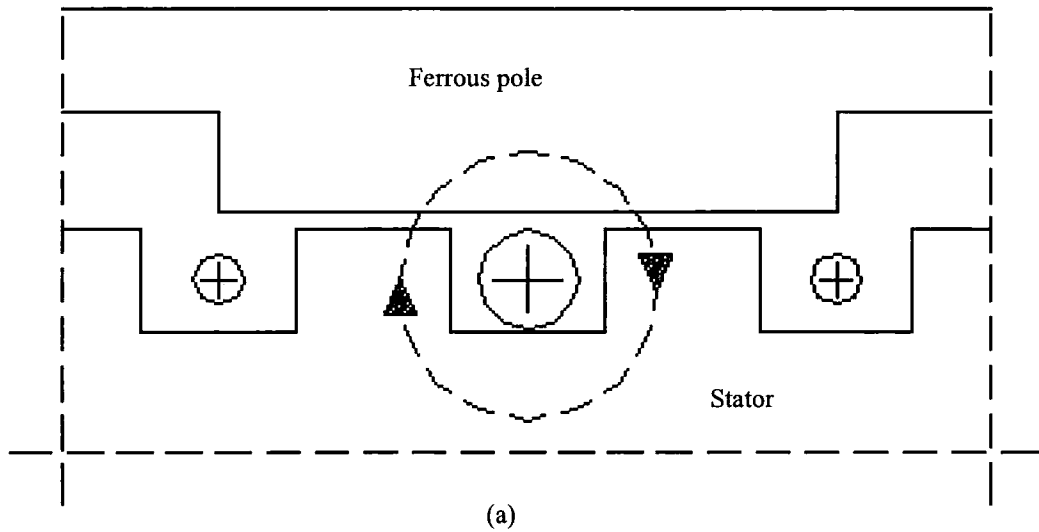


Figure 7.13 Q axis leakage flux

7.5.7.4.2 D Axis Leakage

Figure 7.14a shows a cross section of ferrous pole and stator slots with the armature conductors energised to set up flux in the D axis. Compared with section 7.5.7.4.1 the armature MMF's are displaced resulting in two MMF sources of half per unit driving flux in two reluctance paths, Figure 7.14b. The tooth reluctance, S_{tooth} in the middle of the pole is the same as section 7.5.7.4.1 but the two reluctance values either side, S'_{tooth} are calculated based upon the pole geometry.

$$S_{tooth}' = \frac{L_{gap}}{\mu_0 \cdot Y_{LEN} \cdot x} \quad (7.42)$$

where

$$x = \frac{\frac{\pi \cdot D_{MEAN} \cdot \tau}{P} - 2 \cdot Y_{WID} - T_{WID}}{2} \quad (7.43)$$

D_{mean} = Mean diameter of stator (m), Y_{WID} = Slot width (m), T_{WID} = slot width (m), τ = Pole arc to pitch ratio, Y_{LEN} = Slot length (m).

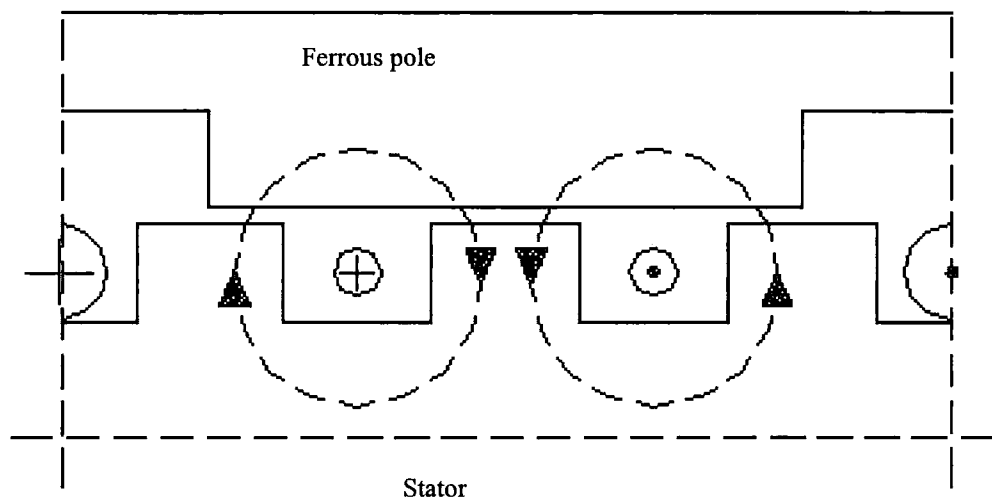
The D axis leakage flux ϕ_{ld} is calculated by applying Kirchoffs law to Figure 7.14b.

$$\phi_{ld} = 2 \cdot \frac{\frac{N_{group}}{2}}{2 \cdot S_{tooth} + S_{tooth}'} \quad (7.44)$$

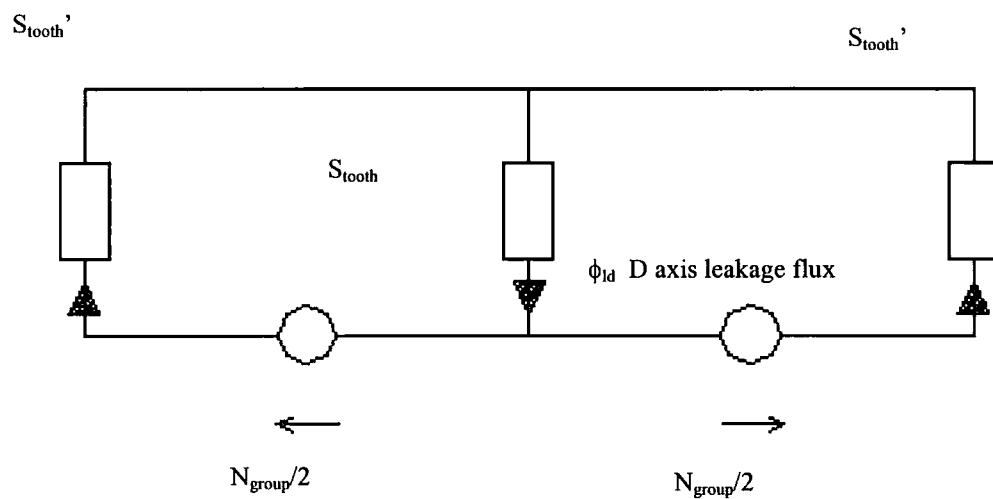
The energy under the ferrous poles for the D axis is given by

$$E_{ld} = \frac{1}{2} \cdot \phi_{2d}^2 \cdot S_{tooth} \cdot P + \left(\frac{\phi_{2d}}{2} \right)^2 \cdot S_{tooth}' \cdot P \quad (7.45)$$

Then the D axis leakage inductance can be calculated in a similar way to equation(7.41)



(a)



(b)

Figure 7.14 D axis leakage flux

7.5.7.4.3 Variation in D and Q Axis Leakage Inductance

The leakage reactance L_{lq} was assumed to vary in a sinusoidal way between the D and Q axis inductance with respect to power factor pf , equation (7.46).

$$L_{lqd} = (L_{lq} - L_{ld}) \cdot pf + L_{ld} \quad (7.46)$$

With the total stator leakage inductance varying with the internal power factor there was some difficulty establishing the phase angle between the internal EMF with respect to the load current. Unfortunately the internal power factor relied on the value for leakage inductance which also relied on the internal power factor. To simplify the problem the leakage inductance was related to the external power factor of the machine. That is the power factor between the terminal voltage and load current.

The design methodology for a loaded machine is as follows;

1. A target voltage, load current and power factor is specified and the leakage inductance calculated
2. From the leakage inductance, stator resistance and load power factor an internal power factor is established
3. Using the internal power factor the armature excitation F_a is calculated and using the equivalent circuits discussed previously an EMF is calculated.
4. The stator leakage reactance and stator resistance is used in conjunction with the load current to obtain the terminal voltage from the internal EMF calculated in 3.

7.5.8 Finite Element Analysis

While 3 dimensional finite element analysis (FEA) was applied to some design aspects of this machine it was not used as a primary design tool. The FEA tool was limited by its long processing time making it impractical to examine the effect of varying key parameters. With three excitation sources and saturation each simulation took many hours. A further limitation was that only magneto-static solutions were available so an initial estimate of the load angle was required before the FE model could be prepared. Where the FEA was beneficial was in ensuring that unforeseen saturation regions did not affect the predicted outputs. For example, the original design procedure linked the rotor disc thickness to shaft thickness and would have led to localised saturation. By the use of FEA this problem was avoided. Figure 7.15 provides two examples of 3 dimensional FEA plots of the HB machine.

The lumped-parameter design procedure was linear apart from the shaft and FEA provided guidance on the true flux levels within the machine and provided accurate values for the MMF requirements of various iron parts of the machine. FEA was also valuable for predicting the voltage waveform, including the presence of significant slot ripple. This was verified on test and removed by the expedient of misaligning the rotor discs by half of a stator slot pitch.

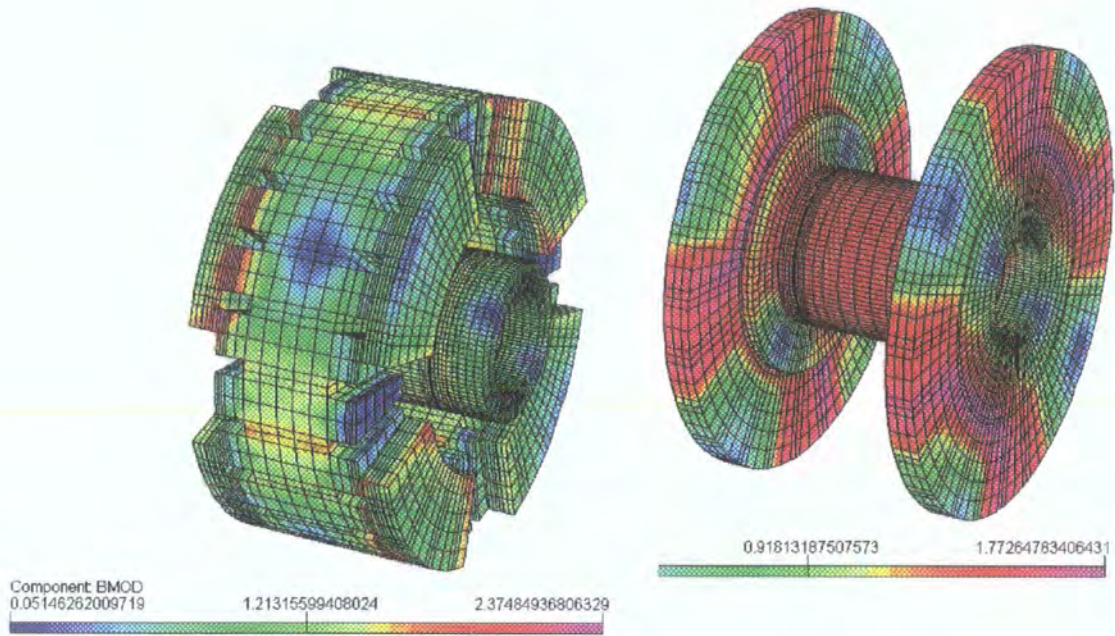


Figure 7.15 Three dimensional FEA plots of HB machine

7.5.9 Pole Face Losses

The stator core can be manufactured commercially by punching indexed slots before toroidally winding the steel. The natural design choice would be to use semi-closed slots to reduce pole face loss but this may reduce slot fills. For production of a single prototype, slots were milled into faces of a smooth core pack, resulting in an open slot shape. The use of open slots and a relatively small air-gap raises fears of eddy current losses in both the ferrous and the magnet poles.

To assess the severity of such losses, a 2 dimensional finite-element package with a rotating machine simulation facility offered by Vector Fields[68] RM-Solver was used. An equivalent radial-flux machine with similar values of pole pitch, airgap etc was modelled, Figure 7.16. The results indicated that the losses were significant if mild steel

was used for the ferrous poles and therefore composite poles were necessary to reduce the heating and losses.



Figure 7.16 Pole face losses

7.10 Prototype Dimensions

The lumped parameter circuit approach was programmed into Excel to aid the design process. A target rating of 12kVA at 1500rpm, 415V was proposed and Table 7.1 provides details of the machine dimensions, and Table 7.2 provides the electrical parameters. Before the initial prototype was constructed, shaft saturation was not properly allowed for, nor was the stator leakage reactance modelled in detail. For these reasons the prototype did not achieve the target 12kVA rating. However once experience had been gained from the prototype, and the model improved to reflect shaft saturation and stator leakage, the model provided a reasonable representation of the real machine discussed in Chapter 8.

Description	Units	Dimensions
STATOR OD (ACTUAL)	mm	286
STATOR ID	mm	160
STATOR TOTAL WIDTH	mm	85
STATOR BACK IRON	mm	51
SLOT DEPTH	mm	17
SLOT WIDTH	mm	10.5
NO. OF SLOTS		24
SHAFT OD (BETWEEN ROTOR PLATES)	mm	97
SHAFT ID	mm	47
SHAFT CSA (MAX)	mm ²	5655
SHAFT CSA (INCLUDING HOLES)	mm ²	4651
HOLE DIAMETER IN SHAFT	mm	10
NO. OF HOLES IN SHAFT (radial x axial)		4x3
ROTOR PLATE OD	mm	276
ROTOR PLATE THICKNESS	mm	26
INTER-POLAR HOLE DIA (HOLES FOR ASSEMBLY)	mm	16
MAGNET THICKNESS	mm	9
MAGNET/FERROUS POLE OUTER RADIUS	mm	135
MAGNET/FERROUS POLE INNER RADIUS	mm	80
MAGNET/FERROUS POLE ARC		2/3
SHIM THICKNESS	mm	7
EXCITER OD	mm	130
EXCITER ID	mm	105
EXCITER LENGTH	mm	85
ROTOR PLATE SKEW	deg	7.5°
AIR GAP	mm	1.5

Table 7.1 12kVA machine dimensions

Description	Units	Dimensions
STATOR CONNECTION		SERIES STAR
NO OF STATOR TURNS/PHASE		272
TURNS/COIL		34
WIRE DIA	mm	1.8
COIL/POLE/PHASE		2
EXCITER COIL		
EXCITER COIL WIRE DIA	mm	0.85
NO. OF TURNS ON EXCITER		1500

Table 7.2 Electrical parameters

7.11 Discussion

A new type of synchronous generator has been described which is likely to be more compact and efficient than conventional machines. The 3 dimensional structure makes the electromagnetic analysis difficult with complex leakage fields in parallel with an excitation coil and shaft that can saturate in either direction. To simplify this complex problem saturation has been ignored in the pole, teeth and core to at least keep these elements linear. These areas are over sized and restricted to moderate flux density levels. The author has focussed primarily on zero power factor operation initially as this is the most demanding operating point and forms the basis for the equivalent circuit. However Q axis stator leakage inductance has been accounted for in the model.

Chapter

8.

The Haydock Brown Machine Construction and Test

The following chapter discusses the construction and test of a 4-pole HB machine with a nominal rating of 12kVA. Test results are compared to predictions, observations made and design improvements suggested.

8.1 Stator Assembly

The stator was constructed from strips of M4 material 0.3mm thick and wound in a toroidal fashion on a mandrel. This meant the internal diameter of the core could be accurately controlled but the outer diameter had some variation. The outer diameter can never be exactly round and so this variation had to be accommodated in the stator support system. Milling formed the slots in the toroidal core. There was some difficulty during the milling process as the tool distorted the slot. The solution was to support the area around the slot with a jig to reduce this distortion. Figure 8.1 provides a picture of the finished stator core.

For volume manufacture, slots can be punched prior to being wound removing the milling operation. The slot pitch would need to be varied as the core is wound but manufacturers have perfected this process.

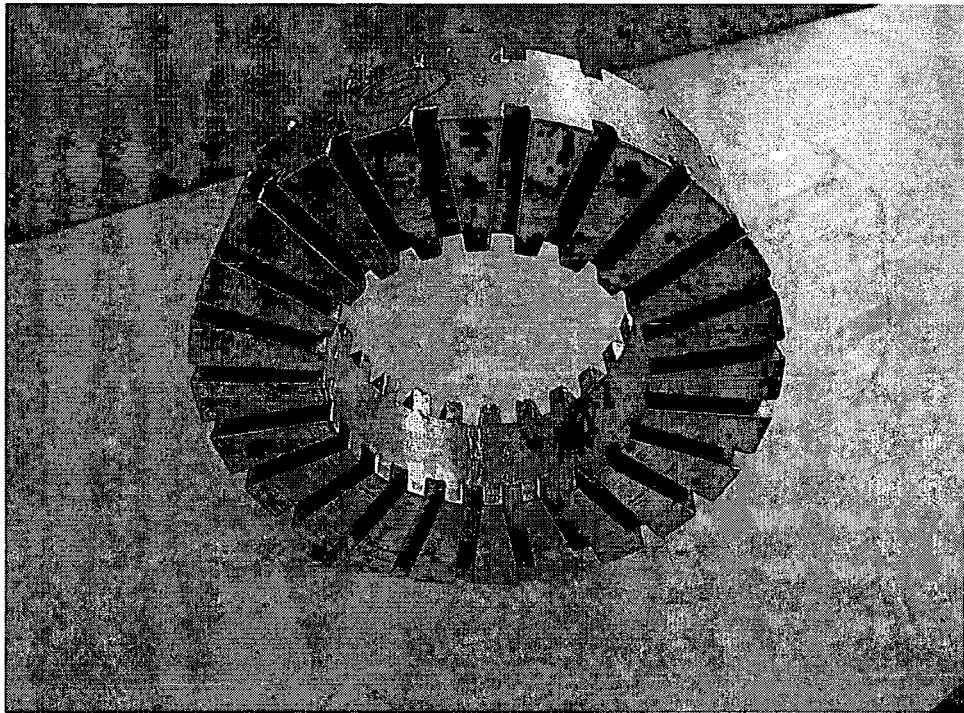


Figure 8.1 Finished stator core

Before winding the copper into the slots, the inner and outer circumference and the slots were insulated using Nomex/Polyester/Nomex (5/2/5) insulating paper suitable for a class H temperature rise. For a commercial machine, the slot liners could be moulded individually, or as part of a spider that incorporates insulation on the inner and outer surface of the stator as well as providing support for the excitation coil.

With reference to Table 7.2, thirty-four turns of 1.8mm^2 wire was wound into each slot using a toroidal winding machine, Figure 8.2. Here two adjacent coils are wound to form a group and the leads brought out. The stator had 24 slots and a 4 pole 3 phase star winding structure. As only two coils are wound at a time, cable ties are required to secure the coils in position. There was some difficulty winding copper into the slots, as downward facing slots were wound blind, and the fills for these slots was not as good as

the slots facing upward. The copper in the slots was tapped back with a block and mallet to ensure they did not encroach in the air-gap, a high temperature adhesive was applied to hold the coils in the slots. Toroidal winding machines tend to wind in a given direction to prevent loss of tension. If slot '1' is a phase start, slot '2' is a group finish, and slot '8' a start and slot '7' a finish for the next group. The windings are fully pitched and four groups in series make up the required 272 turns.

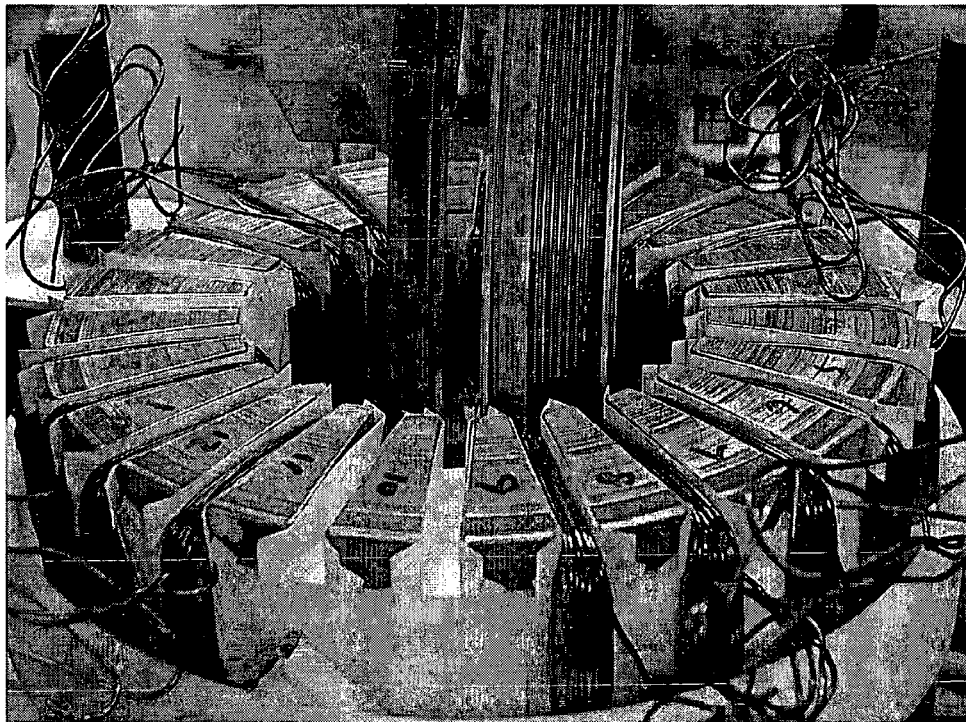


Figure 8.2 Stator during winding process

The excitation coil was constructed from 1500 turns of 0.85mm diameter, wound onto a former, taped, removed from the former and then impregnated. Nomex paper was then wound around the outer circumference to insulate the excitation coil from the main stator winding, Figure 8.3. Final coil Dimensions were: outer diameter, 130mm, inner diameter 105mm and length 85mm.

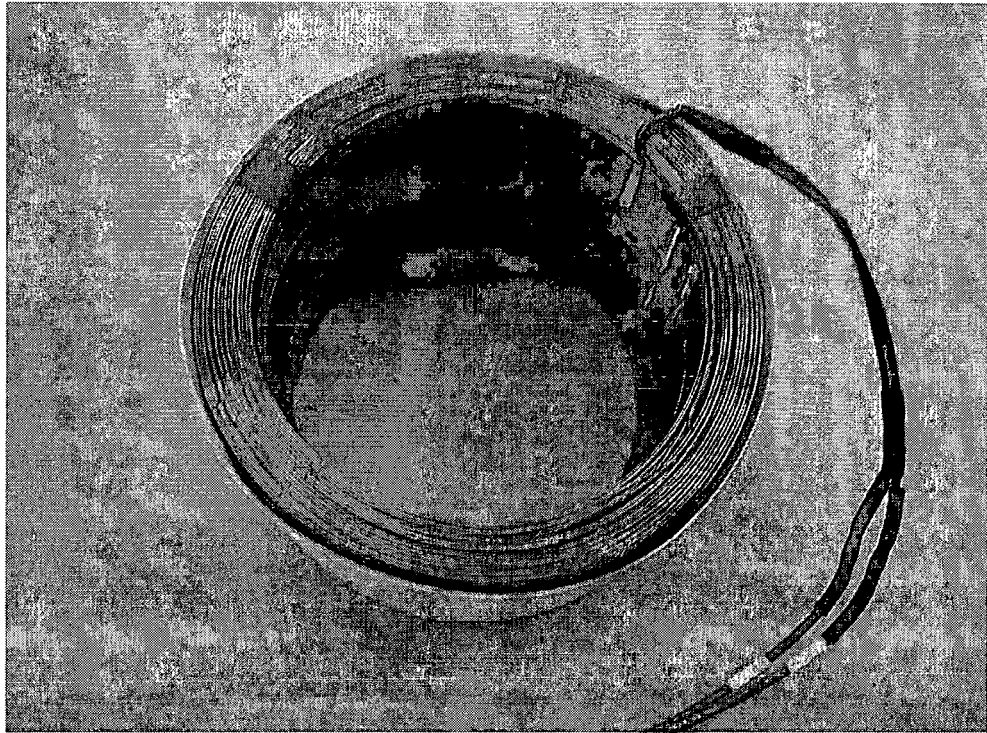


Figure 8.3 Finished excitation coil

Fortunately the end windings on the stator inner diameter of the armature winding splayed during the winding process, allowing a coil larger than originally specified to be inserted. Figure 8.4 shows the finished stator. There was some give in the windings and the coil had to be tapped into position using a mallet. Cable ties threaded through the stator end windings were used to provide additional support to the coil.

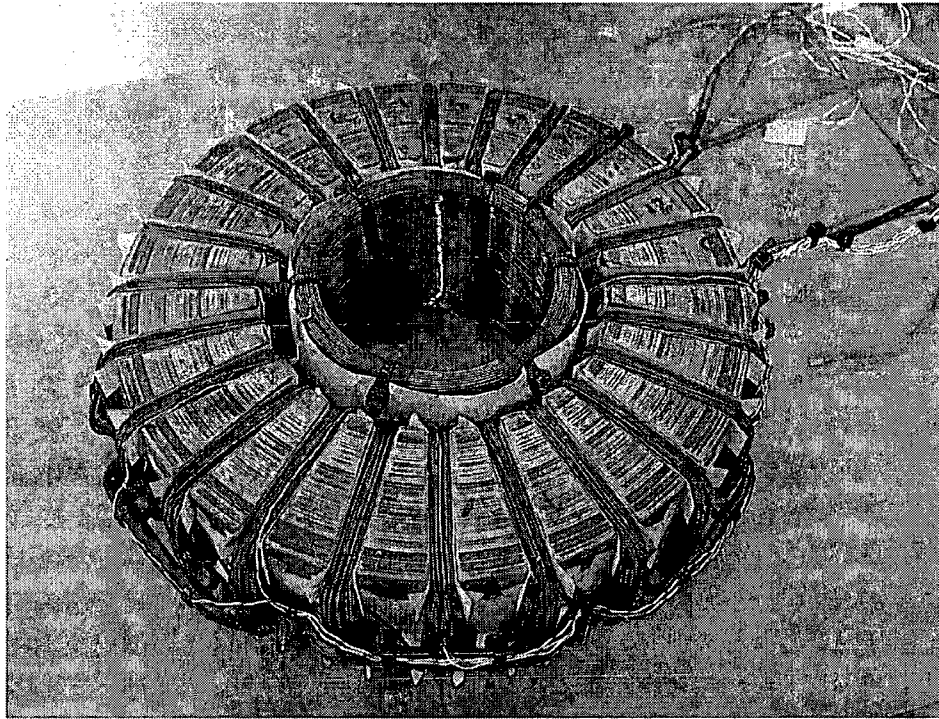


Figure 8.4 Complete stator

The leads for the excitation coil are fed through the same stator slot for access to the excitation supply, and to avoid any mutual coupling effects. A conventional electronic automatic voltage regulator (AVR) of a few hundreds watts was used to control the coil excitation. The AVR takes its power from the main stator output winding and is rated between 190-250V. A single thyristor delivers current to the excitation coil and has a maximum continuous rating of 4A. The coil resistance was designed to ensure no more than 7.5A could be drawn from the AVR, which is the maximum transient current the AVR can deliver.

8.2 Rotor Assembly

The shaft was machined from EN1A steel which has a low carbon content with a good BH characteristic, see Figure 7.6 which is based on a measured sample. The shaft was hollow at one end with four 10mm diameter radial holes placed in three rows axially along the shaft, this allowed air to be drawn into the centre of the machine, Figure 8.5. The drilled and taped holes in this figure allow the rotors to be bolted onto the shaft. Each plate was bolted to the shaft but indexed with respect to each other by half a slot pitch to reduce tooth ripple in the output waveform. Hence the pairs of holes shown in Figure 8.5 show that the machine could be tested with and without a skew.

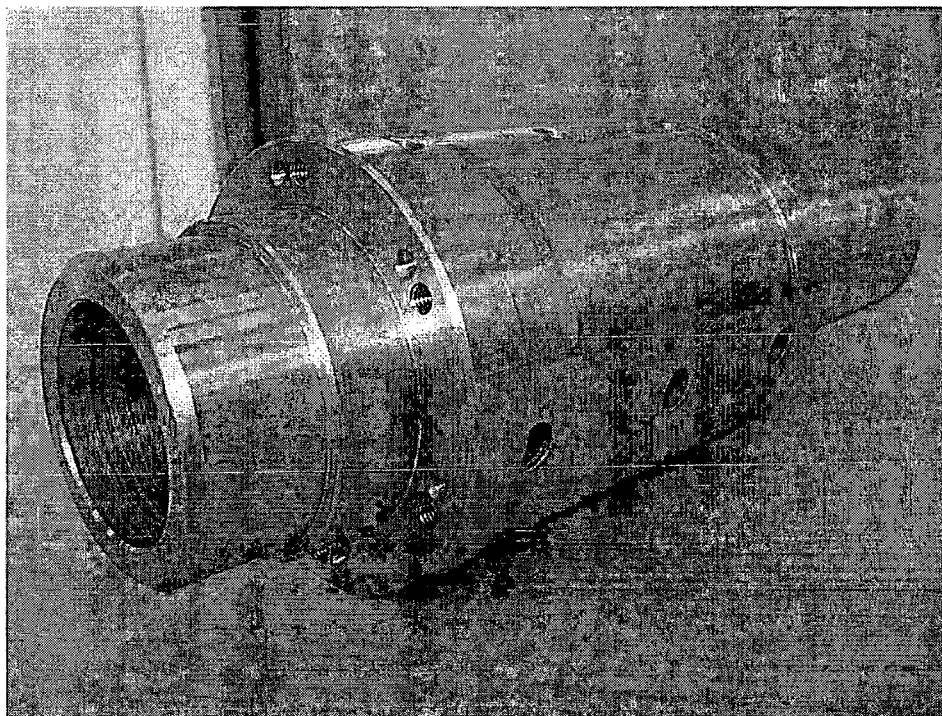


Figure 8.5 Non drive end view of shaft

The rotor plates are cast from AM1 grade steel, Figure 8.6, which also has a low carbon content and good BH characteristics. Bolted onto these plates are the magnets and ferrous

pole shims. The shim was an attempt to reduce inter-polar leakage flux by spacing the rotor discs further away from the stator. The ferrous poles are made from composite material (Somaloy 500) to reduce additional eddy current losses caused by the wide slot openings. The magnets and composite poles are glued to the shim with high temperature adhesive, Permabond F246. As an additional safety measure a commercial machine would perhaps require a non-ferrous spider to provide axial and radial support to the magnets and composite poles. For volume manufacture the shaft and one of the rotor plates are likely to be cast as one piece to save material and machining operations. Each disc has a machined area on the back to support balance weights and through holes to aid assembly.

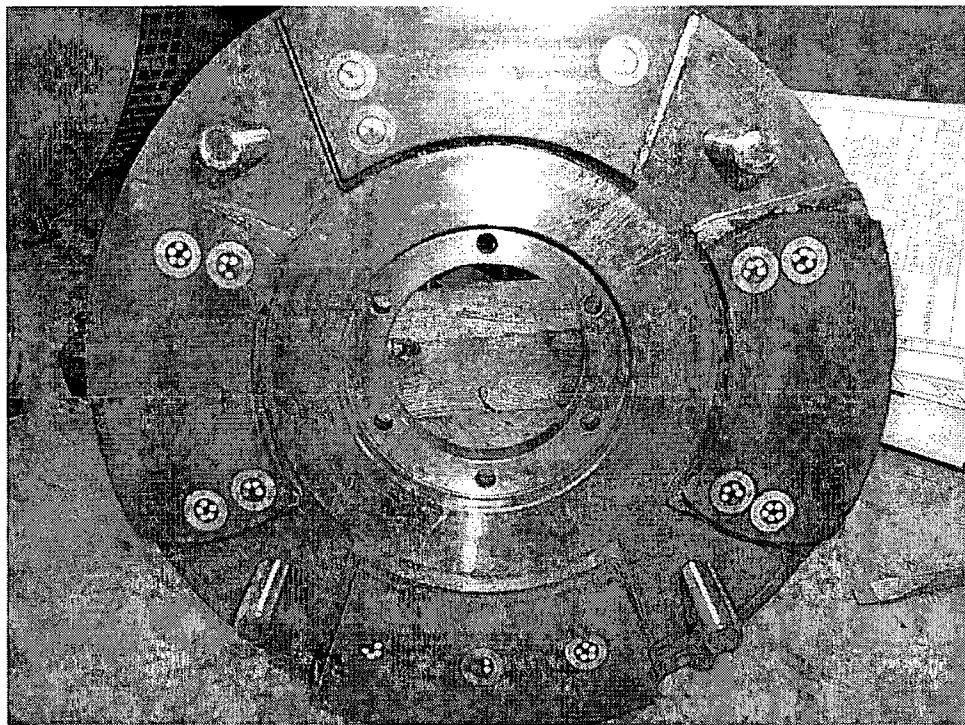


Figure 8.6 View of rotor plate

8.3 End Brackets

Two symmetrical end brackets were used to provide bearing support for the shaft and support for the stator with respect to the rotors. Both end brackets are cast from aluminum so as not to promote additional leakage flux. Figure 8.7 shows one of the end brackets. A steel insert was required to reduce wear and provide accurate location of the bearing. Clamping teeth are machined to locate onto the stator core pack providing stator support. This arrangement caused some assembly issues, as the stator clamping teeth had to be tailored to suit the stator core pack. For volume manufacture tight tolerance of the support teeth and core pack would be required to make the system work commercially. The end brackets are likely to be manufactured from high-pressure die-casts for a commercial machine. This would aid volume manufacture, reduce material and remove a number of machining operations.

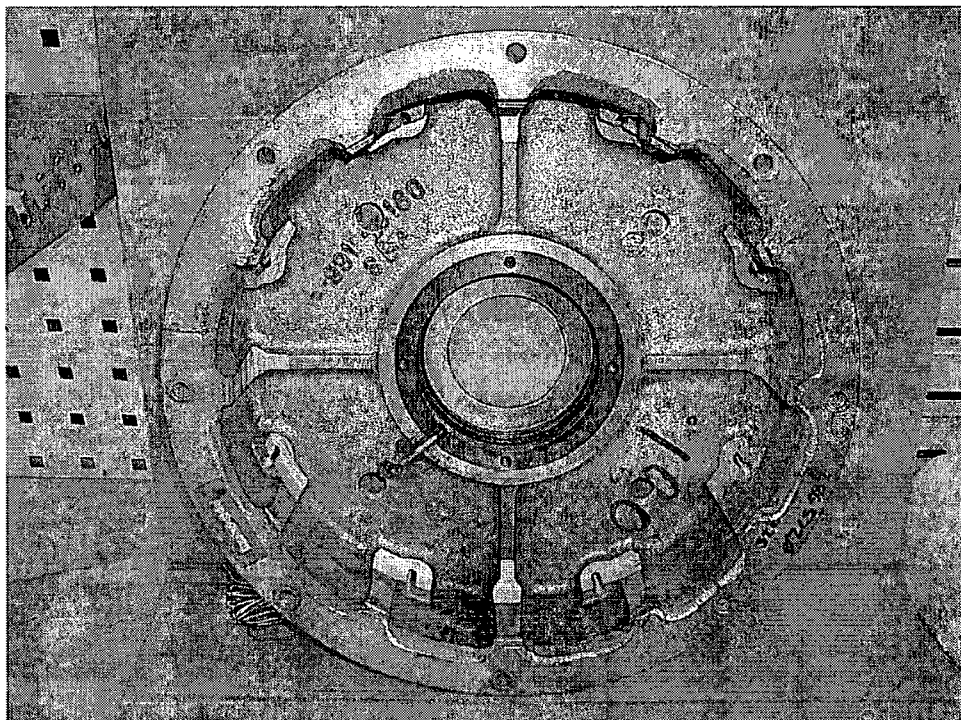


Figure 8.7 Aluminum end bracket

8.4 Assembly

The generator was assembled by first bolting the drive end rotor plate to the shaft and supporting the shaft within the drive end bracket. With the non-drive end of the shaft facing vertically upwards, the stator was lowered into position. To prevent the rotor magnets pulling the stator down, threaded bolts are placed in the rotor so that the stator can be offered to the rotor in a controlled manner. Once the stator is located on to the end bracket teeth, the bolts are removed from the rotor and placed into the non drive rotor plate ready to be offered to the stator. This allows the non drive end rotor to be positioned in a controlled manner. Once the non drive end rotor plate is in position the non drive end bracket is bolted into place and the machine is assembled.

Generators are normally coupled to engines using the Society of Automotive Engineers (SAE) standard flywheel and coupling arrangements, which for this machine was SAE 5 for the flywheel housing and SAE 6.5 for the coupling. This allows the generator to be coupled to most industrial engine types of similar rating. Figure 8.8 shows the generator coupled to a Lister engine for test. The compactness of the new generator topology is clearly apparent from this figure.

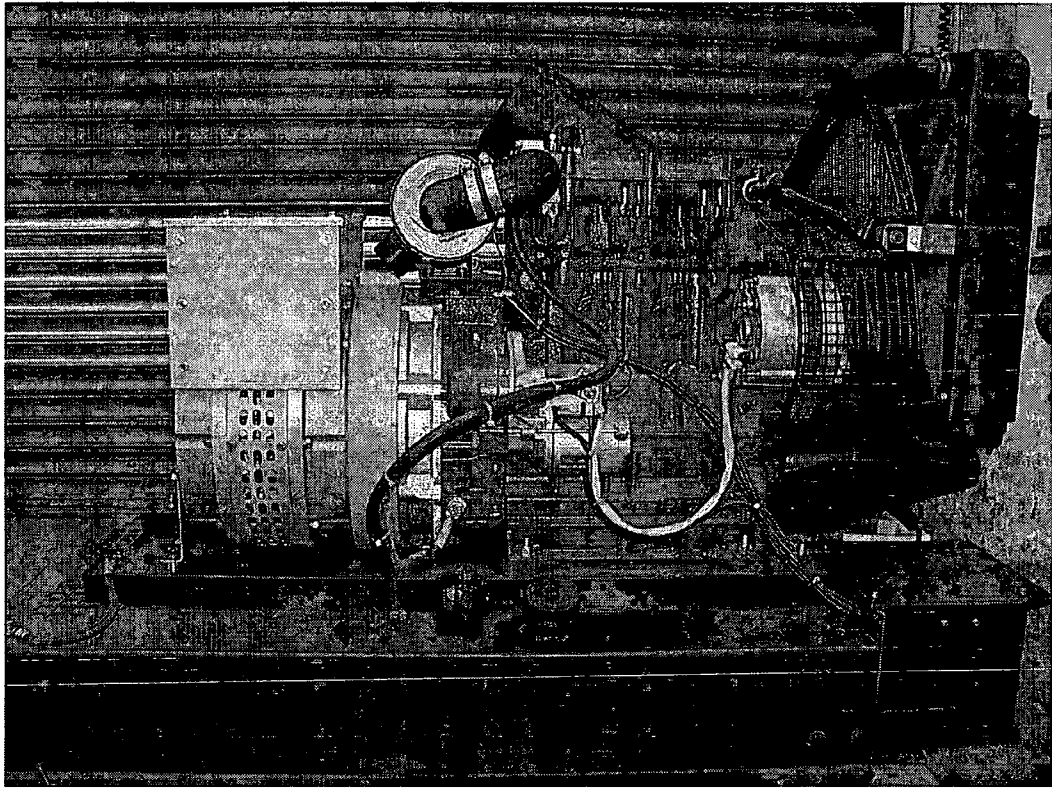


Figure 8.8 Complete generating set

8.5 Test and Validation

A number of tests were carried out and comparisons were made with predictions derived from the magnetic equivalent circuit model in Chapter 7.

8.5.1 Static Inductance Test

The stator core was tested independently and placed on a non ferrous bench. One phase was energised with 50Hz current of 10 Amps and the voltage was measured. Making an allowance for phase resistance the leakage inductance was calculated, Table 8.1.

V	A	R	Z	X_L	L(mH)
24.5	10.0	0.5	2.5	2.4	7.6

Table 8.1 Measured slot leakage and end winding leakage inductance

As the stator is free standing, the flux distribution on the stator sides and on the inner diameter is different to that when the stator is within the machine. Making allowance for these differences but applying the same calculation methods discussed in Chapter 7, the stator leakage reactance was calculated to be 2Ω . There are two main sources of error in this calculation. Firstly the leakage flux on the stator corners has not been included, secondly the stator only had one phase energised at a time, which is likely to include additional harmonics. No correction was made to the calculated reactance for the values are acceptably close to measured bearing in mind the complex nature of such fields when the machine is in operation. For example the end brackets are aluminum and likely to screen out any corner fields on the stator due to eddy current effects. When the machine is loaded for 3-phase operation the space harmonics will reduce.

8.5.2 No Load Voltage Waveform

Figure 8.9 shows the no load line to neutral voltage. Clearly a respectable voltage waveform has been generated. For example the no load voltage line to neutral had a Total Harmonic Distortion (THD) of 4.4% and the line to line voltage had a THD of 4%, see Table 8.2. In industry machines with a THD of less than 5% are widely accepted.

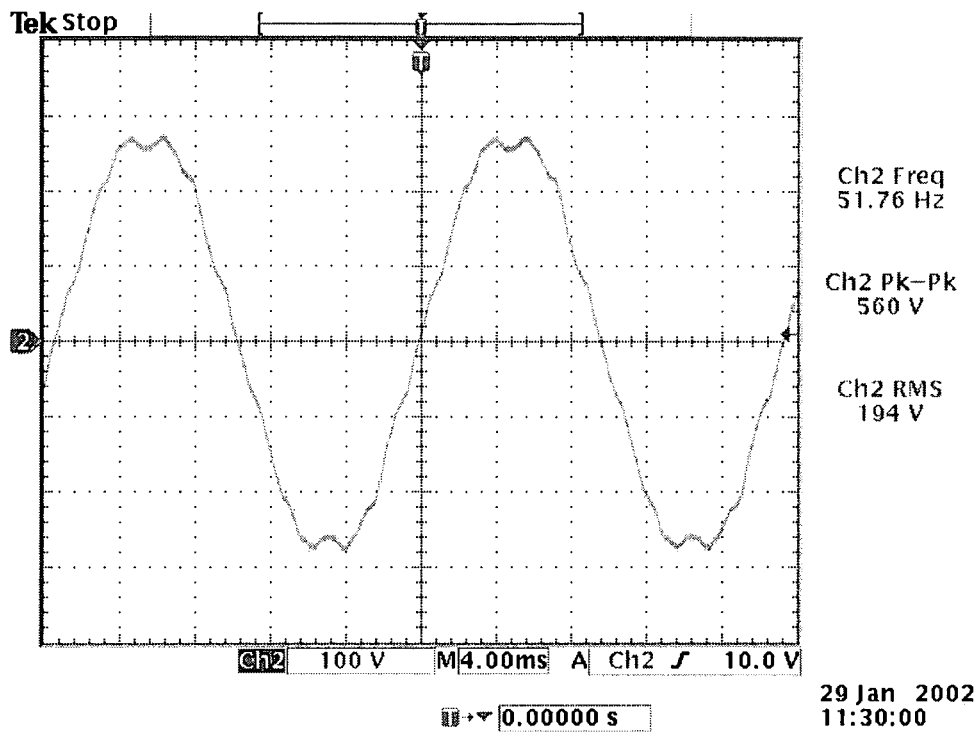


Figure 8.9 No load voltage waveform line to neutral

There still appears to be a finite trace of slot ripple in the no load waveform which could be improved by smearing the magnet and/or pole sides to reduce the reluctance variation.

	V_{L-L}	%	V_{L-N}	%
1	357.2	100.0	196.5	100.0
3	0.911	0.3	2.2	1.1
5	10.61	3.0	6	3.1
7	4.85	1.4	2.6	1.3
9	0.134	0.0	0.45	0.2
11	8.79	2.5	5	2.5
	THD	4.0	THD	4.4

Table 8.2 Compares no load, line to line and line to neutral voltages

8.5.3 Full Load Waveforms

As expected with a fully pitched coil when load was applied the harmonic distortion increased as armature reaction interacts with the excitation flux. Table 8.3 provides a harmonic analysis of the voltage for a 0.8 power factor load current of 8.4A and a coil current of 1.8A.

	V _{L-L}	%	V _{L-N}	%
1	350.80	100	200.00	100
3	0.93	0.27	17.93	8.97
5	5.84	1.66	3.06	1.53
7	2.70	0.77	1.51	0.76
9	0.28	0.08	2.72	1.36
11	7.00	2.00	4.07	2.04
	THD	2.7	THD	9.4

Table 8.3 Harmonic analysis for 0.8 power factor load

Table 8.4 presents the harmonics in the voltage waveform for unity power factor load.

The load current was 14A and the coil current 1.7A.

	V _{L-L}	%	V _{L-N}	%
1	343.20	100	199.70	100
3	1.65	0.48	30.30	15.17
5	3.60	1.05	0.86	0.43
7	1.20	0.35	1.35	0.68
9	0.03	0.01	2.68	1.34
11	4.25	1.24	2.28	1.14
	THD	1.7	THD	15.1

Table 8.4 Harmonic analysis for 1 power factor load

The triplen voltage harmonics tend to cancel in a 3-phase system hence the 3rd, 9th, etc are suppressed in the line to line voltages and the THD reduced.

The third harmonic voltage for the loaded condition is quite high for line to neutral loads and malfunction of technical loads is a possibility. This problem can be easily resolved by short pitching the windings. A two-thirds pitch is particularly suited to cleaning up the third harmonic. One small point to note with a two-thirds pitch is that it also acts as a current sink for third harmonic currents that cause additional heating in the machine, an issue very rarely recognised in the industry.

With respect to this machine a single layer winding is desirable to keep the winding structure simple. This complicates the winding design as a two-thirds pitch winding is more easily achieved with a double layer winding. A single layer winding is possible with a fully pitched coil in series with a coil short-pitched by 60 electrical degrees. Unfortunately this results in a poor winding factor of 0.727.

A more suitable alternative is to index the rotor plates with respect to each other. That is if the plates are indexed with respect to each other by 2 slots (60 electrical degrees), the 3rd harmonics will cancel. Slot ripple has to be reduced so indexing the plates by 1½ slot pitch will significantly reduce the triplen harmonics and suppress the slot ripple. This will result in an effective winding factor of 0.89.

8.5.4 No Load Magnetisation Curve without Magnets

The machine was first constructed without magnets so that the performance of the excitation coil alone could be assessed. Figure 8.10 shows the no load magnetisation graph without magnets, this was obtained by monitoring the output voltage and varying

the dc current in the excitation coil. From this graph the measured and calculated values follow a similar trend demonstrating the shaft model is reasonably good. The BH characteristic in the model was measured from a sample of material used in the shaft. Other than the shaft the rest of the magnetic circuit will operate with very low flux density and is likely to be linear. The calculated values differ from the measured with respect to the air-gap and leakage field reluctance, identified by the different air-gap lines dotted in Figure 8.10. Comparing measured with calculated there is a maximum error of 13.9% at 0.5A and a minimum error of 5.4% at 4A.

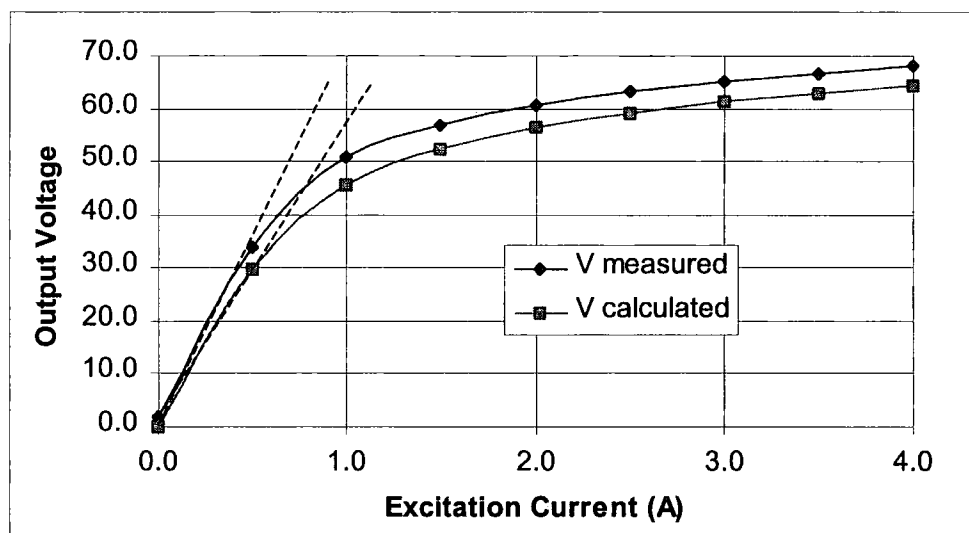


Figure 8.10 No load magnetisation graph without magnets

8.5.5 Short Circuit Curve without Magnets

Figure 8.11 highlights the short circuit curve for the machine without any magnets. Here the output of the machine was shorted through a power analyser and the output current with respect to excitation current recorded.

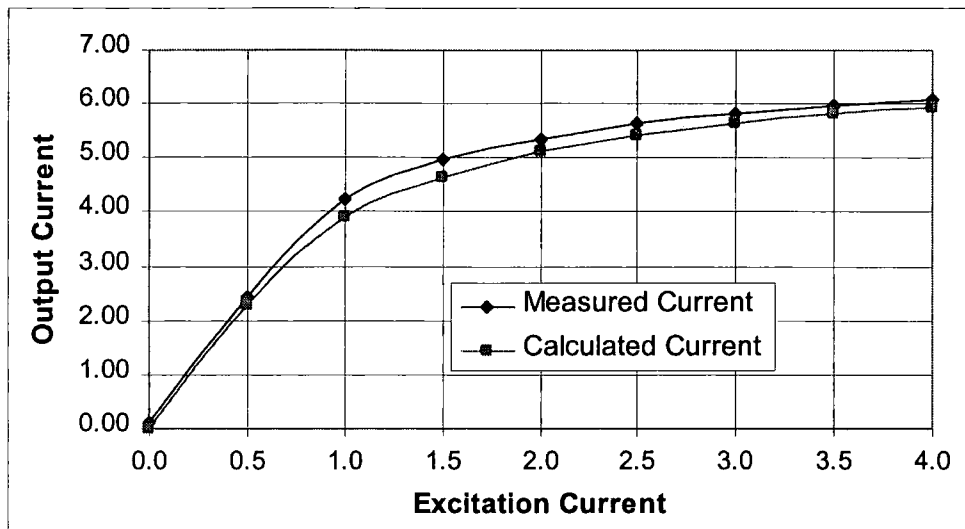


Figure 8.11 Short circuit curve without magnets

For low and high excitation currents there is very good agreement between measured and calculated. This suggests the stator armature leakage is well represented in the equivalent circuit. There is a maximum error of 8.3% at 1A but it has already been identified that the air-gap and leakage fields are not quite correct. For an excitation level of 4A the error reduces to 2.4%. The calculated level of current being lower than measured is consistent with what was observed for the no load case, Figure 8.10. The low levels of short circuit current ensured thermal effects did not mask the measured results.

8.5.6 Open Circuit Voltage with Magnets

With the magnets in the machine the excitation coil current was varied from -4A to $+4\text{A}$ and the no load output voltage monitored. The close correlation between measured and calculated shown in Figure 8.11 is extraordinarily close considering the imperfections in the magnetic circuit. For example with no allowance made for pole, teeth or core-back in the magnetic circuit, a measured voltage lower than calculated was expected. Magnets

also have variable performance, which was discussed in Chapter 5. Therefore the close correlation is due to a combination of second order effects such as those described above negating some of the basic assumptions in the model. Points to note are that the calculated voltage as a result of the excitation coil is still underestimated. For the -4A loading point the shaft is heavily saturated as the coil and magnets are forcing flux into the shaft in the same direction, hence the calculated and measured voltages are similar.

This open circuit voltage, Figure 8.12, was taken before the machine had any load applied. After various loads were applied the no load magnet voltage tended to stabilise at a slightly lower level of around 194V compared to an initial 201V . The author has observed this effect before in permanent magnet machines and should be recognised as a general issue with permanent magnet machines. The no load magnet voltage was observed to vary slightly from day to day both up and down.

Comparing Figures 8.10 and 8.12 reveals that the effect of the field current is greater when magnets are present. For example, a 4A field current applied in the absence of magnets causes an EMF of just under 70V to be induced, whereas the same current increases the EMF by around 110V when used in conjunction with magnets. The difference is a consequence of the non-linear behavior of the shaft. Magnets produce flux in one direction and the current first reduces this to zero, then creates shaft flux in the opposite direction. The available range, if leakage and magnetic loading in the shaft is ignored, could be double compared to the case of no magnets, assuming the machine is designed so that the magnets alone fully saturate the shaft.

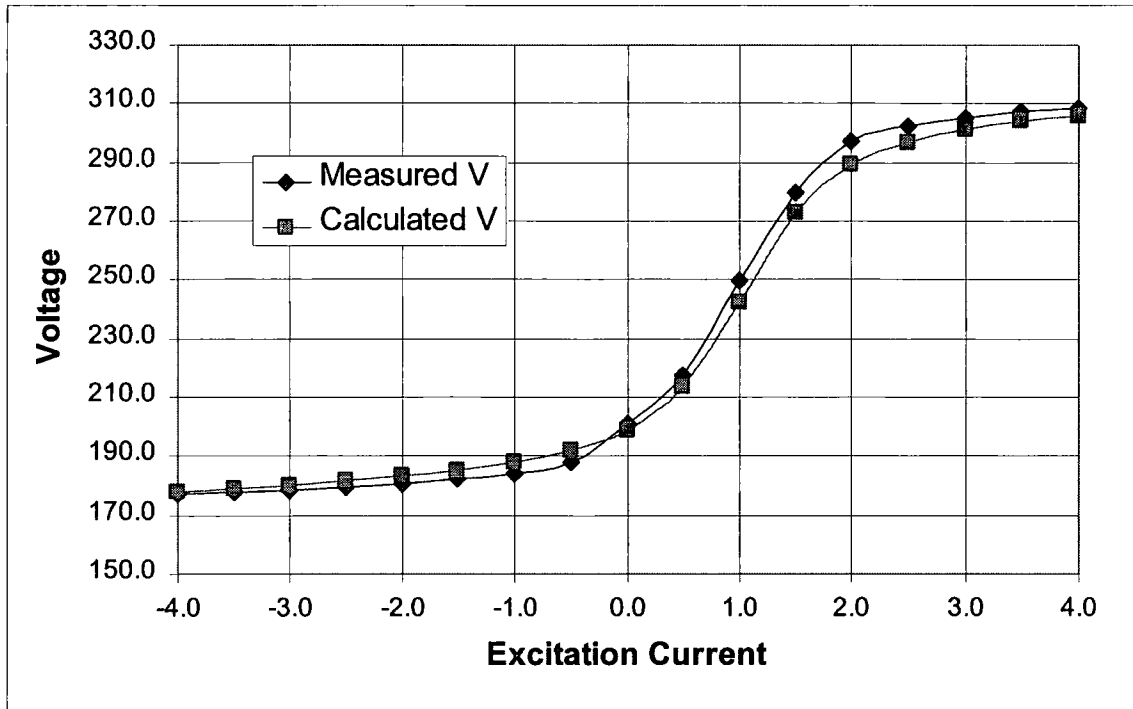


Figure 8.12 No load voltage with magnets

8.5.7 Zero Power Factor Loading

Here the coil excitation current was fixed for different excitation levels, zero power factor load applied and the terminal voltage recorded, Figure 8.13. The measured no load voltage was slightly lower than calculated but as load current increased the measured voltage was higher. This observation suggests the calculated internal impedance was slightly high.

The model did not include an allowance for the increased magnet temperature due to the proximity of the stator as load current was drawn. Therefore the calculated results should have been slightly higher than measured. This discrepancy is likely to be the result of a higher calculated leakage reactance.

Overall there was very good agreement between measured and calculated performance, indicating that the parameters representing the permanent magnets, ferrous poles, non-linear shaft and the D-axis armature MMF are acceptably accurate.

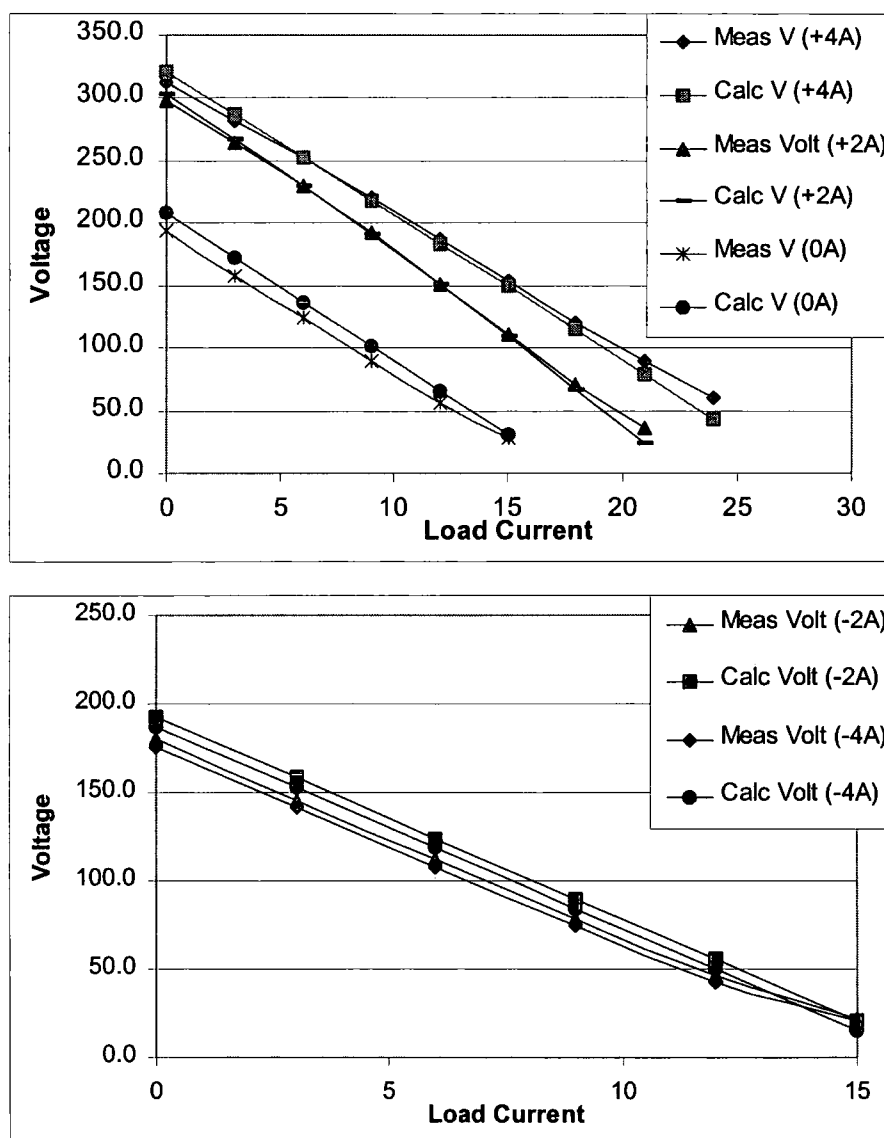


Figure 8.13 Zero power factor loading with fixed excitation

8.5.6 0.8 Power Factor Loading

Tests were repeated but this time with a 0.8 power factor load. 0.8 power factor was chosen, as most standalone generators are sold commercially at a 0.8 power factor rating. Clearly from Figure 8.14 the model has represented the machine very well. As with the zero power factor case the predicted no load voltage was higher but the model had slightly higher internal impedance

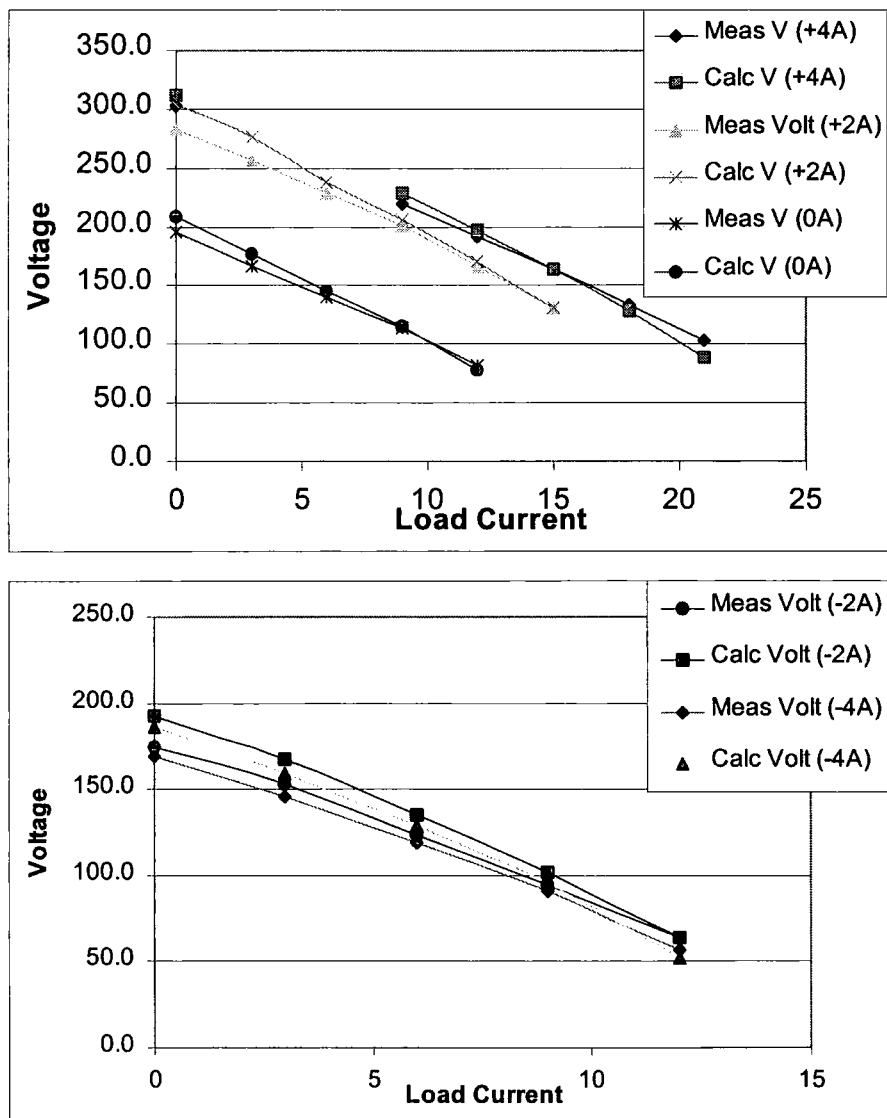


Figure 8.14 0.8 power factor loading for fixed excitation

8.5.7 Unity Power Factor Loading

All tests have been performed with a diesel engine as the prime mover. With finite power available from the engine there was some difficulty regulating the speed as load was applied, with calculated and measured results suffering from slight frequency variations. For the +4A case the tests had to be performed by first loading the generator to limit the amount of power drawn from the engine, hence the incomplete set of results. Other than for the 0A excitation case all the calculated results were greater than measured. This discrepancy is likely to be due to how the Q axis flux is modelled. Modelling in the Q axis is more difficult than the D axis with flux paths not as well defined. Bearing in mind that the lower power factor load is more demanding and will establish the rating of the machine, the unity power factor readings are acceptably close and clearly follow the trend of the measured result. For the 0A case it is not clear why this has not followed a similar trend to the other results. However maintaining engine speed was difficult and experimental error will be present.

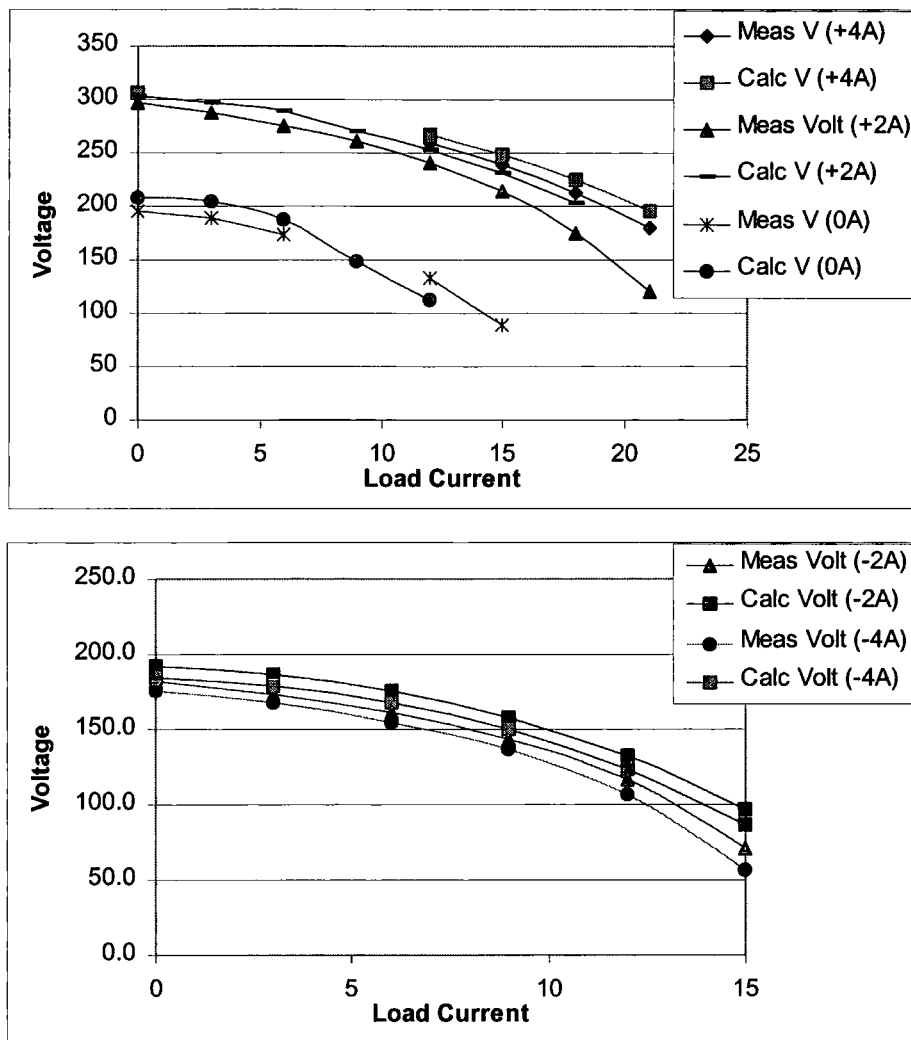


Figure 8.15 Unity power factor loading for fixed excitation

8.5.8 Thermal Tests

Cooling this machine was a concern as the required shaft cross sectional area restricts the available cross sectional area for the cooling circuit. In addition the excitation coil obstructs the airflow. Any compromises in terms of the shaft cross sectional area or area available for the excitation coil compromised the electromagnetic performance of the machine. The machine is unusual in that the shaft has to be sized to provide the required flux, to give the internal EMF. In more conventional machines the magnetic circuit for

the armature and the excitation system are shared, so that the magnetic cross sectional areas do not have to be oversized to support the required internal EMF. A decision was made by the author to design for the highest electromagnetic torque possible and accept the compromised thermal performance. This seemed logical, as an effective cooling system would be of no value if the machine could not transmit enough torque to match the thermal limit.

The main observation during testing was that as the machine was loaded the magnet performance tended to degrade with temperature, placing more emphasis on the excitation system. As a direct result of the shaft saturating, when the machine was loaded and the terminal voltage being maintained at a constant level, it was easy to over excite the coil, as an increase in excitation did not give a relative increase in flux. This coupled with the increasing stator resistance as temperature increases also put additional demands on the excitation system. For these reasons the thermal loading of the machine is quite moderate.

Time	Volts	Amps	kW	kVA	Excitation (A)	Excit. coil Temp. (°C)	Air In (°C)	Air out (°C)
09:30	200.6	-	-	-	0.320	28	9.9	21.8
09:35	202.9	9.99	-	6.079	2.364	38	11.3	25.3
09:45	203.4	10.09	-	6.179	2.437	46.8	12.8	29.3
10:00	203.9	10.39	4.940	6.349	2.6411	57	13.8	33.3
10:15	204.7	10.55	5.226	6.461	3.4391	81.2	12.5	38.1
10:30	203.1	10.42	5.141	6.343	3.257	94.4	15.8	42.5
10:45	202.1	10.36	5.085	6.274	3.2161	97	16.4	45.8
11:00	201.2	10.31	5.043	6.220	3.180	100.6	19.8	42.5
11:15	200.7	10.23	5.017	6.187	3.1666	100.1	15.6	48.8
11:30	200.2	10.25	4.987	6.152	3.1466	102.2	16.3	49.1
11:45	200.1	10.25	4.983	6.144	3.1364	105.2	18.4	51
12:00	199.7	10.23	4.957	6.122	3.1216	105.3	18.3	50.9
12:15	199.4	10.21	4.948	6.101	3.1143	105.6	17.5	50.9
12:30	199.3	10.21	4.945	6.097	3.1132	103.9	16.1	51.9

Table 8.5 6kVA 0.8 power factor heat run

Table 8.5 provides details of the temperature of the machine after a 3-hour heat run when loaded with 6kVA at 0.8 power factor. At shut down the rise by resistance on the stator windings was recorded as 67K. Clearly the excitation current has increased from 2.64A cold to 3.1A hot. A 6.5 kVA at 0.8 power factor loading was tried but the excitation coil went into a thermal run away condition.

In addition a unity power factor load of 9kVA was applied to the machine, Table 8.6.

While the author is well aware of the lower excitation duty for a unity power factor load, the performance for this machine was significantly improved. The excitation levels are clearly much lower and the load could have been increased further. Unfortunately the power available from the engine was limited and so this loading does not reflect the maximum power from the generator. The rise by resistance for this loading at shut down was 90K.

Time	V	A	kW	Excitation (A)	Excit. coil Temp. (°C)	Air In (°C)	Air out (°C)
08:25	197.1	-	-	-	9.900	11.5	10
08:30	200.4	15.38	9.122	1.966	18.4	12.2	20.3
08:45	200	15.38	9.122	2.049	34.6	13.2	30.7
09:00	200	15.38	9.117	2.092	43.8	13.8	34.5
09:15	200	15.38	9.121	2.1528	50.9	13.7	41.2
09:30	200	15.38	9.124	2.1928	61.1	14.6	45.4
09:45	200	15.37	9.122	2.2507	69.9	15.2	51.6
10:00	200	15.38	9.124	2.281	76.9	15.3	54
10:15	200	15.36	9.122	2.3055	77.1	16.2	55.8
10:30	200	15.36	9.113	2.3345	82.2	15.9	56.2
10:45	200	15.36	9.111	2.3717	84.6	17	60.1
11:00	200	15.36	9.117	2.3977	87.7	16.7	59.5
11:15	200	15.36	9.114	2.4187	89	17.8	61.7
11:30	200	15.35	9.112	2.436	90.8	18.8	63.3

Table 8.6 9kVA, unity power factor heat run

8.6. Design Variations

The magnetic equivalent circuit model has been demonstrated to provide a reasonable representation of the machine at 0.8 power factor, and was used with confidence to study the effect of varying the stator inner diameter on the rating of the machine. Regulated output voltage and fixed stator outer diameter were assumed. A solid shaft was assumed with diameter set by the stator inner diameter and the radial thickness of the excitation coil. The magnet and iron pole radial dimensions were adjusted to be the same as the stator. The rotor plate thickness was adjusted to avoid saturation.

To assess the useful range of load current, for which voltage regulation can be achieved, the no load voltage due to the magnets alone was taken as a reference. The excitation coil was energised with its thermal limit of 4500 AT; although this limit would vary somewhat according to the machine dimensions. Load current at 0.8 power factor was applied and the voltage recalculated. The load current was adjusted until the voltage was equal to the original voltage created by the magnets alone. Figure 8.16 presents results from these studies. Figure 8.16a shows the voltage and current for varying stator inner diameter, expressed as a fraction of the outer diameter. Figure 8.16b gives the corresponding VA capacity displaying a shallow curve that peaks around 0.63.

The effect of the excitation coil cross sectional area was assessed by increasing the stator inside diameter from 170 to 180mm, to provide space for an additional 5mm radial depth for the coil. The increased excitation current available is not reflected in increased

armature flux linkage and it is concluded that the machine has an inherent electromagnetic excitation limit set by shaft saturation.

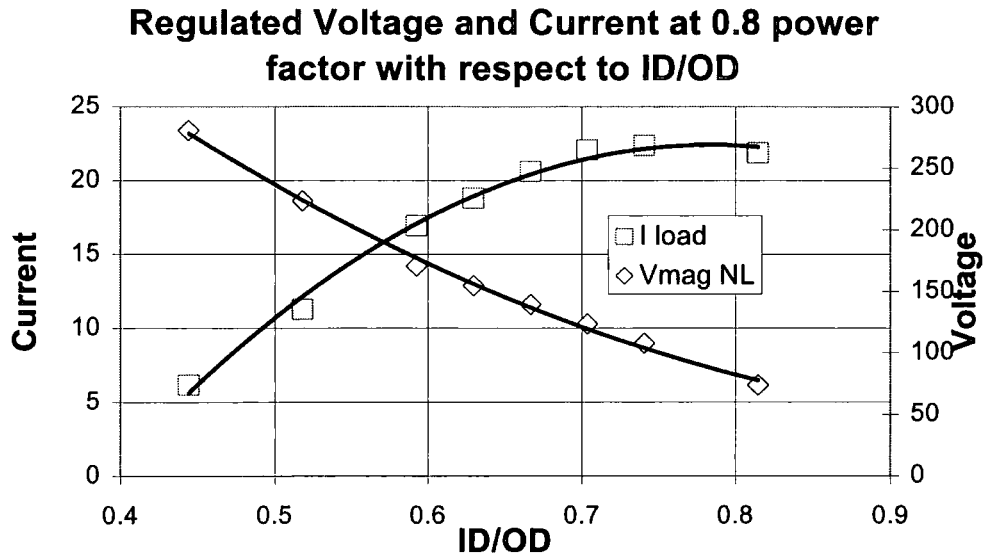


Figure 8.16a Output current and regulated voltage for 0.8 power factor

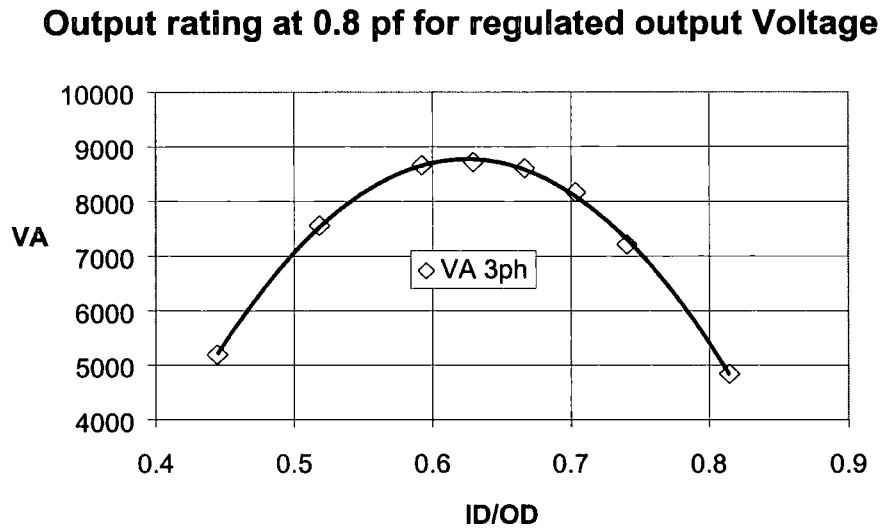


Figure 8.16b Variation in output rating for 0.8 power factor load

Figure 8.16 Design variations

The observation of an optimum ratio between inner and outer diameter corresponds closely with the theoretical ratio of $1/\sqrt{3}$ for axial flux machines with purely permanent magnet excitation.

Concluding that the machine design was near an optimum, alternatives for improvement were considered. For example a buck and boost controller was considered but did not provide much increase in power density.

8.7 The Haydock Brown Hybrid Machine

One observation was made by the author with respect to this research, is that reducing the shaft cross sectional had the counter intuitive effect of increasing the no load voltage. Unfortunately this increase in voltage became offset when load current was drawn, for the excitation coil lost its ability to compensate for the effects of armature reaction. This phenomenon gave rise to a new idea of replacing the ferrous poles with a hybrid of permanent magnet material and ferrous material, Figure 8.17. The advantage of this is first that the ferrous pole in the original Haydock Brown concept is under utilised electromagnetically. Secondly the hybrid magnet encouraged magnet flux to form in local loops between the rotor and stator, rather than taking a path through the shaft. In doing so the MMF requirements to set a given flux level within the machine is greatly reduced as MMF is not lost across the shaft. The machine therefore benefits from a higher no load voltage but retains the ability to counter the effect of armature reaction. One disadvantage of this arrangement is that when considering the case of magnets alone, the shaft is not as saturated when compared to the original HB machine concept. As

discussed earlier this affects the voltage range variation, as a fully saturated shaft allows the excitation coil to control twice the level of flux compared to the case when the shaft is saturated in just one direction only. However this limitation is offset by the net reduction in armature inductance due to the increased use of permanent magnet material.

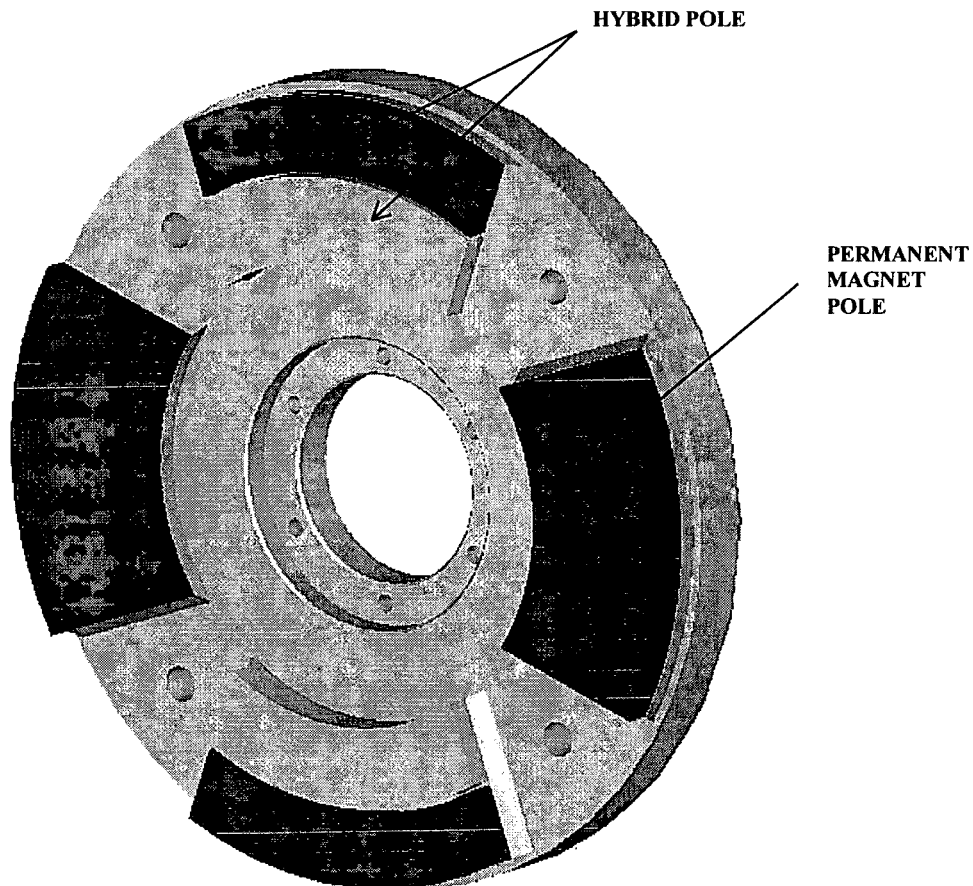


Figure 8.17 Rotor design of Haydock Brown Hybrid rotor plate

This concept was tested on the machine discussed with a 50% split between magnet and ferrous pole. Tests indicated that at 0.8 power factor the rating of the machine increased to 8kVA. This is a 33.3% increase in rating compared to a 50% increase in permanent magnet material. Commercially this appears to be a more attractive machine in terms of cost, weight, size and efficiency, and is the subject of future research.

8.8 Discussion

A new form of electrical machine offering brushless excitation control with low power dc circuitry has been successfully constructed, and improvements for a production machine discussed. The generator has been coupled to a diesel engine and tests compared to predictions. The lumped-parameter equivalent circuit model developed in Chapter 7 has been proven to provide a reasonable model of the machine. Some small refinement may still be required in the Q axis but not thought essential at this stage in the development.

While the design process is difficult once experience of prototype machines has been gained and relative comparisons made in FEA, designs can be readily adjusted with a degree of confidence.

Using the model in Chapter 7, an inherent excitation limit for the HB machine operated as a generator has been identified, and a maximum VA rating with respect to stator inner diameter over outer diameter has been shown.

In the future a novel Hybrid version of the original Haydock Brown machine appears to offer many advantages when compared to a conventional synchronous generator.

Conclusion and Further Work

9.1 Conclusion

The thesis has described two different axial flux generator topologies for the power generation industry. The Variable Speed Integrated Generating set (VSIG) has allowed full engine integration and benefited from a multi pole design, while the fixed speed arrangement offers many benefits within the existing synchronous speed market.

An electrical machine suited to variable speed power generation has been researched. The author would not claim to have contributed to either the concept of the TORUS machine nor to the advantages of variable speed operation. However taking a laboratory prototype of a few kW up to in excess of 50kW and making the machine ready for manufacture is an important development. The author has made a significant contribution to the research of the TORUS machine. Certain observations have been made concerning practicalities as well as developing design rules for the minimisation of magnet mass. VSIG's are likely to be introduced generally to the market in the medium to long term. Companies such as Hygen, Onan and Honda already market variable speed systems below 10kW's. The cost and reliability of the power electronics and associated controls are still causing concern in the market place for the higher ratings but certain applications such as UPS, military and telecommunications would readily benefit.

During the course of this research a novel machine designed for fixed speed operation has been researched that has many advantages over the conventional synchronous machine. Compact size and efficiency have been realised by the application of high-energy permanent magnet materials. The fundamental problem of regulating permanent magnet machines has been overcome, this historical breakthrough is likely to create a whole family of novel machines in the future. With regards to market acceptance, the introduction of the Haydock Brown Hybrid machine (HBH machine), offers many near term advantages in the market place and is close to exploitation and is therefore considered first in the following sections.

9.1.1 Fixed Speed Power Generation

Table 9.1, briefly compares a conventional synchronous generator with the HBH machine of the same rating. It should be remembered the Hybrid version was not designed but tried after the design and test of the original HB concept. Therefore the design is not optimal so further size and cost reductions will be possible in the future.

	Units	8kVA Conventional Synchronous Machine	Haydock Brown Hybrid Machine	Notes
Length	mm	364.5	242	34% reduction
Width	mm	400	360	10% reduction
Height	mm	414	412	Similar
Cubic Volume	mm ³	6.00E+07	3.59E+07	40% reduction
Weight	kg	85	85	Similar
Efficiency	%	76.3	88	11.7% improvement

Table 9.1 Comparison between a conventional synchronous machine and the Haydock Brown Hybrid machine

On a material cost basis the HBH machine appears to be approximately 30% more expensive than the conventional synchronous machine. Material costs for new ideas with no established supply history is subjective. The permanent magnets tend to make up a significant proportion of the cost but market trends suggest this cost should reduce over time. The main advantage of this topology is it is simple to manufacture and could be fully automated. The parts count for a conventional generator is in the region of 750 compared to 225 for this concept. Clearly inventory and manufacturing costs could be significantly reduced.

With the axial length of the HBH machine being comparatively small, costs can be reduced for the generating set builder. For example, shorter length means a shorter bedplate, reduced canopy size and reduced shipping costs. The end user also desires compact size to reduce civil works and real-estate costs. This reduction in length is accompanied by a reduction in width, ensuring the generator does not foul on air filters, starter motors, etc, mounted around the engine flywheel housing. The weight of the HBH machine is similar to a conventional machine but different processes, such as a high-pressure die-cast frame and detailed mechanical analysis, will realise some additional weight savings. It should also be understood if an integrated generating set concept is considered, like with the TORUS machine, similar advantages are possible. Another key advantage is the higher efficiency. In the power generation industry this advantage is not just a 'green' issue, it makes real economic sense to have the generators efficiency as high as possible. This ensures more power appears at the generator terminals for a given engine size making the overall generating set package more compact and lower cost.

The main concerns for the HBH topology are that earlier studies in Chapter 3 suggested the axial flux machine is volumetrically compromised for lower pole numbers. It is known that active material content for axial flux machines is compromised due to the restricted electric loading. The compact size is achieved through integration of the excitation system into the main machine structure and the use of high energy density permanent magnets. Therefore if the topology was transformed into the radial plane, even more advantages may present themselves. Unfortunately a sensible method for doing this has not been discovered to date.

9.1.2 Variable Speed Power Generation

Variable speed generating sets are likely to have a good medium to long term future. To put the variable speed generating set into context, consider the graph in Figure 9.1 which shows the vision General Motors has of the future car industry.

By the year 2020 it is expected Hybrid Electric Vehicles (HEV) will make up 50% of the global car market. Many of the elements needed to make a HEV are common to a VSIG. Therefore with the economies of scale, issues such as market acceptance, cost and reliability will be well established for this type of technology.

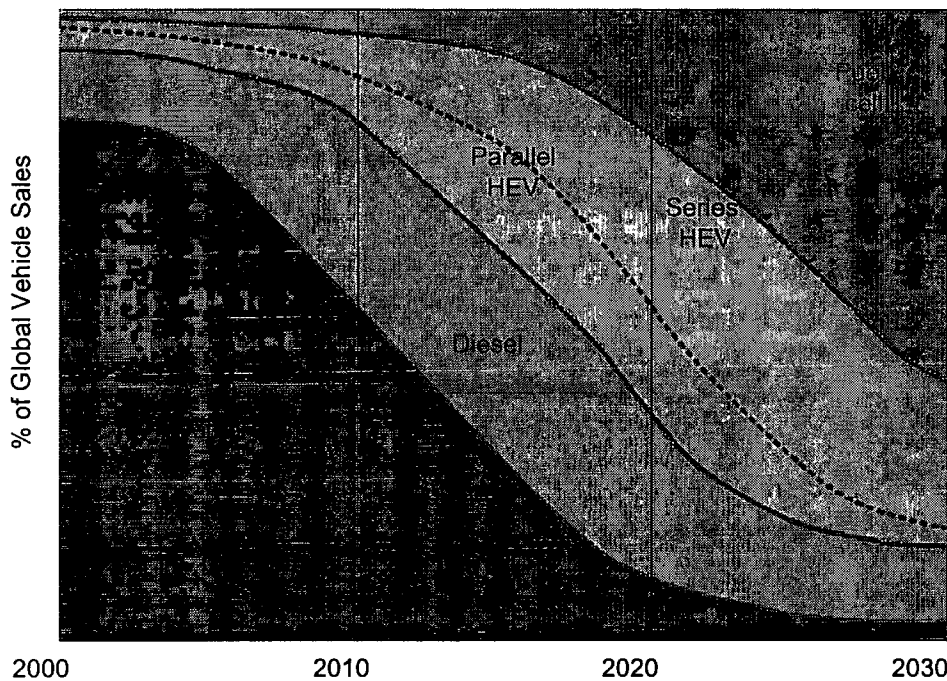


Figure 9.1 A slide showing General Motors vision of the future car industry

The axial machine with all its engine integration benefits is clearly the right solution for the variable speed application. The weight of axial flux generator is 25% that of conventional, excluding the flywheel and coupling disc weight in a conventional generator. The axial flux generator only takes up 15% of the volume. A direct comparison with a synchronous generator is unfair, as the VSIG requires additional power electronics and control. However research shows the overall package size is half that compared to a conventional generating set. At the time of writing the VSIG cost appears to be around 3 times that of the conventional. This additional capital cost is offset when compared to the maintenance and fuel costs over the life cycle of the set. Dependent upon load profile and battery capacity the total capital and running costs could be halved.

9.2 Further Work

9.2.1 Fixed Speed

A full investigation into the Haydock Brown Hybrid machine is necessary. To date all the analysis has assumed linearity in the pole, tooth and core back so saturation effects should be considered. Looking into the detail of certain aspects such as slot profile, magnet and ferrous pole shape all need to be explored to try and optimise the design. The HBH machine is a new form of electrical machine with a complex electromagnetic structure that could take decades to analyse completely. In addition the derivation of an electrical equivalent circuit for this type of machine that satisfies all operating conditions appears challenging, considering the interaction of three excitation sources, non linearity, significant leakage and variation of stator leakage with power factor.

Thermal issues have not been addressed. The electromagnetic limit set by the shaft dominates the design, and thermally the machine is only running at moderate temperatures. There is still merit in researching the cooling circuit as if the shaft cross sectional area could be increased while retaining the same cooling, ratings could be enhanced.

Another issue is the transient analysis of the machine. When load is applied the armature reaction flux tries to pass into the rotor plates and shaft. However with the rotor and shaft being manufactured from a solid conductor, eddy current effects should prevent any rapid change of flux in these regions. This may appear advantageous as the armature reaction flux is faced initially with a high reluctance to reduce the initial transient voltage drop.

Unfortunately the AVR feeding the excitation coil is required to force field flux into the shaft to maintain a constant terminal voltage at the generator. This rapid change in flux will constrain the excitation system and the author is not quite sure of the machines transient performance.

Another area of research is to explore multi-pole versions of the HB concept particularly for variable speed type applications. To be able to regulate the voltage on the dc bus with low power electronics is a definite advantage that could significantly reduce the cost and complexity of the full line current power electronics.

9.2.2 Variable Speed

The TORUS concept with an air-gap winding has been identified as having very low internal impedance. The thermal limit sets the maximum continuous torque the generator can deliver. This additional permanent magnet excitation is therefore not being economically used. With such low impedance the issue of short circuit current, mechanically and thermally stressing the winding is a major concern. Solutions for increasing the machine impedance so that the magnet excitation becomes the torque limiting design parameter should be sought. One approach, which has been used in the HB concept, was to use a slotted stator structure. This has problems, as the reluctance variation due to slotting is likely to introduce additional losses on the magnets and stator teeth, this is compounded by the higher operating frequency. The investigation of a suitable slot profile that balances these losses with manufacturing aspects would be of interest.

Another suggestion would be to replace every other magnet with a ferrous pole to reduce magnet content and increase the machine impedance. The issue of how to secure the windings in position during a short circuit will still be of concern, but at least these forces would be dramatically reduced.

Application specific design details for the VSIG application require further investigation. The interaction of what parameters with respect to the electrical machine would benefit the system as a whole, need to be explored. For example the VSIG has a requirement for a regulated dc supply. This has been achieved with a 6 pulse rectifier requiring a three phase supply which could have equally been achieved with say a 5 phase system. With a 3 phase system line to line voltages do not support 3rd harmonics and so designing a machine with 3rd harmonic present in the waveform offers no benefit. The author believes a study of pole arc, winding inductance and number of phases for different rectifier configurations would be of interest and has not been previously well researched.

Appendix A

Optimisation Support Data

Coefficients

a ₁	a ₂	a ₃	a ₄	a ₅	a ₆	a ₇	a ₈	a ₉	a ₁₀	a ₁₁
-1.216922	36.19409	-16.70387	0.917965	-10.98375	5.34034	-0.09532	0.861311	-0.426347	0.743755	27.64548
a ₁₂	a ₁₃	a ₁₄	a ₁₅	a ₁₆	a ₁₇	a ₁₈	a ₁₉	a ₂₀	a ₂₁	a ₂₂
-12.31202	-0.803921	-0.799189	-0.097483	0.086973	-0.110875	0.097274	-0.120756	-1.01432	0.386426	0.068823
a ₂₃	a ₂₄	a ₂₅	a ₂₆	a ₂₇						
1	0.038574	-0.00715	0.009803	-0.008274						

K	T	L _w	L _m	E _{rms}	E _{model}	%error
0.66	1	7.5	10	50.5	50.5	0.00
0.66	1	7.5	6	37.3	37.3	0.00
0.66	1	7.5	2	15.8	15.8	0.00
0.66	1	4.25	10	66.7	66.7	0.00
0.66	1	4.25	6	51.2	51.2	0.00
0.66	1	4.25	2	23.1	23.1	0.00
0.66	1	1	10	93.7	93.7	0.00
0.66	1	1	6	77.3	77.3	0.00
0.66	1	1	2	40.2	40.2	0.00
0.66	0.81	7.5	10	48.6	48.6	0.00
0.66	0.81	7.5	6	35.7	35.7	0.00
0.66	0.81	7.5	2	15	15.0	0.00
0.66	0.81	4.25	10	63.9	63.9	0.00
0.66	0.81	4.25	6	48.8	48.9	-0.13
0.66	0.81	4.25	2	21.9	21.9	0.00
0.66	0.81	1	10	89.1	89.1	0.00
0.66	0.81	1	6	73.1	73.0	0.08
0.66	0.81	1	2	37.8	37.8	0.00
0.66	0.52	7.5	10	38	38.0	0.00
0.66	0.52	7.5	6	27.9	27.9	0.00
0.66	0.52	7.5	2	11.7	11.7	0.00
0.66	0.52	4.25	10	49.7	49.7	0.00
0.66	0.52	4.25	6	37.9	37.9	0.00
0.66	0.52	4.25	2	17	17.0	0.00
0.66	0.52	1	10	69.1	69.1	0.00
0.66	0.52	1	6	56.7	56.7	0.00
0.66	0.52	1	2	29.3	29.3	0.00
					max error	0.08
					min error	-0.13

Table A.1 Coefficients for the 4th order polynomial used to describe E_{model} compared to pre-computed FEA solutions

FEA solution K=0.5						FEA solution K=0.66						FEA solution K=0.85					
T	L _w	L _m	E _{rms}	E _{model}	%ERRO	T	L _w	L _m	E _{rms}	T	L _w	L _m	E _{rms}	E _{model}	%ERROR		
1	7.5	10	64.8	65.4	-0.91	1	7.5	10	50.5	1	7.5	10	26.6	26.6	-0.14		
1	7.5	6	48.1	48.3	-0.41	1	7.5	6	37.3	1	7.5	6	19.7	19.7	0.13		
1	7.5	2	20.4	20.5	-0.29	1	7.5	2	15.8	1	7.5	2	8.3	8.3	-0.41		
1	4.3	10	86.1	86.4	-0.31	1	4.25	10	66.7	1	4.25	10	35.1	35.2	-0.23		
1	4.3	6	66.3	66.3	0.01	1	4.25	6	51.2	1	4.25	6	27	27.0	-0.02		
1	4.3	2	30	29.9	0.30	1	4.25	2	23.1	1	4.25	2	12.2	12.2	0.13		
1	1	10	121.8	121.3	0.39	1	1	10	93.7	1	1	10	49.4	49.4	-0.04		
1	1	6	100.6	100.1	0.51	1	1	6	77.3	1	1	6	40.8	40.8	0.07		
1	1	2	52.4	52.1	0.66	1	1	2	40.2	1	1	2	21.3	21.2	0.45		
					max error						0.66						
					min error						-0.91						
										max error						0.45	
										min error						-0.41	

K			0.5	0.66	0.85
T	L _w	L _m	Normalised Erms with respect to k		
1	7.5	10	1.28	1.00	0.53
1	7.5	6	1.29	1.00	0.53
1	7.5	2	1.29	1.00	0.53
1	4.25	10	1.29	1.00	0.53
1	4.25	6	1.29	1.00	0.53
1	4.25	2	1.30	1.00	0.53
1	1	10	1.30	1.00	0.53
1	1	6	1.30	1.00	0.53
1	1	2	1.30	1.00	0.53
average			1.29	1.00	0.53

Table A.2 Normalised E_{rms} for values of K

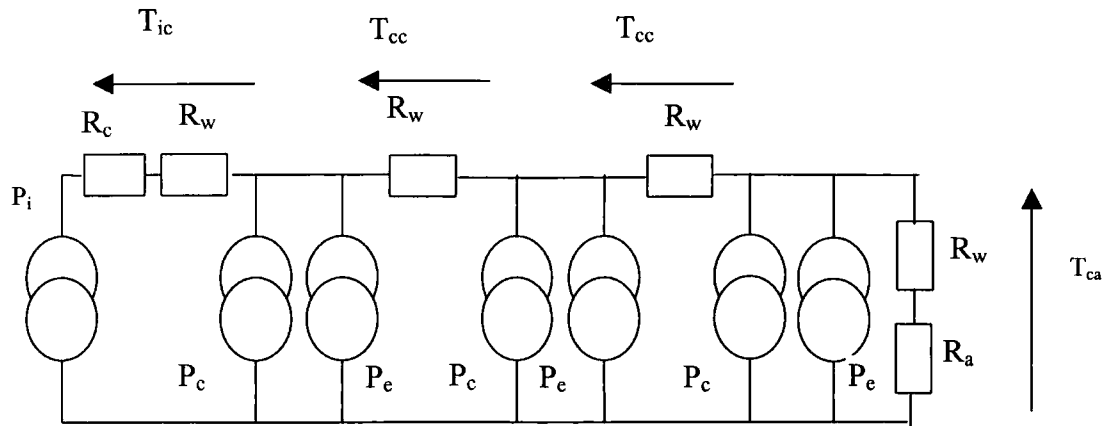
K	pole arc	L_w	L_m	E_{rms}	E_{model}	%error
0.5	0.79	7.5	10	62	62.4	-0.59
0.5	0.79	7.5	6	45.7	45.8	-0.21
0.5	0.79	7.5	2	19.3	19.2	0.35
0.5	0.79	4.25	10	81.9	82.0	-0.09
0.5	0.79	4.25	6	62.6	62.7	-0.09
0.5	0.79	4.25	2	28.1	28.1	0.10
0.5	0.79	1	10	114.6	114.2	0.32
0.5	0.79	1	6	94.1	93.6	0.52
0.5	0.79	1	2	48.6	48.4	0.35
0.5	0.47	7.5	10	45.6	45.6	-0.04
0.5	0.47	7.5	6	33.5	33.5	-0.11
0.5	0.47	7.5	2	14.1	14.1	0.11
0.5	0.47	4.25	10	59.8	59.6	0.31
0.5	0.47	4.25	6	45.8	45.5	0.75
0.5	0.47	4.25	2	20.5	20.4	0.33
0.5	0.47	1	10	83.4	83.0	0.53
0.5	0.47	1	6	68.6	68.2	0.56
0.5	0.47	1	2	35.5	35.3	0.63
0.58	1	7.5	10	58.3	58.5	-0.41
0.58	1	7.5	6	43.2	43.2	-0.09
0.58	1	7.5	2	18.3	18.3	-0.09
0.58	1	4.25	10	77.2	77.3	-0.16
0.58	1	4.25	6	59.4	59.4	0.08
0.58	1	4.25	2	26.8	26.8	0.08
0.58	1	1	10	108.9	108.6	0.26
0.58	1	1	6	89.8	89.6	0.21
0.58	1	1	2	46.7	46.6	0.21
0.58	0.8	7.5	10	56	56.1	-0.17
0.58	0.8	7.5	6	41.2	41.2	0.01
0.58	0.8	7.5	2	17.3	17.3	-0.03
0.58	0.8	4.25	10	73.6	73.7	-0.19
0.58	0.8	4.25	6	56.5	56.4	0.22
0.58	0.8	4.25	2	25.3	25.3	0.15
0.58	0.8	1	10	103	102.8	0.20
0.58	0.8	1	6	84.5	84.2	0.30
0.58	0.8	1	2	43.7	43.6	0.25
0.58	0.5	7.5	10	42.5	42.8	-0.72
0.58	0.5	7.5	6	31.2	31.4	-0.78
0.58	0.5	7.5	2	13.1	13.2	-0.70
0.58	0.5	4.25	10	55.7	56.0	-0.48
0.58	0.5	4.25	6	42.6	42.7	-0.18
0.58	0.5	4.25	2	19.1	19.2	-0.30
0.58	0.5	1	10	77.5	77.8	-0.43
0.58	0.5	1	6	63.4	63.9	-0.81
0.58	0.5	1	2	33	33.0	-0.11
0.85	0.83	7.5	10	25.7	25.8	-0.54
0.85	0.83	7.5	6	18.9	19.0	-0.46
0.85	0.83	7.5	2	7.97	8.0	-0.16
0.85	0.83	4.25	10	33.9	34.0	-0.26
0.85	0.83	4.25	6	25.9	26.0	-0.37
0.85	0.83	4.25	2	11.7	11.7	0.37
0.85	0.83	1	10	47.3	47.4	-0.25
0.85	0.83	1	6	38.95	38.9	0.16
0.85	0.83	1	2	20.2	20.1	0.33
0.85	0.57	7.5	10	21.1	21.4	-1.22
0.85	0.57	7.5	6	15.5	15.7	-1.09
0.85	0.57	7.5	2	6.5	6.6	-1.01
0.85	0.57	4.25	10	27.6	28.0	-1.29
0.85	0.57	4.25	6	21.1	21.3	-1.06
0.85	0.57	4.25	2	9.5	9.6	-0.54
0.85	0.57	1	10	38.4	38.9	-1.19
0.85	0.57	1	6	31.6	31.8	-0.76
0.85	0.57	1	2	16.4	16.4	-0.29
0.58	0.9	7.5	10	58.1	58.0	0.24
0.58	0.9	3	5	61	60.8	0.29
0.58	0.8	6	10	63.3	62.8	0.76
0.58	0.8	7.5	4	30.7	30.4	1.06
0.58	0.7	3	5	54.4	55.0	-1.09
0.58	0.7	6	3	26.6	25.8	2.96

Table A.3 Compares E_{model} with random pre-computed FEA solutions

Data points to check model for synchronous reactance				
K	$L_{\text{gross gap}}$	Inductance	L_{model}	%error
0.5	5.5	1.477E-05	1.43E-05	3.27
0.5	9.125	9.721E-06	9.75E-06	-0.31
0.5	12.75	7.673E-06	7.66E-06	0.20
0.5	16.375	6.626E-06	6.85E-06	-3.43
0.5	20	6.026E-06	6.18E-06	-2.62
0.58	5.5	1.34E-05	1.31E-05	2.48
0.58	9.125	9.02E-06	8.95E-06	0.74
0.58	12.75	7.21E-06	7.03E-06	2.47
0.58	16.375	6.27E-06	6.29E-06	-0.24
0.58	20	5.74E-06	5.67E-06	1.07
0.66	5.5	1.19E-05	1.18E-05	0.77
0.66	9.125	8.009E-06	8.06E-06	-0.66
0.66	12.75	6.407E-06	6.33E-06	1.18
0.66	16.375	5.575E-06	5.67E-06	-1.63
0.66	20	5.091E-06	5.11E-06	-0.42
0.75	5.5	1.005E-05	1.02E-05	-1.52
0.75	9.125	6.831E-06	6.96E-06	-1.91
0.75	12.75	5.496E-06	5.47E-06	0.52
0.75	16.375	4.796E-06	4.89E-06	-2.01
0.75	20	4.386E-06	4.41E-06	-0.67
0.85	5.5	7.861E-06	8.22E-06	-4.63
0.85	9.125	5.529E-06	5.61E-06	-1.53
0.85	12.75	4.546E-06	4.41E-06	3.01
0.85	16.375	4.024E-06	3.95E-06	1.95
0.85	20	3.716E-06	3.56E-06	4.20

max	4.20
min	-4.63

Table A.4 Compares the polynomial model with pre-computed FEA solutions



P_i = Iron losses (W/m^2) R_c = Thermal resistance of core insulation (m^2k/W)
 P_c = Copper losses (W/m^2) R_w = Thermal resistance of conductor insulation (m^2k/W)
 P_e = Eddy losses (W/m^2) R_a = $1/\text{Thermal coefficient for air}$ (m^2k/W)
 Total Temperature Rise = $T_{ic} + T_{cc} + T_{cc} + T_{ca}$

Figure A.1 Thermal equivalent circuit for three layered winding

Appendix B

Calculation of leakage fields by applying Vector Potential Analysis

The following demonstrates a method for calculating leakage fields. Both cases 1 and 2 concentrate on a calculation method for estimating the field flux over a cylindrical surface. The first case assumes the leakage fields go out to infinity, the second case has a finite cylindrical magnetic boundary. In both cases the fields are related back to an equivalent system of uniform field and constant area based upon the area of the cylindrical surface.

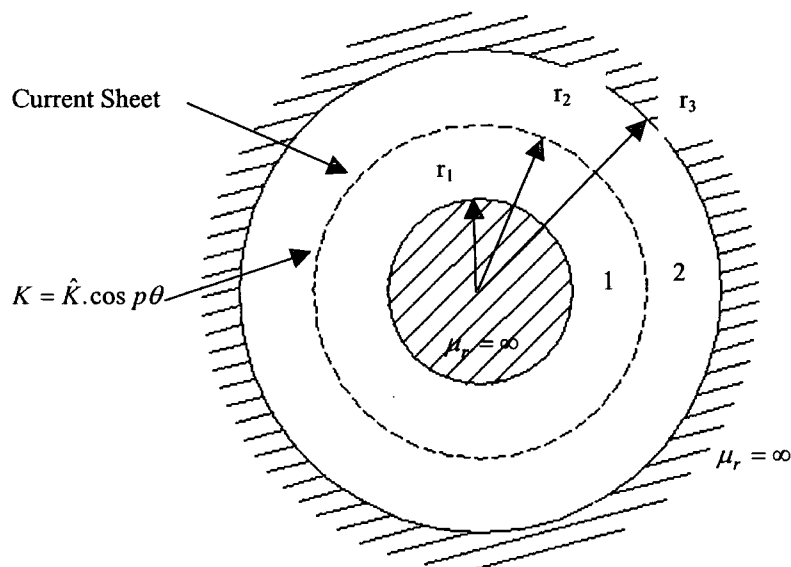


Figure B.1 Simplified model

Important note, unlike the rest of this thesis, P refers to the number of pole pairs.

Laplace equation[77] in polar coordinates states that

$$\frac{1}{r} \frac{\partial A_z}{\partial r} + \frac{\partial^2 A_z}{\partial r^2} + \frac{1}{r^2} \frac{\partial^2 A_z}{\partial \theta^2} = 0$$

Where A_z is the Vector Potential in the axial plane only

Referring to Figure B.1, A_z needs to be of a similar form to K .

Assume $A_z = Ar^m \cos P\theta$

Substituting

$$\frac{1}{r} \cdot \frac{\partial A_z}{\partial r} = A.m.r^{m-2} \cdot \cos P\theta$$

$$\frac{\partial^2 A_z}{\partial r^2} = A.m.(m-1).r^{m-2} \cdot \cos P\theta$$

$$\frac{1}{r^2} \cdot \frac{\partial^2 A_z}{\partial \theta^2} = -A.P^2.r^{m-2} \cdot \cos P\theta$$

Therefore

$$\nabla^2 A_z = 0 = \{m + m.(m-1) - P^2\} A.r^{m-2} \cdot \cos P\theta$$

$$m = \pm P$$

So the general solution is $A_z = A_1.r^P \cdot \cos P\theta + A_2.r^{-P} \cdot \cos P\theta$

Referring to Figure B.1

For region 1, $A = A_{11}.r^p \cdot \cos p\theta + A_{12}.r^{-p} \cdot \cos p\theta$

For region 2, $A = A_{21}.r^p \cdot \cos p\theta + A_{22}.r^{-p} \cdot \cos p\theta$

Where $A_{11}, A_{12}, A_{21}, A_{22}$ are constants.

Boundary conditions

At boundary 1 (r_1) assuming an infinitely permeable material, $B_\theta = 0$

At boundary 2 (r_2) B_θ changes by $\mu_0 \hat{K} \cos p\theta$ and B_r is unchanged - Amperes Law

At boundary 3 (r_3) assuming an infinitely permeable material, $B_\theta = 0$

Using Maxwell equation $B = \nabla \times A$

The radial flux density, $B_r = \frac{1}{r} \cdot \frac{\partial A}{\partial \theta}$

The tangential flux density, $B_\theta = -\frac{\partial A}{\partial r}$

$$B_\theta \text{ region 1} = -p \cdot A_{11} \cdot r_1^{p-1} \cdot \cos p\theta + p \cdot A_{12} \cdot r_1^{-(p+1)} \cdot \cos p\theta$$

$$\text{so } -p \cdot A_{11} \cdot r_1^{p-1} + p \cdot A_{12} \cdot r_1^{-(p+1)} = 0$$

$$A_{11} - A_{12} \cdot r_1^{-2p} = 0 \quad (\text{B.1})$$

$$B_\theta \text{ region 3} = -p \cdot A_{21} \cdot r_3^{p-1} \cdot \cos p\theta + p \cdot A_{22} \cdot r_3^{-(p+1)} \cdot \cos p\theta$$

$$\text{so } -p \cdot A_{21} \cdot r_3^{p-1} + p \cdot A_{22} \cdot r_3^{-(p+1)} = 0$$

$$A_{21} - A_{22} \cdot r_3^{-2p} = 0 \quad (\text{B.2})$$

At boundary 2

$$-p \cdot A_{11} \cdot r_2^{p-1} + p \cdot A_{12} \cdot r_2^{-(p+1)} + p \cdot A_{21} \cdot r_2^{p-1} - p \cdot A_{22} \cdot r_2^{-(p+1)} = \hat{K} \mu_0$$

$$-A_{11} + A_{12} \cdot r_2^{-2p} + A_{21} - A_{22} \cdot r_2^{-2p} = \hat{K} \mu_0 / p \cdot r_2^{p-1} \quad (\text{B.3})$$

$$B_r \text{ in region 1} = + p.A_{11}.r^{p-1}.\sin p\theta - p.A_{12}.r^{-(p+1)}.\sin p\theta$$

$$B_r \text{ in region 2} = + p.A_{21}.r^{p-1}.\sin p\theta - p.A_{22}.r^{-(p+1)}.\sin p\theta$$

So at boundary 2,

$$+ p.A_{11}.r_2^{p-1} + p.A_{12}.r_2^{-(p+1)} = p.A_{21}.r_2^{p-1} + p.A_{22}.r_2^{-(p+1)}$$

$$A_{11} + A_{12}.r_2^{-2p} - A_{21} - A_{22}.r_2^{-2p} = 0 \quad (\text{B.4})$$

Substitute in (B.3) from (B.1) and (B.2)

$$- A_{11} + A_{11}.(r_1/r_2)^{2p} + A_{21} - A_{21}.(r_3/r_2)^{2p} = \hat{K} \mu_0 / p.r_2^{p-1} \quad (\text{B.5})$$

Substitute in (B.4) from (B.1) and (B.2)

$$A_{11} + A_{11}.(r_1/r_2)^{2p} - A_{21} - A_{21}.(r_3/r_2)^{2p} = 0 \quad (\text{B.6})$$

Adding (B.5) and (B.6) and dividing by 2

$$A_{11}.(r_1/r_2)^{2p} - A_{21}.(r_3/r_2)^{2p} = \hat{K} \mu_0 / 2.p.r_2^{p-1} \quad (\text{B.7})$$

Subtract (B.5) from (B.6) and divide by 2

$$A_{11} - A_{21} = -\hat{K} \mu_0 / 2.p.r_2^{p-1} \quad (\text{B.8})$$

Multiply (B.7) by $(r_2/r_1)^{2p}$

$$A_{11} - A_{21} \cdot (r_3 / r_1)^{2p} = \frac{\hat{K} \mu_0}{2 \cdot p \cdot r_2^{p-1}} \cdot (r_2 / r_1)^{2p} \quad (\text{B.9})$$

Subtract B.8 from B.9

$$A_{21} \cdot [1 - (r_3 / r_1)^{2p}] = \frac{\hat{K} \mu_0}{2 \cdot p \cdot r_2^{p-1}} \cdot [(r_2 / r_1)^{2p} + 1] \quad (\text{B.10})$$

So

$$A_{21} = \frac{\hat{K} \mu_0}{2 \cdot p \cdot r_2^{p-1}} \cdot \left[\frac{r_2^{2p} + r_1^{2p}}{r_1^{2p} - r_3^{2p}} \right] = - \frac{\hat{K} \mu_0}{2 \cdot p \cdot r_2^{p-1}} \cdot \left[\frac{r_2^{2p} + r_1^{2p}}{r_3^{2p} - r_1^{2p}} \right] \quad (\text{B.11})$$

Then from (B.8)

$$A_{11} = - \frac{\hat{K} \mu_0}{2 \cdot p \cdot r_2^{p-1}} \cdot \left[\frac{r_3^{2p} + r_2^{2p}}{r_3^{2p} - r_1^{2p}} \right] \quad (\text{B.12})$$

From (B.12) and (B.1)

$$A_{12} = - \frac{\hat{K} \mu_0}{2 \cdot p} \cdot \frac{r_1^{2p}}{r_2^{p-1}} \cdot \left[\frac{r_3^{2p} + r_2^{2p}}{r_3^{2p} - r_1^{2p}} \right] \quad (\text{B.13})$$

From (B.11) and (B.2)

$$A_{22} = - \frac{\hat{K} \mu_0}{2 \cdot p} \cdot \frac{r_3^{2p}}{r_2^{p-1}} \cdot \left[\frac{r_1^{2p} + r_2^{2p}}{r_3^{2p} - r_1^{2p}} \right] \quad (\text{B.14})$$

Case 1

Calculate external end leakage with boundary 3 approaching infinity

Set $r_2 = r_1$ and $r_3 \rightarrow \infty$

$$A_{11} = -\frac{\hat{K}\mu_0}{2.P.r_1^{P-1}} \qquad A_{12} = -\frac{\hat{K}\mu_0}{2.p} \cdot \frac{r_1^{2p}}{r_1^{p-1}}$$

$$A_{21} = 0 \qquad A_{22} = -\frac{\hat{K}\mu_0}{2.p} \cdot \frac{2.r_1^{2p}}{r_1^{p-1}} = -\frac{\hat{K}\mu_0}{p} . r_1^{p+1}$$

For region 2, $A = -\frac{\hat{K}.\mu_0}{P} . r_1 \cdot \left(\frac{r_1}{r}\right)^P . \cos p\theta$

$$\text{B radial} = \frac{1}{r} \cdot \frac{\partial A}{\partial \theta}$$

$$-\frac{\hat{K}\mu_0}{p} \cdot \left(\frac{r_1}{r}\right)^{p+1} . (-p) . \sin p\theta = \hat{K}\mu_0 \cdot \left(\frac{r_1}{r}\right)^{p+1} . \sin p\theta$$

$$\hat{B}_r = \hat{K}\mu_0 \quad \text{at} \quad r = r_1 \qquad \qquad \qquad \text{(B.15)}$$

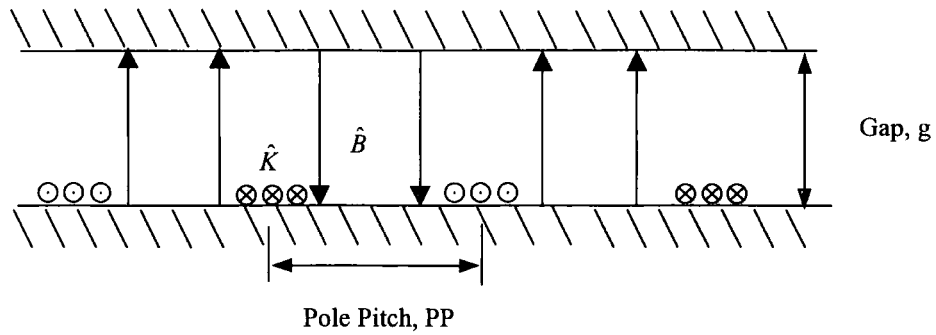


Figure B.2 Equivalent uniform air-gap

For an equivalent uniform air-gap

Current/pole is

$$\hat{K} \cdot \frac{2}{\pi} \cdot PP$$

and applying Ampere's Law

$$2 \cdot g \frac{\hat{B}}{\mu_0} = \frac{2}{\pi} \cdot \hat{K} \cdot PP$$

but from equation B.15

$$\hat{B} = \mu_0 \cdot \hat{K}$$

so

$$2 \cdot g \frac{\mu_0 \cdot \hat{K}}{\mu_0} = \frac{2}{\pi} \cdot \hat{K} \cdot PP$$

Rearranging

$$g = \frac{PP}{\pi}$$

That is the leakage field reluctance can be calculated from an equivalent air-gap length of pole pitch over pie.

Case 2

Calculate internal end leakage $r_2 = r_3$, $r_1 =$ shaft radius

$$\begin{aligned} A_{11} &= -\frac{\hat{K} \cdot \mu_0}{2 \cdot p} \cdot r_3^{(p-1)} \cdot \frac{2 \cdot r_3^{(2p)}}{(r_3^{(2p)} - r_1^{(2p)})} = \\ &= -\frac{\hat{K} \cdot \mu_0}{p} \cdot \frac{r_3^{(p+1)}}{(r_3^{(2p)} - r_1^{(2p)})} \end{aligned}$$

$$\begin{aligned} A_{12} &= -\frac{\hat{K} \cdot \mu_0}{2 \cdot p} \cdot \frac{r_1^{(2p)}}{r_3^{(p-1)}} \cdot \frac{2 \cdot r_3^{(2p)}}{(r_3^{(2p)} - r_1^{(2p)})} = \\ &= -\frac{\hat{K} \cdot \mu_0}{p} \cdot \frac{r_1^{(2p)} \cdot r_3^{(p+1)}}{(r_3^{(2p)} - r_1^{(2p)})} \end{aligned}$$

For region 1

$$A = -\frac{\hat{K} \cdot \mu_0}{p} \cdot \frac{r_3^{(2p+1)}}{r_3^{(2p)} - r_1^{(2p)}} \cdot \left[r^p + \frac{r_1^{2p}}{r^p} \right] \cdot \cos p\theta$$

B radial =

$$\frac{1}{r} \cdot \frac{\partial A}{\partial \theta}$$

$$= -\frac{\hat{K} \cdot \mu_0}{p} \cdot \frac{r_3^{(p+1)}}{r_3^{(2p)} - r_1^{(2p)}} \cdot \left[r^p + \frac{r_1^{2p}}{r^p} \right] \cdot \frac{1}{r} \cdot (-p) \cdot \sin p\theta$$

$$\hat{B}_r \text{ at } r_3 = \hat{K} \cdot \mu_0 \cdot \frac{r_3^{(p)}}{r_3^{(2p)} - r_1^{(2p)}} \cdot \left[r_3^p + \frac{r_1^{2p}}{r_3^p} \right] = \hat{K} \cdot \mu_0 \cdot \frac{r_3^{(2p)} + r_1^{(2p)}}{r_3^{(2p)} - r_1^{(2p)}}$$

$$\text{Equivalent gap} = \frac{PP}{\pi} \cdot \frac{(r_3/r_1)^{(2p)} - 1}{(r_3/r_1)^{(2p)} + 1}$$

That is the leakage reluctance can be calculated from an equivalent air-gap length of pole pitch over pie corrected with respect to the position of the magnetic boundary.

Remember, P in this exercise refers to pole pairs, not the number of poles like the rest of this thesis

References

- [1] Brown N, "Synchronous Generator Case Study", IEE Residential course on Electrical Generators, 1999/2001.
- [2] Anders M, Ola A, Edgar K, Marco S, Jari W, "Micro Turbines: speeding the shift to distributed heat and power", Engineering Technology, May 2001.
- [3] Brown N, Haydock L, "Full Integration of an Axial Flux Machine for Reciprocating Engine Variable Speed Generating Sets", IEE Seminar, Axial Airgap machines, May 2001.
- [4] Laughton M A, "Fuel Cells", IEE Power Engineering Journal, Feb 2002, Vol. 16, No1.
- [5] Electrical Engineers Reference Book, 8th Edition, 1955, George Newnes Ltd, page 29-18.
- [6] YANG L, "Further development of NdFeB magnet industry in China". Magnews Summer 1999.
- [7] "A permanent magnet electrical machine" Application No 0115857.5, priority date 28/6/01, Newage International Ltd.
- [8] "A method of and Apparatus for Automatically Mounting Permanent Magnets on a Member Formed of Ferrous Metal" Application No 0009755.0, priority date 19/4/00, Newage International Ltd.

[9] "A Toroidal AC Machine and an Annular Winding Carrier", Application No 0110783.8, priority date 2/5/01, Newage International Ltd.

[10] "Windings", Application No 0110784.6, priority date 2/5/01, Newage International Ltd.

[11] "A Method of Fixing Unmagnetised Magnetisable Members to a Rotor Disc", Application No GB02/00092, Priority Date 10/01/01, Newage International Ltd.

[12] "A Permanent Magnet AC machine", Application No 0207127.2, priority date not known, Newage International Ltd.

[13] "A Motive Power Transmission", not yet filed, Newage International Ltd.

[14] "An AC Power Generating System", Application No GB01/00169, Priority date 21/1/00, Newage International Ltd.

[15] "A Permanent Magnet AC Machine", Application No GB01/03323, Newage International Ltd.

[16] "Electrical Machine Components", Application No GB01/05426, Newage International Ltd.

[17] Mahon L L J, "Diesel Generator Handbook", ISBN 0-7506-1147-2

[18] Brown N, Bumby J R, Haydock L, "Foresight Vehicle: A toroidal, axial flux generator for hybrid IC engine/battery electric vehicle applications", SAE 2002.

[19] Bumby J R, Brown N, "Auxiliary Power Units: A Role for the TORUS Generator?", IEE colloquium on HEV, Durham, April 2000.

[20] Chen Z, McCormick M, Brown N, Haydock L, "A Voltage Source Active Rectifier with Controllable Power Factor and Minimized Harmonics", EPE2001.

[21] Chen Z, McCormick M, Brown N, Haydock L, "A Study of the Effects of PWM Switching Power Electronic Converters on AC Systems", ICEM2001.

[22] Say M G, "Alternating Current Machines", Longman Scientific & Technical, 5th Edition.

[23] Ruqi Li, Rene Spee, Alan K Wallace and G.C. Alexander, "Synchronous Drive Performance of Brushless Doubly-Fed Motors", IEEE Trans of Industrial Applications, Vol 30, No4, July/Aug 1994

[24] 'Concycle', Newage AVK SEG, Barnack Road, Stamford, Lincs. PE9 2NB.
www.newage-avkseg.com

[25] Hendershot J R, Miller T J E, "Design of Brushless Permanent Magnet Motors", Clarendon Press, Oxford, 1994.

[26] Honda Y, Higaki T, Morimoto S, Takeda Y, "Rotor Optimisation of a multilayer interior PM synchronous motor", IEE Proc. Vol. 145, Iss. 2, p119, March 1998.

[27] Chalmers B J, Akmes R, "Analysis of the voltage regulation characteristic of a permanent-magnet alternator with inverse saliency", Electrical Machines and Power Systems, vol 25, pp317-326, 1997.

[28] Binns J K, Low T S, "Performance and application of multi-stacked imbricated PM generators", IEE proc, Vol 130, Pt B, No6, Nov 1983.

[29] McGrow L, Pollock C, "Low Cost Brushless Generators", IEEE IAS, Oct. 1999.

[30] Wang C, Nasar S A, Boldea I, "Three-phase flux reversal machine (FRM)", IEE Proc, Electric Power Appl, Vol 146, No2, March 1999.

[31] Llibre J F, Matt D, "Vernier Reluctance Magnet Machine For Electric Vehicle", Proc. International Conf. Elec. Mach., SEPT 94, Vol 1, PP251-256

[32] Weh H, May H, "Achievable Force Densities for PM Excited Machines in New Configurations", ICEM 86, PP1107-1111.

[33] The Turbo Genset Company Ltd. Unit 3, Heathrow Summit Centre, Skyport Drive, Hatch Lane, West Drayton, Middlesex UB7 OL J, info@turbogenset.com.

[34] JEUMONT INDUSTRIE - 27, rue de l'Industrie - B.P. 189, 59 573 Jeumont Cedex, FRANCE, www.jeumont-framatome.com.

[35] Brown N, Haydock L, Spooner E, "3 Dimensional Finite Element Analysis Of A Toroidally Wound Axial Flux Permanent Magnet Generator", UPEC99, Vol 2, Sept 99.

[36] Brown N, Haydock L, Spooner E, Bumby J, "Optimisation Of Axial Flux PM Generators by Pre-Computed 3D-FEA Modelling", ICEM2000, Vol13.

[37] Brown N, Haydock L, "User Experience of Electromagnetic CAD for Electrical Machine Design", MAGSOC, FEB 2001

[38] Bumby J R, Brown N, Haydock L, "Axial Flux Machines and their Use in Hybrid Electric Vehicles", MagSoc, May, 2002.

[39] Brown N, Bumby J, Haydock L, "An Idealised Geometric Approach to Electromagnetically Comparing Axial and Radial Flux Permanent Magnet Machines", ICEM 2002.

[40] Zhang Z, Profumo F, Tenconi A, "Axial-Flux Versus Radial-Flux PM motors", Electromotion, Vol 3, 1996, p134

[41] Brown N L, Mebarki A, Haydock L, "Design Aspects of a 200kW, 3600RPM, Permanent Magnet Generator for use in a Variable speed integrated generator", PEMD, April 2002, Pub No 487, pp 474-479.

[42] Campbell P, Principals 'Principals of a permanent-magnet, axial-field dc machine', Proc IEE, 1974, 121, (12), pp. 1489-1494.

[43] Rash N M, Spooner E, Howe D, "A permanent magnet alternator for use as an electrodynamic railway brake", IEE Conf No 254, Electrical Machines, Design and Applications, 1985.

[44] Evans P D, Brown D, Eastham JF, "A Study of Permanent Magnet Disc Motor Design", BICEM 87, Beijing, China, 1987, pp 729-732.

[45] Spooner E, Chalmers B J, "Toroidally-Wound, Slotless, Axial-Flux, Permanent Magnet, Brushless-DC Motor", Proc. Int. Conf. Elec. Machines, Pisa, Sept 1988.

[46] El-Missiry M M, Zuncheng Z, Spooner E, "The Thermal Performance of a slotless, Torroidal-Stator, PM Alternator", Proc. UPEC, Aberdeen, Sept 90.

[47] Spooner E, Chalmers B J, El-Missery M M, Kitzman I, "The Design of an axial-flux, slotless, torroidal-stator, PM Machine for Starter/Alternator Applications", Proc. UPEC, Aberdeen, Sept 90.

[48] Spooner E, Chalmers B J, El-Missery M M, Wei W, Renfrew A C, "Motoring performance of the toroidal PM machine 'TORUS'", EMDA 1991.

- [49] Spooner E, Chalmers B J, "TORUS':A slotless, toroidal-stator, PM generator", IEE Proc, Vol 139, No 6, Nov 1992.
- [50] Di Napoli A, Caricchi F, Crescimbinì F, Noia G, "Design criteria of a low speed axial flux PM Synchronous Machine", Proc. Int Conf. Evolution and Modern Aspects of Synchronous Machines, Zurich, Switz, Aug 1991.
- [51] Caricchi F, Crescimbinì F, Napoli D, Honorati O, Lipo T A, Noia G, Santini E, "Development of a IGBT Inverter Driven Axial Flux PM Synchronous Motor Drive", Proc. 4th EPE conf. Vol. 3, pp. 482-487, 1991.
- [52] Caricchi F, Crescimbinì F, Honorati O, Santini E, "Performance Evaluation of An Axial-Flux PM Generator".
- [53] Stiebler M, Okla O, "A PM Toroid Wind-Generator", ICEM'92, Manchester, UK, pp1043-1047, Sept 1992.
- [54] Jensen C, Lipo T,"A low loss PM brushless dc motor utilising Tape Wound Amorphous Iron", IEEE Trans. On ind. App., Vol 28, No3, June 1992
- [55] Wei W, Spooner E, Jinning L, "Field Analysis for disk type PM generators", Wuhan, China, pp74-79, Oct 93.
- [56] Dostal Z, Lipo T, Chalmers B J , "Influence of current waveshape on motoring performance of the slotless PM machine TORUS", Proc, IEE Int Conf on Elec Mach and Drives, Oxford, UK, 93, pp376-380.
- [57] Pan H, Renfrew A C, "Research into wide speed range control of a TORUS Motor", IEEE Cat. No 95TH8130, 1995.

[58] Chalmers B J, "The TORUS generator", IEEE/KTH, Stockholm Power Tech Conference, Sweden, June 1995.

[59] Chalmers B J, Green A M, Reece A B J, Al-Badi A H, "Modelling and simulation of the TORUS generator", IEE Proc Elec Power Appl, Vol 144, No 6, Nov 97.

[60] Green A M, Al-Badi A H, "Modelling and Simulation of a TORUS Generator using PSPICE", UPEC'97.

[61] Wu W, Spooner E, Chalmers B J, "Design of slotless torus generators with reduced voltage regulation", IEE Proc Electr. Power Appl., No5, Sept 95.

[62] Caricchi F, Crescimbin F, Santini E, "Basic Principal of Axial-Flux PM machines Having Counter-Rotating Rotors", Proc. IEEE-IAS annual meeting, Colorado, USA, Oct94.

[63] Caricchi F, Crescimbin F, Fedeli E, Noia G, "Design and Construction of a Wheel-Directly-Coupled Axial-Flux PM Motor Prototype for EVs", IEEE-IAS annual meeting, Colorado, USA, Oct94.

[64] Caricchi F, Crescimbin F, Mezzetti F, Santini E, "Multi-Stage Axial-Flux PM Machine for Wheel Direct Drive", IEEE-IAS, Orlando, Vol 1, 679-684, Ocy. 1995.

[65] Caricchi F, Crescimbin F, "Axial-Flux PM Machine with water cooled ironless stator", Proc of IEEE Power Tech Conf., Stockholm, June 95, pp98-103.

[66] Caricchi F, Crescimbin F, A. Di Napoli, "Prototype of innovative wheel direct drive with water-cooled axial-flux PM motor for electric vehicle applications", IEEE Proc, USA, Vol 2, 764-770, March 96.

[67] Carter, "The electromagnetic field in its engineering aspects", 1954.

[68] Opera-3D Reference Manual, Vectorfields Ltd, Oxford, England, March 1998.

[69] Lander, "Power Electronics", 2nd Edition, McGraw-Hill Book Company, 1987, p275.

[70] Evans PD, Eastham JF, 'Double Disc Alternator with AC side Excitation, IEE Proc, Vol 130, Pt B, No2, March 1983.

[71] Evans P D, Eastham J F, "Disc geometry homopolar synchronous machine", IEE Proc B, Electr. Power Appl., 1980, 127, (5), pp 299-307

[72] Evans P D, Eastham J F, "Slotless-disc alternator with AC-side excitation", IEE Proc. B, 1983,130, (2), pp 95-102.

[73] Evans P D, Eastham J F, "Disc geometry single-phase alternator with slotless stator and AC-side excitation", *ibid*, 1986, 133, (4), pp 270-278.

[74] Eastham JF, Coles PC, Ibrahim M " Double Disc Alternators with Hybrid Excitation", IEE Trans Mag, Vol 28, No 5, Sept 1992, pp3039-3041.

[75] Evans P D, Coles P C and Ibrahim M I, "Double Disc Alternators with Hybrid Excitation", IEEE Trans MAG, Vol. 28, No 5, Sept, 1992.

[76] "Direct Control of air gap flux in permanent magnet machines", US Patent No 6057622, dated May 2000.

[77] Kreyszig E, "Advanced Engineering Mathematics", John Wiley & Sons, 1993

